Asteroseismology of a Possible Blue Straggler Star KIC 11145123

Yoshiki Hatta

Contents

Abstract

Asteroseismology, a branch of stellar physics where we infer interiors of stars based on measurements of stellar oscillations, has been firmly established with the advent of the space-borne missions such as MOST, CoRoT, Kepler, and TESS, enabling us to identify evolutionary stages and investigate internal structure and internal dynamics of the stars; the interiors of the stars are no longer observationally inaccessible places for us, and a large number of asteorseismic studies have been currently greatly contributing to the development of stellar physics in the way the other branches have not been able to do.

KIC 11145123 is one of the Kepler targets, and it has been actively studied asteroseismically. Its well-resolved frequency splittings for p, g, and mixed modes have allowed us to reveal various fascinating aspects of the star, among which there remain two important issues to be solved.

The first issue is related to its evolution. Spectroscopic analyses of the star with Subaru/HDS indicate that the star is a blue straggler star, thought to be born via some interactions with other stars. Although all of the previous theoretical models of the star are computed assuming single-star evolution, high initial helium abundances of > 0.30 are preferred, which partly supports the possibility that the star has experienced some interactions during the evolution. However, non single-star evolution where such interactions are taken into account has not been tested yet. To construct such a non-standard model of the star is one of the primary goals of this dissertation.

The second issue is related to the internal rotation of the star. Based on detailed asteroseismic analyses of the star, it has been pointed out that the convective core of the star is rotating around 5 times faster than the other regions of the star. This suggestion is of great importance because the current understanding of the stellar internal rotation obtained based on the other asteroseismic researches is that stars are rotating almost rigidly throughout them without any strong velocity shear inside them. Nevertheless, the suggestion of the fast core rotation is still far from being a convention in the community because of the model-dependence of the inference, leading to the second goal of this dissertation, namely, to infer the internal rotation of the star based on another model (which is actually the model obtained in the non-standard modeling) to check whether the suggested fast-convective-core rotation really exists or not.

The non-standard modeling of the star is conducted with two steps. In the first step, a number of stellar models for some parameter range are calculated assuming single-star evolution, and models reproducing the general trend of the observed pattern of g-mode period spacings ΔP_{g} are chosen as "candidate models". The grid-based modeling results in the overshooting parameter $f_{\mathrm{ovs}} \sim 0.027$ for low-mass range $(1.2 - 1.6 M_{\odot})$. The sum of squared residuals normalized by the observational uncertainties between the modeled g-mode frequencies and the observed ones is smaller $(\sim 3 \times 10^5)$ than that for the previous models $(\sim 10^6)$. In the second step, the chemical compositions in the envelopes of the "candidate models" obtained in the first step are modified (fixing the deep regions of the models so that the g-mode frequencies are not affected) based on a novel scheme developed in this dissertation. Another set of parameter range is prepared, and grid-based modeling is carried out to find the best model which reproduces the observed p-mode frequencies best. The best model thus constructed has the following parameters: $M = 1.36 M_{\odot}$, $Y_{\mathrm{init}} = 0.26$, $Z_{\mathrm{init}} = 0.002$, $f_{\mathrm{ovs}} = 0.027$, and Age $= 2.169 \times 10^9$ years old. The modification is down to the depth of $r/R \sim 0.67$ and the extent is $\Delta X \sim 0.06$ (ΔX is a difference in hydrogen abundance between the candidate model and the modified model) at the surface. The residuals between the model and the observation are

comparable with those for the previous models, suggesting that it is possible that the star was born with a relatively lower initial helium abundance of ~ 0.26 compared with that of the previous models (> 0.30) and then experienced some modification of the chemical compositions in the envelope.

Based on the envelope-modified model, we have carried out rotation inversion with one of the most standard methods, the Optimally Localized Averaging (OLA) method, and we have also compared the results with the ones which were obtained based on the previous model of the star (computed assuming single-star evolution). We do not see a strong model dependence in the results, and the results are generally common for the two models. The deep radiative region is rotating slightly slower than the envelope does as has been indicated by Kurtz et al. (2014). The latitudinally differential rotation has been confirmed with significance more than 2σ in a rather model-independent way, where the high-latitude region is rotating slightly faster than the low-latitude region is. We have also confirmed the hint for the fast-convective-core rotation for both models.

Resolutions for the two issues concerning KIC 11145123 are thus given by this dissertation. Firstly, the possibility that the star has experienced some interactions during the evolution has been tested for the first time. Though we cannot exclude another possibility that the star has evolved as a single star throughout its life, the results of the test favors a scenario where the envelope of the star has been somehow modified, which is consistent with the formation channel of blue straggler stars. Secondly, the existence of the fast-core rotation is confirmed for both the standard model and the non-standard model, showing little model dependence of the inference. This result should shed new light on the current understanding of the stellar internal rotation, and it also could be an important constraint on theoretical works focusing on the angular momentum transfer inside stars.

Acknowledgement

I have spent every single moment in my five-year doctoral course enjoying studying and researching stellar physics, especially asteroseismology, thanks to the persistent supports of my main supervisor, Takashi Sekii. He never avoids discussing with me, even when I ask him a bunch of silly questions. I would like to express the deepest appreciation to him (as a supervisor who helps a novice in astronomy to become a rookie-seismologist), and also, the greatest respect to him (as a helio-/asteroseismologist who always impresses me with his brilliant way of thinking).

I am also profoundly grateful to my assistant supervisors. Hirohisa Hara always gives me critical and insightful comments on my research. Discussions with him are, because the number of seismologists in Japan is small, very valuable to me, and every time motivates me to work on my research more, in a positive way. Othman Benomar, who is sharing the same office at NAOJ, shows me how a young scientist should be; he is always energetically researching, and at the same time, he helps me when I am faced with some technical problems. Yukio Katsukawa, though he is my ex-assistant supervisor, often kindly cares about me and gives me chances chatting with him on the corridor, which somehow makes me free from some stresses.

I would like to thank one of my collaborators, Masao Takata, who is as bright as Takashi, but in a way different from Takashi, which realizes the intellectually entertaining discussions among us in our weekly held group meetings. I have learned innumerable topics from the discussions.

My colleagues at SOKENDAI/NAOJ are also thanked. In particular, I am indebt to the same grade students, namely, Hiroyuki Ishikawa, Yuta Kawamura, Satoshi Tanioka, Koh Hosokawa, and Noriharu Watanabe. The good old days spent with all of you are precious treasures for me.

Finally, I would like to express my gratitude to my parents, who always support and encourage me to be able to focus on what I am doing, including research activities. I was never able to go through the five-year doctoral course without them.

Chapter 1

Introduction

Stars are one of the most important and ubiquitous components of the Universe. The study of stars, in particular stellar physics, is one of the oldest research fields, but at the same time, one of currently the most actively tackled, still developing, and mysteriously fascinating branches.

Stars have been protagonists in this Universe since its birth. Cosmological observations tell us that there was an epoch called the Cosmic Dark Ages when everything was surrounded by darkness after the Big Bang. The observations, however, also tell us that the Universe has been somehow re-ionized to some extent since then. The most promising candidate for the re-ionization process is ionization by the Ultraviolet photons emitted by the First Stars which are defined as stars born from primordial gases produced only by the Big Bang nucleo-synthesis with no heavy elements. The First Stars, however, have never been found yet. They are also important because they had kicked off chemical enrichment of the Universe via nuclear fusion inside them and supernova explosions. The "polluted" gases subsequently lead to births of next generations of stars. Then, explosion, pollution, and birth, again and again. This is the way the Universe has evolved; stars are playing a central role in this mechanism.

It is fairly easy to find other examples in astronomy where stars are regarded as essential elements to help better understand what are hidden from us in the celestial worlds; they play roles in building the cosmological ladder, understanding how galaxies have been formed (galactic archaeology), characterizing host stars in exoplanet hunting, etc. But that is not all. Another important aspect of stellar physics that must be considered is the fact that, because of extreme environments realized in stars which are otherwise almost impossible for us to set up in laboratories on the earth, they are ideal laboratories for a broad range of fundamental physics such as microphysics, plasma physics, and (magneto-)hydrodynamics. This feature clearly shows that stars themselves are interesting not only as indicators for other astronomical phenomena but also as subjects to be investigated on their own right.

One of the most successful and firmly established fields in stellar physics is the study of stellar structure and evolution. It is Emden who was the first to propose that stars were gaseous spheres, and with Lane, he devised a system of equations to describe the internal structure of stars, which is currently known as the Lane-Emden equation. Such analytical attempts to understand the interiors of stars continued to be developed by Eddington, Chandrasekhar, and so on, along with the contemporary advances in fundamental physics like nuclear physics. The field finally bloomed with the advent of electronic computers which enable us to numerically calculate stellar structures and evolution. The life of stars can be mostly explained, and the interiors of them are no longer be completely inaccessible places.

Nevertheless, we do not know everything at all yet. The first sentence in the preceding paragraph should read in the following way: (Most people believe that) one of the most successful and firmly established fields in stellar physics is study of stellar structure and evolution.

Let us take an example of the most well-studied star in the Universe; the Sun. How precisely do we know about structure and evolution of the closest star? In the case of the Sun, it is relatively simple to construct the model compared with the cases of the other stars because we have a set of precise measurements of the radius, the luminosity, the mass, and the age of the Sun. Despite such rather tight constraints, the study of the solar eigenoscillations, global helioseismology, shows a significant 0.1 percentage difference in sound speed between the theoretical model and the real Sun. The discrepancy is quite small, but not smaller than the estimated uncertainties, indicating that there is something missing in the physical prescriptions of the solar model, and thus, there should be room for improvements even in the case of the most tightly constrained stellar model.

Let alone the other stars, with full of a variety of characteristics in terms of mass, chemical composition, evolutionary stage, and internal dynamics. On one hand, such diversity helps us to carry out statistical studies on stellar clusters and galaxies, or to find some rare phenomena that are not observed for the Sun. On the other hand, the diversity demands us to leave a simple picture of stellar structure and evolution. Binarity is one example. Although there are 1-dimensional stellar evolutionary codes which are claimed to be able to treat processes arising from binarity such as mass accretion, it is still challenging to validate the schemes due to a lack of observational information on internal structures affected by the processes. As it has been considered that a significant fraction of stars have been making up binary systems, validating the existing numerical schemes is one of the most highly prioritized subjects in stellar physics.

Rotation is another example of a process which may affect the stellar structure and evolution, and there has been no established schemes which precisely incorporates physics related to rotation. More than that, rotation has a huge impact on dynamics (e.g., dynamo mechanism) inside stars. It must be instructive to mention that the famous twenty-two-year magnetic cycle of the Sun which is thought to be caused by the dynamo mechanism in the solar interior is still not fully understood.

We are thus currently surrounded by innumerable unsolved problems in stellar physics, such as discrepancies between the standard theory and the observations in terms of the stellar structure and evolution, the effects of binarity and/or rotation on the stellar structure and evolution, and internal dynamics of stars. One of the most recently contributing research fields to challenge these mysteries is asteroseismology, a branch of stellar physics in which we can probe the interiors of stars based on observation of the stellar oscillations. With the unprecedentedly precise measurements of stellar oscillations brought about by the modern spacecrafts, asteroseismology is now blooming and it is providing us a wealth of invaluable, direct information on internal structures and dynamics of millions of the observed stars.

In this dissertation, asteroseismic analyses of KIC 11145123, which is one of the most actively studied Kepler targets because of its high-quality frequency measurements and of its uniqueness with respect to the evolutionary stage and internal dynamics, are presented. The detailed investigations of the interior structure and dynamics of the star shed new light on our understandings of stellar physics, and it also could be a milestone for future asteroseismic studies which are promisingly becoming possible by next-generation space missions.

This chapter comprises three sections. In the first section, basic backgrounds of physics inside low-mass main-sequence stars are introduced together with a few issues regarding internal structure and dynamics of such low-mass stars, which used to be observationally inaccessible subjects in astronomy before asteroseismology are established. The second section is devoted to an introduction of asteroseismology; the main theme of this dissertation. Not only its basic concepts but also the latest achievements realized by asteroseismology, some of which are giving us totally novel perspectives on internal physics of low-mass main-sequence stars, are presented. On the intersection of the preceding two topics is asteroseismology of KIC 11145123. Previous asteroseismic studies of the star and prospects for further analyses are demonstrated in the third section.

1.1 Evolution of low-mass ($1.2M_\odot$ to $2.1M_\odot$) stars; from ZAMS to TAMS

Since most parts in this dissertation are dedicated to investigating internal physics of low-mass main-sequence stars, we firstly would like to provide a brief introduction to the structure and evolution of stars with masses ranging from $1.2M_\odot$ to $2.1M_\odot$, and evolutionary stages from Zero Age Main Sequence (ZAMS) stage to Terminal Age Main Sequence (TAMS) stage. ZAMS is defined as an evolutionary stage when a star initiates stable nuclear hydrogen burning at the central region. TAMS is defined as an evolutionary stage when the star has exhausted almost all the hydrogen at the central region. We would like to make a little remark on internal dynamics of the low-mass stars as well. For more details and comprehensive discussions about the structure and evolution of low-, intermediate-, and high-mass stars, please refer to Kippenhahn et al. (2012), Weiss et al. (2004), etc. Readers are also recommended to refer to Maeder (2009) for cases where rotation or magnetic fields are taken into account. Such so-called non-standard physics in the study of stellar structure and evolution are briefly introduced in Subsection 1.1.2 later in this section.

Some of the figures in this section are produced by myself based on computations with a commonly-used 1-dimensional stellar evolutionary code, Modules for Experiments in Stellar Astrophysics (MESA; see a series of papers, e.g., Paxton et al., 2011, 2013, 2015), with version 9793. No rotation, magnetic field, nor deviation from spherical symmetry is assumed in the computations.

1.1.1 A standard case

It is generally considered that stars are born basically via contraction of a part of a molecular cloud (e.g. Kippenhahn et al., 2012) with the dynamical timescale $\tau_{\mathrm{dyn}} \sim \rho^{-1/2}$, where ρ is the density of the system. As contraction proceeds, the pressure gradient inside the gas-accreting object gets stronger, and it gradually reaches hydrostatic equilibrium where the gravity and the pressure gradient are balanced. It is, however, not in thermal equilibrium; the energy flux from the center to the surface of the object is not equal to the energy generation rate, and thus, gravitational contraction continues with, in this case, the so-called Kelvin-Helmholtz timescale $\tau_{\mathrm{KH}} \sim E_g/L$, where E_g and L are the gravitational energy and the luminosity of the object, respectively. Such gravitational contraction stops when the temperature of the central region gets high enough ($\sim 10^7$ K) due to the contraction that the nuclear hydrogen burning begins. The object no longer needs gravitational contraction to compensate for the energy loss caused by the energy flux because the nuclear energy release replaces the (local) gravitational energy one. The object is now in both hydrostatic and thermal equilibrium, and this evolutionary stage is defined as the ZAMS stage; the birth of a main-sequence star (Figure 1.1).

Once a star starts hydrogen burning, it evolves with the nuclear timescale defined as $\tau_{\mathrm{nuc}} \sim$

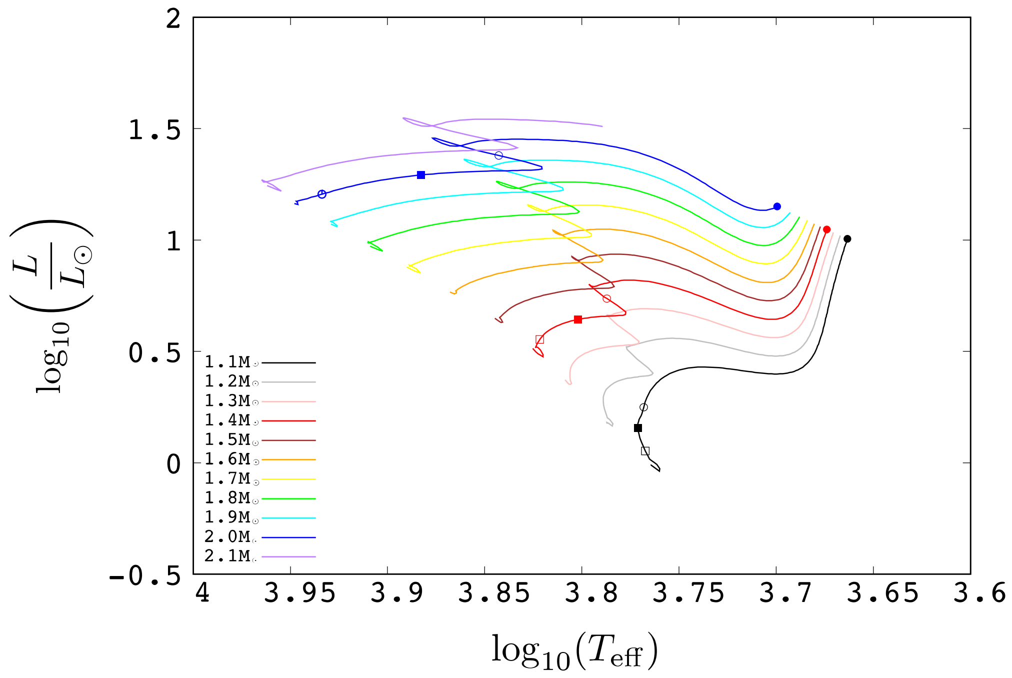

Figure 1.1: Evolutionary tracks for various stellar models with different masses ranging from $1.1M_\odot$ to $2.1M_\odot$. The models are computed via MESA, version 9793 (Paxton et al., 2015). The initial hydrogen abundance $Y_{\rm init}$ and the initial metallicity $Z_{\rm init}$ are 0.280 and 0.02, respectively. Elemental diffusion is activated, and moderate overshooting over convective boundary is assumed just for models with a convective core. Open squares correspond to an evolutionary stage when the central hydrogen mass fraction $X_{\rm c}$ is 0.605. Filled squares and open circles correspond to when $X_{\rm c}$ is 0.305 and 0.005. Filled circles represent when the photospheric radius of a model reaches $5R_\odot$, considered as being close to, or almost on, the red giant branch.

qM_*/L_*, where q, M_*, and L_* are the energy release per unit mass produced by hydrogen burning, the mass, and the luminosity of the star, respectively. This timescale gives rough estimates for the lifetime of main-sequence stars. For example, in the solar case ($M_\odot \sim 2.0 \times 10^{33}\,$g, $q \sim 6.3 \times 10^{18}\,$erg/g, and $L_\odot \sim 3.8 \times 10^{33}\,$erg/s), we obtain a rough estimate for the solar main-sequence lifetime as 1.1×10^{11} years. This is actually ten times larger than the solar main-sequence lifetime expected based on 1-dimensional stellar evolutionary calculation; not all of the solar mass is converted to helium, and we overestimated the mass.

Though the position on the HR diagram will not drastically change during the evolution from ZAMS to TAMS (from open squares to open circles in Figure 1.1), the internal structure significantly changes mainly owing to the nuclear reaction which converts hydrogen to helium. We find the signatures of the evolution in, for instance, the hydrogen content profile and the Brunt-Väisälä frequency. The Brunt-Väisälä frequency is a frequency of gravity waves, and it is related to convective stability (c.f. Schwartzschild criterion), which is defined as

$$N^2 = -g\left(\frac{d\ln\rho}{dr} - \frac{1}{\Gamma_1}\frac{d\ln P}{dr}\right), \tag{1.1}$$

where r, g, ρ, P, and Γ_1 are the radius, the gravitational acceleration, the density, the pressure, and

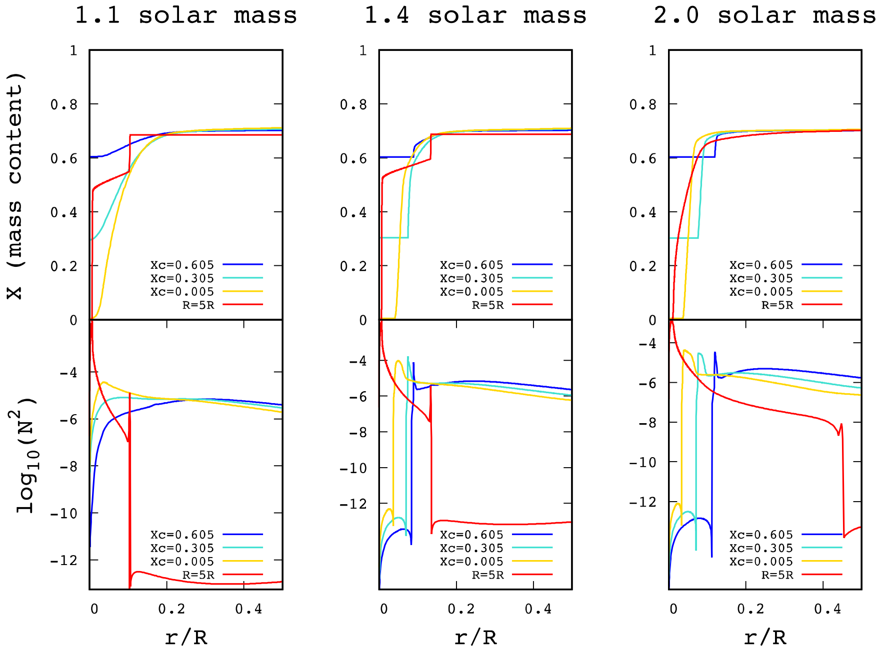

Figure 1.2: Hydrogen content profiles of stellar models with different masses at various evolutionary stages (upper panels). The position of each model on the HR diagram is shown as squares or circles in Figure 1.1. For example, the blue curve in the top-left panel is the hydrogen content profile of a model represented as a black open square in Figure 1.1. It is readily seen that the hydrogen abundance in the nuclear burning region decreases as the stars evolve. Bottom panels show the distributions of the Brunt-Väisälä frequency, in units of μHz (see the definition of the Brunt-Väisälä frequency in the text.) We see that sharp features in the Brunt-Väisälä frequency correspond to places where steep chemical composition gradients are located. It is also seen that how the core regions evolve is dependent on the mass of the models.

the first adiabatic exponent, respectively. Figure 1.2 shows the hydrogen profiles and the Brunt-Väisälä frequencies of various stellar models with different masses and evolutionary stages. It is clearly seen that hydrogen around the central region decreases as a star evolves in all the cases, and that the Brunt-Väisälä frequency varies its distribution correspondingly.

One interesting point is that there is a transition around $1.2M_\odot$ where a less massive model has a radiative core and a convective envelope with uniform composition (see the hydrogen profile of $1.1M_\odot$ model in Figure 1.2), and a more massive model contrarily has a convective core with uniform composition and a radiative envelope (see the hydrogen profile of $1.4M_\odot$ model in Figure 1.2). This transition can be qualitatively explained based on a difference in the temperature sensitivity of different kinds of nuclear reactions. In a lower mass range, the pp-chain reaction is dominant over the CNO cycle owing to the relatively lower temperature in the central regions. The temperature sensitivity of the pp-chain reaction is roughly $\sim T^4$, and thus, the temperature gradient around the nuclear burning region is not steep enough to render the adiabatic temperature gradient $\nabla_{\rm ad}$ larger than the radiative temperature gradient $\nabla_{\rm rad}$, leading to a convectively stable core. On the other hand, in a higher mass range, the central temperature is high enough for the CNO cycle to dominate the pp-chain reaction (e.g. Kippenhahn et al., 2012). The temperature sensitivity of the CNO cycle

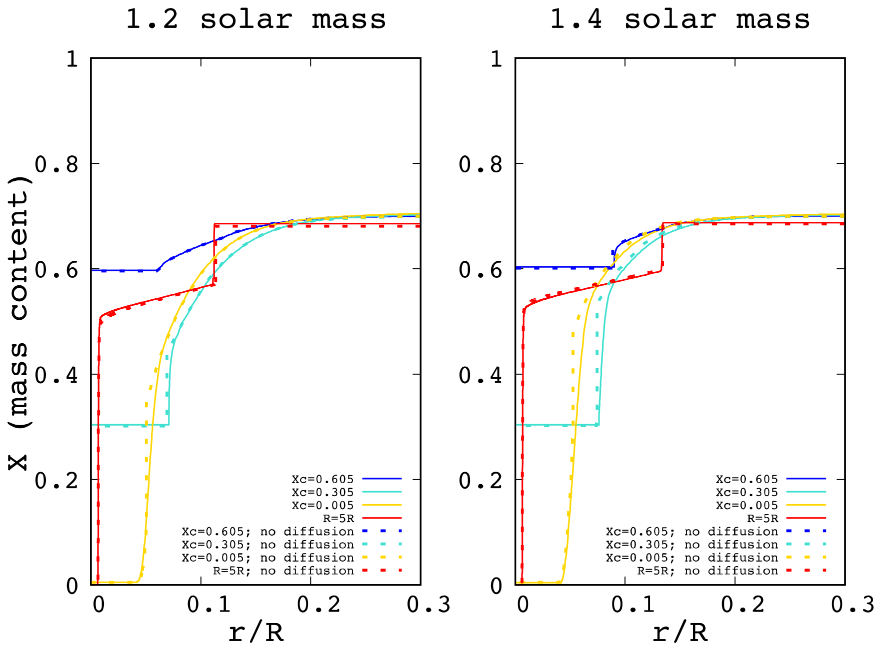

Figure 1.3: Hydrogen content profiles of models with (solid curves) or without (dotted curves) elemental diffusion. Though the hydrogen profiles of $X_\mathrm{c} = 0.605$ (blue curves) and $R = 5R_\odot$ (red curves) models are almost the same independent of whether diffusion is adopted or not in the computation, significant differences can be found in the hydrogen profiles of $X_\mathrm{c} = 0.305$ (turquoise curves) and $X_\mathrm{c} = 0.005$ (yellow curves) models; models computed without diffusion show steeper chemical composition gradients than those with diffusion (see hydrogen profiles around $r/R \sim 0.05$). For more information on effects of the other mixing processes other than the diffusion on the chemical composition profile, see e.g., Miglio et al. (2008).

is $\sim T^{18}$, and the temperature gradient is so steep that $\nabla_\mathrm{ad} < \nabla_\mathrm{rad}$, leading to a convectively unstable core. Therefore, whether a star has a convective core or a radiative core strongly depends on the mass of the star; more accurately, the existence of a convective core depends on the central temperature which is dependent on the stellar mass. We can see the signature as a difference in evolutionary tracks in Figure 1.1 (compare the black solid track and the grey track).

Note that the explanation in the preceding paragraph is just a qualitative one. The threshold mass for the transition from radiative-core models to convective-core models is dependent not only on the stellar mass but also dependent on other stellar global parameters such as the initial chemical composition. In addition, the chemical composition gradient left behind just above the nuclear burning core has a significant impact on the onset of convection as well. This can be understood based on an alternative expression of the Brunt-Väisälä frequency as follows:

$$N^2 \sim \frac{g^2\rho}{P}(\nabla_\mathrm{ad} - \nabla + \nabla_\mu), \tag{1.2}$$

where ∇ and ∇_μ are the actual temperature gradient and the chemical composition gradient, the latter of which is defined as

$$\nabla_\mu = \left(\frac{\partial \ln \mu}{\partial \ln P}\right)_{\rho,T}. \tag{1.3}$$

To derive Equation (1.2), the equation of state for an ideal monatomic gas is assumed (e.g. Miglio et al., 2008). Equation (1.2) indicates that the dynamical convection is more prone to be stabilized in the presence of the positive chemical composition gradient $\nabla_\mu > 0$. The stabilization thus affects internal mixing processes of the star and also affects whether a certain position inside the star is convectively unstable or not in a way different from that without a positive chemical composition gradient. It is therefore not straightforward to determine exact positions of convective boundaries for stellar models for this mass range. See more details in e.g. Gabriel and Noels (1977) and Gabriel et al. (2014). Further complication arises from the fact that the chemical composition gradient of a star at a certain evolutionary stage is a result of the internal mixing processes which have been at work until then; the chemical composition gradient and the internal mixing processes interrelate with each other (Figure 1.3). As such, direct observational information on chemical composition gradients of stars at present should be of great help to understand the internal mixing processes of the stars, e.g. overshooting (Pedersen et al., 2018), semiconvection (Gabriel et al., 2014), diffusion (Michaud et al., 2015), rotationally induced mixing (Maeder, 2009), and so on. That is the reason why studies of stellar non-radial oscillation (asteroseismology), based on which we can probe the interiors of the stars, could be useful (e.g. Miglio et al., 2008; Cunha et al., 2015, 2019).

Then, how about the envelope? In contrast to the deep interiors where the hydrogen nuclear burning and several mixing processes affect the chemical composition along evolution, the envelope is usually believed to keep the initial composition since its birth; there are just minor nuclear burnings such as the lithium burning, and the outermost convective layers are often fairy thin, both of which seldom affect the chemical composition there in the case of stars with the mass range considered in this section.

However, observations have indicated that this is often not the case, and there are two factors playing important roles in determining the chemical composition profile in the envelope of the low-mass stars. One is rotation. It is a well-known fact that most low-mass stars with relatively early spectral types are rotating quite fast, sometimes reaching the break-up velocity of $\sim$ a few hundred km/s (Abt and Morrell, 1995). Such fast rotation possibly induces mixing inside them, and the chemical composition can be uniform in the envelope (and possibly, also in a part of the deep region, of course). Another one is diffusion. Though the diffusion was expected to be not at work inside stars due to the relatively long timescale $\tau_{\text{diff}} \sim 10^{13}$ years (Kippenhahn et al., 2012) compared with those of the other physical mechanisms, several phenomena such as inhomogeneities of the surface chemical compositions of Am and Ap stars have required the presence of the diffusion (Michaud et al., 2015). Interestingly, the observed rotation for both Am and Ap stars are mostly slow with $P_{\text{rot}} \sim$ a few weeks, which probably hinders rotationally induced mixing, leading to the dominance of the diffusive process. It is crucial to understand both of the mechanisms, and astero-/helioseismology could again be a key to tackle these problems by probing envelope structures of low-mass stars.

In any case, the star finally ends up with exhausting almost all the hydrogen around the core, reaching the TAMS stage. The hydrogen shell burning gradually initiates, and then the stars leave the main sequence toward the Red Giant Branch (RGB) in thermal timescale. The core (envelope) rapidly shrinks (expands) along the evolution (Kippenhahn et al., 2012). By the time the models are close to RGB, the internal structures are totally different from those when they used to be on the main sequence; the radiative core and the convective envelope are separated by a thin shell where hydrogen burning is occurring (Figure 1.2). This structure is common for all the models in this relatively low-mass range.

1.1.2 Two specific topics among non-standard physics of stars

In the previous subsection 1.1.1, a standard view of structure and evolution of low-mass stars are shortly reviewed based on the results of the computations by the 1-dimensional evolutionary code, MESA. The term "standard" in this context means that "spherical symmetry, no rotation, no magnetic fields, no interactions with other celestial objects are assumed in calculations of stellar structure and evolution." These assumptions are acceptable for us to roughly grasp characteristics of stellar structure and evolution. But "non-standard" prescriptions are sometimes required to better understand effects of the "non-standard" physics on the stellar structure and evolution. It is, moreover, observationally well-accepted that such non-standard physics are common for various types of stars. In this subsection, the significance of "non-standard" physics is demonstrated mainly from the observational point of view. We especially focus on two subjects. One is related to the existence of blue straggler stars which are thought to be born via binary interactions, and the other is internal rotation, both of which are intimately concerned with primary topics in this dissertation.

Blue straggler stars

The structure and evolution of stars in binary systems are the same as those of single stars given that there is no interaction among them because of, for instance, such a wide orbit that they are too distant to interact. However, this is often not the case, and there are a quite large number of observational evidences where binary interactions matter; Algol-type binary systems where evolutionary stages of the components seem to be somehow reversed, cataclysmic variables which are experiencing runaways of hydrogen burning at the surface of white dwarfs which are thought to be triggered by mass accretion onto them, type Ia supernovae which are also caused by mass accretion onto white dwarfs exceeding the Chandrasekahar limit, binary mergers for a variety type of stars some of which have been observationally confirmed by gravitational waves as binary blackhole mergers, etc. As such, binary interactions are rather common and they must have considerable effects on the structure and evolution of the components.

One of the observational evidences for binary interactions is the existence of blue straggler stars. Since KIC 11145123, which is the main subject of this dissertation, is categorized as a blue straggler star spectroscopically, a brief introduction to blue straggler stars is presented in the following paragraphs. For a comprehensive reviews on the current understanding of blue straggler stars, refer to Boffin et al. (2015).

The existence of blue straggler stars was reported by A. Sandage in 1953 for the first time. In the color magnitude diagram of the globular cluster M3, he found that some stars are on the main sequence significantly above the main-sequence turn-off point of M3 (Figure 1.4). The standard theory of stellar structure and evolution tells us that massive stars leave the main sequence more quickly than the lower mass stars, because nuclear timescales ($\tau_{\mathrm{nuc}} \sim qM_*/L_*$, see Subsection 1.1.1) for massive stars are much shorter than those of low-mass stars. Therefore, to explain the origin of the strange stars Sandage discovered in M3, some kinds of mechanisms in which stars are rejuvenated or able to live longer than usual are required. Importantly, such blue stragglers are rather common at least in the Local Group, and a significant number of blue stragglers have been observed in various environments including globular clusters, open clusters, fields, dwarf galaxies, and so on (e.g. Boffin et al., 2015), suggesting that there might be common mechanisms to produce this kind of stars.

There have been a large number of suggestions for the origin of blue straggler stars, which

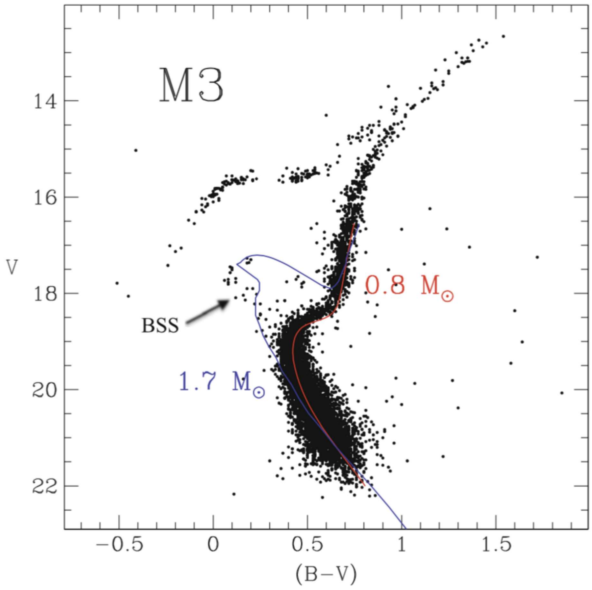

Figure 1.4: Color magnitude diagram of a globular cluster M3 (cited from Boffin et al., 2015). Most of the cluster members are on an isochron whose turn-off mass corresponds to that in the case of $0.8M_{\odot}$ (red curve). There, however, exist a number of stars which are still on the main sequence. These stars are bluer compared with stars of the same ages on the $0.8M_{\odot}$ isochron, which shows how this kind of stars were dubbed "blue straggler."

are well summarized in Leonard (1989). The currently most promising mechanisms are binary interaction, which is strongly supported by high binarity of blue straggler stars (Boffin et al., 2015), and stellar collision, which is indicated by observed high frequency of blue straggler stars in dense regions such as cluster cores (Boffin et al., 2015). In any case, it is generally considered that a progenitor of a blue straggler star must have experienced some interactions with the other celestial bodies during the evolution to significantly alter the properties of the star. It should be noticed that there has never been a direct observation for the origin of the blue straggler formation; the issue has not been settled yet.

It is then quite instructive for us to theoretically model structure and evolution of blue straggler stars to acquire some hints about formation scenarios of them. However, we have to take into account non-standard physics such as interactions with other stars during the evolution, and the subject has not been established. One reason is that it is very difficult to validate numerical schemes with such non-standard prescriptions. Although there are several numerical codes treating, for example, mass accretion during the evolution, they are such phenomenological schemes with multiple free parameters, and in addition, calibrating the schemes with observations has not been actively studied (e.g. Brogaard et al., 2018). Timescale also matters. The timescale of mass accretion depends on the stability of the Roch-Lobe overflow occurring in the binary system, and it is sometimes of the order of the nuclear timescale, where we have to couple stellar evolution and mass accretion. See Boffin et al. (2015) for more detailed information on the current theoretical studies of blue straggler stars, such as the evolution of binary merger products or that of stellar collision products.

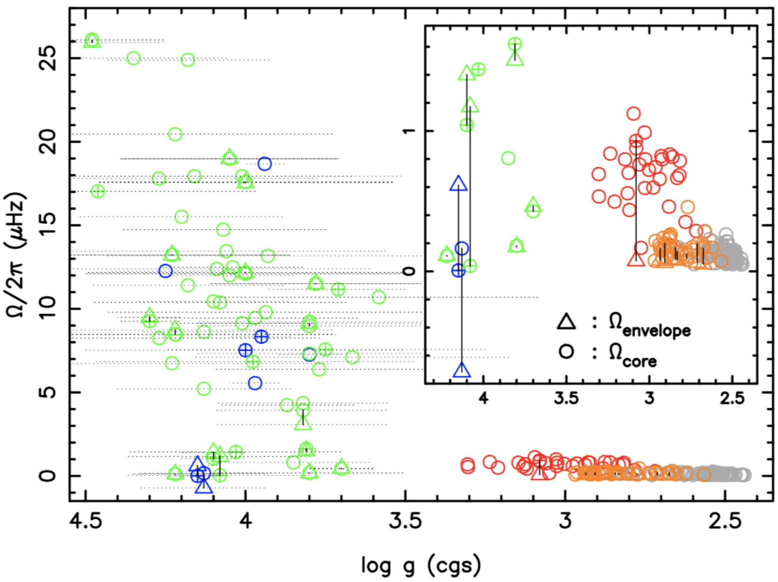

Figure 1.5: Asteroseismically inferred rotation rate for B-type main-sequence stars (blue symbols), for A/F-type main-sequence stars (green symbols), and for more evolved stars (red, orange, and grey symbols). Horizontal axis is the logarithm of the observed surface gravitational accelerations, roughly showing the evolutionary stages of the targets. Core rotation rates and envelope rotation rates are expressed with open circles and open triangles, respectively. When we focus on the stars for which both core rotation and envelope rotation have been measured, we find that the contrasts between them are always not so large (below a few factors). This trait is not compatible with the results of previous numerical (hydrodynamical) simulations of angular momentum transfer inside the stars, indicating that we should take into account extra mechanisms for angular momentum transfer. This figure is cited from Aerts et al. (2017).

Internal rotation

Rotation is universal, and it is widely known that a large number of stars are rotating fast enough that the effects on the structure cannot be ignored (e.g., deformation caused by the centrifugal force) and evolution (e.g., transfer of angular momentum and mixing of chemical elements by rotation-induced mixing). There have been numerous observations reporting that there exist correlations between rotation and other stellar parameters including age, magnetic activities, chemical peculiarities, and so on (see e.g. Maeder, 2009), which is the reason why rotation is regarded as one of the most important characteristics of stars in stellar physics. Rotation also plays a key role in stellar internal dynamics (e.g., dynamo mechanism). In this small subsection, we point out an issue on internal dynamics, especially on the internal rotation profile and the angular momentum transfer during the evolution, of low-mass main-sequence stars evolving from ZAMS to TAMS and beyond.

Naively speaking, the standard framework described in Subsection 1.1.1 provides us a simple view about stellar structure and evolution; a contracting core and an expanding envelope, either in nuclear or thermal timescale. This simple description leads to an expectation that the contracting core rotates faster and faster, and the expanding envelope rotates slower and slower if the angular momentum is locally conserved during the evolution. This is also confirmed based on previous numerical simulations with (only) hydrodynamical effects.

Nevertheless, recent asteroseismic studies, which have succeeded in inferring internal rotation profiles of various types of stars ranging from main sequence (e.g. Aerts et al., 2017) to red giant branch (e.g. Deheuvels et al., 2012), shows that there is a significant discrepancy between the theoretical expectation and the observation (Figure 1.5); the cores of stars are not rotating as fast as expected, and the contrast between the core rotation and the envelope rotation is not so strong as the hydrodynamical numerical simulations suggested. Though the number of such asteroseismic inferences of stellar internal rotation has been not so large (∼a few hundreds) yet, it is evident that we should consider extra effects (e.g., magnetic fields, internal gravity waves) other than the hydrodynamical ones to cause angular momentum transfer inside stars during the evolution. That is currently one of the most active fields in stellar physics (e.g. Aerts et al., 2019; Fuller et al., 2019).

1.2 Asteroseismology

As analyses in this dissertation are mostly by means of asteroseismology, we would like to offer a brief introduction to the study of stellar oscillations in this section. In the first subsection, a brief introduction to asteroseismology, concerning the history, the mathematical formulations, and the method, is given. Secondly, we focus on current observations brought about by the Kepler spacecraft, and also show some typical sub-groups of oscillating stars frequently found in the observations. Recent studies and the results which are related to this dissertation are finally given in the last subsection.

More thorough introductions to asteroseismology and detailed discussions about the mathematical formulations, observational techniques, and the statistical methods to draw inferences can be found in e.g., Unno et al. (1989), Pijpers (2006), Aerts et al. (2010).

1.2.1 An introduction to asteroseismology

Despite the fact that asteroseismology has been a currently developing field and the fact that it is rather recent that much attention has began to be paid to the field, it is not correct to consider the subject is totally a new branch of stellar physics.

In this subsection, a brief history of astero- and helioseismology, the study of the solar oscillations, is firstly reviewed. Then, a few equations to describe linear adiabatic stellar oscillations are given. After some of asteroseismic observational aspects, namely, frequency determination and mode identification are demonstrated, we close this subsection with a comparison between asteroseismology and helioseismology, which would be helpful for readers to acknowledge both difficulties and advantages of the study compared with helioseismology.

A brief history of astero- and helio-seismology

Mira is a star, whose variability in its brightness was noticed around the end of the sixteenth century. As more sophisticated observations had been conducted, it was shown that the star is variable not only in brightness but also in radial velocity with the same phase, thus showing that the star is really oscillating (repeatedly contracting and expanding). The Mira-type variability, in addition to those of the other types of variability as Cepheid-type one, is of great help to measure distances farther than ones which can be determined based on annual parallax via well-known period-luminosity relations found by Leavitt. But asteroseismology has not begun with the discovery of these so-called classical variables. This is because they usually oscillate with radial modes which are eigenmodes constructed by waves propagating the whole interior of the star. In addition, the number of detected modes is also small. Therefore, what we can extract from frequencies of classical variables are at best mean density of the stars. We had to await detections of non-radial oscillations to extract somewhat more localized information on interiors of stars.

The Sun is the first star, for which non-radial oscillations were detected, and the seismic concepts and techniques have been applied to directly infer the interior of the object. In 1962, Leighton detected the so-called solar five-minute oscillation for the first time (Leighton et al., 1962). They did not know the origin at the beginning, and the five-minute oscillation was thought to be caused by convective overshooting beyond the photosphere. As further observations had been carried out, it was shown that the oscillation is independent of convective motion, and also shown that it is rather a manifestation of superpositions of a large number of solar eigenmodes (e.g. Deubner, 1974); the birth of helioseismology. After the confirmation of the existence of solar eigenmodes, it was not long until helioseismologists began to utilize the observations to probe the solar interior directly.

For example, we can calculate the solar model with a 1-dimensional evolutionary code, and then, we can also compute the eigenfrequencies of the model. Comparison of those frequencies with the observed ones tells us the difference between the structure of the computed 1-dimensional model and that of the real solar structure (Christensen-Dalsgaard et al., 1996). This is one of the ways to infer the solar structure based on the helioseismic observations. To show every single piece of how helioseismology has been contributing to reveal the internal structure and dynamics of the Sun so far is almost impossible with this humble dissertation. Readers therefore should refer to e.g., Gough et al. (1996), Thompson et al. (2017) for more details.

The point here is that the Sun, which used to be often considered as just one of the ordinary non-variable stars in the universe, was found to be oscillating with many modes including both radial and non-radial modes. Why not the other stars? The successful achievements of helioseismology simply implied the feasibility of seismic studies of stars; asteroseismology (Christensen-Dalsgaard et al., 1984). However, in contrast to the successful establishment of helioseismology, it took a long time for researchers to apply asteroseismology to real stars. Stars are too distant from us and too faint to observe the non-radial oscillations, the amplitudes of which are typically of the order of 10^{-3} magnitude in brightness. The stars are observed as point sources as well, and the number of the eigenmodes, even though detected, is too small due to the so-called cancellation effect (see the later small subsection, "comparison with helioseismology") to perform detailed seismic analyses as has been done by helioseismology. We had many difficulties in terms of the observation of the stellar oscillations (see more detailed historical backgrounds in Chapter 2 of Aerts et al., 2010).

That situation has been drastically changed since the advent of an era of space missions focusing on exoplanet hunting and measuring stellar oscillations such as MOST (Walker et al., 2003), CoRoT (Baglin et al., 2006), Kepler (Koch et al., 2010), and TESS (Ricker et al., 2014). The Kepler spacecraft especially outstands among them. It has provided us with four-year-long continuous light curves of hundreds of thousands stars covering a broad range of stellar evolutionary stages with unprecedented precision of the measurements of the order of 10^{-6} magnitude in brightness, enabling us to perform seismic analyses of the observed stars. Of course, we still cannot analyze the stars in details as in helioseismology, but at least, we can conduct estimation of global stellar parameters (Chaplin and Miglio, 2013), determination of evolutionary stages (Bedding et al., 2011), calibration of stellar models (Sanchez et al., 2017), and inferring internal rotation profiles (Aerts et al., 2019), and so on. Asteroseismology is still in its infancy, and it is definitely such a promising field that multiple future space missions are planned at the time of writing. (e.g. PLATO)

Basic mathematical formulations

The analytical studies of stellar non-radial oscillations have a long history, some of which dates back to the middle of the nineteenth century. One of the reasons why the analyses of stellar non-radial oscillations have been a matter of interest for such a long time is that stellar non-radial oscillations are closely related to, for instance, the stellar stability such as the convective stability. Therefore, the theory of stellar non-radial oscillations is, not completely of course but, well-established. Refer to Roseland for the early history of the studies, and Unno et al. (1989) for the history later on.

In this small subsection, spherical symmetry, no rotation, no magnetic fields are assumed in the equilibrium model as in Subsection 1.1.1. We also do ignore them in the analysis of non-radial oscillations, i.e. the effects of asphericity, rotation, and magnetic fields on eigenfrequencies are neglected. Note that if we can treat them as perturbations which are small enough to neglect terms higher than the second order, we can relate frequency changes to the perturbations and so-called sensitivity kernels of the unperturbed model. This perturbative approach is of great use to infer stellar interiors and it is shown in the end of this small subsection. The effects of asphericity, rotation, and magnetic fields on the equilibrium structures are reviewed in Maeder (2009), and those on non-radial oscillations based on non-perturbative approaches are in e.g. Unno et al. (1989). For more detailed derivations of the following equations, refer to e.g. Unno et al. (1989) and Aerts et al. (2010).

The starting point is a system of equations of hydrodynamics, namely, equation of momentum conservation, equation of mass conservation, equation of energy conservation, and Poisson's equation,

$$\rho\left(\frac{\partial}{\partial t}+\boldsymbol{v}\cdot\nabla\right)\boldsymbol{v}=-\nabla P-\rho\nabla\Phi, \tag{1.4}$$

$$\frac{\partial\rho}{\partial t}+\nabla\cdot(\rho\boldsymbol{v})=0, \tag{1.5}$$

$$\rho T\left(\frac{\partial}{\partial t}+\boldsymbol{v}\cdot\nabla\right)s=\rho\epsilon-\nabla\cdot\boldsymbol{F}, \tag{1.6}$$

and

$$\Delta\Phi=4\pi G\rho. \tag{1.7}$$

Density ρ, velocity $\boldsymbol{v}$, pressure P, gravitational potential Φ, temperature T, specific entropy s, and local flux $\boldsymbol{F}$ are functions of (r,θ,ϕ,t) in a spherical coordinate where r, θ, ϕ, and t are the distance from the center, colatitude, longitude, and time. Energy production rate per unit mass ε is a function of thermodynamic parameters such as ρ, P, T. The gravitational constant is represented by G. Note that viscosity of the fluids and Lorentz force are neglected.

The next step is to separate all the quantities with unperturbed and perturbed parts as, for example,

$$\rho(r,\theta,\phi,t)=\rho_0(r)+\rho'(r)Y_l^m(\cos\theta)e^{i\omega t}, \tag{1.8}$$

where ω is the angular frequency, and l and m are the spherical degree and the azimuthal order of the spherical harmonics, respectively. For the unperturbed quantities with subscripts '0', the first-derivatives in horizontal direction in space and time are zero, i.e. $\partial/\partial\theta=\partial/\partial\phi=\partial/\partial t=0$ because the spherical symmetry is assumed for the equilibrium model. The prime symbol represents the Eulerian perturbation. Substituting the expressions for the set of equations (1.4) to (1.7) and retaining only the first-order terms lead to a set of linearized equations,

$$\frac{1}{\rho}\frac{dP'}{dr} + \frac{g}{\rho c^2}P' - (\omega^2 - N^2)\xi_r + \frac{d\Phi'}{dr} = 0, \tag{1.9}$$

$$\frac{1}{r^2}\frac{d}{dr}(r^2\xi_r) - \frac{g}{c^2}\xi_r + \frac{P'}{\rho c^2}\left(1 - \frac{L_l^2}{\omega^2}\right) - \frac{l(l+1)}{\omega^2 r^2}\Phi' = 0, \tag{1.10}$$

and

$$\frac{1}{r^2}\frac{d}{dr}\left(r^2\frac{d\Phi'}{dr}\right) - \frac{l(l+1)}{r^2}\Phi' = 4\pi G\rho\left(\frac{P'}{\rho c^2} + \frac{N^2}{g}\xi_r\right), \tag{1.11}$$

where g, c, ξ_r, N, and L_l are the gravitational acceleration, the adiabatic sound speed, the radial displacement, the Brunt-Väisälä frequency (defined in Subsection 1.1.1), and the Lamb frequency which is defined as

$$L_l^2 = \frac{l(l+1)c^2}{r^2}. \tag{1.12}$$

The subscripts '0' are omitted for the unperturbed quantities. It should be noted that the adiabatic assumption is adopted ($\partial(\delta s)/\partial t = 0$), and thus the conservation of energy (Equation 1.6) is not explicitly shown here. The set of the three equations is a system of equations for linear adiabatic stellar oscillations. The equations (1.9) to (1.11) with some boundary conditions can be solved for a set of appropriate frequencies ω_{nl} and radial displacements $\xi_{r,nl}$, i.e. it is an eigenvalue problem. The eigenfrequencies and the eigenfunctions are independent of the azimuthal order m because of the assumption of spherical symmetry; there is no preferential direction with respect to the axis of the oscillation. This forth-order eigenvalue problem is usually numerically solved.

To qualitatively understand behaviors of the eigenmodes, we reduce the order of the eigenvalue problem from the fourth to the second by accepting an assumption that the Eulerian perturbation of the gravitational potential Φ' is negligible. This is a frequently adopted assumption in asteroseismology (Cowling approximation) and it is acceptable when the number of the radial order n or the spherical degree l are high enough, which is confirmed based on the results of the numerically solved fourth-order stellar eigenoscillation problem. The second-order linear differential equation thus obtained has the following form

$$\frac{d^2\xi_r}{dr^2} + k_r^2\xi_r = 0, \tag{1.13}$$

where the radial wavenumber k_r is defined as

$$k_r^2 = \frac{1}{\omega^2 c^2}(\omega^2 - N^2)(\omega^2 - L_l^2). \tag{1.14}$$

On the course of the derivation of the expressions above, the radial dependence of the quantities is neglected for simplicity (local treatments).

The sign of the squared radial wavenumber k_r^2 determines whether the wave is propagative or not propagative (evanescent). Propagative waves are satisfying either of the following conditions

$$\omega^2 > N^2 \quad \text{and} \quad \omega^2 > L_l^2 \tag{1.15}$$

or

$$\omega^2 < N^2 \quad \text{and} \quad \omega^2 < L_l^2. \tag{1.16}$$

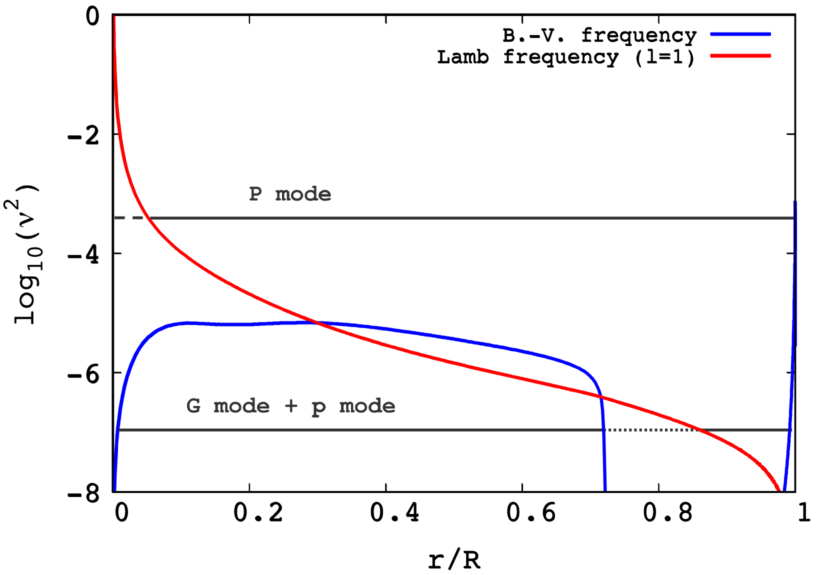

Figure 1.6: Propagation diagram of a solar model. Horizontal axis is the fractional radius, and the vertical axis is the logarithm of the squared frequency which is in unit of μHz. The red and the blue curves are representing the Lamb frequency for $l = 1$ and the Brunt-Väisälä frequency, respectively. For a mode with a particular frequency, this propagation diagram tells us which part inside the star the mode is propagative (indicated by solid lines) or evanescent (indicated by dotted lines) based on the two conditions (1.15) and (1.16).

Eigenmodes constructed with waves fulfilling the former condition is called pressure modes (p modes) whose dominant restoring force is pressure. On the other hand, eigenmodes constructed with waves fulfilling the latter condition is called gravity modes (g modes) whose dominant restoring force is gravity (buoyancy force).

Figure 1.6 is a so-called propagation diagram of a solar model, which shows where a wave with a certain eigenfrequency (here denoted by ω) is propagative or evanescent. It is seen that p modes, which are usually oscillating with relatively high frequencies ($\sim$ 3 mHz), are propagative in the outer region (see the upper black horizontal line in Figure 1.6, indicating that the frequency satisfies the condition 1.15 almost throughout the model; this mode is thus a p mode.) In contrast, g modes, which are usually oscillating with relatively low frequencies (below a few hundreds μHz), are propagative only in the inner radiative region and they are mostly evanescent in outer convective region (see the lower black horizontal line in Figure 1.6); this is because the buoyancy force cannot act as a restoring force in convectively unstable regions. The thick convective envelope thus prevents us from detecting solar g modes. Solar g modes are believed to be excited in the solar interior, but their (theoretically computed) amplitude are as small as a few mm/s (Appourchaux et al., 2010) at the surface of the Sun because of the thick evanescent region. Such amplitudes are too small to detect with the current observational equipments.

Figure 1.7 shows a propagation diagram for a stellar model with 1.4 solar mass around the TAMS

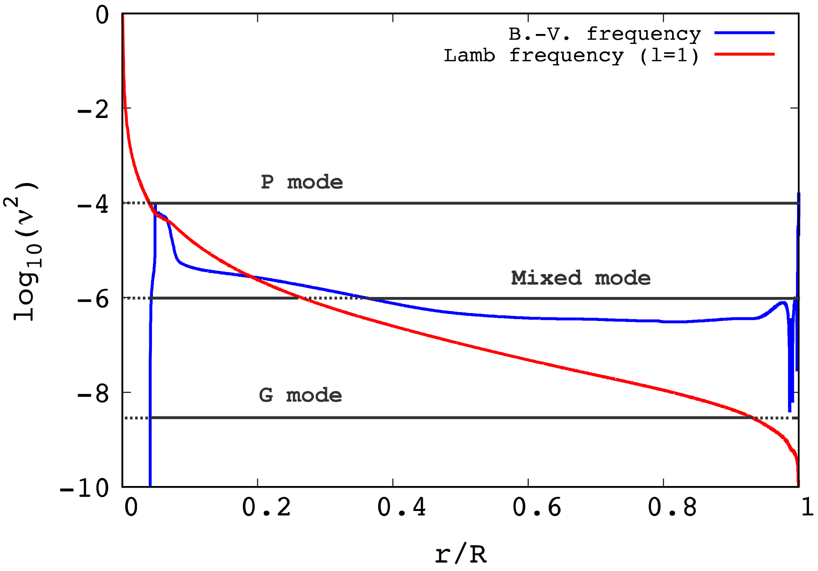

Figure 1.7: Propagation diagram of a $1.4M_\odot$ model around the TAMS stage.

stage. A major difference between the two figures 1.6 and 1.7 is in the Brunt-Väisälä frequencies. The $1.4M_\odot$ model has a convective core and a radiative envelope as explained in Subsection 1.1.1, and the g modes are thus propagative in the outer envelope (see the bottom black line in Figure 1.7), contrary to the case of the solar model. This is suggesting the possibility that we can detect g modes with significant amplitudes, which is actually the case in recent observations (see Subsection 1.2.2). Some of the eigenmodes with moderate frequencies can be propagative both in g-mode and p-mode cavity (the middle black line in Figure 1.7). They are called mixed modes, which behave as g modes in the g-mode cavity and as p modes in the p-mode cavity. Whether such mixed modes are in reality constructed or not, roughly speaking, depends on the thickness of the evanescent zone linking the p- and g-mode propagative regions.

One important point is that different modes propagate different region, meaning that the different modes have different information on the interiors of the star. Therefore, it is of great importance in asteroseismology to observe as many modes as possible in order to infer interior structures in detail. Further analysis to obtain the eigenconditions, eigenfrequencies, and so on for high-order g modes is addressed in Chapter 2.

Finally, the fourth-order differential equation is revisited. It is often convenient for further analyses if we rewrite the system of the equations in vector form as below:

$$\begin{aligned} \omega^2 \rho \boldsymbol{\xi} &= -\nabla(\rho c^2 \nabla \cdot \boldsymbol{\xi}) - \nabla(\nabla P \cdot \boldsymbol{\xi}) + \rho \nabla \left[G \int \frac{\nabla' \cdot \{\rho(\boldsymbol{r}')\boldsymbol{\xi}(\boldsymbol{r}')\}}{|\boldsymbol{r}-\boldsymbol{r}'|} dV' \right] + \frac{\nabla P}{\rho} \nabla \cdot (\rho \boldsymbol{\xi}) \\ &\equiv \mathcal{L}(\boldsymbol{\xi}), \end{aligned} \tag{1.17}$$

where the displacement vector is expressed by $\boldsymbol{\xi}$. Note that the quantities in Equation (1.17) are functions of r as well as θ and ϕ. The third-term in the right hand side of Equation (1.17) represents the Eulerian perturbation of the gravitational potential Φ' with the Green's function for the Poisson's equation. The linear differential operator is represented by $\boldsymbol{\mathcal{L}}$.

The above equation combined with the orthogonality of the eigenfunctions (see e.g. Unno et al., 1989) can be further formally cast into an integral form,

$$\int \boldsymbol{\xi}^* \cdot \mathcal{L}(\boldsymbol{\xi}) dV = \omega^2 \int |\boldsymbol{\xi}|^2 \rho dV. \tag{1.18}$$

It is shown that the equation suffices the variational principle based on zero boundary conditions at the surface, leading to the following equation

$$\omega^2 = \frac{\displaystyle\int (\boldsymbol{\xi} + \Delta\boldsymbol{\xi})^* \cdot \mathcal{L}(\boldsymbol{\xi} + \Delta\boldsymbol{\xi}) dV}{\displaystyle\int |(\boldsymbol{\xi} + \Delta\boldsymbol{\xi})|^2 \rho dV} + o(|\Delta\boldsymbol{\xi}|^2), \tag{1.19}$$

which means that the perturbation of eigenfunctions is not affecting the frequency when the terms higher than the second order are neglected. Equation (1.19) is useful to relate perturbed structures to perturbed eigenfrequencies without the need to compute the eigenfunctions, as below:

$$\Delta\omega^2 = \frac{\displaystyle\int \boldsymbol{\xi}^* \cdot \Delta\mathcal{L}(\boldsymbol{\xi}) dV - \omega^2 \int |\boldsymbol{\xi}|^2 \Delta\rho dV}{\displaystyle\int |\boldsymbol{\xi}|^2 \rho dV}. \tag{1.20}$$

Equation (1.20) is applied in rotation inversion, structure inversion, and formulation of modulated patterns of g-mode period spacings.

More careful discussions about orthogonality, completeness of the eigenfunctions can be found in Dyson and Schutz (1979).

Observation

One of the important points shown in the previous small subsection is that the different modes (with different n, l, m) propagate different regions inside the star, leading to the different eigenfrequencies. Therefore, it is essential for us to know frequencies and mode indices of eigenmodes in order to carry out asteroseismic analyses for real stars and understand the interiors. Basic concepts of frequency measurements, determination, and mode identification are thus presented here.

First of all, we would like to demonstrate how oscillations of a star are observed. Assuming that the star is spherically symmetric, stellar pulsation can be described as superpositions of individual modes which are expressed as functions consisting of oscillatory exponential components ($e^{i\omega_{nlm}t}$), spherical harmonics ($Y_l^m(\theta, \phi)$), and radial-dependent components ($f_{nl}(r)$). The indices n, l, and m are the radial order, the spherical degree, and the azimuthal order, respectively, and ω_{nlm} is the angular frequency of the corresponding mode. Then, the radial velocity field of the star $v(r, \theta, \phi, t)$ can be expressed as

$$v(r, \theta, \phi, t) = \sum_{n,l,m} f_{nl}(r) Y_l^m(\theta, \phi) e^{i\omega_{nlm}t}. \tag{1.21}$$

The velocity field at the surface of the star is

$$v_{\mathrm{s}}(\theta, \phi, t) = v(R, \theta, \phi, t), \tag{1.22}$$

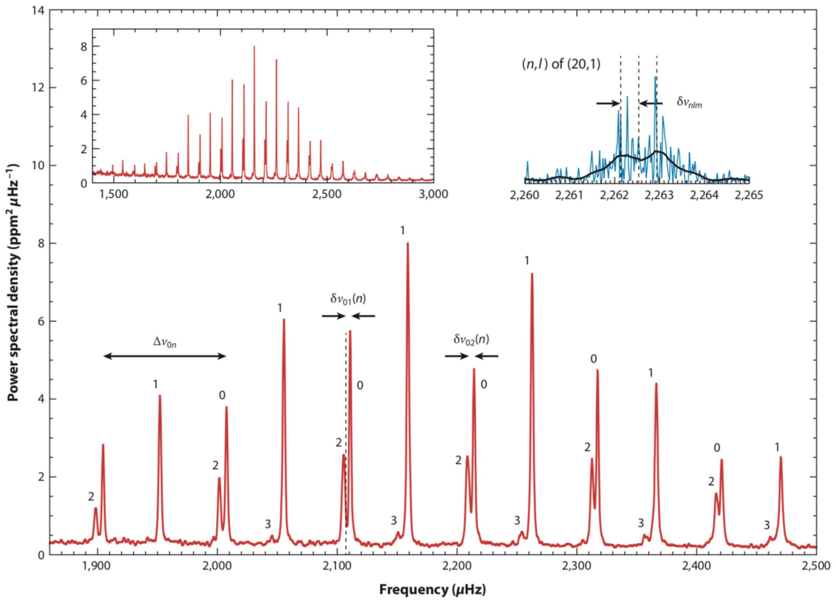

Figure 1.8: Power spectrum of 16 Cyg A observed by Kepler (Chaplin and Miglio, 2013). The upper-left window shows the whole range of the spectrum. The bottom window is a closer look to the spectrum. The numbers just above the peaks are the spherical degrees l of the modes. The upper-right window is a much closer look. The blue line is a raw spectrum and the black one is a smoothed one. *Rotational splitting* is expressed as $\delta\nu_{nlm}$ though it is hard to resolve the signals. Rotational splitting will be described in Subsection 1.2.3 where it is given as $\delta\omega_{nlm} = \delta\nu_{nlm}$. The bell-shaped structure of the detected peaks as a whole is often seen in power spectra of solar-like oscillating stars, which is demonstrated in Subsection 1.2.2.

where R is the radius of the star. Because we cannot resolve the surface of a distant star except for cases with some interferometric techniques, what we observe is the integrated Doppler velocity variation (or the integrated intensity variation) (more details in Chapter 4 in Aerts et al., 2010),

$$v(t) = \iint v(R, \theta, \phi, t) \sin\theta \, d\theta \, d\phi, \tag{1.23}$$

where the spatially resolved information on the velocity field of the star has been lost. As $v(t)$ is still proportional to $e^{i\omega_{nlm}t}$ according to the equation (1.21), we can obtain the amplitude spectrum by Fourier transforming $v(t)$, but we do not have direct access to the identification of the mode due to the lack of spatial resolution, i.e. we have to determine the corresponding indices (n, l, m) by some other way. This procedure is called mode identification, which is described in the latter part of this small subsection.

Figure 1.8 shows an example of a power spectrum obtained by Fourier transforming the light curve of a solar-like star Cyg 16 A which has been observed by the Kepler spacecraft. It is apparent that there are a number of peaks representing the eigenmodes of the star. We can estimate, for instance, the frequencies with statistical methods such as Maximum Likelihood Estimation (Appourchaux et al., 1998) or Bayesian estimation (Benomar et al., 2009) assuming models which represent observed power spectra, or directly fitting observed light curves with sinusoidal components. As extracting asteroseismic parameters (the frequencies, the mode widths, the mode heights, and so on) from light curves is critical for detailed analyses to infer the interiors and dynamics, frequency analysis is one of the most prominent subjects in asteroseismology (Aerts et al., 2010).

Finally, let me come back to mode identification. As it has been described in the previous paragraphs, the spatial information on stellar oscillations is lost, and thus we have to assign mode indices to each of observed peaks (usually they are recognized as a peak with a threshold $S/N \sim 4$) by comparing with theoretical models. A straightforward way is to construct an equilibrium model of the star with a 1-dimensional stellar evolutionary code, to calculate the eigenfrequencies of the model by solving linear adiabatic oscillation, to compare the theoretical eigenfrequencies, for which we already know the mode indices, with the observed frequencies, and finally to let mode indices of an observed peak be those of one of the computed eigenfrequencies which is the closest to the frequency of the peak. It is, however, often the case that such stellar modeling is not successful for reproducing all the observed frequencies, and that is difficult to validate the mode identification thus done.

In either case, we need models to compare with observations, and it is of great difficulty to construct totally reliable models. Therefore, we usually start with observables like the large separations $\Delta\nu$ or the g-mode period spacings ΔP_{g}, both of which represent averaged quantities of the stellar interior (e.g. Tassoul, 1980), and after we roughly grasp structural and pulsational properties of the observed stars, we move on to model calculations.

Comparison with helioseismology

There is little difference between asteroseismology and helioseismology from the theoretical point of view; the set of equations for the linear adiabatic oscillations is the same. Considerable differences, however, reside in the observations.

In helioseismic observations, we can resolve the surface of the Sun and obtain time series of 2-dimensional images with a cadence of, for instance, ~ 45 seconds (in the case of HMI: Schou et al., 2012). By decomposing the 2-dimensional images with spherical harmonics and Fourier transforming the time series of the decomposed images, the power spectrum is computed as a function of the spherical degree, the azimuthal order (related to the horizontal wavenumber), and the temporal frequency. In other words, we do not have to carry out mode identification of the solar eigenmodes in terms of the spherical degree; here is a main difference from the case of asteroseismology. Note that for the radial orders we have to perform mode identification in helioseismology as well except for when fundamental modes (f modes) whose radial order is zero are seen. How to assign the radial orders to the observed peaks is basically the same as it is described in the small subsection 1.2.1.

Another difference also arises from the lack of the spatial resolution in asteroseismic observations. The integration of the brightness variations caused by stellar eigenoscillations all over the surface has cancellation effects on higher-degree modes, and, in asteroseismology, we usually do not observe eigenmodes with spherical degrees higher than 3. Compared with helioseismic observations where eigenmodes with high spherical degree ~ 1000 has been observed, the number of detected modes in asteroseismology is smaller than that in helioseismology by four digits if the azimuthal order is also considered. Therefore, it is quite difficult to carry out asteroseismic inversion to infer internal structures or internal rotation because the lack of the data easily renders the inverse problems highly ill-posed ones; we usually cannot infer interiors of stars as in detail as in helioseismology.

However, there are also good points in asteroseismology, diversity sometimes helps. One example is the detection of g modes. Because the Sun has a thick convective envelope, g-mode waves are evanescent there and the amplitudes at the solar surface are too small to detect (see the small

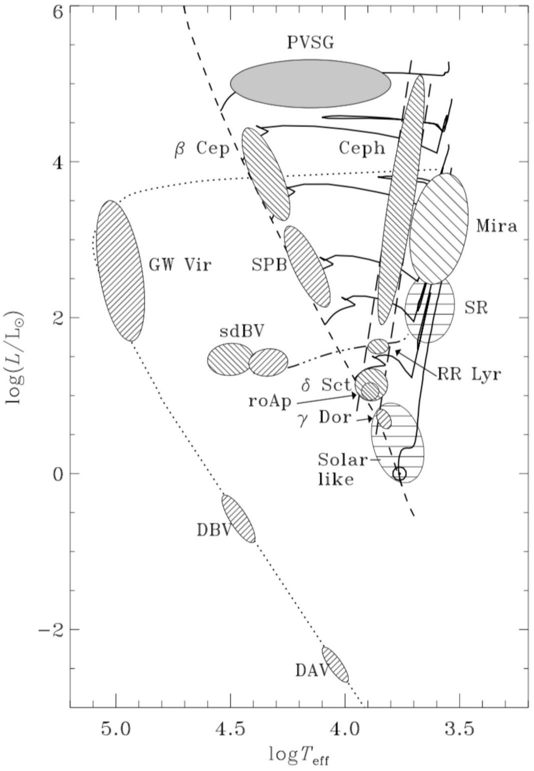

Figure 1.9: Locations of various types of variables on the HR diagram (cited from Aerts et al., 2010). The typical properties of solar-like pulsators, δ Sct stars, and γ Dor stars are demonstrated in the text. Observational properties for other main-sequence pulsators (roAp, SPB, and β Cep), more evolved pulsators (SR and PVSG), white dwarf pulsators (GW Vir, DBV, and DAV), and classical variables (Mira, Ceph, and RR Lyr) are intensively explained in e.g. Aerts et al. (2010).

subsection 1.2.1), hindering us from probing the deep radiative region of the Sun. In contrast, there have recently been a large number of g-mode pulsators observed by several spacecrafts, enabling us to infer much deeper regions which are somewhat impossible in helioseismology. Excitation mechanisms are also different for some kinds of pulsators. In the case of the Sun, it is observationally confirmed that the solar eigenmodes have finite widths, which are claimed to be caused by the intrinsic stochasticity of the convectively driven mechanism. On the other hand, multiple stars are oscillating based on other excitation mechanisms (for more detail, see e.g. Aerts et al., 2010) which render modes more coherent than those of the Sun, sometimes leading to more precise measurements of eigenfrequencies.

1.2.2 Seismic properties of low-mass main-sequence stars

It is currently known that there are multiple kinds of variables across a broad range of the HR diagram as shown in Figure 1.9. Among them, three subgroups of variables, namely, solar-like pulsators, δ Scuti stars, and γ Doradus stars, are demonstrated in this subsection focusing on their positions on the HR diagram, oscillation spectra, frequencies, mode indices, excitation mechanisms, and so on, as these variabilities are typical for low-mass main-sequence stars with masses 1.2-2.1$M_\odot$. The other variables are discussed in e.g. Aerts et al. (2010).

Solar-like pulsators

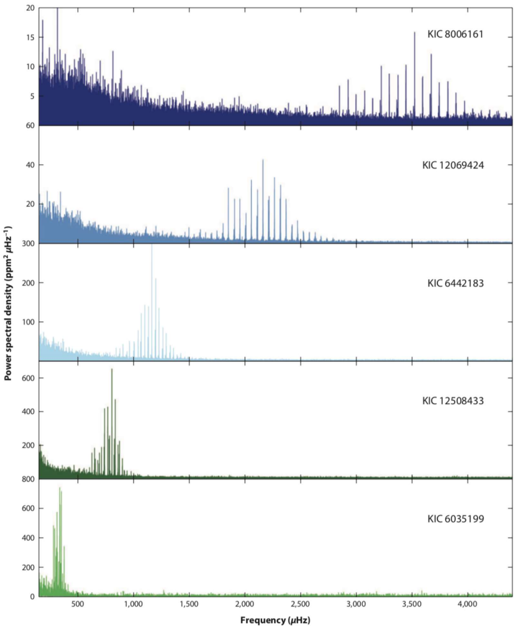

Figure 1.10: Power spectrum densities for several solar-like pulsators observed by the Kepler spacecraft (cited from Chaplin and Miglio, 2013). The effective temperatures of the stars get smaller and smaller from top to bottom, i.e. the stars are arranged younger to older from top to bottom. Comb-like structures and bell-curve shapes are common in all the spectra. Bumps in the lower frequency regions are thought to be caused by background noises mainly caused by granulations at the surfaces of the stars. It is also seen that $\nu_{\max}$ (explained in the text) gets smaller as the star evolves.

Solar-like pulsators are literally stars which are oscillating with properties similar to those of the Sun, and they are thus located close to the Sun on the HR diagram (Figure 1.9). Figure 1.10 illustrates typical power spectra of solar-like pulsators at different evolutionary stages. Comb-like structures and bell-curve shapes are common in the spectra for all of the stars; which are believed to originate from a common excitation mechanism where near-surface superadiabatic convection plays a critical role. Typical frequencies of solar-like stars are of the order of mHz corresponding to periods of a few minutes. Based on a comparison of the observation with theoretical calculations, they are thought to be oscillating with high-order p modes; the radial orders of the observed eigenmodes are relatively high $\sim$ a few dozens. The spherical degree is at most three due to the cancellation effect described in Subsection 1.2.1.

It should be noted that the solar-like pulsation is also observed for more evolved stars with convective envelopes such as red giant stars (Figure 1.10) because of the same excitation mechanism. The frequency which corresponds to the highest peak of the bell-curve shaped spectrum is, interestingly, correlating with the evolutionary stage of the pulsator (Figure 1.10), which is often used

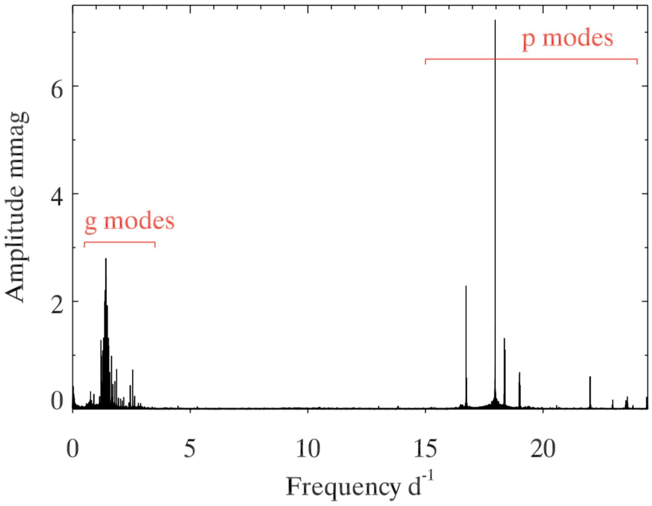

Figure 1.11: Amplitude spectrum of a δ Sct and γ Dor hybrid pulsator KIC 11145123 (Kurtz et al., 2014) (see the definition of what a hybrid pulsator is in Subsection 1.2.3). G-mode region (γ Dor oscillation) and p-mode region (δ Sct oscillation) are apparently separated (some of the modes are *mixed modes* which behave as a p mode in the outer envelope and as a g mode in the core region.) The widths of the peaks are very narrow thanks to the coherence of the modes, and thus, the observational uncertainties are astonishingly small ($\sim 10^{-7}\,\mathrm{d}^{-1}$).

to estimate ages of the pulsators in, for instance, galactic archaeology. The procedure to estimate global parameters based on the so-called $\nu_{\max}$ is presented in e.g. Chaplin and Miglio (2013).

δ Scuti stars

δ Scuti (δ Sct in short) stars are one of the frequently-observed variables and the prototype was already discovered around the beginning of the twentieth century. They are considered as slightly evolved stars with masses 1.5–2.0$M_\odot$ (Figure 1.9), and located around a bluer edge of the Cepheid instability strip; the oscillations are believed to be excited by the κ mechanism where the He-ionization zone is playing an important role. We do not see any bell-curve shaped structures as seen in the spectra of solar-like pulsators (see the high-frequency region ranging from 15–20 d^{-1} in Figure 1.11), and they are thought to be oscillating with p modes whose radial orders are lower than 10. A typical frequency of a δ Sct star is 10–100 μHz, a few hours in periods, and the amplitudes are relatively high compared with those of solar-like pulsators (Figure 1.11).

Though this subgroup has been known for a long time, it has been quite challenging to correctly interpret observed spectra of δ Sct stars. One reason is that stars are often rotating fairly fast ($\sim$ 100 km/s) in this mass range, and thus we cannot neglect effects of rotation both on the structures and the oscillations. Another point is related to the existence of outermost thin convection zones that these low-mass stars typically have. In such outermost thin convective zones, superadiabaticity is dominant and non-adiabatic effects have to be taken into account in analyzing the oscillations. The prescriptions correctly treating convection and oscillation simultaneously has, nonetheless, not been established yet. For more detailed discussions about rotational effects on stellar oscillations and those for convection-oscillation interactions, see e.g. Tassoul (1980) and e.g. Dupret et al. (2005) respectively.

γ Doradus stars

We find γ Doradus (γ Dor in short) stars close to, though slightly redder and less luminous than, δ Sct stars on the HR diagram (Figure 1.9). They are slightly smaller in mass than δ Sct stars, with masses around 1.3–1.6$M_{\odot}$. The first discovery of γ Dor stars as a variable was in 1995. This rather recent discovery is mainly due to typical frequencies of γ Dor stars, which are of the order of $\sim$ μHz or a few days in periods (see the low-frequency region ranging from 0–5 d^{-1} in Figure 1.11). Such periods longer than a day are difficult to detect by ground-based telescopes without any multisite observing campaigns or any special (for example, multi-photometric) observations. We have to avoid diurnal cycles on the earth and we had to await the advents of space telescopes such as Hipparcos to detect such long-period pulsators (for detailed historical backgrounds from the observational perspective, see Chapter 2 of Aerts et al., 2010). Theoretical computations show that γ Dor oscillations are high-order (the radial orders are higher than a few dozens) g modes. The excitation of the g mode is attributed to so-called convective-blocking mechanism where convective overshooting below the base of the convective envelope contributes much.

One of the most well-known properties of γ Dor stars is the g-mode period spacing ΔP_g, which is defined as a difference between g-mode periods with consecutive radial orders and the same spherical degree. Asymptotic analysis of stellar non-radial oscillations demonstrates that the mean value of the ΔP_g is inversely proportional to an integral of the Brunt-Väisälä frequency. This theoretical prediction has been currently confirmed in a model-independent manner, and the mean ΔP_g is often used as an indicator for stellar evolutionary stage because the Brunt-Väisälä frequency is strongly dependent on the evolutionary stage of the star as described in Subsection 1.1.1. Interpreting the ΔP_g is one of the main subjects in this dissertation, and it is discussed in Chapter 2.

1.2.3 Recent studies and the results related to this dissertation

The goal of this subsection is to concisely present what we have learned so far with asteroseismology and future prospects of the current studies. In particular, we would like to concentrate on three themes, namely, estimation of evolutionary stages with the g-mode period spacing ΔP_g, asteroseismic modeling of δ Sct and γ Dor hybrid pulsators, and asteroseismic inference on stellar internal rotation.

G-mode period spacing ΔP_g

The detection of high-order g modes in various types of stars (γ Dor, SPB, β Cep, RGB, Red Clump stars, white dwarf stars) is such a fortune that we are now able to probe the g-mode propagation regions inside the stars, namely, the deep radiative regions. In particular, for such high-order g modes, we can utilize asymptotic theory (see Chapter 2), leading to a simple relation between the Brunt-Väisälä frequency N^2 of the star and the g-mode period spacing which is defined as the difference in period between two neighboring g modes, with consecutive radial orders and the same spherical degree. Because N^2 is considerably dependent on the evolutionary stage of the star, the observed g-mode period spacings can be used as an indicator for the evolutionary stage. This is how we asteroseismically infer evolutionary stages for high-order g-mode pulsators, and the method has been used in a large number of studies (e.g. Bedding et al., 2011). For more information, see Chapter 2.

One of the examples where g-mode period spacings are successfully used to infer stellar evolutionary stages is Bedding et al. (2011). They have measured g-mode period spacings for evolved

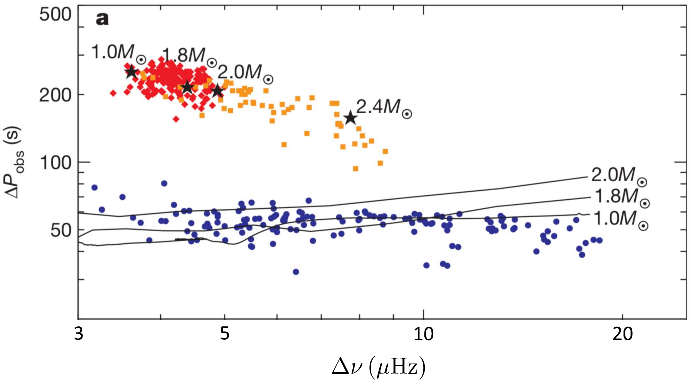

Figure 1.12: So-called asteroseismic diagram for the observed red giants (hydrogen-shell burning stars) and red clump stars (helium-core burning stars). Cited from Bedding et al. (2011). Horizontal axis is the large separation $\Delta\nu$, which is defined as a difference in frequency between two neighboring high-order p modes with consecutive radial orders and the same spherical degree, and is generally considered to be related to the dynamical time scale $t_{\rm dyn} \propto \sqrt{\rho}^{-1}$ (ρ represents the mean density) of the stars (see, for example, Aerts et al., 2010). Vertical axis is $\Delta P_{\rm g}$ as described in text. Based on the comparison between the theoretical evolutionary computations for red giants (black lines) and those for red clump stars (black star symbols) with the observation, Bedding et al. (2011) have succeeded in separating the two categories (blue circles, and red and orange circles, respectively.)

stars (on the red giant branch) observed by the Kepler spacecraft, and they have succeeded in differentiating red giant stars from red clump stars (Figure 1.12) based on the values of the observed g-mode period spacings. Since red giant stars and red clump stars sometimes overlap with each other on the HR diagram, it is often the case that we cannot differentiate them photometrically nor spectroscopically. Bedding et al. (2011) thus have shown the high potential of g-mode asteroseismology, which enables us to carry out analyses we have not been able to do. The study is also useful for other kinds of studies such as galactic archaeology (Miglio et al., 2013) by combining it with the other observations as spectroscopy and stellar kinematics.

The mean value of the g-mode period spacings is thus useful for inferring stellar evolutionary stages, which is one of the global parameters of a star, as we see in the last paragraph. But we can further investigate internal structures in detail by focusing on the patterns of observed g-mode period spacings; it has been analytically shown that the patterns are highly dependent on the Brunt-Väisälä frequency (N^2; see the definition in Subsection 1.1.1) profile (e.g. Miglio et al., 2008), especially dependent on sharp features in N^2. Therefore, based on the patterns of g-mode period spacings, it is possible for us to extract information on sharp features in N^2 located in the deep radiative regions. There have been numerous attempts where the relation between the patterns of g-mode period spacings and N^2 is investigated via 1-dimensional evolutionary calculations changing prescriptions for mixing processes (e.g. Pedersen et al., 2018). As it is demonstrated in Subsection 1.1.1, we do not fully understand the chemical composition profiles of stars, which strongly affect N^2, especially in the case of low-mass stars such as γ Dor. So, attempts to interpret the patterns of g-mode period spacings are one of the most prominent subjects in asteroseismology.

Patterns of g-mode period spacings are also useful for inferring internal rotation of γ Dor stars (Bouabid et al., 2013), and Li et al. (2020), for example, have inferred a few hundred γ Dor stars' rotation rates in the deep radiative regions. This method is applicable for rapidly rotating stars, and thus it can be complementary to the perturbative approach to infer internal rotation of stars (see 'Asteroseismic inference on stellar internal rotation' later in this subsection.)

Asteroseismic modeling of δ Sct and γ Dor hybrid pulsators

It is readily seen that δ Sct stars and γ Dor stars are located close to each other on the HR diagram (Figure 1.9), suggesting the possibility that there should be stars with both δ Sct and γ Dor properties, so-called δ Sct and γ Dor hybrid pulsators. Thanks to the observations by the Kepler spacecraft, it has recently come to be recognized that such hybrids are rather common entities (Bradley et al., 2015), and that about 50% of δ Sct stars discovered so far are also pulsating with γ Dor-type oscillation, which is much higher than previously expected. The important point is that the δ Sct and γ Dor hybrid pulsators are oscillating with low-order p modes and high-order g modes. We can therefore probe outer envelopes by the p modes and deep radiative regions by the g modes; most of the interiors therefore can be probed for the δ Sct and γ Dor hybrids. This characteristic is especially of great help to calibrating prescriptions in stellar evolutionary calculations (Sanchez et al., 2017). Equilibrium models thus obtained are subsequently used for further asteroseismic analyses, for example, rotation inversion (Kurtz et al., 2014), and the procedure to find models which reproduce the observed frequencies is called asteroseismic modeling.

It should be mentioned that typical relative differences between modeled frequencies (which are computed based on an equilibrium model) and observed frequencies are about a few percent, which are much larger than those of the solar case (see “Comparison with helioseismology” in the last subsection). Furthermore, observational uncertainties in asteroseismology are often so small that residuals normalized by the uncertainties tend to be fairly large. Although there have been several attempts to perform structure inversion with which the relative differences in sound speed and density between a reference equilibrium model and the real star are estimated based on statistical methods (Kosovichev and Kitiashvili, 2020), we are often confronted with the high degree of ill-posedness which prevents us from correctly inferring the relative differences. This problem is caused, for example, by the relatively small number of the detected modes in asteroseismology (see “Comparison with helioseismology” in the last subsection). As such, filling the gap between the theory and the observation via asteroseismology has been not really completely successful yet. For more detailed discussions about the current status of asteroseismic modeling and structure inversion in helio- and astero-seismology, refer to e.g. Buldgen et al. (2019).

Finally, let me introduce Chen et al. (2020); this study has been the first to carry out asteroseismic modeling of a δ Sct star (KIC 10736223) in an Algol-type binary. They have modeled the star taking into account the mass accretion during the evolution with MESA, and have drawn a conclusion that the star has just undergone the mass accretion. The residuals between the frequencies of their model and the observation are still large, but these kinds of studies definitely put constraints on, for instance, mass accretion schemes adopted in stellar evolutionary codes, in which a number of phenomenological prescriptions and assumptions need to be validated.

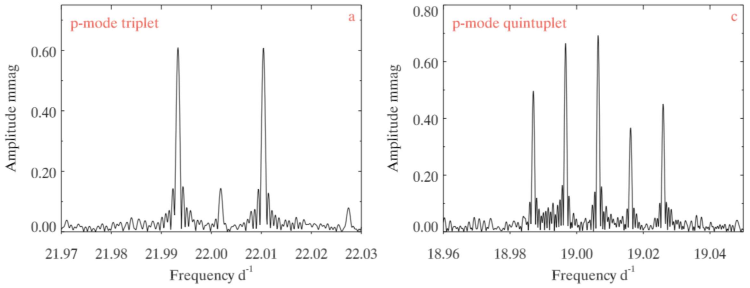

Figure 1.13: Example of observed rotational splitting. This is actually an expanded amplitude spectrum of KIC 11145123 in p-mode frequency range (Figure 1.11). Since the number of the split modes are three (triplet) in the left panel, it is most likely that this is a mode with $l = 1$. Meanwhile, the quintuplet in the right panel is likely $l = 2$. Based on this rough mode identification and equation (1.24) we can roughly estimate the rotation of the star (see text). This figure is partly cited from Kurtz et al. (2014).

Asteroseismic inference on stellar internal rotation

What the Kepler spacecraft has achieved is not only the precise measurements of brightness variabilities but also the four-year long continuous observation, which has realized frequency resolution of the order of a few μHz, leading to detections of a phenomenon called rotational splitting — an essential observable in rotation estimation (Figure 1.13), especially for main-sequence stars and red giants (interestingly, the rotational splitting of white dwarfs have been reported much before the Kepler data has come, see for example Kawaler et al., 1999).

The frequency shift due to rotational splitting is related to internal rotation rate as

$$\delta\omega_{nlm} = m(1 - C_{nl})\overline{\Omega}, \tag{1.24}$$

where C_{nl} is the Ledoux constant which is related to the perturbation in eigenfrequencies caused by the Coriolis force (see the definition in e.g. Aerts et al., 2010) and $\overline{\Omega}$ is a rotation rate. Note that here the rotation is assumed to be uniform throughout the star. The expression (1.24) can be obtained from the equation (1.20). The derivations can be found in, for instance, Aerts et al. (2010).

Once we measure rotational shifts $\delta\omega_{nlm}$ and compute C_{nl} based on a reference model to represent the star, the rotation rate $\overline{\Omega}$ can be estimated based on the equation (1.24). It should be noted that what we really observe is a series of rotational shifts for detected modes with mode indices (n, l, m), and we have a system of equations represented by the equation (1.24) (the equation has rather complex forms if we take into account radial and latitudinal dependences of the internal rotation, see Chapter 4.) Then, we have to estimate the rotation rates by inverting the set of the equations; this procedure is called rotation inversion.

The number of the Kepler targets for which rotation inversion has been carried out is around several dozens for now (Aerts et al., 2017). The evolutionary stages are ranging from the main sequence to somewhat more evolved stars as red giant stars, allowing us to study the temporal variation of internal rotation profiles along with the evolution (e.g. Deheuvels et al., 2012). The current understanding thus established is summarized by Aerts et al. (2019) that almost all the main-sequence stars investigated so far are exhibiting nearly rigid rotation throughout them, and that, in spite of the core contraction phase they have experienced before they reached the red giant branch, the contrast between the core rotation rate and the envelope rotation rate is generally much smaller than expected based on the numerical simulations of angular momentum transfer inside stars (e.g. Tayar and Pinsonneault, 2013) (see Figure 1.5 in Subsection 1.1.2). Though several mechanisms (angular momentum transfer by internal gravity waves, magnetic fields, and so on) to explain the observed much-smaller contrast between the rotation rate of the core and the envelope have been suggested (e.g. Fuller et al., 2019), this issue has not been settled yet. In addition, several asteroseismic analyses focusing on inferring internal rotational profile in detail (e.g. Benomar et al., 2018) have reported the significant detections of the rotational velocity shear with the factor $\sim$ a few, suggesting that the stars are rotating rigidly throughout most of the interiors, but rotating not completely rigidly as the current understanding is.

1.3 Asteroseismology of KIC 11145123

The final section in this chapter is specifically dedicated to the introduction to asteroseismology of KIC 11145123 which is one of the Kepler targets (Huber et al., 2014). Though there have recently been a huge number of stars to be asteroseismically investigated, the star outstands in terms of multiple aspects such as the high-quality observation done for the star and various intriguing results successively obtained based on the observation, with respect to the internal rotation profile, structure, and evolutionary stage of the star, etc. This star, nevertheless, is not only merely a star exhibiting such fascinating characteristics, but also an important subject in the context of stellar physics generally.

First of all, we present the context of asteroseismology of KIC 11145123; how and why the star was found, what results have been obtained so far based on asteroseismic analyses of the star, and mysteries simultaneously having arisen are discussed. We then provide the readers with brief reviews of the previous researches in which asteroseismology has been utilized to infer a variety of features of the star. Specific procedures are especially emphasized. In the last subsection, we mention the current status of our understanding of the star, problems to be solved, and the goals in this dissertation.

1.3.1 Context

The discovery of KIC 11145123 is closely related to a historical background of studies on stellar internal rotation. As is described in the small subsection 'Asteroseismic inference on stellar internal rotation', the Kepler spacecraft has provided us with a large number of detections of rotational splitting for stars with various evolutionary stages. Among the fruitful Kepler targets, the first asteroseismic analyses to infer the internal rotation of stars and, if possible, the angular momentum transport inside stars during the evolution have been carried out for evolved stars such as red giant and sub giant stars (Deheuvels et al., 2012). This is because these evolved stars are more luminous than the main-sequence stars, and it was much easier to extract rotational splitting (than it was for the main-sequence stars) with the data available at that time (the Kepler spacecraft was launched in 2010). Based on the analysis, they have concluded that the core of the stars is rotating faster than the envelope with a factor of at most 10, which is much smaller than the expected contrast for such evolved stars (see the small subsection 'Asteroseismic inference on stellar internal rotation'.)

Then, how about the internal rotation profiles of main-sequence stars? That was the next question to be addressed in the community of asteroseismology as of around 2013 after Deheuvels et al. (2012). To the end, D. W. Kurtz carefully looked for main-sequence stars (among the Kepler targets) which exhibit rotational splitting for both p modes and g modes, which enables us to infer the internal rotation of the envelope and the core at the same time. KIC 11145123 is one of three stars thus to be found among the vast samples of the Kepler Input Catalog; such main-sequence stars are hardly found even in the Kepler targets. Kurtz et al. (2014) immediately conducted asteroseismic analyses to infer the internal rotation profile of the star, and found that the star is rotating almost rigidly with rotation period of $\sim 100\,\mathrm{d}$, which is the first confirmation of such almost-rigidly rotation of main-sequence stars, and the result is consistent with previous study (Deheuvels et al., 2012), helping to establishing the current understanding of the internal rotation of stars.

Interestingly enough, on the course of asteroseismic modeling of the star, Kurtz et al. (2014) noticed that higher initial helium abundance ~ 0.3–0.4 is much favorable to reproduce the observed p-mode frequencies. But such higher initial helium abundance is difficult to explain for a simple single star, and thus, Kurtz et al. (2014) pointed out the possibility that the star is a blue straggler star which is thought to be born via some interactions with the other stars (see Subsection 1.1.2.) Interestingly again, the hypothesis above is partly supported by the inferred internal rotation profile where the outer envelope is rotating slightly faster than the core is; we need some mechanisms of angular momentum transfer to realize the rotational profile, and interacting with other stars can be a straightforward explanation.

Another peculiarity has been pointed out by Gizon et al. (2016). They analyzed the observed p-mode frequency splitting to estimate the asphericity of the star sensed by p modes, and found that the star is less oblate than is expected based on the rotation period. They attributed the oblateness smaller than the expected value to a possible existence of weak magnetic fields on the surface of the star, but it is still challenging to explain the origin of the fields without a thick convective envelope as the Sun has. Mysterious aspects of the star have been gradually revealed as more asteroseismic analyses have been performed.

To better comprehend properties of the star from a different perspective, Takada-Hidai et al. (2017) have conducted the spectroscopic observation of the star with Subaru/HDS. The primary result is that they found the star to be spectroscopically a blue straggler star as suggested by Kurtz et al. (2014). Thus, the star has probably experienced some interactions with other stars, which could be a reason for the peculiar characteristics asteroseismically confirmed. Another important finding in their study is that their best model of the star asteroseismically constructed based on the low metallicity prefers higher initial helium abundance as that of Kurtz et al. (2014), which is still too high for an ordinary single star.

Why have the high initial helium abundances been suggested for the star in the previous studies? One possibility is that the star has been really born in such high helium environments contaminated by stellar winds from already existing asymptotic giant branch stars. This multiple main-sequence phenomena (Bastian and Lardo, 2018) has been recently observed for some globular clusters. The star, however, is a field star based on the analysis of Takada-Hidai et al. (2017), and thus it is currently not in the high helium environments. The other possibility is that the star was originally born as a star with an ordinary initial helium abundance, and somehow obtain the helium from the outside, leading the star to be a blue straggler with high helium abundance in its envelope. Still, we have not had a clear answer to that point so far.

In addition to the unsolved problem concerning the formation history of the star, detailed asteroseismic analyses to infer the 2-dimensional internal rotational profile of the star by Hatta et al. (2019) demonstrated that the rotational profile is not so simple as previously suggested by Kurtz et al. (2014); the study especially suggested a hint of the fast-convective-core rotation which

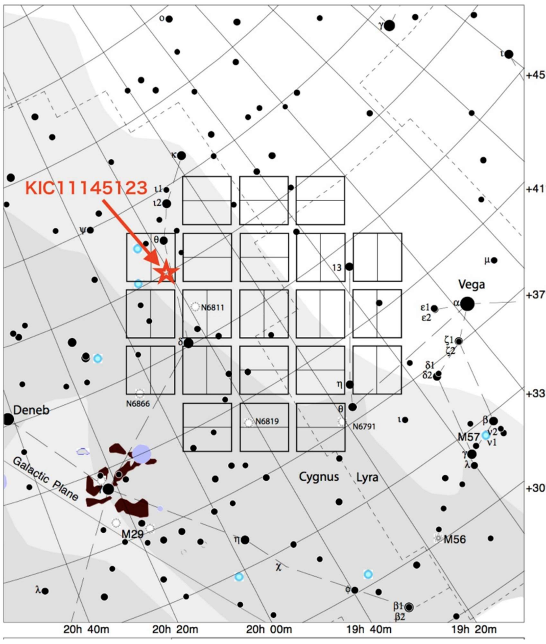

Figure 1.14: Kepler field and the position of KIC 11145123 indicated as a red star. Figure courtesy of M. Takata.

has never been pointed out. Though the suggestion seems to be significant in the context of the current understanding of stellar rotation, the best model of Kurtz et al. (2014) has been used where single-star evolution is assumed. Thus, the model dependence matters if the star has not evolved as a single star but has evolved as a blue straggler interacting with the other stars. Such model dependence has not been checked so far.

1.3.2 Previous studies of KIC 11145123

KIC 11145123 is one of the stars that have been observed by Kepler for four years (Figure 1.14). The effective temperature and the surface gravity were estimated photometrically (Huber et al., 2014) as $T_{\rm eff} = 8050 \pm 200$K and $\log g = 4.0 \pm 0.2$ (in cgs units). Thus, the star was thought to be an ordinary main-sequence A-type star. However, asteroseismology has disclosed many mysterious features of the star which cannot be explained if we regard the star as an ordinary main-sequence star (see the preceding subsection 1.3.1). In this subsection, previous asteroseismic studies of the star are briefly reviewed.

Kurtz et al. (2014)

The first asteroseismic research of the star has been conducted by Kurtz et al. (2014). They firstly measured the frequencies of the 76 detected modes (45 g modes and 31 p modes) (Figure 1.11) using a non-linear least-squares method. Based on an assumption that the triplets (Figure 1.13) are corresponding to modes with $l = 1$, and that the quintuplets (Figure 1.13) are corresponding to modes with $l = 2$, they determined the rotational shifts. They subsequently estimated averaged internal rotation using averaged p-mode rotational shifts and those of g modes.

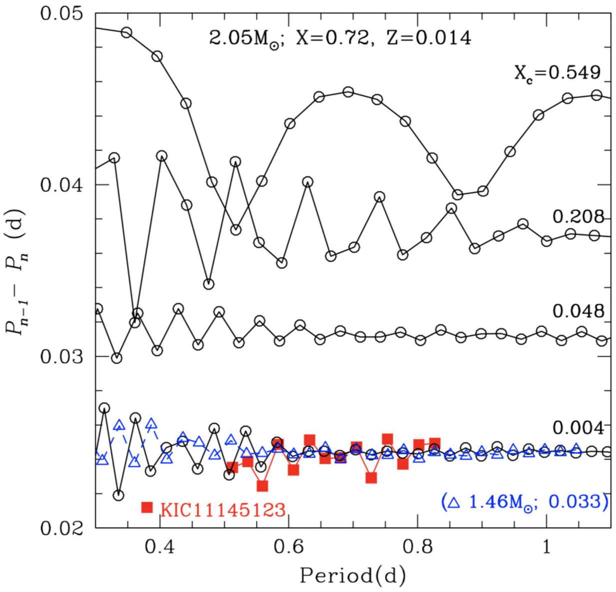

Figure 1.15: Observed g-mode period spacings ΔP_{g} (red squares) and modeled ones (open circles and blue open triangles) cited from Kurtz et al. (2014). A model with $M = 2.05\,M_{\odot}$, $X_{\mathrm{init}} = 0.72$, and $Z_{\mathrm{init}} = 0.014$ (open circles), shows that ΔP_{g} gradually decreases with decreasing hydrogen content at the core X_{c}, i.e. ΔP_{g} decreases as the star evolves (see Subsection 1.2.3). The amplitudes of modulations also gradually decrease during the evolution. It is theoretically predicted that amplitudes and "period"s of modulations are dependent on the structure of the Brunt-Väisälä frequency N (Miglio et al., 2008). This topic is also discussed in Chapter 2 in this dissertation. The g-mode period spacing ΔP_{g} of the best model in Kurtz et al. (2014) is illustrated with blue open circles, and the mean of the observed ones is fitted when the central hydrogen abundance is 0.033. Almost all the hydrogen has been consumed.

As we have described in Subsection 1.2.1, it is known that p modes probe the outer envelope and g modes probe the deep radiative region of the star. We can develop this idea to interpret p-mode rotational shift $\delta\omega_{\mathrm{p}}$ as a frequency difference caused by the rotation in the outer envelope Ω_{p}, and g-mode rotational shift $\delta\omega_{\mathrm{g}}$ as a frequency difference caused by the rotation in the core Ω_{g} (Kurtz et al., 2014). They used this property and model-independently found that the envelope of the star rotates slightly faster than the core does, namely, $\Omega_{\mathrm{p}} > \Omega_{\mathrm{g}}$. This is the first case in which we have found a star's envelope rotating faster than the core.

Then, they modeled the star so that the model would reproduce the observed T_{eff}, $\log g$, and frequencies. They aimed to fit the averaged g-mode period spacings $\overline{\Delta P_{\mathrm{g}}} = 0.024\,\mathrm{d}$ (Figure 1.15) and some of the p-mode frequencies (Figure 1.16). On the course of fitting the observed frequencies, they conducted mode identification. Their best model indicated that the star is at the TAMS stage. Another consequence of the modeling is that the initial helium content Y is extremely high (~ 0.34) for such a field star. Furthermore, they have carried out rotation inversion to estimate the internal rotation based on the best model. They have confirmed the same results that the star rotates almost rigidly with the period of 100 d, and that the envelope of the star rotates slightly faster than the core.

From their results obtained by asteroseismology, they suggested that the star could be a blue straggler (see Subsection 1.1.2) and it has experienced interactions with other celestial objects such

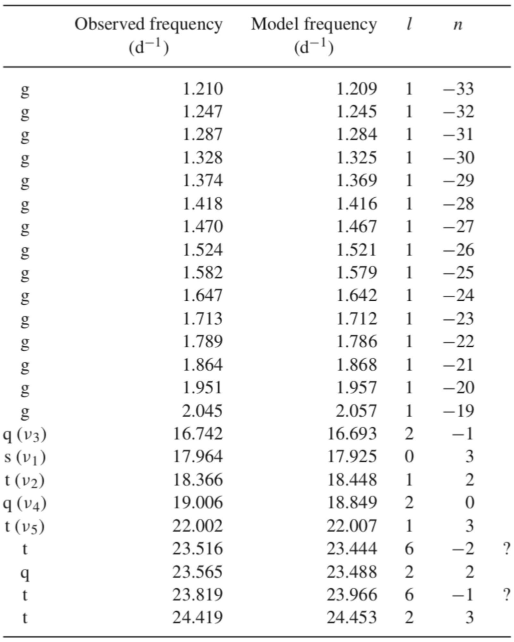

	Observed frequency (d^{-1})	Model frequency (d^{-1})	l	n	
g	1.210	1.209	1	−33	
g	1.247	1.245	1	−32	
g	1.287	1.284	1	−31	
g	1.328	1.325	1	−30	
g	1.374	1.369	1	−29	
g	1.418	1.416	1	−28	
g	1.470	1.467	1	−27	
g	1.524	1.521	1	−26	
g	1.582	1.579	1	−25	
g	1.647	1.642	1	−24	
g	1.713	1.712	1	−23	
g	1.789	1.786	1	−22	
g	1.864	1.868	1	−21	
g	1.951	1.957	1	−20	
g	2.045	2.057	1	−19	
q (ν_3)	16.742	16.693	2	−1	
s (ν_1)	17.964	17.925	0	3	
t (ν_2)	18.366	18.448	1	2	
q (ν_4)	19.006	18.849	2	0	
t (ν_5)	22.002	22.007	1	3	
t	23.516	23.444	6	−2	?
q	23.565	23.488	2	2	
t	23.819	23.966	6	−1	?
t	24.419	24.453	2	3	

Figure 1.16: Table of the observed and the modeled frequencies by Kurtz et al. (2014). The first column shows the mode properties, and the last two columns represent the spherical degree l and the radial order n from left to right. Though g-mode frequencies apparently are already fitted relatively well, some of the p-mode frequencies are not fitted well and there are significant deviations. Note that the observational uncertainties are of the order of $10^{-7}\,\mathrm{d}^{-1}$. Mode identification of modes with question marks are not reliable so that they were not used in the subsequent analyses in Kurtz et al. (2014).

as collision and mass transfer, in order to explain the peculiar internal rotation and the extremely high helium abundance.

Gizon et al. (2016)

The second asteroseismic analysis has been carried out by Gizon et al. (2016). Based on the frequency determination, the mode identification, the equilibrium model of the star, and the eigenfunctions and the frequencies obtained by Kurtz et al. (2014), they carried out asteroseismic analyses focusing on the frequency shifts caused by the asphericity in the structure, and they succeeded in measuring the star's oblateness. They however found that the star is less oblate than expected from its rotation. They attributed the smaller oblateness to existence of weak magnetic fields at the surface of the star. However, the outer convective layer of the star is modeled as too thin to produce such a magnetic field via the usual dynamo mechanism. This is another mysterious aspect of the star.

Takada-Hidai et al. (2017)

To shed lights on the ambiguous understandings of the star, Takada-Hidai et al. (2017) analyzed the star spectroscopically with Subaru/HDS. They measured the atmospheric parameters T_{eff} and $\log g$, and the metallicity of the star [Fe/H] from the equivalent widths of the iron lines, and found that the star has rather lower metallicity ($Z = 0.003$) than in the previous model of the star (Kurtz et al., 2014), namely, $Z = 0.01$. They also estimated the surface abundance by calculating the equivalent width of each element, and subsequently, they conducted abundance analysis to spectroscopically categorize the star. By comparing abundance pattern of the star with those of the other stars such as Am stars, Ap stars, blue stragglers, they concluded that the star is spectroscopically a blue straggler, supporting the suggestion by Kurtz et al. (2014). However, they also found that the upper limit for the mass of a companion star of the star is 70 M_{J} (M_{J} is the mass of Jupiter) via the phase modulation technique (Murphy et al., 2016) and they concluded that the star probably has currently no companion. This conclusion seems to be incompatible with their other conclusion that the star is a blue straggler in terms of how a blue straggler is born; the star must have experienced some interactions with its companion (see Subsection 1.1.2), but the companion is gone. How the star could be a blue straggler is another interesting topic.

Hatta et al. (2019)

Hatta et al. (2019) have expanded the study of Kurtz et al. (2014) focusing on the internal rotation profile of the star. Based on the rotational shifts, the rotational splitting kernels, and the equilibrium model determined by Kurtz et al. (2014) (for what the rotational shifts and the rotational splitting kernels are, see, e.g., Subsection 4.3.1), they have carried out 2-dimensional rotation inversion to, especially, check the possibility of the latitudinally differential rotation of the star, and they have confirmed that the high-latitude region in the envelope is rotating slightly faster than the low-latitude region, thus exhibiting the so-called anti-solar-like rotation (Lund et al., 2014).

In addition to the existence of the latitudinally differential rotation of the star, they have also found a hint that the convective core might be rotating much faster ($\sim$ 5 times faster) than the other regions of the star, via detailed analyses of behaviors of the estimates obtained by inversion. They claim that the fast-core rotation has been successfully measured because they have used mixed modes to probe the convective core which cannot be probed by high-order g modes; it is usually the case that high-order g modes are used to infer deep internal rotation of γ Dor stars (see Subsection 1.2.3). Though there still remains several issues about their results in terms of, for example, the model-dependence of the inference, their findings are shedding new light on the current understanding of the stellar internal rotation (see Subsection 1.2.3).

1.3.3 Two issues and room for improvements

In this final subsection, two issues concerning asteroseismology of KIC 11145123 are introduced.

What is the best model of the star?

The first issue is related to the evolution of the star. As Takada-Hidai et al. (2017) have suggested, the star is spectroscopically a blue straggle star, and therefore, the star may have experienced some interactions with other stars. Interestingly, the models, obtained by Kurtz et al. (2014) and Takada-Hidai et al. (2017) assuming single-star evolution for the star, both have high initial helium abundance of > 0.30. Such high initial helium abundance is rather rare for an ordinary single star, and the high initial helium abundance of the models may also suggest (from the theoretical point of view) the possibility of the star having experienced some interactions with other stars; it was born as a single star with an ordinary initial helium abundance of ~ 0.26 and then obtained extra helium from the outside via interactions with other stars. However, there have been no attempts to model the star assuming non single-star evolution with relatively low initial helium abundance. Because it has recently been recognized that some stars in globular clusters exhibit high initial helium abundance of ~ 0.40 (Bastian and Lardo, 2018), it is of great importance to compare the previous models of the star (computed based on an assumption of single-star evolution) and a new model of the star (computed based on an assumption of non single-star evolution) to understand how the star was born and evolved until now.

Is the fast-core rotation reasonable?

The second issue is related to the internal rotation, in particular, the fast-core rotation of the star. The previous studies asteroseismically inferring internal rotation of the star have been mostly based on the models calculated assuming single-star evolution for the star. Therefore, it is necessary for us to check whether the previous inferences on the internal rotation of the star are changed or not depending on the choice of the models; model-dependence of the inference. It is, of course, impossible to eliminate completely such model dependence in rotation inversion (because the rotational splitting kernels depend on the models), but it should be instructive to discuss, for example, the existence of the inferred fast-core rotation, which is especially sensitive to the model dependence (see the details in Section 4.3).

1.4 Structure of this dissertation

Based on the backgrounds described in this chapter, detailed asteroseismic analyses covering various subjects are demonstrated throughout this dissertation. Among them, the central topic is the asteroseismology of KIC 11145123 featured in Chapter 4. Two other chapters, Chapters 2 and 3 are mainly devoted to methodologies which are to be applied in the asteroseismic studies of KIC 11145123, but more than that, both of the chapters contain numerous discussions which are invaluable in broader contexts of stellar physics. This is the reason why Chapters 2 and 3 are independent from Chapter 4. Below are specific contents in each chapter.

Chapter 2 is dedicated to the analysis of g-mode period spacings $\Delta P_{\rm g}$, especially focusing on analytical formulations of the $\Delta P_{\rm g}$ patterns. These analytical expressions are compared with numerically computed $\Delta P_{\rm g}$ patterns based on some stellar models, enabling us to validate the formulations. A part of the result in Chapter 2 is applied to asteroseismic non-standard modeling of KIC 11145123 in Chapter 4. The other parts of the chapter are independent from the other chapters because $\Delta P_{\rm g}$ patterns are frequently observed quantities for a large number of high-order g-mode pulsators, and the topics are not limited just for KIC 11145123.

In Chapter 3, a novel scheme for calculating a stellar equilibrium model whose chemical compositions in the envelope are modified is presented. A large part of this chapter is devoted to validating the scheme, and in the end, an example of the applications of the scheme is shown, e.g. the non-standard modeling of KIC 11145123 in a rather simple manner. This newly developed scheme is also applicable for other studies, which is the reason why this chapter is also independent as a chapter.

Combining the case studies demonstrated in Chapters 2 and 3, detailed asteroseismic studies of KIC 11145123 are presented in Chapter 4. The first goal is to construct an envelope-modified model of the star (based on the scheme developed in Chapter 3) reproducing the observed $\Delta P_{\rm g}$ pattern (following procedures explained in Chapter 2) and some of the p-mode frequencies. This is done in a much more systematic way than in Chapter 3, and the tentative envelope-modified model of the star is given which reproduces as many observables as possible for the moment. The second goal is to infer the internal rotation of the star by performing rotation inversion. The tentative model is used as one of two reference models (the other is the previous model of Kurtz et al., 2014), and the results are compared to draw a conclusion about a hint of fast-convective-core rotation suggested by Hatta et al. (2019).

Finally, we conclude in Chapter 5 concentrating on the evolutionary stage, internal structure, and internal dynamics of KIC 11145123.

Chapter 2

G-mode period spacing pattern of γ Doradus stars

Space missions such as Hipparcos, MOST, CoRoT, Kepler, and TESS have enabled us to find stars oscillating with periods of about a day, which used to be quite difficult targets for us to observe with ground-based telescopes on the earth due to the diurnal effect. That is one of the main reasons that a large number of high-order g-mode low-frequency pulsators, γ Dor stars, SPB stars, β Cep stars, and so on, have been found recently, and thus, we can now probe deep regions (~ 0.1 in fractional radius) of the pulsators; remembering the case of the Sun (we can probe as deep as ~ 0.5 in fractional radius via, for instance, helioseismic rotation inversion), g-mode asteroseismology has been definitely revealing new physics.

One difficulty of g-mode asteroiseismology is (this is also the case for p- or mixed-mode asteroseismology, of course) that we cannot carry out inversion as precisely as in helioseismology because the number of detected modes are much smaller than that in helioseismology (see the small subsection 1.2.1). Instead, the g-mode period spacing ΔP_{g}, which is defined as a difference between two g-mode periods with consecutive radial orders and the same spherical degree, is often used to infer somewhat averaged properties of the interiors of the stars. This is because asymptotic theory for high-order stellar eigenmodes shows that ΔP_{g} is inversely proportional to the integral of the Brunt-Väisälä frequency throughout the propagation zone as will be shown in the following sections. Therefore, a mean value of observed g-mode period spacings $\overline{\Delta P_g}$ is frequently used as an indicator for a stellar evolutionary stage, leading to multiple significant studies (see Subsection 1.2.2). Actually, as shown later, the evolutionary stage of the previous stellar model of our main target KIC 11145123 used to be determined based on the observed $\overline{\Delta P_g}$.

More can be explored if we pay attention to modulated patterns of ΔP_{g}, not just a mean value $\overline{\Delta P_g}$. Such modulated patterns of ΔP_{g} around a mean value $\overline{\Delta P_g}$ have been frequently observed, and the apparent discrepancy between the theory, which predicts a constant value for ΔP_{g}, and the observations, which clearly show oscillatory ΔP_{g} patterns as a function of g-mode periods, can be explained by the existence of the chemical composition gradient just above the convective core, which leads to variation in N^2 (see Section 2.2). In other words, we can in principle infer chemical composition gradients inside stars based on modulated patterns of observed ΔP_{g}, which could be shedding new light on our understanding of how a convective core grows together with mixing processes during the evolution; as it is described in Subsection 1.1.1, the interrelation between mixing processes and the chemical composition gradients inside stars are still not fully understood, especially for 1.2–2.0$M_\odot$ stars.

In this chapter, modulated patterns of $\Delta P_{\rm g}$ (for γ Dor stars because they are relatively less massive main-sequence stars) is discussed both from the theoretical and observational points of view. First, a basic expression relating high-order g-mode periods to the Brunt-Väisälä frequency is presented, and several examples where $\overline{\Delta P_g}$ can be used as an indicator for stellar ages are illustrated. Observations actually revealing modulated $\Delta P_{\rm g}$ patterns are also shown. Secondly, theoretical descriptions for modulated $\Delta P_{\rm g}$ patterns are given with simple numerical computations to check the validity of the analysis. Some of the analyses have been newly developed. Then, the theoretical descriptions are used to understand $\Delta P_{\rm g}$ patterns of realistic stellar models (Section 2.3). It is shown that the newly developed expressions are useful for extracting the information on the extent of the overshooting above the convective core boundary. An application to KIC 11145123 is finally presented in Section 2.4, which is incorporated in the later analysis in Chapter 4. Several suggestions are presented to resolve a discrepancy between the modeled $\Delta P_{\rm g}$ pattern obtained in Section 2.4 and the observed one for KIC 11145123.

Reference stellar models are computed via MESA, version 9793, and eigenfrequency calculations for stellar models are done by GYRE (Townsend and Teitler, 2013). Theoretical discussions are mostly based on Tassoul (1980), Unno et al. (1989), Miglio et al. (2008), and Cunha et al. (2019); see them for more thorough derivations and discussions.

A final remark concerns a history of analyses of $\Delta P_{\rm g}$ patterns. It is of a great interest to mention that the first detection of modulated $\Delta P_{\rm g}$ patterns was done for not main-sequence g-mode pulsators but for white-dwarf pulsators (Winget et al., 1982). Though the physical origin of modulated $\Delta P_{\rm g}$ patterns of white dwarfs is thought to be the same as those of main-sequence g-mode pulsators, the internal structures of these stars significantly differs from each other. Since we focus more on low-mass main-sequence stars in this dissertation, we purposely do not discuss white-dwarf $\Delta P_{\rm g}$ patterns in this chapter. Readers should refer to such discussions in, e.g., Chen (2016)

2.1 Introduction

2.1.1 Starting point: asymptotic solution for high-order g modes

Let us begin with the second order equation for stellar linear adiabatic oscillation obtained based on the Cowling approximation where the Eulerian perturbation of the gravitational potential is neglected (Equation 2.1)

$$\frac{d^2\xi_r}{dr^2} + k_r^2\xi_r = 0, \tag{2.1}$$

in which the radial wavenumber k_r is defined as

$$k_r^2 = \frac{1}{\omega^2 c^2}(\omega^2 - N^2)(\omega^2 - L_l^2). \tag{2.2}$$

In the asymptotic limit for high-order g modes, $\omega^2 \ll N^2$ and $\omega^2 \ll L_l^2$, we thus have

$$k_r^2 \sim \frac{l(l+1)N^2}{\omega^2 r^2}. \tag{2.3}$$

Equation (2.1) with Equation (2.3) can be solved, for example, via the WKBJ approximation. Note that it is assumed in the WKBJ approximation that wavelengths of eigenfunctions are much shorter than the scale height of the backgrounds (that of the Brunt-Väisälä frequency in this case).

This is such an important assumption that a deviation from the mean value of ΔP_g is closely related to the deviation from the condition as it is demonstrated in Subsection 2.2. The WKBJ approximation results in the following eigenfunction

$$\xi_r \propto \frac{1}{\sqrt{k_r}}\sin\left(\int_{r_0}^{r} k_r dr + \frac{\pi}{4}\right), \tag{2.4}$$

where r_0 is the lower boundary of the propagation zone above which $k_r^2 > 0$.

Posing appropriate boundary conditions (see e.g. Unno et al., 1989) for the eigenfunction (2.4) leads to the eigenvalue condition as below:

$$\int_{r_0}^{r_1} k_r dr = n\pi, \tag{2.5}$$

where n is a natural number, and where r_1 is the upper boundary of the propagation zone below which $k_r^2 > 0$. By substituting the explicit form of k_r for the eigenvalue condition (2.5) and expanding the integrand of the left hand side of the eigenvalue condition to the first-order, we have periods of high-order g modes;

$$P_n = \frac{2n\pi^2}{l(l+1)}\left(\int_{r_0}^{r_1} N d\ln r\right)^{-1}. \tag{2.6}$$

If we take a subtraction $P_{n+1} - P_n$ for a certain spherical degree l, the g-mode period spacing ΔP_g can be obtained

$$\Delta P_\mathrm{g} = \frac{2\pi^2}{l(l+1)}\left(\int_{r_0}^{r_1} N d\ln r\right)^{-1}. \tag{2.7}$$

It should be noted that the derivations above are just qualitative demonstrations. For more decent derivations, see Tassoul (1980), Unno et al. (1989), Miglio et al. (2008), and Cunha et al. (2019).

2.1.2 Mean ΔP_g as an indicator of stellar evolutionary stages

Firstly, let us take a look at the way the Brunt-Väisälä frequency varies as a star evolves. Figure 2.1 shows the Brunt-Väisälä frequencies of several stellar models at different evolutionary stages. It is clearly seen that the Brunt-Väisälä frequency gets more centrally concentrated along with evolution, which is attributed to higher densities around the central region for more evolved models and also attributed to chemical composition gradients just above the nuclear burning cores (for the contribution of the chemical composition gradient ∇_μ to the Brunt-Väisälä frequency, see Equation 1.2).

Then, it is expected that $\int N d\ln r$ gradually increases as the star evolves because of the centralization of the Brunt-Väisälä frequency together with the component $\sim 1/r$ in the integrand, resulting in the decrease of the asymptotic value of ΔP_g which is inversely proportional to $\int N d\ln r$ (Equation 2.7). We can see the expected variation in Figure 2.2. Intriguingly, the decrease of the asymptotic value of ΔP_g is monotonic, this is one of the reasons why the mean value of observed g-mode period spacings can be used as an indicator for the evolutionary stage of the star.

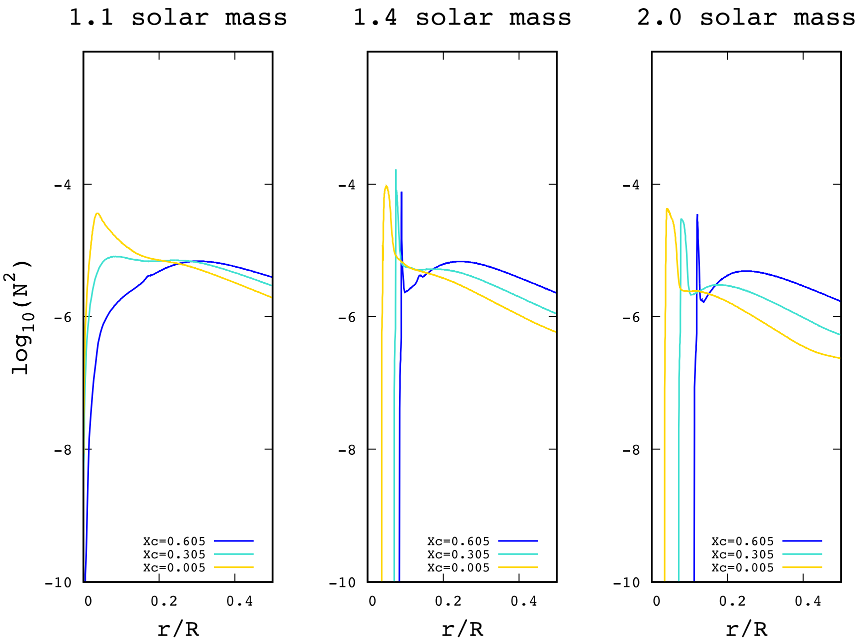

Figure 2.1: Brunt-Väisälä frequencies for several models ($1.1M_\odot$, $1.4M_\odot$, and $2.0M_\odot$, from left to right, respectively) at different evolutionary stages which are represented by the hydrogen mass contents at the center of the models X_c ($X_\mathrm{c} = 0.605$, $X_\mathrm{c} = 0.305$, and $X_\mathrm{c} = 0.005$, arranged in the following order, blue, cyan, and gold). Note that the $1.1M_\odot$ model has a radiative core and that each of the other two models has a convective core; we can see the difference in the Brunt-Väisälä frequencies below $r/R \sim 0.1$.

2.1.3 Deviation from the mean ΔP_g

As shown in the previous subsection, the asymptotic value of ΔP_g is of great use for inferring stellar evolutionary stages. Here is one caveat; we often see deviations from the theoretical expectations. According to Equation (2.7), ΔP_g should be a constant value which is determined by the integral of the Brunt-Väisälä frequency. However, this is never the case; we see deviations both in theoretical calculations (Figure 2.3) and in observations (Figure 2.4). Such deviations are thought to be caused by some sharp features in the Brunt-Väisälä frequency (see e.g. Figure 2.1). To theoretically analyze extents to which sharp features in the Brunt-Väisälä frequency have impact on ΔP_g patterns is, and to explain observations based on the theoretical analysis are main themes in this chapter. Note that though observed ΔP_g patterns often deviates from (theoretically expected) constant values, they still oscillate around the mean values as in Figure 2.3 and Figure 2.4, thus partly validating the method in which we utilize the mean value of the observed g-mode period spacings to infer stellar evolutionary stages.

2.2 Theoretical description for modulated patterns of ΔP_g

It was pointed out by D. O. Gough for the first time that a sharp feature or a discontinuity of equilibrium structures such as the sound speed and the Brunt-Väisälä frequency in mode cavities

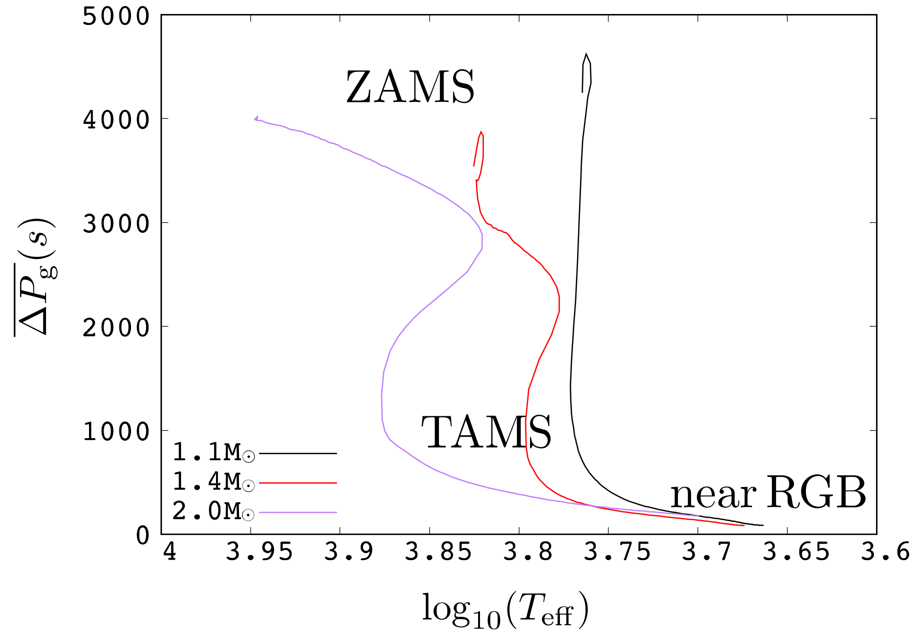

Figure 2.2: Evolutions of asymptotic values of $\overline{\Delta P_{\rm g}}$, which is inversely proportional to $\int N d\ln r$, for three models with masses $1.1 M_\odot$ (black), $1.4 M_\odot$ (red), and $2.0 M_\odot$ (purple). Note that the $\overline{\Delta P_{\rm g}}$ is computed following Equation (2.7); the stellar linear adiabatic oscillation has not been carried out. Roughly speaking, the $\overline{\Delta P_{\rm g}}$ is around $4000\,s$ at ZAMS, and then it decreases as the star evolves toward TAMS ($\overline{\Delta P_{\rm g}} \sim 1000\,s$). When the model is close to RGB, $\overline{\Delta P_{\rm g}} \sim$ a few hundred seconds.

can cause a phenomenon called mode trapping for some modes, which leads to oscillatory modulated patterns of asteroseismic quantities such as the large separation $\Delta\nu$, the small separation $\delta\nu$ (the above two are for p modes), and $\Delta P_{\rm g}$ (for g modes). Explicit forms for the large separation $\Delta\nu$ and the small separation $\delta\nu$ are obtained in almost the same manner as we obtain $\Delta P_{\rm g}$ except for an assumption that $\omega^2 \gg N^2$ and $\omega^2 \gg L_l^2$ in the asymptotic limit for high-order p modes. For more details, see e.g. Tassoul (1980) and Unno et al. (1989). An important point is that such oscillatory patterns have been also observed for the solar p modes, and they are used to probe structures around the convective boundaries in detail (Christensen-Dalsgaard et al., 1995).

Although it is not until recently that high-order g modes were detected (for low-mass main-sequence stars) and that oscillatory patterns of $\Delta P_{\rm g}$ around somewhat averaged values were reported, the high potential of $\Delta P_{\rm g}$ patterns to infer detailed structures deep inside low-mass main-sequence stars with masses $1.2 - 2.0 M_\odot$ have been recognized by the community for a while. There have thus been several attempts to theoretically analyze the oscillatory $\Delta P_{\rm g}$ patterns, e.g. Montgomery et al. (2003), Miglio et al. (2008), Cunha et al. (2019), and so on. These studies can be divided into two ways based on how they theoretically quantify the $\Delta P_{\rm g}$ patterns.

One is based on the variational principle (see Subsection 1.2.1) where modulated $\Delta P_{\rm g}$ patterns are considered as a result of perturbed eigenfrequencies, which originate from a perturbation to the Brunt-Väisälä frequency. This method has been basically discussed by Montgomery et al. (2003)

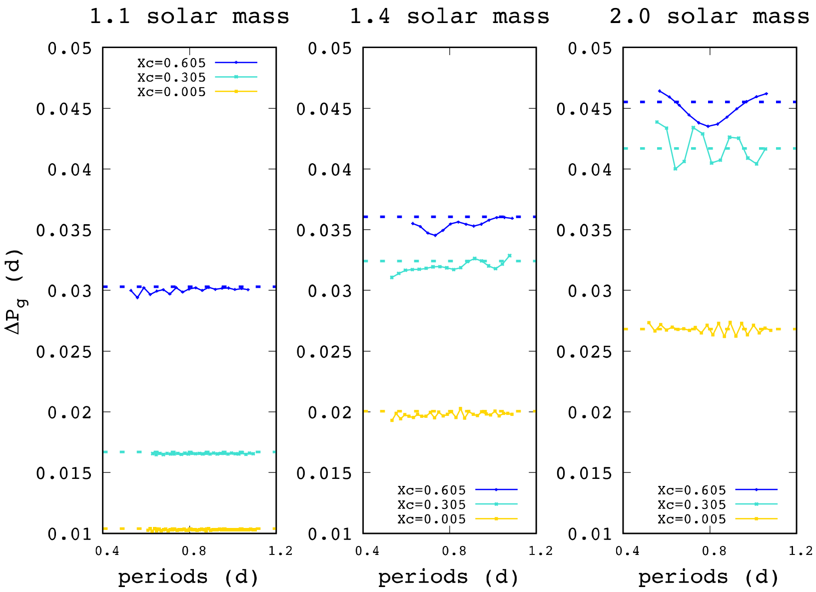

Figure 2.3: $\Delta P_{\rm g}$ patterns for several stellar models at different evolutionary stages (the meanings of colors and positions of the panels are the same as in Figure 2.1). They are calculated in the following ways: first, a set of $l = 1$ g-mode eigenfrequencies for each stellar model is obtained by solving linear adiabatic oscillation via GYRE. Then, $P_{n+1} - P_n$ (vertical axis) and $(P_{n+1} + P_n)/2$ (horizontal axis) are computed. In most cases, the numerically computed $\Delta P_{\rm g}$ patterns show deviations from constant values (dotted lines) which are computed based on Equation (2.7) with the Brunt-Väisälä frequencies of the corresponding stellar models.

and Miglio et al. (2008), and we followed their analyses with a few new expressions derived by myself (see Subsection 2.2.1.)

Though the analysis based on the variational principle is applicable for any perturbation in the Brunt-Väisälä frequency, the perturbation has to be small enough that terms higher than the second-order can be neglected and that the variational principle is valid; this assumption is often not acceptable when we deal with, for instance, chemical composition gradients inside low-mass main-sequence stars, where even a discontinuity may develop. In that case, we can derive solutions for g-mode eigenfrequencies. See details in Subsection 2.2.2.

2.2.1 Interpretation of $\Delta P_{\rm g}$ pattern based on variational principle

The first step is to obtain the equation that relates g-mode frequency difference $\delta\omega_n$ (or period difference δP_n) to perturbation in the Brunt-Väisälä frequency δN, where n is the radial order. To this end, we rewrite the second-order differential equation (2.1) in an integral form as

$$\int \mathcal{L}(\xi_r)\xi_r^* dr = -\int k_r^2 \xi_r \xi_r^* dr, \tag{2.8}$$

where $\mathcal{L}$ is a linear differential operator defined as d^2/dr^2. The explicit form of k_r is given by the expression (2.3). The asterisk represents complex conjugate, though $\xi_r^* = \xi_r$ in the case of linear

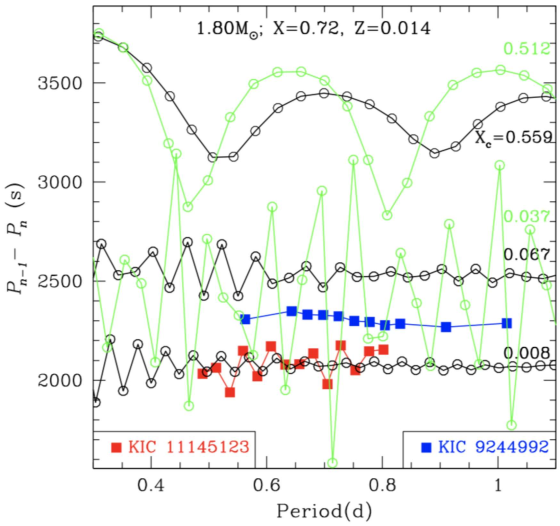

Figure 2.4: Comparison of observed modulated $\Delta P_{\rm g}$ patterns for KIC 9244992 (blue Saio et al., 2015) and for KIC 11145123 (red Kurtz et al., 2014) with theoretically calculated patterns with diffusion (black) and without diffusion (green) via a linear adiabatic oscillation code developed by M. Takata. Both the observations and theoretical results are showing modulated patterns. It is also clear that the presence of diffusion in stellar evolution calculation strongly affects the resulting $\Delta P_{\rm g}$ patterns. Cited from Saio et al. (2015).

adiabatic oscillation.

Because $\mathcal{L}$ is self-adjoint in this case with appropriate surface-zero boundary conditions, it is shown that the eigenfunctions satisfy the variational principle; the first-order perturbation of a certain eigenfunction does not affect the corresponding eigenfrequency. That can be explicitly expressed in the following way:

$$\int \mathcal{L}(\xi_r)\xi_r^* dr = -\int \left(\frac{l(l+1)(N^2+\delta N^2)}{(\omega^2+\delta\omega^2)r^2}\right)\xi_r \xi_r^* dr, \tag{2.9}$$

where the perturbed eigenfrequency $\delta\omega$ is directly related to the perturbation in the Brunt-Väisälä frequency δN.

Substituting the zero-th order equation (2.8) for the above equation (2.9) and neglecting perturbed quantities higher than the second-order leads to the linear equation as below:

$$\int k_r^2 \left(\frac{\delta N}{N}\right)\xi_r^2 dr = -\frac{\delta P_n}{P_n}\int k_r^2 \xi_r^2 dr, \tag{2.10}$$

which can, combined with the asymptotic expression for the eigenfunction ξ_r (2.4), further be simplified

$$-\frac{\Pi_0^{-1}}{2}\frac{\delta P_n}{P_n} = \int \frac{N}{r}\left(\frac{\delta N}{N}\right)\sin^2\left(\int_{r_0}^{r} k_{r'}dr' + \frac{\pi}{4}\right)dr, \tag{2.11}$$

in which r_0 represents the bottom of the mode cavity, identical to the convective core boundary in the case of low-mass $(1.2-2.0M_\odot)$ main-sequence stars. The parameter Π_0^{-1} is expressed as

$$\Pi_0^{-1} \equiv \Pi_r^{-1}(r_1), \tag{2.12}$$

where the buoyancy radius Π_r^{-1} is defined in the following way:

$$\Pi_r^{-1} \equiv \int_{r_0}^{r} N d \ln r'. \tag{2.13}$$

The upper boundary of the mode cavity is r_1, which is often assumed to be identical to the surface of the star. Note that a relation $\delta P_n / P_n = -\delta\omega_n / \omega_n$ is used to derive Equation (2.10), which is easily obtained from the definition $\omega_n = 2\pi / P_n$.

With the newly introduced variable (2.13), Equation (2.11) has a rather simple form as follows:

$$-\frac{\Pi_0^{-1}}{2} \frac{\delta P_n}{P_n} = \int \left(\frac{\delta N}{N}\right) \sin^2\left(\Pi_r^{-1} + \frac{\pi}{4}\right) d\Pi_r^{-1}. \tag{2.14}$$

We can derive explicit forms for $\Delta P_{\rm g}$ patterns as a function of the g-mode periods once we parameterize the perturbation in the Brunt-Väisälä frequency δN as Miglio et al. (2008) has done, and analytically compute Equation (2.14). Three specific ways of parameterization of δN are presented in the following small subsections.

Parameterization of δN with a step function; following Miglio et al. (2008)

Here, the results of the analysis by Miglio et al. (2008) are reproduced with the purpose of showing exact procedures to formulate the g-mode period spacings $\delta P_{\rm g}$ based on the variational principle. For more detailed derivations and confirmation of the validity of the analyses can be found in the original paper (Miglio et al., 2008).

The simplest parameterization of δN can be achieved with a step function $H(\Pi_\mu^{-1} - \Pi_r^{-1})$ as below:

$$\frac{\delta N}{N} = \frac{1-\alpha^2}{\alpha^2} H(\Pi_\mu^{-1} - \Pi_r^{-1}), \tag{2.15}$$

where Π_μ is the buoyancy radius for the position of the discontinuity, and the factor $(1-\alpha^2)/\alpha^2$ is representing the strength of the discontinuity (see the left panel in Figure 2.5).

By substituting the parameterized expression for δN (2.15) for the equation (2.14), we can compute the integral analytically, resulting in the following expression:

$$\frac{\delta P_n}{P_n} = -2\Pi_0 \left(\frac{1-\alpha^2}{\alpha^2}\right) \left[\frac{\Pi_\mu^{-1}}{2} + \frac{\omega_n}{2L} - \frac{\omega_n}{2L} \cos\left(2n\pi\Pi_0\Pi_\mu^{-1}\right)\right], \tag{2.16}$$

where $L = \sqrt{l(l+1)}$.

This is a rather simple formulation, but also it is revealing a few important points with respect to the behavior of modulated $\Delta P_{\rm g}$ patterns. The first point is the dependence of amplitudes of modulated $\Delta P_{\rm g}$ patterns on extents of the jumps ($(1-\alpha^2)/\alpha^2$); the amplitude is simply proportional to $(1-\alpha^2)/\alpha^2$, and the amplitude gets larger as the extent of the jump increases. The second point is that the oscillatory patterns of $\Delta P_{\rm g}$ (see e.g. Figure 2.3 and 2.4) can be explained by the presence of the sinusoidal component in the equation (2.16), and that the period of the oscillation is determined by a ratio between Π_0^{-1} and Π_μ^{-1}; which is also a conclusion of Subsection 2.2.2. The ratio is related to the position of the discontinuity, and thus, the period of the oscillatory $\Delta P_{\rm g}$ patterns can be used to infer the position.

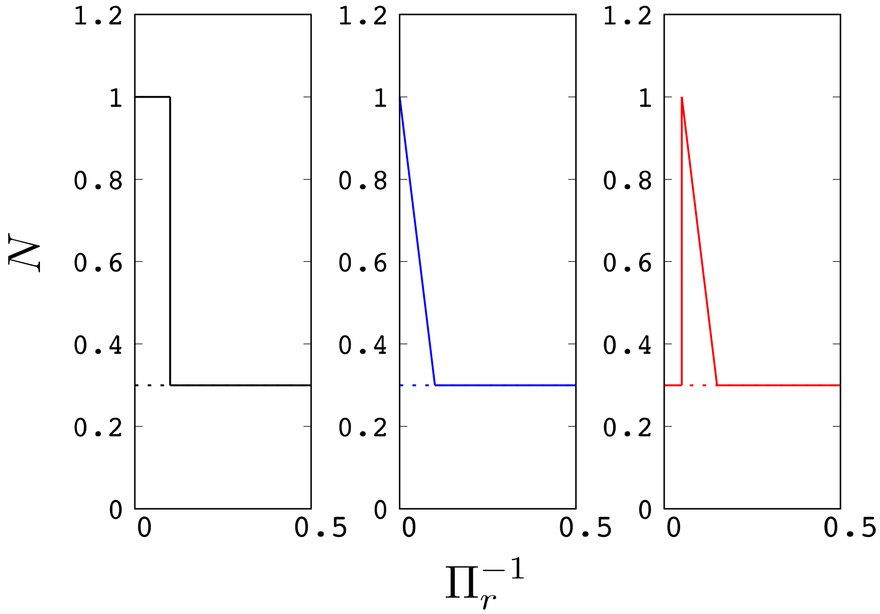

Figure 2.5: Schematic view for three ways of parameterization of δN. Note that curves are showing sums of the unperturbed Brunt-Väisälä frequencies (represented by dotted lines) and δN. The parameterization by a step function (left), that by a ramp function (middle), and that by partly a ramp function with unperturbed region around the very center (red) are shown.

Parameterization of δN with a ramp function; following Miglio et al. (2008)

Here, the results of the analysis by Miglio et al. (2008) are again reproduced with the same purpose in the preceding small subsection. For more detailed derivations and confirmation of the analyses can be found in the original paper (Miglio et al., 2008).

The parameterization of δN is done with a ramp function as below:

$$\frac{\delta N}{N} = \frac{1-\alpha^2}{\alpha^2}\frac{\Pi_\mu^{-1} - \Pi_r^{-1}}{\Pi_\mu^{-1}} H(\Pi_\mu^{-1} - \Pi_r^{-1}), \tag{2.17}$$

see an example of the profile in Figure 2.5. It should be noted that the buoyancy radius of at the center of the star $r = 0$ is zero.

We can analytically compute the integral (2.14) by inserting the expression (2.17) and integrating by parts once. The result is

$$\frac{\delta P_n}{P_n} = \left(-\frac{1-\alpha^2}{\alpha^2}\Pi_0\Pi_\mu\right)\left[\frac{1}{2}(\Pi_\mu^{-1})^2 + \frac{\omega_n}{2L}\Pi_\mu^{-1} - \left(\frac{\omega_n}{2L}\right)^2 \sin\left(2n\pi\Pi_0\Pi_\mu^{-1}\right)\right]. \tag{2.18}$$

The expression above seems to be much complex compared with the expression (2.16), but when we pay attention to the sinusoidal component in the expression, it is readily understood that the amplitude of the oscillatory ΔP_g pattern is proportional to $(1-\alpha^2)/\alpha^2$ as in the expression (2.16) and that the period of the oscillation is determined by a ratio between Π_0^{-1} and Π_μ^{-1} as well. The essential points are thus not changed. One difference is that the amplitude also depends on the buoyancy radius of the discontinuity Π_μ^{-1} and on the g-mode periods P_n, which is not indicated in the case of the simpler parameterization of δN and it is later demonstrated that the parameterization in this small subsection is better-describing (than that in the preceding small subsection) oscillatory ΔP_g patterns calculated based on realistic stellar models.

Parameterization of δN considering an overshooting region; NEW

A novel formulation is presented in this small subsection with a parameterization of δN by a modified ramp function as shown in the right panel of Figure 2.5. In the previous two formulations, it is assumed that δN is finite at the bottom boundary of the g-mode cavity where $\Pi_r^{-1} = 0$. But it is ordinarily seen based on 1-dimensional stellar evolutionary calculations that the Brunt-Väisälä frequency is rather smooth around regions just above the convective core because of the presence of the overshooting zone although the chemical compositions are well-mixed and the adiabatic temperature gradient ∇_ad is nevertheless smaller than the radiative temperature gradient ∇_rad; the Brunt-Väisälä frequency is finite there. Thus, we can not consider the perturbation to the Brunt-Väisälä frequency in the overshooting zone.

The parameterization of δN is given as below:

$$\frac{\delta N}{N} = \begin{cases} 0 & (\Pi_r^{-1} \leq \Pi_{\mu_1}^{-1}) \\ \frac{1-\alpha^2}{\alpha^2} \frac{\Pi_{\mu_2}^{-1} - \Pi_r^{-1}}{\Pi_{\mu_2}^{-1} - \Pi_{\mu_1}^{-1}} H(\Pi_{\mu_2}^{-1} - \Pi_r^{-1}) & (\Pi_{\mu_1}^{-1} \leq \Pi_r^{-1}), \end{cases} \tag{2.19}$$

where $\Pi_{\mu_1}^{-1}$ and $\Pi_{\mu_2}^{-1}$ represent the buoyancy radius for an innermost position and an outermost position between which δN is finite, respectively.

We can obtain the corresponding expression for oscillatory ΔP_g patterns in the case of the assumed δN almost in the same way as in the small subsection 2.2.1 except that we have extra terms which otherwise vanish in the preceding manipulations where $\Pi_{\mu_1}^{-1} \to 0$ and $\Pi_{\mu_2}^{-1} \to \Pi_\mu^{-1}$,

$$\begin{aligned} \frac{\delta P_n}{P_n} =& \left(-\frac{1-\alpha^2}{\alpha^2} \Pi_0 (\Pi_{\mu_2}^{-1} - \Pi_{\mu_1}^{-1})^{-1} \right) \\ \times & \left[\frac{1}{2} (\Pi_{\mu_2}^{-1} - \Pi_{\mu_1}^{-1})^2 + \frac{\omega_n}{2L} (\Pi_{\mu_2}^{-1} - \Pi_{\mu_1}^{-1}) \cos\left(2n\pi\Pi_0\Pi_{\mu_1}^{-1} \right) - \left(\frac{\omega_n}{2L} \right)^2 \left(\sin\left(2n\pi\Pi_0\Pi_{\mu_2}^{-1} \right) - \sin\left(2n\pi\Pi_0\Pi_{\mu_1}^{-1} \right) \right) \right], \end{aligned} \tag{2.20}$$

We obtain the expression (2.18) if we take limits $\Pi_{\mu_1}^{-1} \to 0$ and $\Pi_{\mu_2}^{-1} \to \Pi_\mu^{-1}$.

Interestingly, the expression (2.20) contains two oscillatory components, one of which has a period determined by a ratio between Π_0^{-1} and $\Pi_{\mu_1}^{-1}$, and the other has a period determined by a ratio between Π_0^{-1} and $\Pi_{\mu_2}^{-1}$, indicating that not only a sharp feature in the Brunt-Väisälä frequency but also the extent of the overshooting have significant impacts on the oscillatory ΔP_g patterns.

Because this is the first time that the relation between the extent of overshooting and the oscillatory ΔP_g patterns has been suggested, we would like to check the validity of the expression by comparing with numerically computed ΔP_g patterns. Figure 2.6 shows the comparison, and it is clearly seen that the theoretical expression explains the results of numerical computations moderately well. Be sure that this is valid only for perturbations which are small enough that terms higher than the second-order can be ignored. Such deviations from the variational principle can be found in, for instance, the right panel in Figure 2.6.

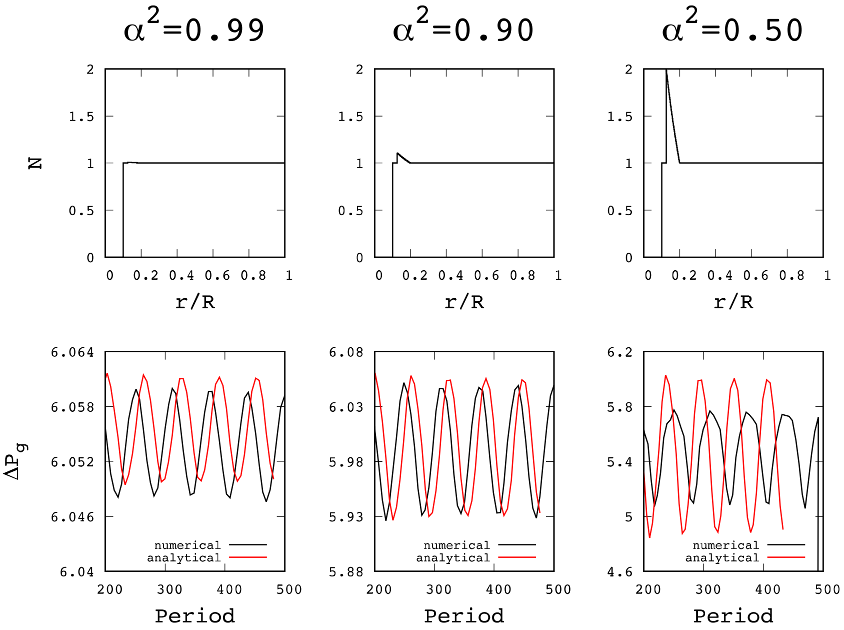

Figure 2.6: Comparison of the analytical expression (2.20) for oscillatory $\Delta P_{\rm g}$ patterns (red curves) with numerically computed ones (black curves) is illustrated in the bottom row. The numerically computed $\Delta P_{\rm g}$ patterns are obtained by directly solving the eigenvalue problem (2.1), where the radial wavenumber k_r is given by each Brunt-Väisälä frequency N shown in the top row. The strength of a discontinuity is represented by α^2; it increases from left to right ($\alpha^2 = 0.99$ to $\alpha^2 = 0.50$). The analytical expressions reproduce the numerically calculated oscillatory $\Delta P_{\rm g}$ patterns fairy well in the case of small perturbations (left and middle panels), though they deviated from each other in the rightmost panel, which clearly shows that the assumption that the perturbation is small enough to apply the variational principle is broken down.

2.2.2 Interpretation of $\Delta P_{\rm g}$ pattern based on exact eigenfunction

An alternative strategy is taken in this subsection to theoretically explain modulated patterns $\Delta P_{\rm g}$. Namely, expressions for g-mode periods are presented, mainly based on the way by Cunha et al. (2019). This can be done by assuming two asymptotic eigenfunctions for both inside and outside the discontinuity and posing boundary conditions which demand the continuity and the smoothness of the eigenfunctions at the discontinuity. Then, we end up with an eigenvalue condition, which is somehow a modified version of that presented in Subsection 1.2.1, and solving the condition provides us with the g-mode eigenfrequencies under the existence of a discontinuity in the Brunt-Väisälä frequency (in the small subsection 'In the case with a discontinuity'); we do not have to rely on the assumption that the sharp features in the Brunt-Väisälä frequency can be treated a small perturbation. This procedure can also be applied for smoother profiles of the Brunt-Väisälä frequency with slight modifications to the original formulations, which is demonstrated in the small subsection 'In the case with a slope'.

In the case with a discontinuity

First of all, we divide the g-mode cavity ($r_0 < r < r_1$) into two regions by a discontinuity in the Brunt-Väisälä frequency located at $r = r_\star$. Eigenfunctions for the two regions are given based on the assumption that the asymptotic approximation is valid (in other words, the wavelengths are much shorter than the scale heights of the backgrounds except for the discontinuity). Below are the explicit forms of the eigenfunctions

$$\xi_{\rm in} = \widetilde{\xi_{\rm in}} \frac{1}{\sqrt{k_{\rm in}}} \sin\left(\int_{r_0}^{r} k_{\rm in} dr + \frac{\pi}{4} \right), \tag{2.21}$$

and

$$\xi_{\rm out} = \widetilde{\xi_{\rm out}} \frac{1}{\sqrt{k_{\rm out}}} \sin\left(\int_{r}^{r_1} k_{\rm out} dr + \frac{\pi}{4} \right), \tag{2.22}$$

where $k_{\rm in}$ and $k_{\rm out}$ are the radial wavenumber defined as (2.3) for the inner region and that for the outer region. There are constants related to the amplitudes of the eigenfunctions, $\widetilde{\xi_{\rm in}}$ and $\widetilde{\xi_{\rm out}}$.

Then, let us consider that the inner eigenfunction and the outer one are linked continuously and smoothly. The conditions can be expressed as the following boundary conditions at the discontinuity $r = r_\star$:

$$\xi_{\rm in}(r_\star) = \xi_{\rm out}(r_\star), \tag{2.23}$$

and

$$\left. \frac{d\xi_{\rm in}}{dr} \right|_{r=r_\star} = \left. \frac{d\xi_{\rm out}}{dr} \right|_{r=r_\star}, \tag{2.24}$$

with which the constants $\widetilde{\xi_{\rm in}}$ and $\widetilde{\xi_{\rm out}}$ can be eliminated, leading to a relation

$$\frac{K_{\rm in}^\star}{K_{\rm out}^\star} \sin\left(\int_{r_\star}^{r_1} K_{\rm out} dr + \frac{\pi}{4} \right) \cos\left(\int_{r_0}^{r_\star} K_{\rm in} dr + \frac{\pi}{4} \right) + \sin\left(\int_{r_0}^{r_\star} K_{\rm in} dr + \frac{\pi}{4} \right) \cos\left(\int_{r_\star}^{r_1} K_{\rm out} dr + \frac{\pi}{4} \right), \tag{2.25}$$

where $K_{\rm in}^\star = K_{\rm in}(r_\star)$ and $K_{\rm out}^\star = K_{\rm out}(r_\star)$.

Following the treatment in Cunha et al. (2019), we define a new parameter for the strength of the discontinuity as below:

$$A_\star \equiv \frac{K_{\rm in}^\star - K_{\rm out}^\star}{K_{\rm out}^\star}. \tag{2.26}$$

The relation (2.25) can be cast into the following simple form:

$$C \sin\left(\int_{r_0}^{r_\star} K_{\rm in} dr + \frac{\pi}{4} + \phi \right) = 0, \tag{2.27}$$

where C and ϕ are defined by a system of two equations, namely,

$$\begin{cases} C \sin(\phi) = (A_\star + 1) \sin\left(\int_{r_\star}^{r_1} K_{\rm out} dr + \frac{\pi}{4} \right) \\ C \cos(\phi) = \cos\left(\int_{r_\star}^{r_1} K_{\rm out} dr + \frac{\pi}{4} \right) \end{cases} \tag{2.28}$$

Equation (2.27) represents the eigenvalue condition in the presence of a discontinuity in the Brunt-Väisälä frequency. Though we need some special techniques to solve the eigenvalue condition (2.27), the eigenfrequencies can be obtained based on the analysis of the condition. See for more details Appendix of the original paper (Cunha et al., 2019). The result is shown below:

$$\frac{\Delta P}{\Delta P_{\rm as}} \sim \left[1-\left(\Pi_0\Pi_\star^{-1}\right)\frac{-A_\star\sin\tilde{\beta}_1+A_\star^2\cos^2\tilde{\beta}_2}{(1+A_\star\cos^2\tilde{\beta}_2)^2+(0.5A_\star\cos\tilde{\beta}_1)^2}\right]^{-1}, \tag{2.29}$$

where $\Pi_\star^{-1}=\Pi_r^{-1}(r_\star)$ and $\Delta P_{\rm as}=2\pi^2\Pi_0/L$. The phases $\tilde{\beta}_1$ and $\tilde{\beta}_2$ inside the sinusoidal components in the equation above are defined as

$$\tilde{\beta}_1=\frac{2L}{\omega}\Pi_\star^{-1}+2\delta, \tag{2.30}$$

and

$$\tilde{\beta}_2=\frac{L}{\omega}\Pi_\star^{-1}+\frac{\pi}{4}+\delta, \tag{2.31}$$

respectively. The extra phase term represented by δ is necessary to quantify the phase jump produced around the boundaries of the g-mode cavity. This is beyond the scope of this dissertation, and thus, see Appendix of the original paper (Cunha et al., 2019) for more discussions.

There are clear differences in explicit forms between the expression (2.29) and the ones derived based on the variational principle such as the expression (2.16). For instance, the eigenfrequency is given as a continuous variable (ω) in the former case, and it is discrete (ω_n) in the latter cases. The oscillatory components are not represented by pure sinusoidal ones in the former case as well. However, the periods of oscillatory $\Delta P_{\rm g}$ patterns are essentially the same; if we replace the continuous variable ω with the discrete one ω_n and inserting $P_n=2\pi/\omega_n$ into the expression (2.29) with the help of Equation (2.7), we find that the period is dependent on a ratio between Π_0^{-1} and Π_μ^{-1} as shown in the expression (2.16).

Cunha et al. (2019) have also carried out the validation of the expression (2.29) by comparing with the numerically calculated oscillatory $\Delta P_{\rm g}$ patterns, which we do not intend to repeat here.

In the case with a slope; NEW

In the previous small subsection, the g-mode cavity is divided into two zones (whose backgrounds are considered to be smooth compared with the wavelength of the eigenfunctions) by a discontinuity. Such discontinuous structure is rather rare inside stars; there usually are sharp features with finite gradients such as chemical composition gradients above a convective core (see Figure 1.2 in Chapter 1). It is thus convenient for us to formulate oscillatory $\Delta P_{\rm g}$ patterns in the presence of a sharp feature with a finite gradient as schematically shown in Figure 2.7, which is the main theme in this small subsection.

We follow almost the same procedures and assumptions as in the previous small subsection to derive the expression, except for a different definition of the strength of sharpness, which is

$$A_\star\equiv\left(\frac{K_{\rm in}^\star-K_{\rm out}^\star}{K_{\rm out}^\star}\right)\exp\left(-(B_\star\Delta)^\eta\right), \tag{2.32}$$

where we have three additional variables, namely, $B_\star$, Δ, and a free parameter η, respectively. The former two, $B_\star$ and Δ, are defined as

$$B_\star\equiv k_r(r_{\rm mid}), \tag{2.33}$$

and

$$\Delta\equiv r_{\mu_2}-r_{\mu_1}, \tag{2.34}$$

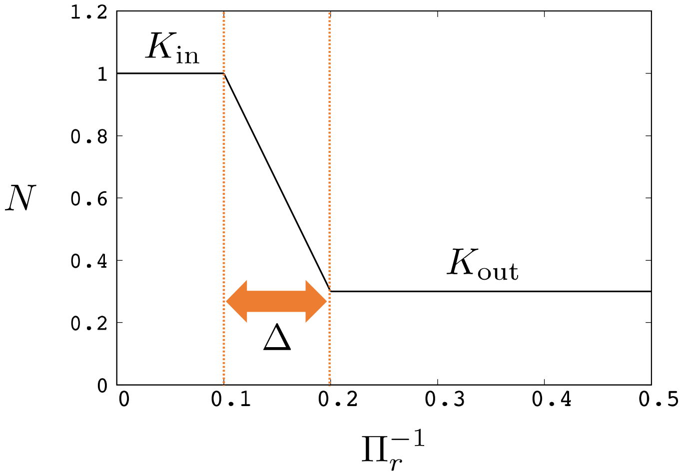

Figure 2.7: Schematic picture of the Brunt-Väisälä frequency considered in this small subsection. The radial wavenumber in the inner cavity and that in the outer cavity are represented by K_{in} and K_{out}, between which is a gradient characterized by the sharpness (defined as a relative difference between K_{in} and K_{out}) and by the width Δ. The larger Δ is, the smoother the gradient is. Note that the unit of the Brunt-Väisälä frequency N and that of the Π_r^{-1} are arbitrary.

where $r_{\mathrm{mid}} = (r_{\mu_2} - r_{\mu_1})/2$. The radial coordinates for the locations of the inner position and the outer one of the gradient are expressed as r_{μ_1} and r_{μ_2}.

The parameters $B_\star$ and Δ are introduced in order to effectively represent a deviation from the original expression (2.29). The parameter $B_\star$ is related to the inverse of the wavelength at the middle of the inner position and the outer one of the gradient, and Δ is related to the scale height of the gradient there. Therefore, when $B_\star\Delta$ is quite small (large), the wavelength is much larger (smaller) than the scale height of the gradient, and thus, the sharp feature can be treated as a discontinuity (almost a flat structure), leading to the expression (2.29) (a constant ΔP_{g}) in these limits.

The final form for oscillatory ΔP_{g} patterns in the presence of a sharp feature with a finite gradient is the same as that (2.29); the definition of $A_\star$ is the only difference. We can, however, see that the formulation explains the oscillatory ΔP_{g} patterns well in this case (Figure 2.8). Especially, it has to be mentioned that adopting the position of the outer boundary of the gradient to compute $\Pi_\star^{-1}$ is much more favorable than adopting the inner boundary for $\Pi_\star^{-1}$, which is clearly suggested by the better-reproduced periods of the numerically calculated oscillatory ΔP_{g} patterns.

Note that the derivation described here is just the crude ones mathematically; asymptotic characteristics of high-order g modes are actually lost inside the gradients (if the scale height is comparable to the wavelength), and we have to consider the effects on the eigenconditions and the eigenfrequencies. That should be further investigated in the forthcoming studies.

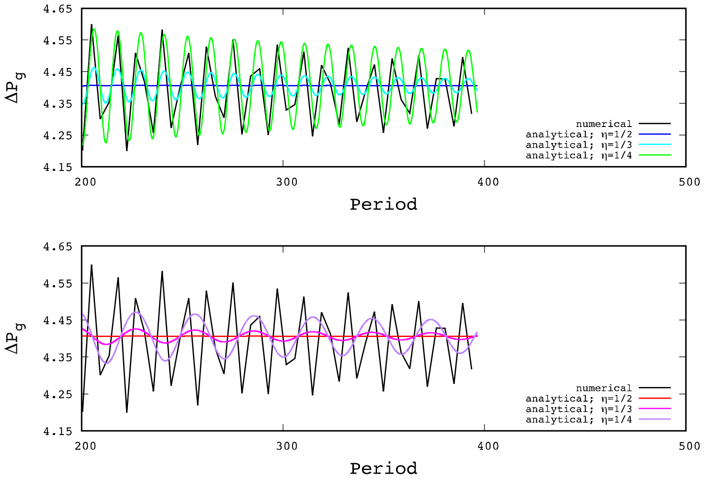

Figure 2.8: Comparison of the theoretical expression (2.29) (colored curves) where an alternatively defined $A_\star$ (2.32) is used, with numerically calculated $\Delta P_{\rm g}$ patterns (black curves). The numerical computations are carried out for the Brunt-Väisälä frequency shaped like the one in Figure 2.7, which is characterized by the strength of the sharpness and the width of the gradient. The top panel shows theoretical $\Delta P_{\rm g}$ patterns, for which the position of the outer boundary of the gradient is used to compute $\Pi_\star^{-1}$, with different free parameters η. The bottom panel shows theoretical patterns as well, though the position of the inner boundary of the gradient is used to compute $\Pi_\star^{-1}$. This comparison clearly illustrates that considering the outer boundary (not inner one) as the characteristic position of the gradient is preferred. Is is also seen that the free parameter η affect the dependence of the oscillatory components' amplitude; for instance, it seems that $\eta = 1/4$ is best producing the numerical results.

2.3 Attempts to describe $\Delta P_{\rm g}$ pattern of realistic stellar models

In this section, oscillatory $\Delta P_{\rm g}$ patterns of realistic stellar models, where the Brunt-Väisälä frequency profile is no longer simple as that is assumed in the analyses in the preceding section, with masses of $1.4M_\odot$ and $2.0M_\odot$ are presented. We firstly attempt to interpret the numerically calculated $\Delta P_{\rm g}$ patterns based on the theoretical formulations developed in the last subsection 2.2. In particular, we would like to concentrate on the ratio between Π_0^{-1} and Π_μ^{-1}, and on the magnitude of a discontinuity (or sharpness) in the Brunt-Väisälä frequency, which are theoretically expected to determine the period of the oscillatory components of $\Delta P_{\rm g}$ patterns. The second purpose of this section is to demonstrate the way different prescriptions for mixing processes inside stars during evolution affect the Brunt-Väisälä frequencies and the resultant oscillatory $\Delta P_{\rm g}$ patterns. Calculations of 1-dimensional stellar evolution and that of eigenfrequencies are via MESA and GYRE, respectively.

2.3.1 Relation between Brunt-Väisälä frequency distribution and $\Delta P_{\rm g}$ pattern

The case of a $2.0M_\odot$ model

We start with an example of a series of $2.0M_\odot$ evolutionary models, which obviously exhibit oscillatory $\Delta P_{\rm g}$ patterns (the right panel in Figure 2.9). We see that as the $2.0M_\odot$ star evolves (or, as

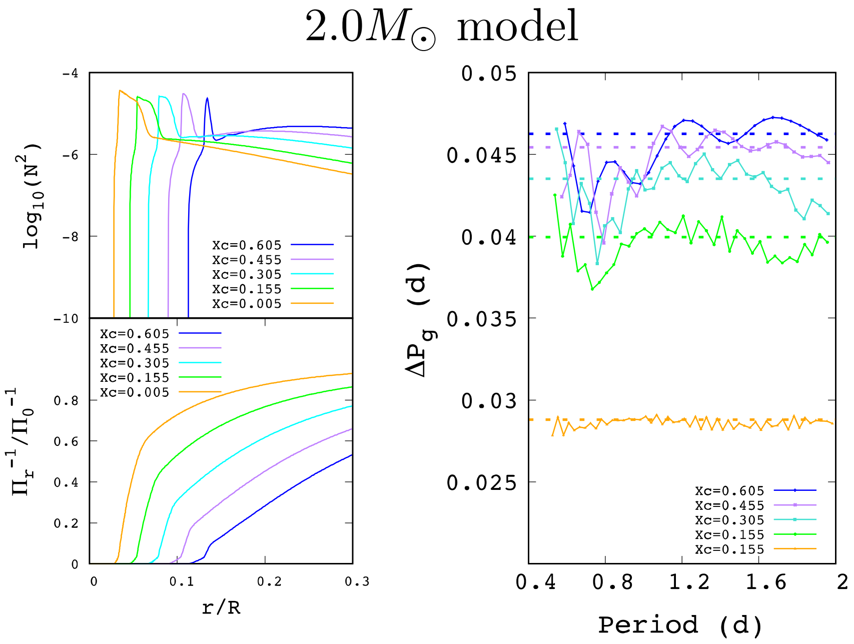

Figure 2.9: Brunt-Väisälä frequencies (top left) and buoyancy radii (bottom left) for a series of evolutionary models with $2.0M_\odot$. Each of the buoyancy radii Π_r^{-1} is normalized by that for the whole g-mode cavity Π_0^{-1} (see the definition 2.12) of each model, directly indicating the periods of the oscillatory ΔP_g patterns (see the text). The corresponding ΔP_g patterns for the models are shown in the right panel. The asymptotic values for ΔP_g computed with the expression (2.7) are indicated by dotted lines. It seems that the ΔP_g patterns are mainly composed by two oscillatory components; one with a longer period $\Delta n \sim 10$ and one with shorter period $\Delta n \sim$ a few.

the central hydrogen content of the star decreases), the convective core shrinks, and the chemical composition gradient develops just above the core, leading to a trapezoidal structure in the Brunt-Väisälä frequency around $r/R \sim 0.1$ (see the top left panel in Figure 2.9). This change in structure along with the evolution can also be confirmed in the mean value of ΔP_g shown by the dotted line in the right panel in the figure, which decrease as the star evolves. The previous discussions in Subsection 2.1.2 about the relation between stellar evolution and temporal variation of the mean value of ΔP_g are simply repeated here.

Then, let us take a closer look at the ΔP_g patterns (Figure 2.10), for example, the one for the evolutionary stage where the central hydrogen content X_c is 0.305 (cyan curves in the figure). One of the most important quantities to interpret the ΔP_g pattern is the ratio between Π_μ^{-1} (the buoyancy radius of the position of a sharp feature in the Brunt-Väisälä frequency) and Π_0^{-1} (that for the whole g-mode cavity). In the case of the model whose X_c is 0.305, there seems to be two sharp features in the Brunt-Väisälä frequency; one is located around $r/R = 0.075$ and the feature is almost a discontinuity, and the other one is located around $r/R = 0.095$ and this feature is smoother than the former one (see the top left panel). We can easily find the ratios Π_μ^{-1}/Π_0^{-1} for the two sharp features based on the bottom left panel in Figure 2.10; roughly saying, ~ 0.04 and ~ 0.25, respectively. According to, e.g., the expression (2.16), the period of the oscillatory component is

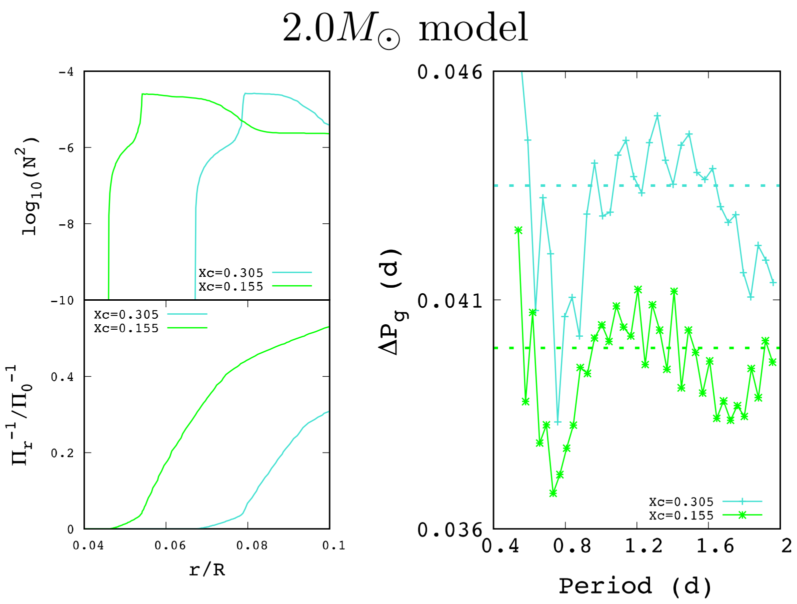

Figure 2.10: Expanded looks into the three panels in Figure 2.9.

given by Π_μ/Π_0, the inverse of the quantity we have just obtained, leading to the analytically derived periods $\Delta n \sim 25$ and $\Delta n \sim 4$ for the almost-discontinuity-like structure and the rather smoother feature, respectively. Interestingly, there seemingly exist such double oscillatory components in the numerically computed ΔP_g patterns, which is somehow consistent with the analytical expressions such as (2.20).

We can also measure the periods of the numerically computed ΔP_g pattern in the right panel in Figure 2.9 by directly counting the number of the points between a certain pair of neighboring peaks. In the case of the $X_\mathrm{c} = 0.305$ model (cyan in Figure 2.10), there seem to be two oscillatory components as mentioned in the last paragraph, and the periods are $\Delta n \sim 30$ and $\Delta n \sim 4$ showing a rather satisfactory consistency between the analytical and the numerical periods.

Although we qualitatively succeed in explaining the periods of the two oscillatory components in the numerically computed ΔP_g pattern, it is much more difficult to discuss the amplitudes of them. This is because the amplitude is dependent on various factors such as the strength of the sharp feature, the g-mode period (note that this ”period” is the period of the eigenoscillation), the buoyancy radius of the position of the sharp feature, and so on. This point is discussed later in the last section of this chapter where the ΔP_g pattern of KIC 11145123 is studied in detail.

The case of a $1.4M_\odot$ model

Another example is a $1.4M_\odot$ model, which does show oscillatory ΔP_g patterns (Figure 2.11). Though it seems that there exists only one oscillatory component (with a longer period) in each of the ΔP_g patterns, it is just the matter of the amplitudes; if we look closer at the patterns (Figure 2.12), we find another oscillatory component with a shorter period as has seen in Figure 2.9.

In order to interpret the ΔP_g patterns, the same approach as in the last small subsection is taken

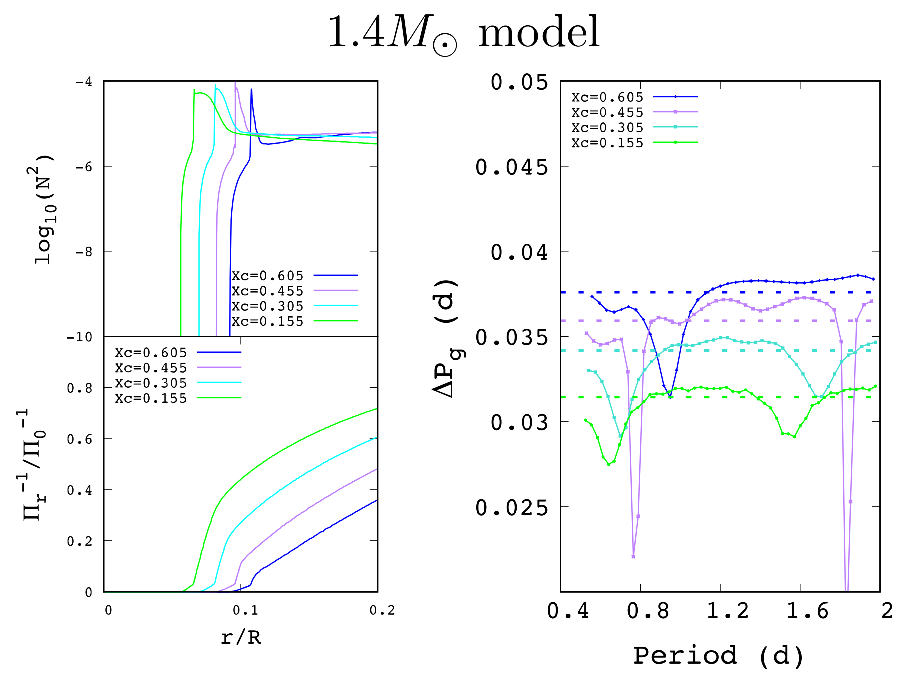

Figure 2.11: Same figures for a series of $1.4M_\odot$ evolutionary models. The Brunt-Väisälä frequencies are more smoother than those for $2.0M_\odot$ models in Figure 2.9. In addition, the Brunt-Väisälä frequencies are also larger than the counterparts in Figure 2.9. Both of the two differences above are leading to different degrees of asymptoticity, which causes the ΔP_g patterns in this figure and those in Figure 2.9 behave differently (see texts for more details).

here. First, based on the Figure 2.11, we determine positions of sharp features in the Brunt-Väisälä frequency and the corresponding ratios Π_μ/Π_0 with which analytically predicted periods for the oscillatory components in the ΔP_g patterns is obtained. Finally, we compare the analytical periods with those obtained by directly measuring the periods in the numerically computed ΔP_g patterns. In the case of the $X_\mathrm{c} = 0.155$ model (green), analytically determined periods are $\Delta n \sim 25$ and $\Delta n \sim 3$ for a longer and a shorter oscillatory component, respectively, and those directly obtained are $\Delta n \sim 30$ and $\Delta n \sim 4$, thus showing a rather fair agreement.

It should be noticed that the period for the longer oscillatory component is almost the same during the evolution (see the purple, the cyan, and the green curves in the right panel of Figure 2.11, indicating that the position of the sharpness which is located just above the convective boundary is not changed as the $1.4M_\odot$ star evolves. This can be qualitatively explained in terms of the pressure scale height, defined as $H_p = -dr/d\ln p$, at the convective boundary. As it is shown later in Section 2.4.2, the thickness of the overshooting region is, in MESA, set to be proportional to the pressure scale height H_p, which can be expressed as $\mathcal{R}T/\mu g$ based on assumptions of the hydrostatic equilibrium ($dp/dr = -\rho g$) and the equation of state for an ideal gas ($p = \rho\mathcal{R}T/\mu$) where $\mathcal{R}$ stands for the gas constant. The temporal variation of H_p is determined by the mean molecular weight, which increases as the star evolves, and by the local gravitational acceleration, which decreases as the star evolves, and thus, two factors counteract each other, leading to mostly the same values of H_p (if the temperature at the convective boundary does not significantly differ) and the thickness

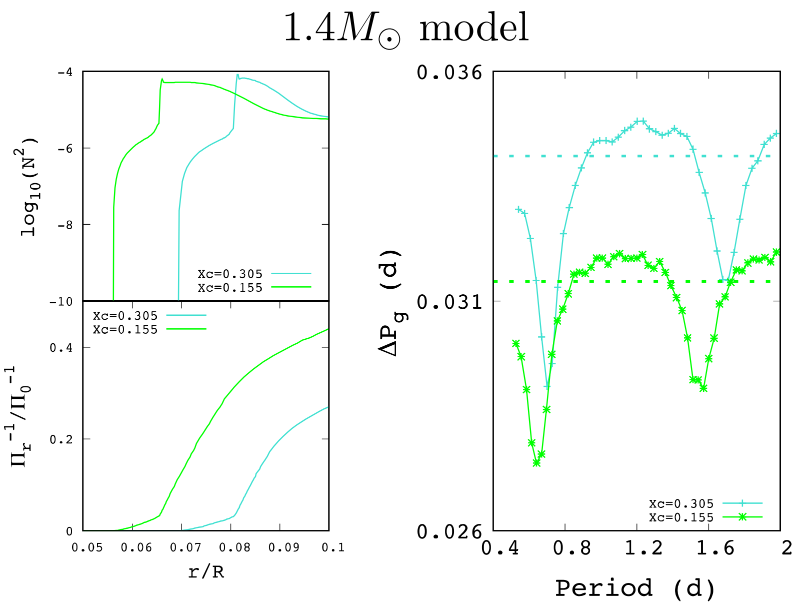

Figure 2.12: Expanded looks into the three panels in Figure 2.11. Note that ranges for the abscissae and the ordinates are slightly different from those in Figure 2.10.

of the overshooting region during the evolution.

Before we close this small subsection, we would like to discuss a difference between the $1.4M_\odot$ and the $2.0M_\odot$ models; the former model exhibits much smoother ΔP_g patterns than the other model does. The difference can be qualitatively explained based on the theoretical expression (2.29) with an alternative definition of the magnitude of a sharp feature (2.32). The important point is that the amplitudes are dependent on two factors. One is a relative difference of the Brunt-Väisälä frequency $(N_2 - N_1)/N_1$, where the index one corresponds to the lower side of a sharp feature and the index two to the upper side. The other factor is the asymptoticity, namely, the ratio between the local wavenumber of the eigenfunctions and the local scale height of the Brunt-Väisälä frequency.

Remembering the two factors, let us consider the oscillatory components with the shorter periods; we have to focus on the bump-like feature of the Brunt-Väisälä frequency. In the case of the $2M_\odot$ model, the feature is basically described by a plateau-like structure and then a sharp negative gradient. The width of the gradient (Δ in Equation 2.32) is thus narrower than that for the Brunt-Väisälä frequency of the $2M_\odot$ model, in which there is no plateau-like structure and a less steeper negative gradient. Therefore, the $1.4M_\odot$ model has a stronger asymptoticity than that of the $2.0M_\odot$ model, resulting in the smoother profile of the ΔP_g pattern. In addition to the width Δ, the value of the Brunt-Väisälä frequency in the negative gradient of the $1.4M_\odot$ model is larger than that of the $2M_\odot$ model (see the top left panels in Figures 2.9 and 2.11), also causing the strong asymptoticity for the $1.4M_\odot$ model because the eigenfunctions has a larger wavenumber for the $1.4M_\odot$ model (remember the wavenumber $k_r \sim LN/\omega r$).

We can also explain the oscillatory components with the longer periods in the same manner, but the situation is opposite in this case; we find an almost discontinuous structure for the $1.4M_\odot$ model and a steep feature with finite positive gradient for the $2.0M_\odot$ model (see the inner sides

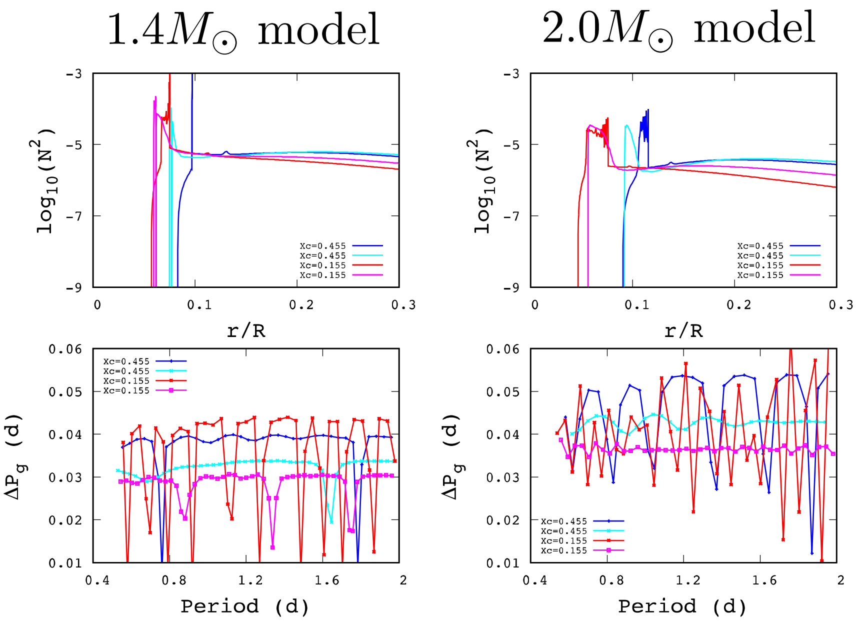

Figure 2.13: Brunt-Väisälä frequencies of various models at two different evolutionary stages ($X_c = 0.455$, represented by blue and cyan, and $X_c = 0.155$, represented by red and magenta) with different prescriptions for mixing processes which are at work inside the models, namely, a prescription with overshooting and without diffusion (red and blue), and one without overshooting and with diffusion (magenta and cyan) (see the top rows). It is clearly seen that the Brunt-Väisälä frequency has a different structure depending on which prescription we adopt. The models without diffusion especially shows multiple jumps of the Brunt-Väisälä frequencies in their chemical composition gradients, leading to much larger amplitudes of their corresponding ΔP_g patterns (bottom rows).

of the bump-like structures in the Brunt-Väisälä frequencies shown in Figures 2.9 and 2.11). Such opposite structures lead to a trend opposite to that for the oscillatory components with the shorter periods, namely, the amplitudes of the oscillatory components with the longer periods are larger in the $1.4M_\odot$ model as seen in Figures 2.9 and 2.11.

2.3.2 Origin of Brunt-Väisälä frequency distribution

The previous sections and subsections are devoted to reveal the relation between the Brunt-Väisälä frequency and the ΔP_g patterns; we are now able to at least qualitatively predict a ΔP_g pattern once a particular Brunt-Väisälä frequency is given (not depending on whether the Brunt-Väisälä frequency is a physically realistic one or not) without numerically calculating the ΔP_g patterns. The next question is what determines a distribution of Brunt-Väisälä frequency along with stellar evolution. As described in Subsection 1.1.1, the Brunt-Väisälä frequency is affected by multiple factors such as mass, chemical composition, internal mixing processes, evolutionary stage, and so on. In this subsection, we would like to focus on the effects of two mixing processes, namely, diffusion and overshooting, on the Brunt-Väisälä frequency because both of them are frequently adopted in calculations of stellar structure and evolution though they are difficult to calibrate as well. The resulting ΔP_{g} patterns computed based on the corresponding models are also presented.

Figure 2.13 shows the Brunt-Väisälä frequencies (top row) and the ΔP_{g} patterns (bottom row) for models with different prescriptions of mixing processes at almost the same age (in terms of the hydrogen mass content at the center of the model X_{c}). There are two prominent points in terms of structural differences in the Brunt-Väisälä frequencies. One is the existence of jump-like structures in N^2 of models computed without diffusion (see the red and blue curves in the top row of Figure 2.13). This is mainly because there are jumps in the chemical composition gradients ∇_{μ} in the case of the no-diffusion models (remember the expression for N^2 1.2); if diffusion is activated in 1-dimensional stellar evolutionary calculations, such jumps are erased. These jump-like structures also affect the ΔP_{g} patterns as is obviously seen in Figure 2.13, and the amplitudes of the ΔP_{g} patterns of the no-diffusion models are much larger than those of the with-diffusion models.

The other is the presence of chemical composition gradients with positive slopes just above the convective core boundary, which are seen in the with-overshooting models (see the magenta and cyan curves in the top row of Figure 2.13). These gradual positive gradients of N^2 just above the convective core boundary arise from the subadiabaticity $\nabla_{\mathrm{ad}} > \nabla_{\mathrm{rad}}$ in the overshooting zones, leading to finite values of N^2. Though these features seem to be trivial, the gradient of N^2 gets fairly large around the outer edge of the overshooting zone at which the temperature gradient abruptly changes, and such discontinuity-like structure definitely affects the ΔP_{g} patterns as we see in Figure 2.13.

Note that the demonstrations shown here are just examples; we have a large number of other choices with respect to which mixing processes (such as semiconvection, rotationally-induced mixing, thermohaline mixing, etc.) we activate and what parameters we adopt in stellar evolutionary computations (see, e.g., Paxton et al., 2011), and each resultant ΔP_{g} pattern differs from one another, which on one hand complicates the analysis of the ΔP_{g} patterns and on the other hand allows us to investigate the physics deep inside the stars.

2.4 The case of KIC 11145123

The final section in this chapter is devoted to the study of oscillatory ΔP_{g} patterns of KIC 11145123 to see, as an example, to what extent the theoretical considerations discussed in the previous sections are helpful for inferring deep interiors of stars, especially regions above a convective core where chemical composition gradients exist. This section is also relevant to the modeling of the star (performed in Chapter 4). In the first place, the observed ΔP_{g} pattern of KIC 11145123 is shown in addition to other basic quantities as observational uncertainties. A rough picture about the deep interior of the star which is brought about by the comparison between the theory and the observation is also given (Subsection 2.4.1). Secondly, fitting procedures to obtain equilibrium stellar models which moderately reproduce the observed ΔP_{g} pattern are presented (Subsection 2.4.2), and then, the results are (Subsection 2.4.3). Finally, we would like to discuss a cause of the discrepancy between the theoretically calculated ΔP_{g} patterns for the equilibrium models and the observed ones. For detailed information on KIC 11145123 and the previous studies of the star, see Section 1.3.

2.4.1 Data

First, we present the observed ΔP_{g} patterns of KIC 11145123. Figure 2.14 shows comparison of the observed ΔP_{g} pattern (red) with the theoretically computed ones (black and blue). The ΔP_{g}

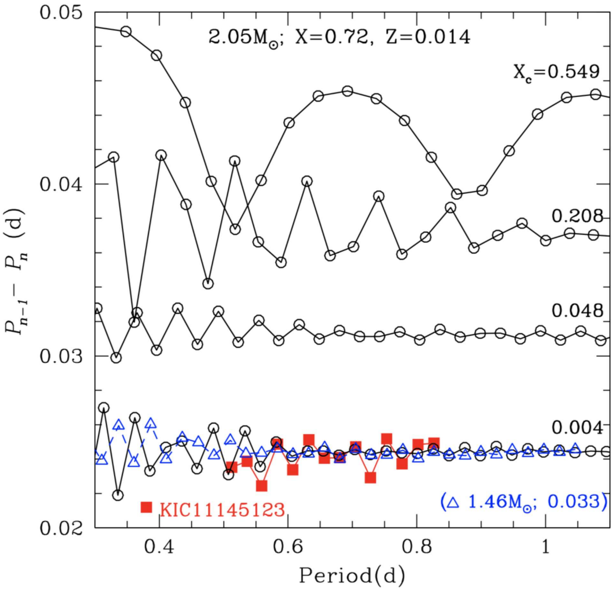

Figure 2.14: The same figure as Figure 1.15 in Section 1.3. See more details in the caption of Figure 1.15

patterns computed based on the best model in Kurtz et al. (2014) is represented by blue curves. The comparison clearly indicates that, not depending on which model we choose, models with fairly low central hydrogen contents tend to match the observation; this is the way Kurtz et al. (2014) concluded that the star is at the TAMS stage. Note, however, that what they fitted is the mean value of the observed g-mode period spacings $\overline{\Delta P_g}$, not the observed ΔP_{g} pattern itself, thus there being room for inferring more detailed information on the deep interior of the star. It should be also instructive to mention the observational uncertainties of the g-mode period spacings. Actually, they are so small that we cannot see the uncertainties in Figure 2.14.

Then, let me explain the observed ΔP_{g} pattern based on the discussions in the previous sections. We especially focus on interpreting periods of oscillatory components, if they exist. One obvious thing is that there exists an oscillatory component with a short period of about $\Delta n \sim$ a few. Remembering that the period is determined by a ratio Π_μ^{-1}/Π_0^{-1}, the short-period oscillation in the ΔP_{g} pattern suggests that Π_μ^{-1} is relatively large and that the region of chemical composition gradient might be rather broad. Another thing that must be mentioned is that there seems to be a linear trend in the ΔP_{g} pattern, namely, a positive slope. That could be related another oscillatory component with a longer period, which might be caused by the existence of the overshooting zone as discussed in Subsection 2.3.2. It is nevertheless difficult to directly extract the period of the longer-period oscillatory component because there are only 14 g-mode period spacings in the observation, and a typical period for a longer-period oscillatory component is $\Delta n \sim 30$ as we see in Subsection 2.3.1.

In the following subsections, we would like to carry out grid-based modeling to infer the present structure of the Brunt-Väisälä frequency of the star and also to understand how such structure has been formed along with the evolution.

2.4.2 Fitting procedure

A few procedures to carry out grid-based modeling are given in this subsection.

Parameter range

The number of parameters in the grid-based modeling is three. They are mass, the extent of overshooting (f_{ovs}), and age (represented by $\overline{\Delta P_{\mathrm{g}}}$). The initial helium abundance is fixed to be 0.26, and this is because of the fact that the numerically computed ΔP_{g} patterns are almost independent of the initial helium abundance as shown later. The initial metallicity is fixed to be 0.003, which is based on the results of spectroscopic study of the star (Takada-Hidai et al., 2017).

We determined the grid for each parameter as below: mass ($1.30 - 1.70 M_{\odot}$, by $0.05 M_{\odot}$) and f_{ovs} (0.010, 0.015, then 0.022-0.030, by 0.001). The mass range is chosen based on the previous studies (e.g. Kurtz et al., 2014) suggesting that relatively lower mass models ($\sim 1.4 M_{\odot}$) favor the observations. The extent of overshooting is determined based on often recommended values around $f_{\mathrm{ovs}} \sim 0.01 - 0.02$. For the grid of age, we have one hundred points between the age when $\overline{\Delta P_g} \sim 2150\,\mathrm{s}$ and the one when $\overline{\Delta P_g} \sim 1950\,\mathrm{s}$, corresponding to around $100,000$ years for one timestep for this mass range. Note that $\overline{\Delta P_g}$ is a quantity computed based on N^2 of the models following the equation (2.7), not numerically computed one.

In total, we have about $10,000$ stellar models.

Settings in MESA

For calculating stellar evolutionary models, a community 1-dimensional stellar evolutionary code MESA (Paxton et al., 2019), version 9793, is used. The tabulated forms of the OPAL equation of state and opacity are used in my calculation. The nuclear network is composed by eight elements whose name is given as 'basic.net' in MESA, based on which nuclear reaction rates are computed. The abundances of heavy elements are scaled by the solar values. The outermost atmospheres are solved assuming Eddington-Grey approximation. We assume no rotation, no magnetic fields, no mass accretion/gain in the calculation. The convective region is solved via Mixing Length Theory with $\alpha_{\mathrm{MLT}} = 1.7$, which is calibrated to reproduce the solar observations (Kurtz et al., 2014). The Schwartzschild criterion for the convective boundary is chosen. The references are found in Paxton et al. (2011).

MESA has many options for prescriptions of mixing processes, such as diffusion, overshooting, semiconvection, thermohaline mixing, rotationally induced mixing, magnetically driven mixing. Among them, we determine to activate diffusion and overshooting, which are relatively easier to implement and understand the physics behind compared with the other mixing processes. The effect of the diffusion is incorporated into the evolutionary calculation by solving so-called Burger's equation which is based on Boltzman's equation in kinematics (Burgers, 1969). Though the scheme for diffusion is considered to be working well for models with $\sim 1 M_{\odot}$, it has been long pointed out that the scheme often overestimates the diffusion velocity of helium in the outermost layer of models with $> 1.3 M_{\odot}$, sometimes leading to the depletion of helium there, which has not been observationally confirmed (Morel and Thevenin, 2002). To avoid such depletion of helium in the outermost layer of the models, some special scheme are implemented (Morel and Thevenin, 2002).

There are basically two ways of incorporating overshooting in the stellar evolutionary calculation. In one, overshooting regions are treated as just an extension of convective regions (determined by the Schwartzschild critetion), and the uniform chemical composition is assumed in the regions (e.g.

Pedersen et al., 2018). In the other, overshooting regions are not assumed to be fully mixed regions, and the efficiency of the mixing there is given by a diffusion coefficient which starts with the diffusion coefficient around the convective core boundary (given based on the Mixing Length Theory) and exponentially decays with a free parameter (Herwig , 2000). We adopt the latter scheme in this study. The free parameter ($f_{\rm ovs}$) determines the extent of overshooting region, which is one of the parameters in our grid.

For mesh control in space and time, we use the default settings in MESA. For more information, see (e.g. Paxton et al., 2011).

Specific procedures

Based on the settings described in the previous small subsection, we calculated a grid of models for the parameter range defined in the second last small subsection. Below is the way how we chose a series of models which moderately reproduces the observed $\Delta P_{\rm g}$ pattern.

For a certain mass M, an initial chemical composition (X, Y, Z), and an extent of the ovreshooting $f_{\rm ovs}$, one evolutionary track is computed with default timesteps in MESA until $\overline{\Delta P_g}$ (included in MESA outputs) reaches 2200 s. Then, we change the timesteps to much smaller ones, corresponding to about $100,000$ years. The evolutionary calculation is restarted with the new timesteps and it is stopped when $\overline{\Delta P_g}$ reaches 1900 s. The procedure above is done because the mean value of the observed $\Delta P_{\rm g}$ of the star is about 2100 s, and it is time-consuming if we conduct evolutionary calculations from ZAMS to TAMS with small timesteps.

All the models whose $\overline{\Delta P_g}$ are between 2200 s and 1900 s are retained, and the (g-mode) eigenfrequencies of the models are computed based on a linear adiabatic oscillation code GYRE (Townsend and Teitler, 2013). We thus obtain the numerically computed g-mode period spacings $\Delta P_{\rm g,num}$ based on the results of oscillation calculation, and look for a model which minimizes the residual between $\Delta P_{\rm g,num}$ and the observed $\Delta P_{\rm g}$. The above procedure is repeated for every set of mass and chemical composition (the number of the latter parameter is just one in this case, and thus the procedure is repeated for every mass, practically).

2.4.3 Results

As a result of the fitting procedure described above, we obtained the best model with a certain value of $f_{\rm ovs}$ for each mass. The sum of the residuals normalized by the observational uncertainties are significantly lower of $\sim 3 \times 10^5$, than that of Kurtz et al. (2014), which is $\sim 10^6$, obviously showing the advantage of fitting the observed $\Delta P_{\rm g}$ pattern rather than fitting just the mean value $\overline{\Delta P_g}$.

Figure 2.15 shows the numerically computed $\Delta P_{\rm g}$ patterns (left panel) and the Brunt-Väisälä frequencies (right panels) of some of the models chosen based on the procedures described in the previous subsections. Models with masses ranging from $1.30 M_\odot$ to $1.60 M_\odot$ are exhibiting almost the same $\Delta P_{\rm g}$ pattern, i.e. they are basically represented by an oscillatory component with a long period, which has succeeded in reproducing the gradual positive slope of the observed $\Delta P_{\rm g}$ pattern. It is also common that another oscillatory component with a shorter period is not evident for models in the mass range. The value of the extent of overshooting is $f_{\rm ovs} = 0.027$.

The relatively more massive model with $1.70 M_\odot$ is showing a $\Delta P_{\rm g}$ pattern different from those of lower-mass chosen models. The value of the extent of overshooting is $f_{\rm ovs} = 0.015$ in this case, which is smaller than that for low-mass counterparts. We see the outcomes in the $\Delta P_{\rm g}$ pattern and in N^2 for the $1.70 M_\odot$ model; the oscillatory component in the numerically computed $\Delta P_{\rm g}$ pattern

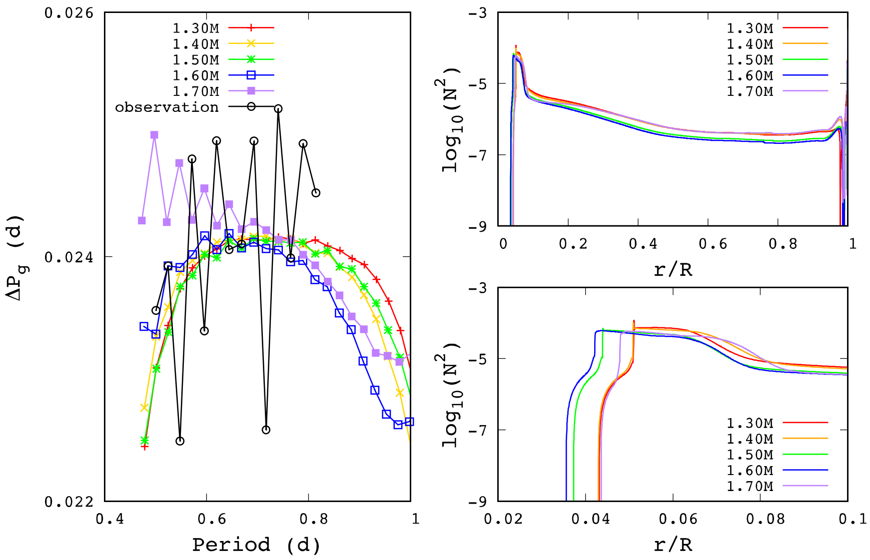

Figure 2.15: $\Delta P_{\rm g}$ patterns of some of the best models obtained based on the procedure (see the text) (colored curves), and the observed $\Delta P_{\rm g}$ pattern of the star is represented by the black curves (left panel). The corresponding Brunt-Väisälä frequencies for the models are presented in the right column. The lower panel is a closer look of the upper panel. Note that the observational uncertainties are so small $\sim 10^{-6}$ d (Kurtz et al., 2014) that there seem to be no error bars.

(the purple curve in Figure 2.15) has a longer period than that of low-mass best models, resulted from the much smaller overshooting region (see the purple curve in the bottom right panel in Figure 2.15) which renders the ratio Π_μ/Π_0 larger.

Note that the observed oscillatory component with a shorter period has not been confirmed in any of the selected models; the amplitudes of the numerical computed ones are much smaller than the observation. It is thus suggesting the possibility that there should be much steeper features in the Brunt-Väisälä frequency of the star (see the discussions in the small subsection 2.3.2), and we have to consider what processes during the evolution renders such structure to exist, which is one of the main topics in the discussion part in this section.

2.4.4 Discussions

As it is demonstrated in the previous section, we have partly succeeded in reproducing the observed $\Delta P_{\rm g}$ pattern of KIC 11145123; the oscillatory component with the longer period $\Delta n > 15$ can be fitted by changing $f_{\rm ovs}$, the extent of overshooting. The models obtained show the residuals smaller than the model of Kurtz et al. (2014), which is definitely an improvement. However, the observed oscillatory component with the shorter period $\Delta n \sim$ a few cannot be reproduced by any of the best models found in our grid. In this section, we investigate the reason why the tentative models cannot reproduce the shorter-period oscillation in the observed $\Delta P_{\rm g}$ pattern. First, the dependence of some

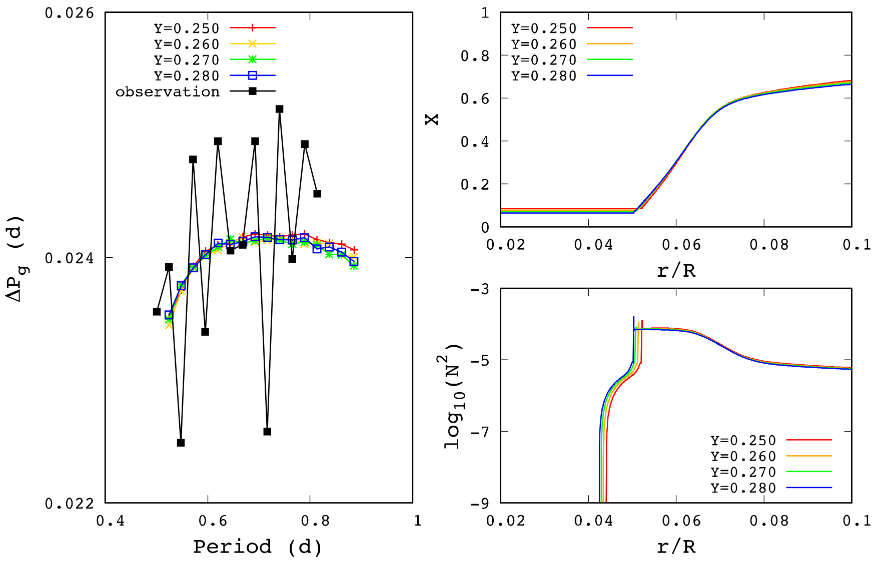

Figure 2.16: Numerically computed $\Delta P_{\rm g}$ patterns of models with a variety of initial helium abundances (colored curves), which almost completely overlap with one another. The observation is represented by the black curve (left panel). The corresponding hydrogen profiles and Brunt-Väisälä frequencies are in the upper right panel and in the lower right panel, respectively. We see little difference in the $\Delta P_{\rm g}$ patterns, the hydrogen profiles, and the Brunt-Väisälä frequencies. For settings of the evolutionary calculations, see the text.

parameters, namely, initial helium abundance, metallicity, and mass on the numerically computed $\Delta P_{\rm g}$ pattern is checked. It is shown that dependence on the initial chemical composition is too small to significantly affect the amplitudes of the oscillatory $\Delta P_{\rm g}$ pattern. We instead confirm the mass dependence of the $\Delta P_{\rm g}$ patterns. Secondly, perturbations in the Brunt-Väisälä frequency δN are artificially added to those of the somewhat smooth models in order to check what features can cause the shorter-period oscillation of the observed $\Delta P_{\rm g}$ pattern.

Little dependence of numerically computed $\Delta P_{\rm g}$ patterns on initial chemical compositions

It is generally considered that the initial chemical compositions (X, Y, Z) are one of the most important parameters which strongly affect the stellar structure and evolution. In particular, the size of the convective core is largely dependent on the initial chemical compositions as introduced in Subsection 1.1.1 for the low-mass stars in this mass range. Thus, they could also affect the Brunt-Väisälä frequency, and accordingly, the $\Delta P_{\rm g}$ pattern. This is the reason why we check the dependence in this small subsection.

Figure 2.16 illustrates numerically computed $\Delta P_{\rm g}$ patterns of several models with various initial helium abundances. The mass of the models is $1.30 M_\odot$, and $f_{\rm ovs} = 0.027$ is adopted to carry out the evolutionary calculations. The metallicity is fixed to be 0.003. The models are fitted to the

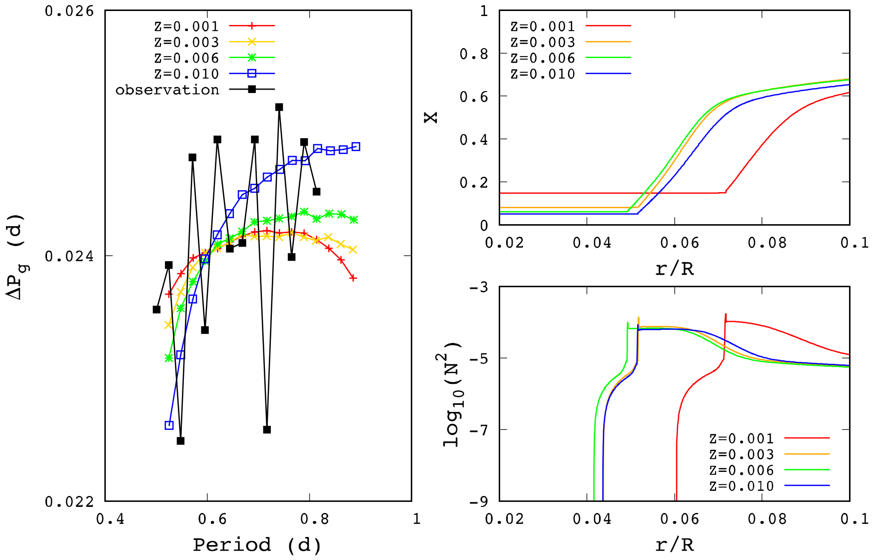

Figure 2.17: Numerically computed ΔP_{g} patterns of models with a variety of initial metallicities (colored curves), which partly overlap with one another. The observation is represented by the black curve (left panel). The corresponding hydrogen profiles and Brunt-Väisälä frequencies are in the upper right panel and in the lower right panel, respectively. For settings of the evolutionary calculations, see the text.

observed ΔP_{g} pattern in the same way as explained in Subsection 2.4.2. Actually, there is little, or no, dependence of the initial helium abundance on the ΔP_{g} pattern, the fact which is later utilized in non-standard modeling of the star in Chapter 4.

The absence of the initial-Y-dependence (here, Y represents the helium abundance) can be understood based on the fact that there apparently is no difference in hydrogen abundances of the models (see the upper right panel in Figure 2.16). The core properties are almost the same, and thus, so are the pressure scale heights at the convective boundary, rendering the longer-period oscillatory component of the ΔP_{g} pattern similar to each other (see discussions in Subsection 2.3.1). In other words, given a particular set of mass, initial metallicity, and the extent of overshooting, there exists just one unique (not completely unique, of course) hydrogen abundance profile (and helium abundance profile as well) which reproduces a mean value of the ΔP_{g} patterns, and importantly, such uniqueness inevitably leads to a similarity in the pressure scale heights at the convective boundaries resulting in the similar ΔP_{g} patterns. Note that the age is different from each other because of the different initial chemical compositions; models with lower initial helium abundances tend to be younger because they usually reach an evolutionary stage with a certain value of central hydrogen abundance faster.

Figure 2.17 is produced in the same way as Figure 2.16 except that the initial metallicity is the variable here and the initial helium abundance is fixed to be 0.255. Although the hydrogen abundance profiles are certainly dependent on the initial metallicity (see the upper right panel in Figure

2.17), the shorter-period oscillatory component of the observed $\Delta P_{\rm g}$ pattern is not reproduced as in the case where we check the initial-Y-dependence in the last paragraphs (Figure 2.16). This might be because negative gradients just outside the bump-like structures in the Brunt-Väisälä frequency are rather smooth so that the asymptoticity of the high-order g modes is high there, leading to the absence of the shorter-period oscillatory components in the modeled $\Delta P_{\rm g}$ patterns (see discussions in Subsection 2.3.1). Actually, the asymptoticity of the g modes is strongly dependent on mass as it is explained in the next small subsection.

Therefore, changing the initial chemical compositions is not leading to resolve the discrepancy between the tentative models' $\Delta P_{\rm g}$ patterns and the observation.

Dependence of numerically computed $\Delta P_{\rm g}$ patterns on mass

As it is shown in the preceding small subsection, changing the initial chemical compositions is not affecting the numerically computed $\Delta P_{\rm g}$ patterns so much, and we are not able to reproduce, in particular, the shorter-period component in the observed $\Delta P_{\rm g}$ pattern of KIC 11145123. In this small subsection, we are going to focus on another important stellar parameter, namely, stellar mass. It has been already mentioned in Subsection 2.4.3 that the relatively high-mass model with $1.7M_\odot$ reproduces the amplitude of the observed $\Delta P_{\rm g}$ pattern better (see the purple curve in Figure 2.15) compared with the other lower mass models, suggesting the potential benefit of checking the mass dependence of the $\Delta P_{\rm g}$ pattern in a broader mass range.

Figure 2.18 shows numerically computed $\Delta P_{\rm g}$ patterns (left), the hydrogen profiles (upper right), and the Brunt-Väisälä frequencies (lower right) for models with different masses obtained in the same way as described in Subsection 2.4.2. The initial helium abundance, metallicity, and the extent of overshooting are fixed to be 0.026, 0.003, and 0.027, respectively. It is evident that amplitudes of the $\Delta P_{\rm g}$ patterns calculated based on the higher-mass models (more massive than $1.7M_\odot$) are relatively large compared with those of low-mass models.

The difference between low-mass models and more massive models in the amplitudes of the shorter-period components in the numerically computed $\Delta P_{\rm g}$ patterns can be attributed to the difference in the hydrogen profiles or the Brunt-Väisälä frequency. We find such a signature, for instance, in the negative gradients just outside the bump-like structures in the Brunt-Väisälä frequency (see a sector between $0.06 < r/R < 0.08$ of the lower right panel in Figure 2.18); as mass increases, the absolute value of the negative gradient increases, and thus, the asymptoticity of high-order g modes becomes less prominent. Furthermore, the Brunt-Väisälä frequency of the higher-mass models are smaller than those of the lower-mass models (see again a sector between $0.06 < r/R < 0.08$ of the lower right panel in Figure 2.18, and compare curves, for example, the pink one and the green one), which decreases the wavenumber of g modes ($k_r \sim LN/\omega r$) of the higher-mass models, weakening the asymptoticity of the g modes more.

Then, what is a cause of the different hydrogen profiles (or the Brunt-Väisälä frequencies)? One possible answer is the balance between the CNO cycle and the pp-chain reaction which are at work in the deep interiors, namely, the convective core and a part of deep radiative region, the latter of which has a profound impact on the hydrogen profiles because there is usually no other mechanisms modifying the chemical composition in the radiative region. In the case of lower-mass models (roughly speaking, $1.2M_\odot < M < 1.6M_\odot$), the pp-chain reaction occurs in a part of the deep radiative region and the hydrogen profile is prone to be smooth. However, as models has larger masses, the CNO cycle dominates the pp-chain reaction even in the deep radiative region, and the hydrogen profile gradually becomes less smooth (or flat) because the ex-radiative region is

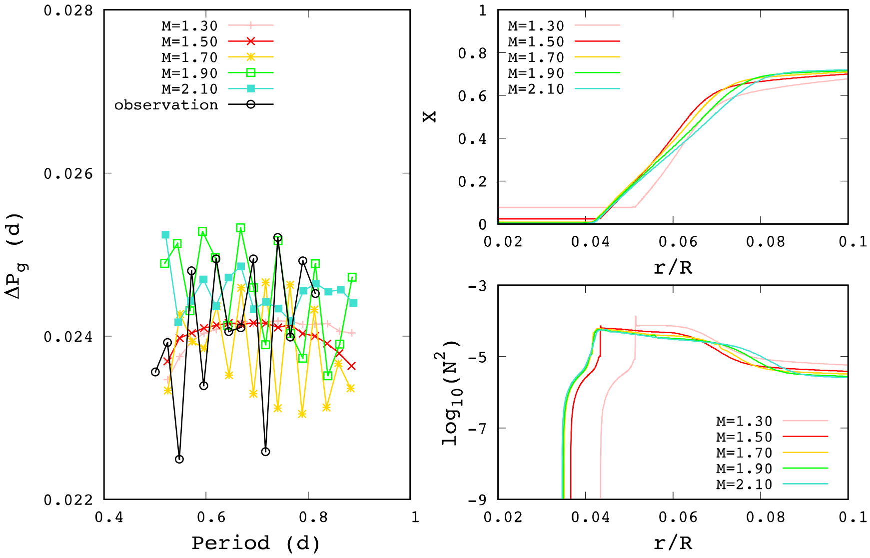

Figure 2.18: Numerically computed $\Delta P_{\rm g}$ patterns of models with a variety of masses (colored curves), which partly overlap with one another. The observation is represented by the black curve (left panel). The corresponding hydrogen profiles and Brunt-Väisälä frequencies are in the upper right panel and in the lower right panel, respectively. We clearly see some improvements in the amplitudes of the computed $\Delta P_{\rm g}$ patterns, especially in the case of more-massive models (yellow, green, and cyan). For settings of the evolutionary calculations, see the text.

now convective due to the conversion from the pp-chain cycle to the CNO cycle there.

How has the observed short-period oscillatory component been reproduced?

The previous discussion presents one possible resolution; we have to model the star with a more massive model to reproduce the observed $\Delta P_{\rm g}$ pattern better than the tentative models do. However, the spectroscopic study of the star indicates that the star is rather a low mass star, with $\log g \sim 4.2$ (in cgs units) and $T_{\rm eff} \sim 7450\,{\rm K}$. We thus would like to find an alternative resolution persisting to lower mass models.

To this end, we artificially add perturbations δN to the Brunt-Väisälä frequency of one of the tentative models, namely, a $1.34 M_\odot$ model with $Y_{\rm init} = 0.26$ and $Z_{\rm init} = 0.003$ (Figure 2.19). We subsequently compute the asymptotic eigenfrequencies obtained by solving the equation (2.1) where the perturbed N^2 is used. Figure 2.19 illustrates the $\Delta P_{\rm g}$ patterns computed based on the perturbed N^2. Though the mean values $\overline{\Delta P_g}$ are smaller than that of the observation (which is because we just add positive δN, and thus the integral $\int N d\ln r$ increases, leading to the decrease in $\overline{\Delta P_g}$), the perturbed $\Delta P_{\rm g}$ patterns have much larger amplitudes for the shorter-period oscillatory components than the unperturbed one does. Such perturbations seem to be too large to develop inside the real stars, but we can find a similar structure in the no-diffusion models (see Figure 2.13), suggesting the possibility that weakening the diffusion process might lead to a better agreement between the

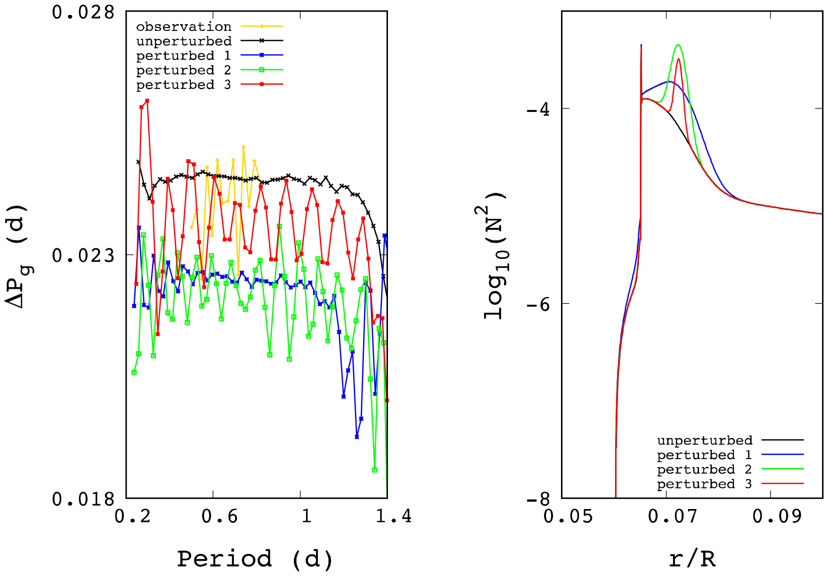

Figure 2.19: Unperturbed Brunt-Väisälä frequency of a $1.34 M_\odot$, $Y_{\rm init} = 0.26$, $Z_{\rm init} = 0.003$ model (black), and three artificially perturbed Brunt-Väisälä frequencies (red, blue, and green). Yellow curves represents the observed $\Delta P_{\rm g}$ pattern (left panel). The corresponding Brunt-Väisälä frequencies are shown in the right panel. Though the way we perturbed the Brunt-Väisälä frequency is not physically motivated one, it is definitely seen that the perturbations leads to better agreements between the models and the observation.

model and the observation, which is discussed in Subsection 4.2.3.

2.5 Summary of this chapter

Theoretical attempts to relate the $\Delta P_{\rm g}$ pattern with some parameters characterizing the distribution of the Brunt-Väisälä frequency have been given based on the asymptotic approximation for high-order g modes. Following the two different treatments, one by Miglio et al. (2008) and one by Cunha et al. (2019), we have presented several new analytical expressions for the $\Delta P_{\rm g}$ pattern, which are validated by comparing them with $\Delta P_{\rm g}$ patterns numerically computed based on simple artificial Brunt-Väisälä frequencies. Then, we have attempted to explain $\Delta P_{\rm g}$ patterns computed based on realistic Brunt-Väisälä frequencies with the analytical expressions. Though it is still challenging for us to completely explain the $\Delta P_{\rm g}$ patterns of the realistic stellar models, we have found that a longer periodic component in the $\Delta P_{\rm g}$ patterns are due to sharp features in the Brunt-Väisälä frequency caused by the convective overshooting. By changing the extent of overshooting $f_{\rm ovs}$ in stellar evolutionary computations, we have found that $f_{\rm ovs} = 0.027$ is most appropriate for reproducing the positive slope seen in the observed $\Delta P_{\rm g}$ pattern of KIC 11145123, which is incorporated to the non-standard modeling demonstrated in Chapter 4. We finally propose that the discrepancy between the $\Delta P_{\rm g}$ pattern of the current best model and the observed one could be resolved by adopting more massive models or by considering some physical mechanisms such as much weaker diffusion which render the chemical composition gradient of the best model much steeper.

Chapter 3

Non-standard modified-envelope modeling

Chapter 3 is primarily devoted to a novel scheme of non-standard modeling developed by us. After the current status of the non-standard modeling of stars, especially those treating mass accretion/loss, is briefly introduced in the first section 3.1, the basic concepts and the theoretical formulations in our scheme of the non-standard modeling are presented (section 3.2). The validity of the developed scheme is checked in detail in the third section 3.3 for each step in the scheme. Then, eigenfrequencies of envelope-modified models computed based on our scheme are compared with those of the original unperturbed models. Structural differences are also discussed in Section 3.4. The scheme is applied for constructing an alternative model of KIC 11145123, which has succeeded in reproducing the observed frequencies of the star with the initial helium abundance of ~ 0.26, lower than ~ 0.34 for the model obtained by Kurtz et al. (2014) (section 3.5). Other possible applications of the developed scheme in a broader perspective with respect to stellar physics are given in Section 3.6, and finally the summary of this chapter is presented in Section 3.7.

3.1 A brief introduction

As is described in Subsection 1.1.2, non-single-star evolution is not uncommon for a significant fraction of stars such as those in multiple stellar systems; they are sometimes interacting with the other stars in the system or they have experienced such interactions at some time during the evolution. There are a large number of stars which are thought to have experienced interactions with other stars, for instance, stars in Algol-type binaries or those of blue straggler stars (see Subsection 1.1.2), and thus, it should be not appropriate to compute stellar models of these stars with ordinary 1-dimensional stellar evolutionary codes as are introduced in Subsection 1.1.1; we need to rely on models calculated in non-standard ways to understand the internal structures to some extent.

There have currently been multiple 1-dimensional stellar evolutionary codes in which mass accretion onto the star or mass loss from the star is taken into account for computing the structure and evolution of the stars (e.g. Paxton et al., 2011). Some codes are also able to simultaneously compute evolutions of stars in a binary system, in which mass transfer from the more massive model to the less massive one via Roche Lobe Overflow can be treated in addition to the orbital evolution of the system (e.g. Paxton et al., 2015). These codes have been frequently utilized for studies of, for instance, mass accretion onto a white dwarf (Nomoto, 1982), mass accretion onto a pre-main-sequence star (Kunitomo et al., 2017), instability of Roche Lobe Overflow in a binary system (Boffin et al., 2015), etc.

However, we can hardly claim that the schemes treating binary interactions in these stellar evolutionary codes are complete; it is especially the case for the schemes concerning mass accretion, where we have to accept several assumptions in terms of the extent to which the envelope are affected, the thermodynamical states and the chemical compositions of accreted materials, how much angular momentum is transferred to the envelope, and so on (Kunitomo et al., 2017). With phenomenological prescriptions, we need to calibrate the schemes by comparing with observational studies, but it is of a great challenge for us to observationally extract information on the interiors of stars (Chen et al., 2020), hindering us from testing the schemes. We have to, instead, rely on numerical simulations of mass accretion onto a star to put constraints on free parameters in the phenomenological prescriptions (Kley and Lin, 1996).

Another issue is related to how to determine the structure of regions affected by mass accretion. The relaxation methods such as the Newton-Raphson method are often used to calculate the mass accreted region (e.g. Paxton et al., 2011). Though the model thus computed satisfies a set of equations (namely, the hydrostatic equation, the equation of mass conservation, the equation of temperature gradient, and the equation of energy conservation; explicit forms can be found in Paxton et al., 2011), it is not obvious whether the regions affected by mass accretion are always retaining the thermal equilibrium states or not, and there is room for incorporating more realistic physics with dynamical timescale into the schemes.

3.2 Formulation

This section concentrates on establishing a new scheme of non-standard modeling taking into account chemical composition modification in the envelope of stars (which is thought to be caused by mass accretion). First, we demonstrate how to model the effects of such modifications of the chemical compositions on the structure of a stellar equilibrium model. We assume that the effects of chemical composition modification can be expressed with four elementary steps (subsection 3.2.1). We also present the mathematical formulations for the steps (subsection 3.2.2), which are to be numerically solved in the non-standard modeling of real stars including KIC 11145123 in the later section 3.4.

Note that, in this section, the alphabet l and m mean not the spherically degree and the azimuthal order used in helio- and asteroseismology, but the local luminosity and the mass inside concentric sphere to describe a stellar model (see Subsection 3.2.1).

3.2.1 Basic concept

Throughout this dissertation, a model of a star at a certain age is considered as a sphere whose interior is divided into multiple spherical layers called mass shells. The mass inside the concentric sphere m is often taken as an independent variable. Dependent variables as functions of m (strictly speaking, they are also functions of time which is assumed to be fixed here), namely, the distance from the center of the star r, the pressure P, the temperature T, the local luminosity l, and the mass fractions for each chemical element X_i (the index i represents each chemical element), together with other parameters such as the thermodynamic quantities (the density ρ, the adiabatic sound speed c^2, and so on), the opacity κ, and the nuclear energy generation rate ε are assigned for each mass shell so that the set of the equations for stellar structure and evolution (see, in particular,

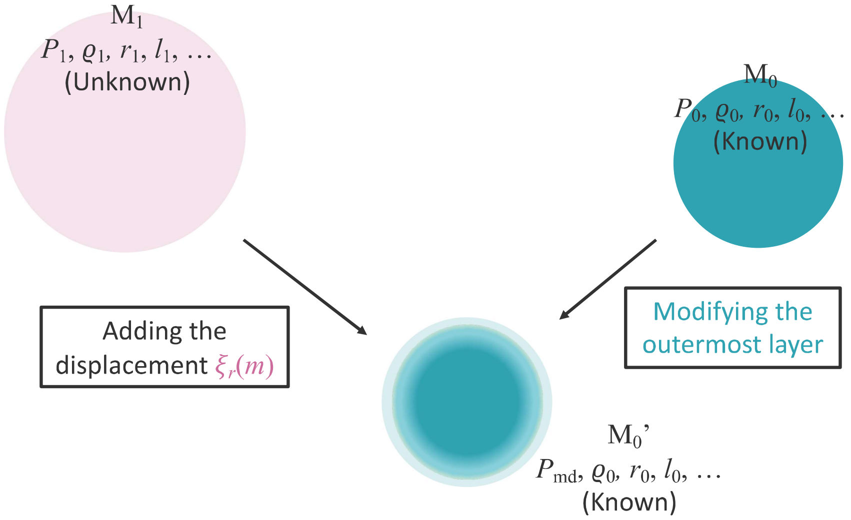

Figure 3.1: Schematic view of the three models and the relations among them.

Section 6 in Paxton et al., 2011) is satisfied with the variables above with certain precisions. This is the standard view of a stellar model, and let us call the model M_0 (see Figure 3.1).

Then, how do we model the effects of the chemical composition modification (which is assumed to be caused by, for instance, mass accretion) on the stellar model M_0 defined in the last paragraph and incorporate the effects on the structural variables (r, P, T, l, X_i)? We simplify the effects with four steps as described in the following paragraphs.

First, we determine a particular mass shell in the model above which the chemical compositions X_i are to be changed. The amount of the modification to X_i is arbitrary, and an example of the explicit forms for the amount is given in the next subsection 3.2.2 as a function of m. We fix the structural parameters other than X_i (namely, r, P, T, and l). The thermodynamic parameters, the opacity, the nuclear energy generation rate, and so on are accordingly changed based on the already computed tables such as OPAL. Note that there are usually two degrees of freedom in terms of the variation in thermodynamic quantities when X_i are changed. In this study, the density ρ (in other words, the distance of the mass shell from the center r) and the temperature T are assumed to be fixed. We can instead select the other sets of parameters to be fixed, for example, the specific entropy s and the density ρ.

The modification introduced in the first step results in the change of the mean molecular weights

μ of the modified mass shells, also leading to the change of the pressure P. This spherical model M_0 is thus no longer in hydrostatic equilibrium state; the hydrostatic equation is not satisfied with the new set of modified parameters (remember that r is assumed to be fixed, and thus the gravitational force is not changed though the pressure gradient is). Let us call this model the perturbed model M_0'. We have to resettle the model M_0' to a hydrostatic equilibrium state by considering that the perturbed state is caused by radial displacements added to another hydrostatic equilibrium state (denoted as M_1 in Figure 3.1) different from the unperturbed model. The model M_1 can be obtained by solving the second order differential equation formulated based on the linear adiabatic radial oscillation which is derived in Subsection 3.2.2. This is the second step.

In the second step, the modification is assumed to be small enough that we can treat the modification as a perturbation, which is required to guarantee the validity of the radial displacements determined by solving the linear differential equation. Therefore, we have to repeat the step 1 and 2 many times to obtain a model whose outer region is significantly modified compared with the unperturbed model M_0. We denote the model obtained in this way as M_1'.

Finally, because the model M_1' is considered to be deviated from a thermal equilibrium state, we have to again resettle the model toward a thermal equilibrium state. This final step can be done by, for instance, applying the Henyey method to the model M_1'. In principle, this stage is somehow similar to the contraction phase of the pre-main-sequence stars for which rates of gravitational energy generation ε_g is negative. Some explanations for ε_g can be found in Subsection 3.3.2.

3.2.2 Equations in the scheme

The mathematical formulations to describe the steps in the last subsection are presented in this subsection. Let me start with the set of equations for stellar structure which the parameters of the unperturbed model M_0 satisfy, expressed as below:

$$\frac{dP_0}{dm} = -\frac{Gm}{4\pi r_0^4}, \tag{3.1}$$

$$\frac{dr_0}{dm} = \frac{1}{4\pi r_0^2 \rho_0}, \tag{3.2}$$

$$\frac{dT_0}{dm} = -\frac{Gm}{4\pi r_0^4}\frac{T_0}{P_0}\nabla_0, \tag{3.3}$$

and

$$\frac{dl_0}{dm} = \varepsilon_{n,0} - \varepsilon_{\nu,0}, \tag{3.4}$$

where the subscripts 0 are representing the unperturbed state of the model M_0. The actual temperature gradient ∇_0 is defined as $(d\ln T_0/d\ln P_0)$. The other parameters have the same meaning as in the last subsection.

In the first step, the outer envelope is modified to some extent, i.e. we artificially add a small perturbation to the chemical composition μ of the unperturbed model M_0

$$\mu_0 \rightarrow \mu_1 = \mu_0 + \delta\mu. \tag{3.5}$$

It is totally up to us to decide how to modify the envelope. For example, in the following section 3.3, we exchange hydrogen with helium assuming that the mass coordinate m is unchanged. The corresponding explicit form for $\delta\mu$ is given there.

We also assume that the temperature and the density are the same as those of the starting model M_0. Based on these assumptions, we can calculate the perturbed pressure $P_{\rm md}$ by interpolating tables of equation of state such as OPAL,

$$P_0 = P(\rho_0, T_0, \mu_0) \rightarrow P_{\rm md} = P(\rho_0, T_0, \mu_1). \tag{3.6}$$

It is then obvious that the perturbed model M_0' is not in a hydrostatic equilibrium state as described in Subsection 3.2.2.

In the second step, we consider that the deviation from the hydrostatic equilibrium state is caused by adding the radial displacement ξ_r to another hydrostatic equilibrium model M_1 (see Figure 3.1). The structural parameters of the model M_1 must satisfy the hydrostatic equation as bellow:

$$\frac{dP_1}{dm} = -\frac{Gm}{4\pi r_1^4}, \tag{3.7}$$

where the subscripts 1 are representing the model M_1. We can relate the new parameters to those of M_0' as

$$r_1 = r_0 - \xi_r, \tag{3.8}$$

$$P_1 = P_{\rm md} - \delta P, \tag{3.9}$$

$$T_1 = T_0 - \delta T, \tag{3.10}$$

and

$$\rho_1 = \rho_0 - \delta\rho. \tag{3.11}$$

If we substitute relations (3.8) to (3.11) for expressions (3.7), we have the following equation

$$\frac{d(P_{\rm md} - \delta P)}{dm} = -\frac{Gm}{4\pi(r_0 - \xi_r)^4}. \tag{3.12}$$

Note that we are not considering perturbed equations for the temperature gradient. For an alternative scheme where the equation of the temperature gradient is taken into account as well can be found in Appendix A. The equation of the energy conservation is also not considered here, and it is validated by the fact that we assume that the local luminosity l is fixed, and that l is strongly dependent on the innermost region to which the modification is added in this case; $\delta l = 0$.

Assuming that the perturbations are small enough to neglect the perturbed quantities of higher than the first order, the equation above can be further simplified as bellow:

$$-\frac{d(\delta P)}{dm} = -\frac{Gm}{4\pi r_0^4}\frac{4\xi_r}{r_0} - \delta h, \tag{3.13}$$

where δh is defined as

$$\delta h \equiv \frac{dP_{\rm md}}{dm} + \frac{Gm}{4\pi r_0^4}. \tag{3.14}$$

The perturbed (thermodynamic) quantities are dependent on how we take the pathway from M_1 to M_0'. We discuss the simplest way where the adiabatic process is assumed. For another way to deal with it, see Appendix A. In the adiabatic processes, there is no heat transfer among the mass shells of the model. We can relate the small perturbations of the thermodynamic quantities such as δP, δT, and $\delta\rho$ to their values $P_{\rm md}$, T_0, and ρ_0 with adiabatic exponents as follows:

$$\frac{\delta P}{P_{\rm md}} = \Gamma_1 \frac{\delta\rho}{\rho_0} \tag{3.15}$$

and

$$\frac{\delta T}{T_0} = (\Gamma_3 - 1)\frac{\delta \rho}{\rho_0}, \tag{3.16}$$

where the two adiabatic exponents are defined as

$$\Gamma_1 \equiv \left(\frac{\partial \ln P}{\partial \ln \rho}\right)_{\mathrm{ad}} \tag{3.17}$$

and

$$\Gamma_3 - 1 \equiv \left(\frac{\partial \ln T}{\partial \ln \rho}\right)_{\mathrm{ad}}, \tag{3.18}$$

and they can be obtained from tables for equation of state.

When we insert expression (3.15) into equation (3.13), it can be rewritten as

$$-\frac{d}{dm}(c_{\mathrm{md}}^2 \delta \rho) = -\frac{Gm}{4\pi r_0^4}\frac{4\xi_r}{r_0} - \delta h. \tag{3.19}$$

The adiabatic sound speed for the model M_0' is expressed as c_{md}^2. Let us then consider the mass conservation in the case of the linear oscillation, namely,

$$\rho' + \nabla \cdot (\rho_0 \boldsymbol{\xi}) = 0, \tag{3.20}$$

based on which we can relate the density perturbation $\delta\rho$ and the radial perturbation ξ_r in the following way

$$\delta \rho = -\rho_0 \frac{1}{r_0^2}\frac{d}{dr_0}(r_0^2 \xi_r). \tag{3.21}$$

We have used a relation between the Eulerian perturbation (ρ') and the Lagrangian perturbation ($\delta\rho$), and we adopt the spherical coordinate to articulate the specific form of the differentiation. For the convenience in later discussions, we express the differentiation in expression (3.21) in terms of the mass coordinate using the expression (3.2)

$$\delta \rho = -\frac{2\rho_0}{r_0}\xi_r - 4\pi r_0^2 \rho_0^2 \frac{d\xi_r}{dm}. \tag{3.22}$$

Combining the expressions (3.19) and (3.22), we finally have a linear differential equation for the radial displacement ξ_r in the case of the adiabatic process as follows:

$$4\pi r_0^2 \rho_0^2 c_{\mathrm{md}}^2 \frac{d^2 \xi_r}{dm^2} + \left[\frac{d}{dm}(4\pi r_0^2 \rho_0^2 c_{\mathrm{md}}^2) + \frac{2\rho c_{\mathrm{md}}^2}{r_0}\right]\frac{d\xi_r}{dm} + \left[\frac{d}{dm}\left(\frac{2\rho c_{\mathrm{md}}^2}{r_0}\right) + \frac{Gm}{\pi r_0^5}\right]\xi_r + \delta h = 0. \tag{3.23}$$

Equation (3.23) can be numerically solved when we have all the properties of the perturbed model M_0'. We can compute the density perturbation $\delta\rho$ based on expression (3.22), and subsequently, the temperature perturbation δT based on expression (3.16). Because the differential equation has been the linearization of the perturbed equation (3.12), we have to iterate the procedure explained above.

After we resettle the perturbed model with one perturbation in the mean molecular weight, we just repeat the same procedure until we obtain the model whose envelope is as modified as we would like to. There are thus no special mathematical formulations in the third step and the fourth step.

3.3 Demonstration of the scheme

In this section, the mathematical formulations developed in the last section are applied for stellar models. There are two primary goals in this section; one is to present numerical procedures to practically carry out the scheme, and the other is to validate the numerical calculations for future applications (as shown in Sections, 3.5, 3.6, and those in Chapter 4). In particular, one of the essential roles of the developed scheme, namely, reestablishing hydrostatic states of stellar models, is mainly tested.

Stellar models are computed via MESA (version 9793 Paxton et al., 2015). Neither rotation nor magnetic fields are assumed in the computation. The OPAL tables are used for both the equation of state and the opacity, and the nuclear reaction rate is obtained by interpolation based on a built-in table in MESA, called 'basic.net'. As mixing processes during the evolution, diffusion and overshooting are activated (for information on prescriptions of the two mixing processes, see Subsection 2.4.2). The free parameter in the Mixing Length Theory α_{MLT} is 1.7. The mass, the initial helium abundance, and the initial metallicity of the models are $\sim 1.4 M_{\odot}$, ~ 0.26, and 0.003, respectively. These settings are determined following those of the best model of Takada-Hidai et al. (2017).

3.3.1 A resettled model obtained for just-once perturbation; step 1 and 2

Perturbation to mean molecular weight in stellar envelope

First, we have to determine an explicit form for the modification in the mean molecular weight μ as has been already mentioned in Subsection 3.2.2. In practice, the equation of state is tabulated as functions of the density ρ, the temperature T, the hydrogen mass fraction X, and the metallicity Z, and the mean molecular weight is provided as one of the outputs in the case of MESA. Therefore, what we perturb are not μ but X and Z. We assume that the metallicity is fixed in the scheme, and the modification in X as a function of the mass coordinate m is expressed as

$$\delta X \equiv X_{\mathrm{md}} - X_0 = -\beta \times \tanh\left(\frac{m - m_{\mathrm{c}}}{\alpha} + 1\right), \tag{3.24}$$

in which X_{md} and X_0 are hydrogen mass fractions for the perturbed model M_0' and the unperturbed model M_0. There are three free parameters in the expression (3.24), namely, β, α, and m_{c} which determine the extent, the width of a transition, and the depth of the modification, respectively (see Figure 3.2). Note that the modification in the helium mass fractions δY is given as δX so that the sum of the mass fractions remains to be one.

Deviation from hydrostatic equilibrium

Based on the modified chemical compositions $(X_{\mathrm{md}}, Y_{\mathrm{md}}, Z_0)$ in addition to the density ρ_0 and the temperature T_0 of the perturbed model (remember that these two variables are assumed to be fixed in the modification of chemical compositions), the thermodynamic quantities such as the pressure P_{md}, the mean molecular weight μ_{md}, the sound speed c_{md}^2 can be obtained by interpolating the equation of state table. A module for interpolating the table for equation of state which is built in MESA is used.

Then, we can compute the deviation from the hydrostatic equilibrium state δh with the expression (3.14). Figure 3.3 illustrates δh computed for the corresponding perturbations in X and

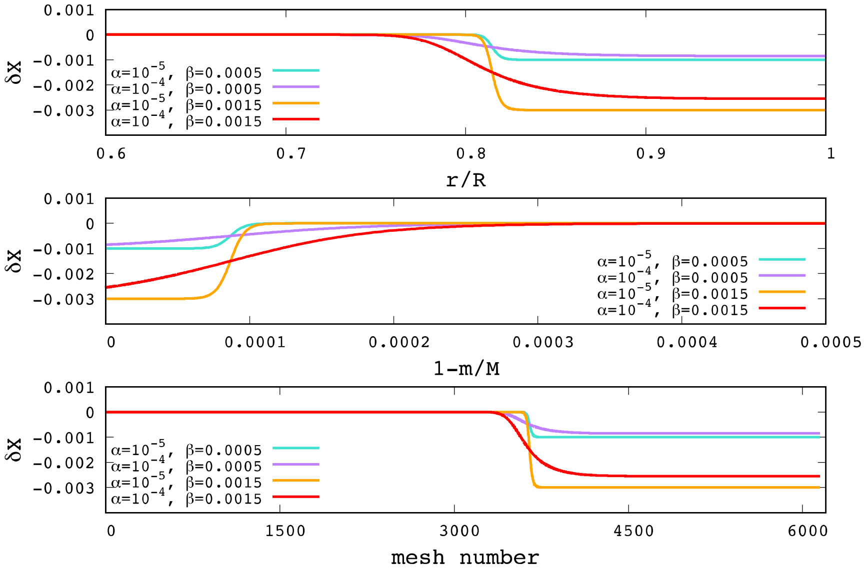

Figure 3.2: Examples of the modifications in the hydrogen mass fraction computed following the equation (3.24), with different abscissas, namely, the fractional radius r/R (top), the fractional mass m/M (middle), and the mesh number (bottom). Note that the fractional mass is represented by $1 - m/M$. Four ways of modification are shown changing the parameters α and β. The parameter m_c is fixed to be 0.99976. It is seen that as β increases the amount of the modification increases as well. Increasing α leads to the shallower transition from the unperturbed region to the perturbed one.

Y (see Figure 3.2). We can qualitatively explain δh based on the equation of state for an ideal gas assuming the full ionization. In that case, $\delta\mu$ can be expressed as $\delta(\mu^{-1}) \sim 4/5\delta X$, where a simple formulation $\mu^{-1} = 2X + 3/4Y + 1/2Z$ and the assumption that $\delta Y = -\delta X$ and $\delta Z = 0$ (the metallicity is fixed) are used. Because the pressure of an ideal gas is inversely proportional to μ, δP can be expressed as $P_0\mu\delta(\mu^{-1})$. The deviation from the hydrostatic equilibrium state is essentially given as the first order derivative of the δP caused by $\delta\mu$ (see the equation 3.14), and thus, we can readily compute δh without actually interpolating the table for equation of state. The semi-analytically computed δh is illustrated in Figure 3.3, and showing a good agreement between the semi-analytical one and those obtained based on the table for equation of state. Nevertheless, the discrepancy gets relatively large in the outermost envelopes where partial ionization of chemical elements is becoming significant.

Resettling to hydrostatic equilibrium

Now we have all the quantities required to solve the ordinary second-order linear differential equation (3.23). As an inner boundary condition, $\xi_r = 0$ at the center of the model is imposed because the radial displacements are considered here. An outer boundary condition is $(d\xi_r/dm) = 0$ at the surface, which is derived from the so-called zero boundary condition $\delta P = 0$ (the Lagrangian per-

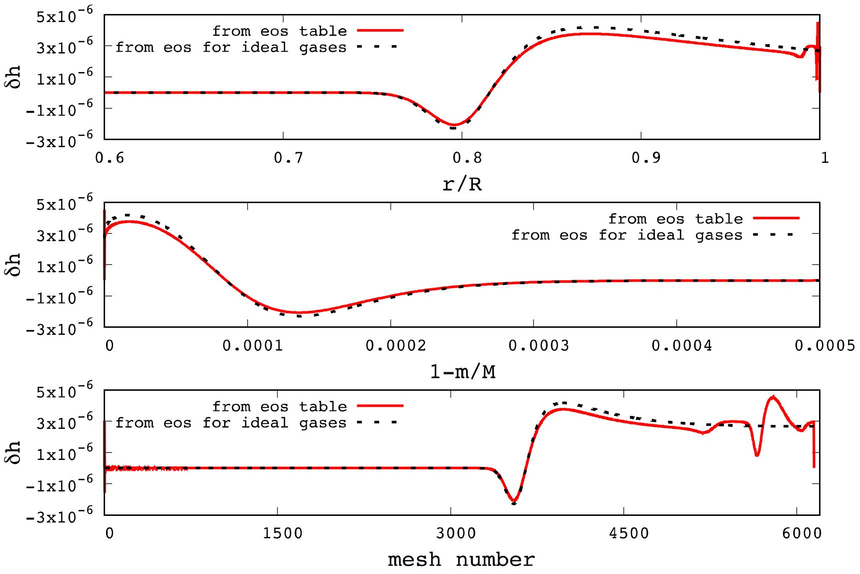

Figure 3.3: Deviation from the hydrostatic equilibrium defined in the expression (3.14), with different abscissae r/R (top), m/M, and the mesh number. The deviation δh is computed following the procedure described in text based on the modification expressed with the parameters $\alpha = 10^{-4}$, $\beta = 0.0015$, and m_c=0.99976, corresponding to the red curve in Figure 3.2 (also red solid curve in this figure). The black dotted curve is computed suming the equation of state for an ideal monatomic gas, and it is clearly seen that the two curves are almost identical except for the outermost regions where the effect of the partial ionization gradually becomes significant. See text for more details.

turbation of the pressure is zero at the surface) often adopted in calculating stellar linear adiabatic oscillations (Unno et al., 1989).

The differential equation is solved based on the second-order implicit scheme where the staggered mesh is adopted to describe the quantities and their derivatives (see, for example, Figure 9 in Paxton et al., 2011) In the scheme, numerical integration is carried out from the center with the boundary condition for ξ_r and two arbitrary initial guesses for $d\xi_r/dm$ there. Each integration provides us with the corresponding surface value of $d\xi_r/dm$, and by interpolating the two initial guesses so that the interpolated $d\xi_r/dm$ to be zero, we determine a new value c with which numerical integration is conducted again to obtain the final solution of the equation (3.23).

The radial displacement ξ_r thus obtained is substituted for the relations (3.8) and (3.10) to compute structural variables r_1 and T_1 of the resettled model M_1. The equation (3.16) is used to compute δT. The expression (3.22) combined with ξ_r presents $\delta\rho$, leading to ρ_1 via the relation (3.11). Based on the newly defined variables, the thermodynamic quantities and the deviation δh are calculated, and if δh is larger than a certain threshold ($\sim 10^{-6}$ in relative difference, which is of almost the same order as that in MESA), the above differential equation is solved again with the new variables. This iteration continues until δh becomes smaller than the threshold (see Figure 3.4).

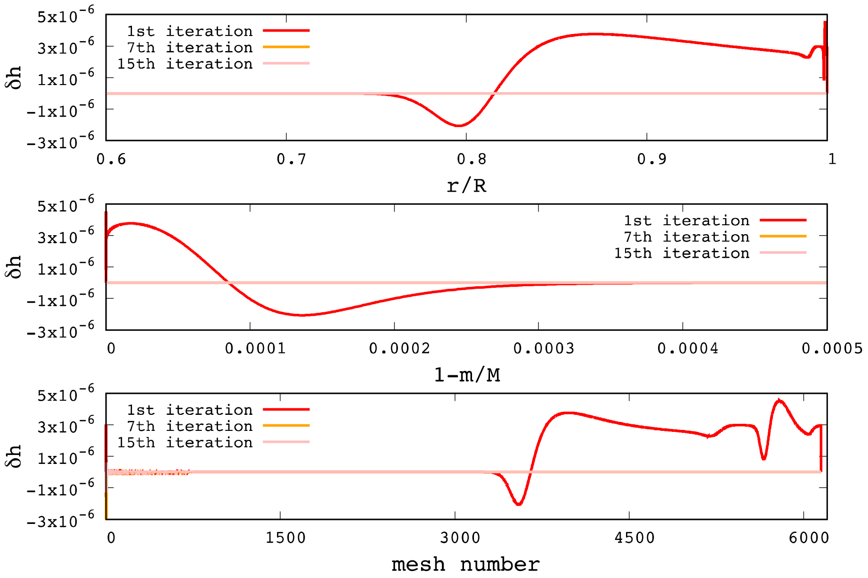

Figure 3.4: A series of deviations from the hydrostatic equilibrium δh iteratively obtained for just once perturbation in the hydrogen fraction. The same set of the parameters α, β, and m_c are used, as is in Figure 3.3, to describe the perturbation. It is evident that δh becomes smaller and smaller (red to pink) as the linear differential equation (3.23) is iteratively solved. Though it seems that δh obtained after the procedure has been iterated seven times (orange) is so small that it is almost totally overlapped with the fifteenth δh (pink), the seventh δh is quite large around the central region (0–50), which is the reason why we needed to iterate the procedure fifteen times to acquire the fifteenth δh.

3.3.2 A resettled model obtained for many-times perturbations; step 3 and 4

In the previous subsections, the numerical implementations of the developed scheme for computing stellar equilibrium models, where effects of the chemical composition modification (thought to be caused by, for instance, mass accretion) are taken into account, are demonstrated in detail, and the validity of the scheme for just-once perturbation has been confirmed. Then, the next thing to be done is to repeat the procedure until the envelope of the model is "significantly" modified compared with the unperturbed one; remember that it has been assumed that the modifications are small enough to be treated as a perturbation terms higher than the first order of which can be negligible.

This subsection is devoted to discussions about the validity of an envelope-modified model which is obtained by repeating the procedure (step 1 and 2) 10^4 times. The modification to the hydrogen fraction is the same on the course of the repetition, and it is given by the expression (3.24) with the following parameters: $\alpha = 10^{-4}$, $\beta = 0.0015$, and m_c=0.99976.

Is it in hydrostatic equilibrium?

It is possible, for instance, that numerical round-off errors which have propagated to be larger and larger during the iterative process lead to some problems in the obtained model. To check such

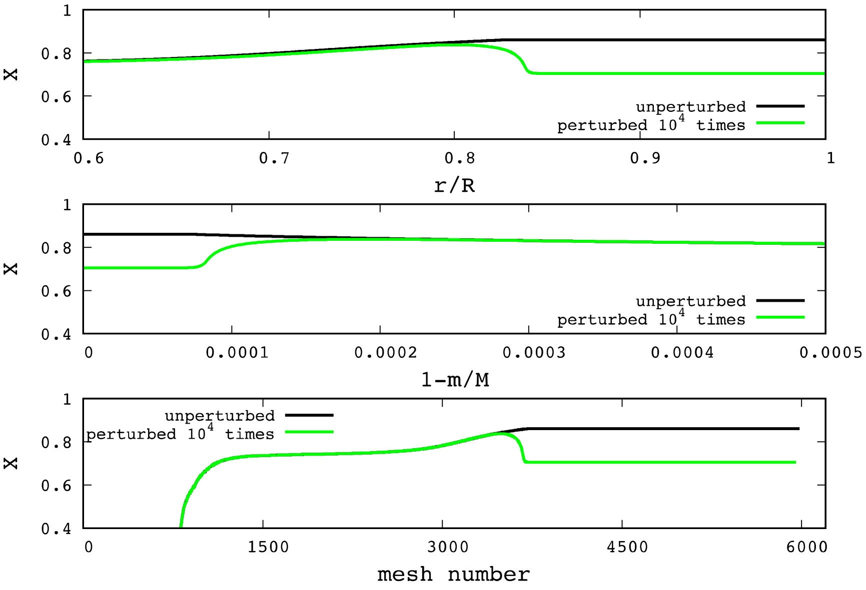

Figure 3.5: Hydrogen fractions for the envelope-modified model (green) and for the unperturbed model (black).

kinds of numerically arising problems, the deviation from the hydrostatic equilibrium δh of the model (obtained after 10^4 repetitions of the steps 1 and 2) is computed and it has been confirmed that δh is at most of the order of 10^{-6} which is almost the same as those for ordinary stellar models computed via MESA. The hydrogen fraction of the envelope-modified model is shown in Figure 3.5.

Toward thermal equilibrium

The envelope-modified model is in a hydrostatic equilibrium state, but it is, generally speaking, not in a thermal equilibrium state. This is because we adopt the assumption of the adiabaticity when the perturbed model is resettled; the timescale for the resettlement is thought to be the dynamical one, and the heat exchange is assumed to be negligible. To check whether the envelope-modified model is really in the thermal equilibrium state or not, we have to compute residuals between the right hand side and the left hand side of the set of the equations for stellar structure (3.1) to (3.4), and if necessary, we also have to resettle the model to the thermal equilibrium state. This can be done, for instance, by putting the model into the Newton-Raphson-style iteration module built in MESA (Paxton et al., 2011).

Figure 3.6 shows a result of such computations, namely, the envelope modified model is put into MESA, and the subsequent evolution is computed based on the Newton-Raphson method incorporated in the code. We see temporal changes of the rates of gravitational energy generation $\varepsilon_{\rm g}$, in units of erg/g/s, for the two models (note that the age of the modified model is fixed during the steps 1 to 4). The energy generation rate $\varepsilon_{\rm g}$ is related to the deviation from a thermal equilibrium

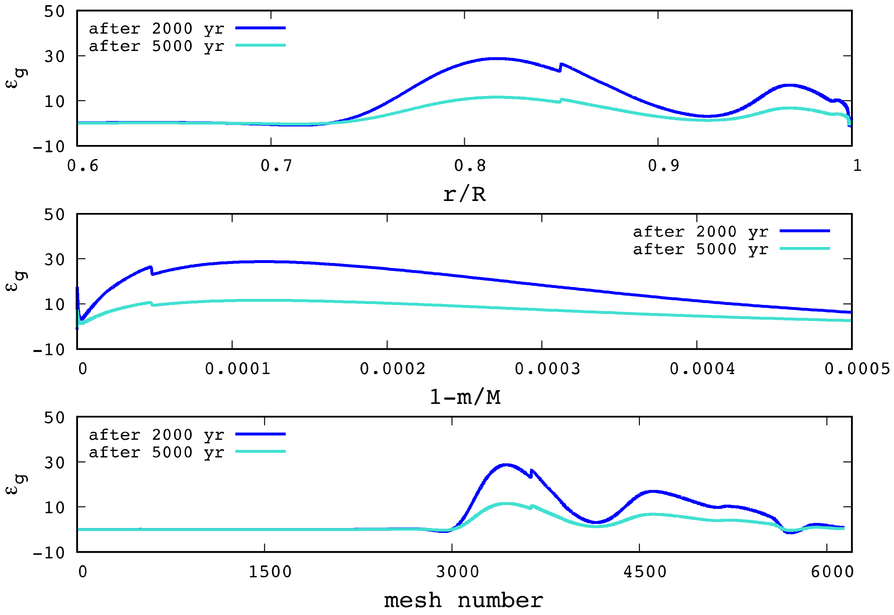

Figure 3.6: Time evolution of the rates of gravitational energy generation $\varepsilon_{\rm g}$ (see text for the definition) in the envelope of the model, after the envelope-modified model is put into MESA to compute the subsequent evolution. It is obvious that $\varepsilon_{\rm g}$ decrease as the model evolves, and additionally, it decreases linearly in terms of time, which enables us to roughly estimate the time scale for an envelope-modified model to regain the thermal equilibrium state.

state (see, e.g. Kippenhahn et al., 2012), and in MESA, it is defined as

$$\varepsilon_{\rm g} \equiv -T\frac{\partial s}{\partial t} = -c_p\frac{\partial T}{\partial t} + \frac{\delta}{\rho}\frac{\partial P}{\partial t}, \tag{3.25}$$

where c_p is the specific heat at the constant pressure, and δ is one of the thermodynamic quantities defined as below:

$$\delta \equiv \left(\frac{\partial \ln \rho}{\partial \ln T}\right)_{P,\mu}. \tag{3.26}$$

Roughly speaking, $\varepsilon_{\rm g}$ decreases linearly in terms of the time as the model evolves. Since typical values for $\varepsilon_{\rm g}$ are around 10^{-2} in the envelope of an ordinary stellar model, we have a crude estimate for the thermal relaxation time as a few million years, which corresponds to the thermal timescale of the stars in this mass range ($\sim 1.4 M_\odot$). Therefore, for the coming discussions from now on (especially in Chapter 4), we evolve the modified-envelope model for the thermal timescale to regain the thermal equilibrium state.

Comparison with a rather simple scheme based on MESA modules

As a final test of our developed scheme, we construct a rather simple scheme based on MESA modules which can, in a way slightly different from our scheme, compute internal structures affected

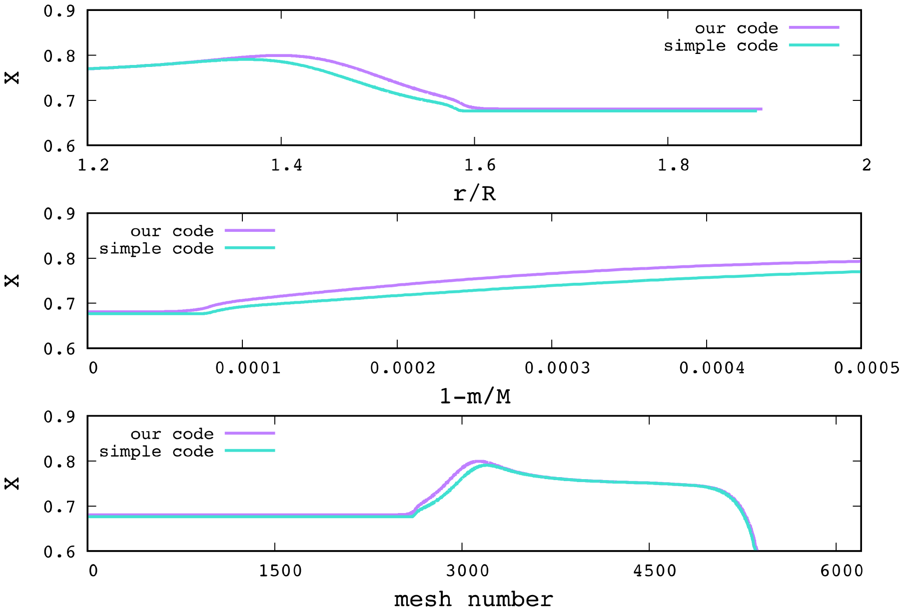

Figure 3.7: Hydrogen profiles of the modified envelope models obtained based on our scheme (purple) and the simple scheme described in the text (cyan) against three different horizontal axes, namely, the fractional radius (top), the fractional mass (middle), and the mesh number of the cell (bottom). Note that the fractional radius is normalized by not the radius of the corresponding model but the solar radius in order to emphasize a difference in the radii of the two models. It should be also noted that the mesh number is arranged from the surface to the center of the model. There does not seem to be a significant difference between the two envelope-modified models.

by chemical composition perturbations. Then, we compare the internal structures determined by our scheme and those determined by the simple one.

The simple scheme is constructed basically in the same way as described in the previous subsections 3.3.1 and 3.3.2. We prepare a stellar equilibrium model and perturb the envelope following the expression (3.24), and the perturbed model deviated from both hydrostatic and thermal equilibrium states are somehow resettled to new equilibrium states. In contrast to the scheme developed by us, where the hydrostatic equilibrium of the deviated model is first retained (by adding radial displacements) and secondly the thermal equilibrium is (based on the Newton-Raphson method equipped with MESA), the simpler scheme simultaneously allows the deviated model to be resettled to the hydrostatic and thermal equilibria by directly carrying out the Newton-Raphson method for the deviated model, which is relatively easy to implement; we just have to exchange the chemical compositions in a MESA input file from the unperturbed one to the perturbed one, put the file in MESA, and run evolutionary calculation, again and again.

Figures 3.7 and 3.8 compare some of the structural variables obtained with our scheme and those obtained with the simpler scheme. Global stellar parameters for the unperturbed model are $M = 1.36M_{\odot}$, $Y_{\mathrm{init}} = 0.250$, $Z_{\mathrm{init}} = 0.002$, and $f_{\mathrm{ovs}} = 0.027$. The age is determined to reproduce the mean ΔP_{g} which is about 2050 s. The parameters for one chemical composition perturbation are as follows: $\alpha = 5 \times 10^{-4}$, $\beta = 0.001$, and $1 - m_{\mathrm{c}}/M \sim 4 \times 10^{-9}$. The perturbation is added two hundred

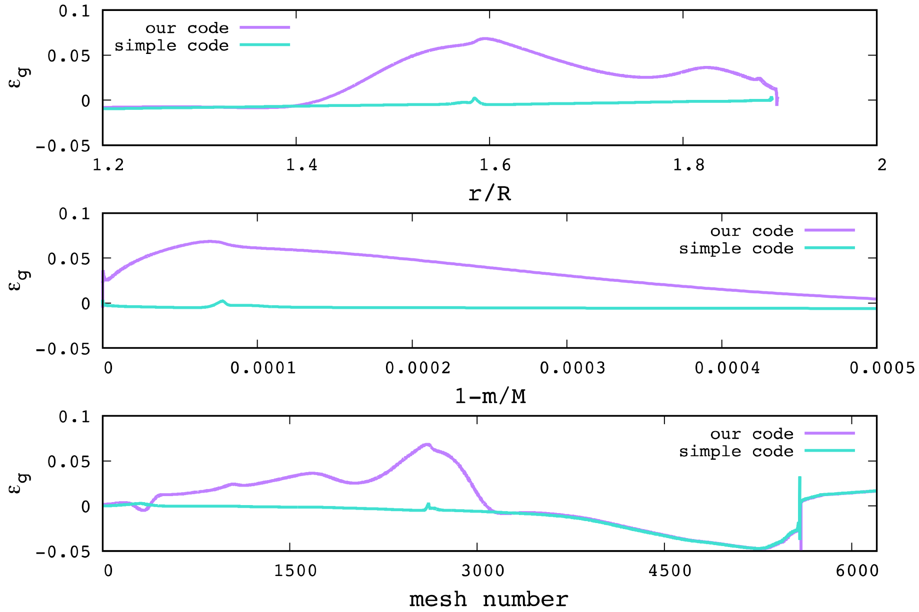

Figure 3.8: Rates of gravitational energy generation ε_g of the envelope-modified models obtained based on our scheme (purple) and the simple scheme described in the text (cyan). The meanings of the horizontal axes are the same as in Figure 3.7. Both models have evolved, in total, 2 Myrs from the same age of a certain (unperturbed) equilibrium model to retain thermal equilibrium state. It is obviously seen that the envelope-modified model computed based on our scheme requires, though quite small (see, for instance, Figure 3.6), some more time to resettle to the thermal equilibrium states.

times. In the case of the simple scheme, the perturbed chemical composition is put into MESA (for carrying out the Newton-Raphson method to obtain the corresponding envelope-modified model) and the model has evolved for 10,000 years every perturbation; a series of envelope-modified models are always in the thermal equilibrium states, which is different from an approach taken in our scheme where the model perturbed two hundred times is resettled to the thermal equilibrium at once (by evolving the model for $200 \times 10,000 = 2\,\mathrm{Myr}$ via MESA).

Although the chemical composition perturbation at once is set to be the same, the hydrogen profile is slightly different from each other (see Figure 3.7). This is partly because the parameter m_c gradually changes as iteration proceeds in the case of the simpler scheme, i.e. the chemical composition perturbation is accordingly different. We nevertheless see a resemblance in the way the hydrogen profiles are modified in the envelopes between the two schemes. Such similarity can be found also in the rates of the gravitational energy generation in a relatively deep region (deeper than $r/R < 1.4$, see the top panel of Figure 3.8), though the envelope region (deeper than $r/R > 1.4$, see the top panel of Figure 3.8) of which exhibits a significant difference, showing that it is necessary for us to evolve the envelope-modified model computed by our scheme for a while to realize its thermal equilibrium state. However, the deviation from the thermal equilibrium state itself is quite small (see Figure 3.6).

In any case, we do not see a significant difference in the outputs of the two schemes, and thus,

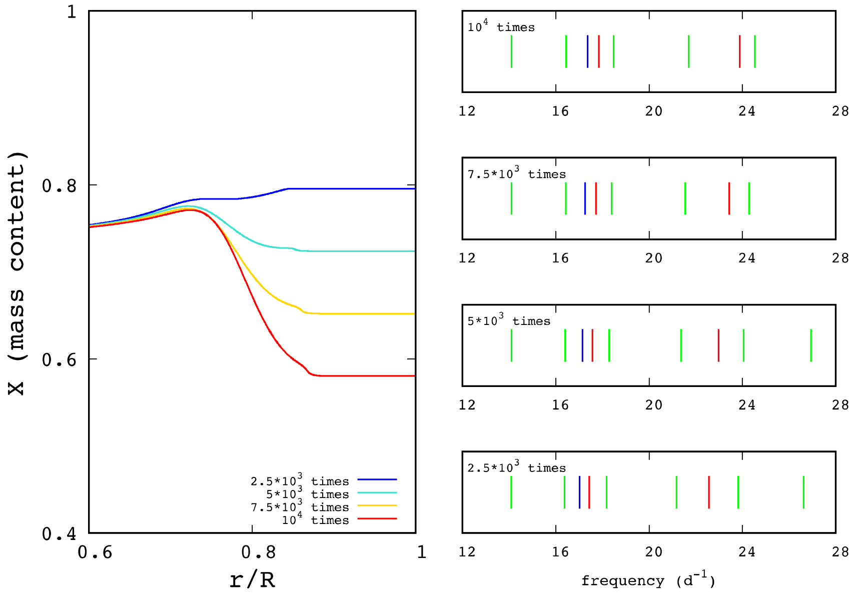

Figure 3.9: Modified hydrogen fractions (left) and the corresponding eigenfrequencies (right). The envelope-modified models (left) are obtained after 2500 (blue), 5000 (turquoise), 7500 (gold), and 10^4 (red) times perturbations. The hydrogen abundance decreases more as the envelope is perturbed more. P-mode eigenfrequencies for radial modes (blue), dipole modes (red), and quadrupole modes (green) are shown in the right panels because the modification of the envelope should mainly affect not the g-mode cavity but the p-mode cavity, leading to the frequency variations for p modes. As expected, the more the envelope is modified, the more the eigenfrequencies is shifted.

our scheme can be validated in this respect as well. Finally, it should be instructive to mention that the whole computation time to obtain a modified model is slightly smaller for our scheme, suggesting a slight advantage of using our scheme. In addition, our scheme allows us to purposely compute stellar structures not in thermal equilibrium states, which might be too rare for us to observe in reality, but is valuable at the same time as later discussed in Subsection 4.2.3 where the possibility of KIC 11145123 being out of the thermal equilibrium states is tested with our scheme.

3.4 Frequency calculation for envelope-modified models

This section is partly independent from the preceding ones, and there is no additional prescriptions for the scheme to be shown. Instead, eigenfrequencies of an envelope-modified model which is in the hydrostatic and thermal equilibrium states are presented because to compute the frequencies is one of the most prominent ingredients for carrying out asterosesimic modeling as is described in Chapter 4.

The basic settings for the eigenfrequency calculation follows. First, we prepare an unperturbed model. The mass and the initial helium abundance is $1.30M_{\odot}$ and 0.260. The metallicity is 0.003, and it is unaltered during the envelope-modifying modeling. The age of the model is determined

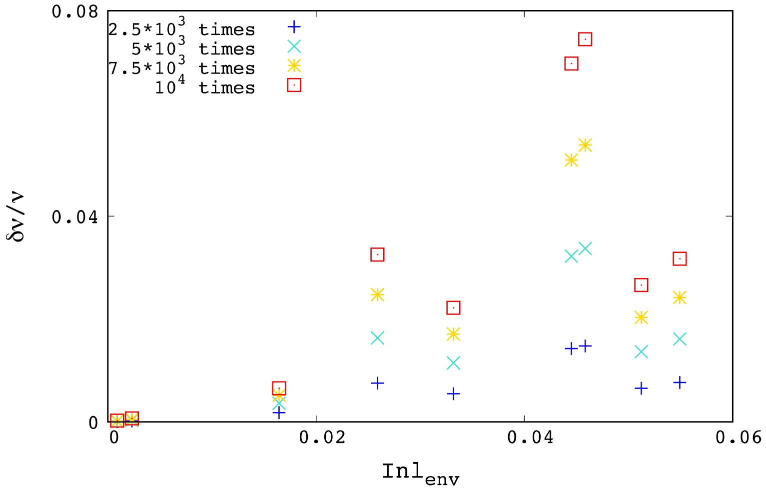

Figure 3.10: Relative frequency variation, defined as $\delta \ln \nu_{ij} = (\nu_{ij} - \nu_{0j})/\nu_{0j}$, against the corresponding envelope mode inertia, defined as $I_j^{\rm env} = \int_{\rm env} \rho |\boldsymbol{\xi}_j|^2 dV$. The indices i and j stand for a model modified with a certain extent (2500, 5000, 7500, or 10^4 times) and a particular mode, respectively. The unperturbed model is designated with $i = 0$. The envelope mode inertia is computed by integrating $\rho |\boldsymbol{\xi}_j|^2$ in a part of the envelope determined by us before hand (here, the envelope is defined as a region $r/R > 0.7$). Note that the total mode inertia (obtained by carrying out the integration throughout the model) is normalized to be $1/4\pi$. Rough proportionality of the relative frequency variation with respect to the extent of modification and the envelope mode inertia can be confirmed.

based on the asymptotic value of the $\Delta P_{\rm g}$ (see the definition in Chapter 2), and the evolutionary calculation is stopped when $\Delta P_{\rm g}$ (computed with the Brunt-Väisälä frequency of the model) is 2100 s. The extent of overshooting $f_{\rm ovs}$ (see Chapter 2) is set to be 0.014. The diffusion process is activated. The default settings in MESA are used for the other prescriptions. Then, the envelope-modifying scheme is applied to the model, with the modifications parameterized as $\alpha = 10^{-5}$, $\beta = 5 \times 10^{-6}$, and $m_{\rm c} = 0.99976$. The modification is added to the unperturbed model 10^4 times, and models perturbed 2500, 5000, 7500, and 10^4 times are preserved for calculations of the eigenfrequencies. The calculation of eigenfrequencies is via GYRE (Townsend and Teitler, 2013), which is a linear adiabatic oscillation code.

The results of the computations are presented in Figure 3.9. We clearly see that the hydrogen is less abundant as the envelope is modified more. The eigenfrequencies for the models (see the right panels in Figure 3.9) are also varying as we perturb the envelope more. Interestingly (and importantly), the amounts of the frequency variations are, roughly speaking, proportional to the amounts of the modification, though the dependence should be non-linear. In addition, the amounts of the frequency variations are different from mode to mode, which is readily confirmed when we see the right panels in Figure 3.9 (compare, for instance, the blue one and the red ones). To see relations between the amounts of frequency variations and the mode properties more clearly, we plot the relative frequency variation against the corresponding (envelope) mode inertia (normalized by the total mode inertia which is here fixed to be $1/4\pi$) in Figure 3.10 because the ratio between an envelope mode inertia and the total one contains information on which part of the star the mode mainly propagates. It is seen that, for an envelope mode inertia, the relative frequency variation is proportional to the extent of modification. We can also see that, for an extent of modification, the relative frequency variation is roughly proportional to the envelope mode inertia, which is understandable because the chemical composition modification in the envelope does not affect properties of a mode if the mode does not have sensitivity (which is represented by the envelope mode inertia) in the modified envelope. These properties are to be utilized in the following section 3.5 and in the forthcoming Chapter 4 where asteroseismic non-standard modeling of one of the Kepler targets, KIC 11145123, is performed.

3.5 The case of KIC 11141523

Why do we need the newly developed scheme for computing stellar models whose envelope is modified but otherwise is in a hydrostatic and thermal equilibrium states? The answer is simple; because such modified envelope structures are believed to be rather common for some types of stars as blue straggler stars (see Subsection 1.1.2) which are thought to have experienced some interactions with other stars. In this final section, a case study of non-standard modeling of one of the Kepler target KIC 11145123, which is spectroscopically a blue straggler, is presented based on our scheme described in the previous sections. Information on KIC 11145123 (the amplitude spectrum, the observed eigenfrequencies, and so on) and the backgrounds of asteorseismic studies of the star can be found in Section 1.3.

Before discussing the non-standard modeling of the star, we would like to emphasize one issue concerning the understanding of the star; the initial helium abundance of the equilibrium model of the star is suggested to be $Y_{\rm init} > 0.30$ which is too high for an ordinary single star (Kurtz et al., 2014; Takada-Hidai et al., 2017) considering the helium abundance of the primordial gases in the current Universe. Though there have recently a number of reports on the existence of stars having $Y \sim 0.40$ in some globular clusters (Bastian and Lardo, 2018) (they are somewhat tentatively believed to be the second generation of stars born from gasses expelled from asymptotic giant branch), we rely on the spectroscopic analyses carried out by Takada-Hidai et al. (2017) and assume that KIC 11145123 is not such a second generation star but a blue straggler star which was born as a single star with an ordinary initial helium abundance and later experienced some interactions with other objects. Then here is one question. Can we construct an alternative stellar equilibrium model of the star whose initial helium abundance is relatively low and whose envelope is modified? This question is closely related to the formation history of the star, and thus, to find an answer to the question is a primary goal in this section.

3.5.1 Fitting procedure

Based on our assumption that the star was born with relatively low initial helium abundance ($\sim$ 0.260) and experienced some interactions with other stars later at some point during the evolution, we carry out asterosesimic and non-standard modeling of the star with two procedures. First, a stellar model with typical initial helium abundance is computed assuming single-star evolution. This model is fitted to reproduce the mean value of the observed g-mode period spacings of the star $\Delta P_{\rm g} \sim 2050\,{\rm s}$. Let me call this model as the "candidate model." Secondly, we modify the envelope of the candidate model to obtain multiple envelope-modified models with different values for the parameters describing the modification (see the equation 3.24). For each modified model, the p-mode frequencies of the model are computed via GYRE, and we compare those with the observed p-mode frequencies, letting models reproducing the observation best be the best model for the star.

A few procedures to carry out asteroseismic and non-standard modeling are given in this subsection. Specific settings are the same as explained in Subsection 2.4.2.

Parameter range

We have two sets of parameter range, one for the first procedure (constructing candidate models) and the other for the second procedure (seeking for the best model among modified-envelope models).

The first set of parameter range consists of four (essentially three, excepting the age) variables, namely, mass M, initial helium abundance Y_{init}, the extent of overshooting f_{ovs}, and age (represented by ΔP_{g}) of the model, and the ranges are determined as follows: 1.36–1.44$M_{\odot}$, by 0.02$M_{\odot}$, 0.24–0.27, by 0.01, 0.023–0.027, by 0.0002, and 2050 (fixed, observed value), respectively. The initial metallicity Z_{init} is fixed to be 0.003 (Takada-Hidai et al., 2017). The mass range is chosen following that of the best model of Takada-Hidai et al. (2017) which is 1.4$M_{\odot}$. The range for the extent of overshooting is selected based on the discussion in Chapter 2. The initial helium is limited to relatively low values because of our assumption as mentioned in the first sentence of Subsection 3.5.1.

The second set of parameter range comprises three variables. They are m_{c} (representing the depth of the modification), α (representing the width of the transition region between the unmodified region and the modified one), and the number of modifications added to a candidate model, the former two of which are in the equation (3.24). In practice, the depth parameter is expressed in not m_{c} but r_{c} (fractional radius) to help intuitively understand the position of the depth, and we choose four values for r_{c} (0.67, 0.70, 0.73, and 0.76). For α, we choose eight values ranging from 10^{-7} to 10^{-3}, and the number of modifications added to a candidate model is 600, and envelope-modified models are retained every five modifications. The parameter β in the equation (3.24) is fixed to be 5×10^{-4}.

Specific procedures

At first, candidate models are obtained for each set of mass, the initial helium abundance, and the extent of overshooting in the parameter range by stopping the evolutionary calculations when ΔP_{g} of the model reaches the observed value of 2050 s. Because ΔP_{g} monotonously decreases as the star evolves, there must, in principle, be a certain evolutionary stage at which ΔP_{g} is identical to the observed value. Then, the candidate models are evaluated based on a comparison between the p-mode (actually some of them are mixed-mode) frequencies of the candidate models and the observed ones. As we see in Section 3.4, the amount of the frequency variations are almost linearly proportional to the extent of the modification and the envelope mode inertia (normalized by the total mode inertia fixed to be $1/4\pi$) Therefore, though we need to have some assumptions on the mode identification, we can roughly prospect which frequencies can be fitted to the observed ones before we actually carry out the envelope-modifying scheme. More specifically, the radial-mode frequency differences between the candidate models and the observation are used as a standard measure, based on which and also on the radial-mode energy density, the theoretically expected deviations can be estimated for all the other modes. Comparison between the theoretically expected deviations and the observed ones enables us to choose which candidate models are appropriate candidates for

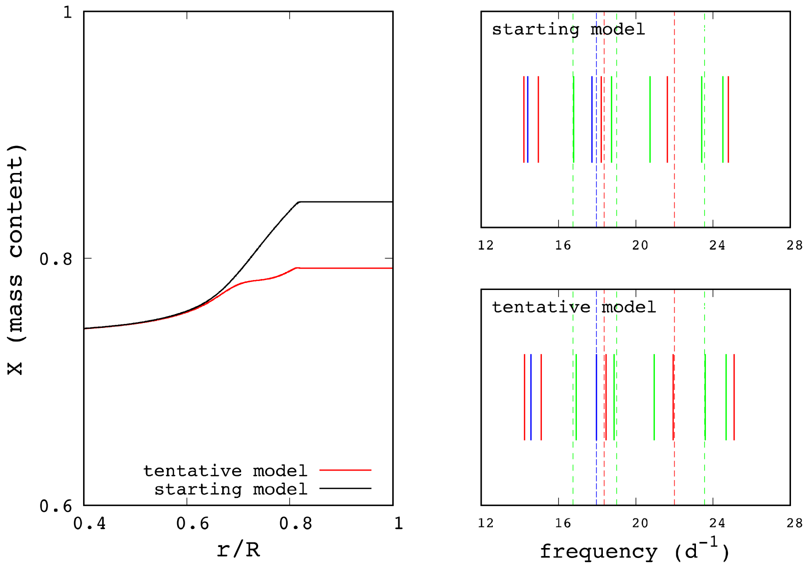

Figure 3.11: Hydrogen fractions for the candidate model (black curve in the left panel) and that for one of the best models obtained via the scheme described in text (red curve in the left pane.) The right column shows the corresponding eigenfrequencies (for high-frequency region $\sim 20\,\mathrm{d}^{-1}$) for the candidate (upper) and that for the best model (lower). The observed frequencies of the star are represented by dotted lines, where radial, dipole, and quadrupole modes are expressed by blue, red, and green lines, respectively.

further envelope-modifying modeling. Several candidate models are chosen in this first procedure.

In the second procedure, the envelopes of the chosen candidate models are gradually modified changing the parameters described in the preceding small subsection. For every five modifications, the eigenfrequencies of the corresponding envelope-modified model are computed via GYRE. This step has been repeated with different sets of parameters in the determined parameter range. Among the envelope-modified models thus calculated, ones reproducing the observed frequencies best are selected as the best models.

3.5.2 Results

As a result of the asteroseismic and non-standard modeling of the star demonstrated in the last small subsection, we obtain a few best models, one of which is discussed below. The model has the following parameters: $1.38M_\odot$, $Y_\mathrm{init} = 0.26$, $f_\mathrm{ovs} = 0.023$, and $r_\mathrm{c} = 0.70$. Figure 3.11 shows the hydrogen fraction (bottom left) and the eigenfrequencies (bottom right) of the model. It is seen that the frequencies of the candidate model (starting model in Figure 3.11) are shifted much closer in frequency to the observed ones by modifying the envelope (tentative model in the figure). Note that the observed frequencies are represented by dotted lines, and that radial, dipole, and quadrupole modes are expressed by blue, red, and green lines, respectively.

Figure 3.12 compares the frequencies of the tentative model and those of Kurtz et al. (2014),

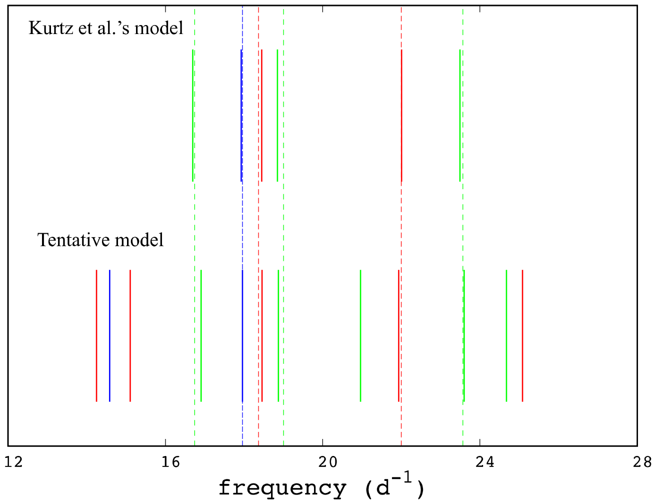

Figure 3.12: Modeled eigenfrequencies, of the previous model of the star of Kurtz et al. (2014) (upper) and those of the tentative model obtained in the previous section, are compared with the observed p-mode frequencies of KIC 11145123 (dashed lines). The meanings of the colors and the types of the lines are the same as those in Figure 3.11.

showing that we have succeeded in constructing an equilibrium model with the non-standard scheme which reproduced the observed p-mode frequencies essentially as precisely as the pervious one. The important point is that this is the first case where such non-standard scheme has been applied to carry out asteroseismic modeling of the star, and the results favor the scenario in which the star was born with an ordinary helium initial abundance and then experienced the envelope modification.

3.5.3 Discussions

The envelope modified model reproduces the observed p-mode frequencies reasonably well compared with the previous model of Kurtz et al. (2014) as we see in the last subsection. Then, how different are the structures of the two models? We especially focus on internal structures, namely, the density and the sound speed, of the models in this subsection. For simplicity, let us denote the previous model of Kurtz et al. (2014) as M_{Kz} and the envelope-modified model as M_{mod} in the following small subsections.

Structures of deep regions

Because both of the models are fitted to reproduce the mean value of the observed ΔP_{g}, it is immediately expected that the structures of a deep region should be almost the same when we compare those of M_{Kz} and M_{mod}. However, as it is discussed in Subsection 2.4.4, there exists, for example, the mass-dependence of the ΔP_{g} patterns, and we have to be aware that the core properties can be different. This is actually the case where the stellar masses of M_{Kz} and M_{mod} are $1.46 M_{\odot}$ and $1.38 M_{\odot}$; though the difference in mass seems to be small, it certainly affects the size of the convective cores (see Figure 3.13, the convective boundaries are indicated as positions at where

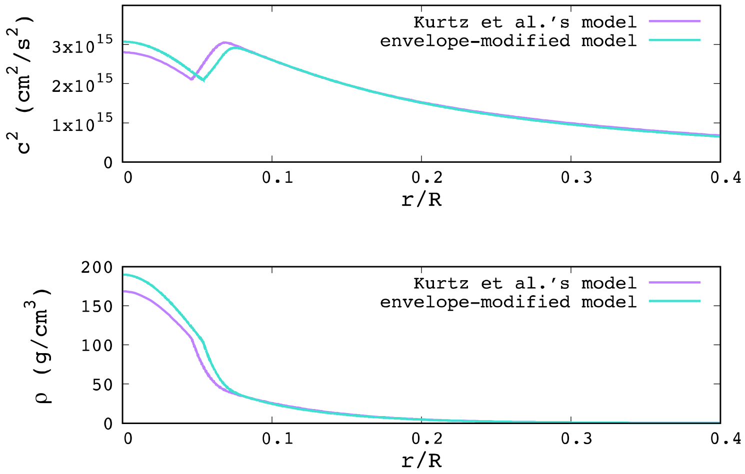

Figure 3.13: Comparisons of internal structures (the sound speed, top, and the density, bottom) of the two models M_{Kz} and M_{mod} focusing on the deep region. Due to slight differences in global parameters such as mass and the initial metallicity, the sizes of the convective core, whose boundaries can be confirmed as positions at which the gradients of the structural parameters abruptly change ($r/R \sim 0.05$), are different.

the gradient of the sound speed abruptly changes). We confirm a similar mass-dependence when we see Figure 2.18 in which $1.30M_{\odot}$ model has a larger convective core compared with $1.50M_{\odot}$ model does. Note that there is no significant difference in the g-mode frequencies of the two models even though the detailed structures are slightly different as exhibited in Figure 3.13. This is because the g modes considered for KIC 11145123 are high-order modes and they are not as sensitive to the detailed structures in deep regions as lower-order modes are. In other words, there are moderate degeneracies among the parameters in terms of the ΔP_{g}.

Structures of envelope regions

In this small subsection, we focus on envelope structures of the models M_{Kz} and M_{mod} which are generally considered to be relevant to p-mode frequencies. Figure 3.14 shows the density and the sound speed of the two models as Figure 3.14, but those in the envelopes in this case. It is quite evident that envelope structures of one model are similar to those of the other model, supporting the fact that the modeled p-mode frequencies are almost the same as seen in Figure 3.12.

Combined with the discussions in the preceding small subsection, we are also able to explain the reason why there are larger difference in the modeled $l = 2$ mode frequencies (green ones in Figure 3.12) compared with the other p-mode ones ($l = 0, 1$, blue, red ones in Figure 3.12) between the models M_{Kz} and M_{mod}. The point is that the $l = 2$ modes are mostly mixed ones and that they propagate both in the deep radiative region and the envelope. Therefore, if the deep radiative region is modified (e.g., fixing the mean value of the ΔP_{g}) while the envelope is fixed, the balance between the two region changes, causing mixed-mode frequencies to vary, which is the case for the

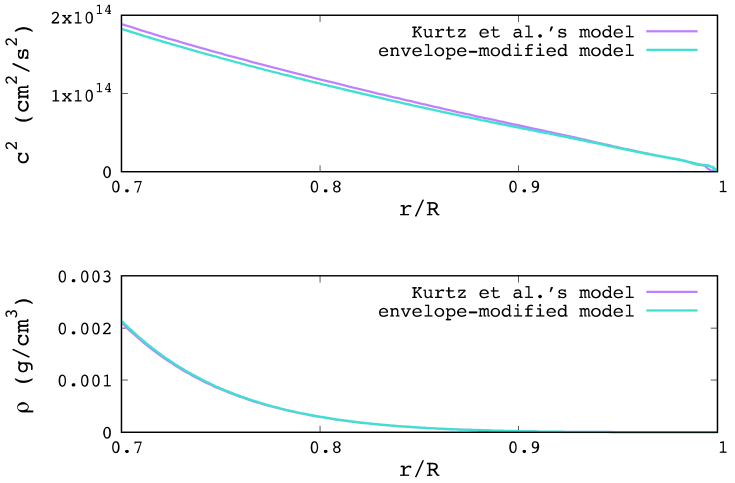

Figure 3.14: Comparisons of internal structures (the sound speed, top, and the density, bottom) of the two models $M_{\rm Kz}$ and $M_{\rm mod}$ focusing on the envelope. There seems to be little difference in the envelope structures of the two models.

two models.

3.6 Other applications of the developed scheme

This section is mostly independent of the previous themes discussed so far, and a part of the non-standard scheme developed by us is re-considerred based on perspectives different from the ones in the preceding sections. We in particular concentrate on one useful function implemented in the scheme, that is, to resettle models deviated from the hydrostatic equilibrium states. Below are two subsections briefly demonstrating the possibility of some applications of the resettling function which may be further extended in the future studies.

Reestablishing hydrostatic states

The first example is related to models computed via any 1-dimensional ordinary stellar evolutionary codes. Even though we do not perturb such ordinary stellar models, any of the models are intrinsically deviated from the hydrostatic equilibrium states, because of numerical limitations; what we actually solve in stellar evolutionary calculations is not the set of non-linear differential equations but the set of non-linear difference equations, inevitably leading to numerical errors caused by the discreteness. It is usually the case that some iterative strategies are taken to solve such a set of non-linear difference equations and some criteria are set to decide when to stop the iteration process. Obviously, as we set stricter criteria, deviations (defined, for instance, as the sum of differences between righthand side and lefthand side of each difference equation) become smaller. There is,

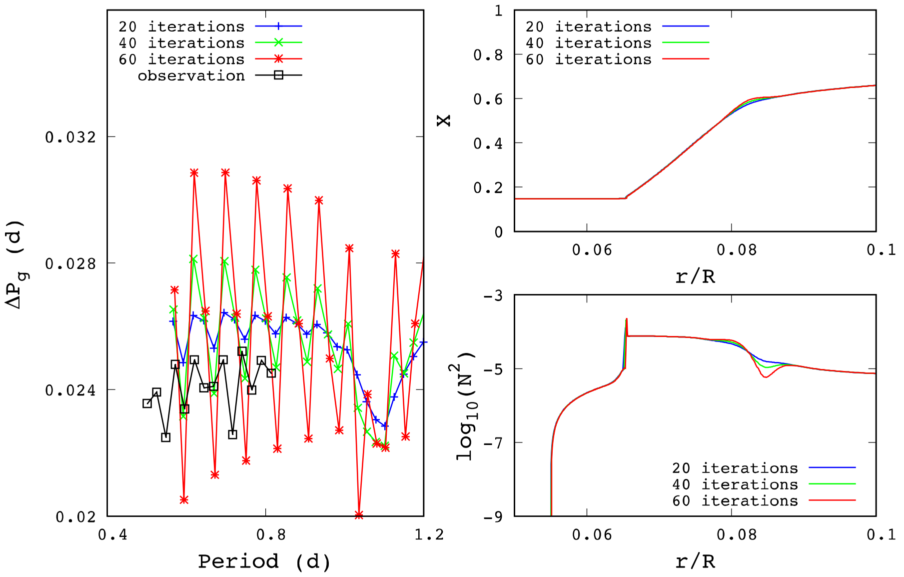

Figure 3.15: Numerically computed ΔP_{g} patterns (colored curves) and the observed ΔP_{g} pattern (black) are shown in the left panel. The corresponding internal structures, namely, the hydrogen profiles and the Brunt-Väisälä frequencies are illustrated in the right upper panel and the right lower panel, respectively. The degree of perturbation becomes larger in the order of blue, green, and red, and correspondingly, an amplitude of an oscillatory component of a numerically computed ΔP_{g} pattern becomes larger. We can confirm that the chemical composition gradient is successfully steepened with our scheme (see the hydrogen profiles or the Brunt-Väisälä frequencies at $r/R \sim 0.08$).

of course, a trade-off because stricter criteria for iteration should lead to a longer computation time. From that point of view, the resettling function in our scheme could help render deviations smaller with less computation time than other existing stellar evolutionary codes. Since such deviation demonstrated above should also affect frequency computations, it is fairly instructive for us to check the relation between deviations and computed frequencies for a range of stellar models in terms of mass, initial chemical compositions, and stellar evolutionary stages, in the near future.

Realizing steeper chemical composition gradients

The second example is related to oscillatory behaviors of the ΔP_{g} patterns deeply discussed in Chapter 2. We here revisit the observed ΔP_{g} pattern of KIC 11145123. As it is demonstrated in Subsection 2.4.4, one possible approach to reproduce the shorter-period components of the observed ΔP_{g} pattern is to add artificial perturbations in the Brunt-Väisälä frequency δN^2 (see Figure 2.19). However, the perturbation δN^2 is not physically motivated one and we do not know whether such structures are really feasible inside stars or not. There is thus room for us to consider more physically motivated perturbations to the Brunt-Väisälä frequency, which can be achieved by the resettling function as shown in the following paragraphs.

Figure 3.15 illustrates ΔP_{g} patterns which are numerically computed based on the perturbed

Brunt-Väisälä frequencies of the stellar models obtained using the resettling function; they are in both hydrostatic and thermal equilibrium states. In order to obtain the perturbed models, we perturb the deep radiative region, instead of the envelope as in the previous sections, so that the chemical composition gradient becomes steeper (for reasons why we focus on the chemical composition gradients, see discussions in Chapter 2), and then, the deviated models are resettled to hydrostatic states with our scheme (see details in Subsection 3.3). It is clearly seen that our scheme successfully provides us with the equilibrium stellar models with the chemical composition gradients much steeper than that of the unperturbed model. It is also verified that an amplitude of the shorter-period component of a numerically computed ΔP_{g} pattern becomes larger as the model is perturbed more (from blue to red in Figure 3.15). As such, our scheme (especially the resettling function) is also of great use for purposes other than carrying out the non-standard modeling of stars.

3.7 Summary of this chapter

A novel scheme for computing 1-dimensional stellar models whose chemical compositions in the envelope are modified has been established based on formulations of the stellar radial oscillation. The scheme has been validated with simple numerical tests for each step, and it has been applied to the coarse-grid-based modeling of KIC 11145123 to find models reproducing the observed $\overline{\Delta P_{\mathrm{g}}}$ and radial-mode frequency. We have successfully obtained a model which is comparable to the previous model of the star computed assuming a single-star evolution. Therefore, the result of the "rough" non-standard modeling suggests the possibility that it is possible to construct a stellar model of the star which was originally born as a single star with an ordinary initial helium abundance of ~ 0.26 and then experienced some modifications in the envelope. This is the first time that such an envelope-modified model is calculated for the star, and the result is consistent with the formation scenario of the star which is spectroscopically a blue straggler, motivating us to carry out the non-standard modeling of the star with the developed scheme in a more systematic and thorough way as described in Chapter 4. Finally, two applications of a part of our scheme, namely, the function resettling deviated models, are shown, demonstrating the high potential of the scheme developed by us in a broader context of stellar physics.

Chapter 4

Asteroseismic analyses of KIC 11145123

The asterosesimic study of KIC 11145123 is of great importance as described in the previous chapters 1 to 3 in various contexts such as the investigation of chemical composition gradients in the deep radiative region of low-mass (1.2–2.1$M_\odot$) main-sequence stars (e.g. in Subsection 1.1.1), the asterosesimic modeling of hybrid pulsators for calibrating the existing schemes in 1-dimensional stellar evolutionary codes (e.g. in Subsection 1.2.3), the study of the formation history of blue straggler stars (e.g. in Subsection 1.1.2), and the inversion analysis to infer internal rotation profiles of stars (e.g. in Subsection 1.2.3). Numerous other examples can be found throughout this dissertation.

In this chapter, we have two primary goals; one is to understand the formation history of the star more, and the other is to infer the internal rotation of the star. We first articulate the motivation for the two goals and subsequently present a brief review on what we have learned so far about the star in Section 4.1. A thorough and systematic strategy is then taken to obtain a best model of the star based on the scheme of the non-standard modeling developed by us (section 4.2). Considering the obtained model as a reference model, we perform rotation inversion to infer the internal rotation profile of the star (section 4.3). The final section is dedicated to comprehensive discussions about the internal physics of the star based on the results we have obtained in this dissertation.

4.1 A brief introduction

4.1.1 Motivation

Though the previous asteroseismic sudies of KIC 11145123 have provided us with a number of fascinating results concerning the interior of the star and the evolutionary stage the star is in, there are, of course, also several issues remained to be solved (see Section 1.3).

The most prominent issue among them is that there has never been an attempt to calculate a 1-dimensional equilibrium model of the star based on the assumption that the star was born as an ordinary star with a relatively low initial helium abundance of e.g. ~ 0.26, then experienced some interactions with other stars during the evolution, and ended up with a chemically modified envelope. Because the spectroscopic analyses (Takada-Hidai et al., 2017) indicate the star to be a blue straggler star (see Subsection 1.1.2), there is room for us to take into account such a non-standard treatment. This may not only solve the problem that the previous models of the star constructed based on the assumption of single-star evolution cannot reproduce the observed p-mode frequencies well (see Subsection 1.3.3), but also lead to a better understanding of the formation history of the star, i.e. if we succeed in calculating a asterosesimically better model than the previous ones in a non-standard way, a formation scenario of the star via, for instance, binary interactions is favored. This is the reason why we attempt to carry out the asterosesimic and non-standard modeling of the star, and the goal of this investigation is to obtain a hint for the formation history of the star.

The issue mentioned in the last paragraph is also relevant to another issue on a possible existence of the fast-core rotation of the star (Hatta et al., 2019). The inference of the convective-core rotation is strongly dependent on where rotational splitting kernels of mixed modes have sensitivity inside the star (see Subsection 1.3.2), which can vary for an alternative model of the star obtained in a non-standard way. Therefore, resultant inferences can be also different to some degree from those of Hatta et al. (2019). This is the reason why we again perform rotation inversion for the new alternative model, and the primary goal is to discuss the presence of the fast-core rotation.

4.1.2 The physical properties of the star so far known

Before starting specific discussions on the non-standard modeling and the rotation inversion of the star, we present a brief summary of the current understanding of the star focusing on the physical properties, which should be helpful for readers to roughly grasp the star.

According to the spectroscopic study of the star (Takada-Hidai et al., 2017) with Subaru/HDS, the effective temperature of the star, the logarithm of the surface gravitational acceleration, the metallicity, and the radial velocity are $T_{\rm eff} = 7600\,{\rm K}$, $\log g = 4.2$ (cgs units), $Z = 0.003$, and $-135.4\,{\rm kms}^{-1}$ respectively. The study also suggested that the star is spectroscopically a blue straggler star, based on the surface abundance pattern. The eigenfrequency analysis results in the detections of multiple peaks in the amplitude spectrum which consists of low-order p, high-order g, and low-order mixed modes (Kurtz et al., 2014), thus showing that the star is a δ Sct and γ Dor hybrid pulsator. Phase modulation analysis (Murphy et al., 2016) mostly disfavors the possibility that the star is a member of a binary system. Recently, kinematical analysis of the star based on the Gaia observation has revealed that the star belongs to the thick disc population (Murphy 2019, private communication).

The tentative models of the star computed assuming single-star evolution favor relatively low masses around $1.4 M_{\odot}$, and thus, the models have a convective core, a deep broad radiative region above, and a thin outermost convective layer. The models also prefer fairly high initial helium abundances of > 0.30 and they are at a TAMS stage (the star has almost exhausted the hydrogen around the nuclear burning convective core).

Frequency splitting is detected for the star, based on which the following features have been indicated: that the star is rotating almost rigidly with the rotation period of ~ 100 d and the envelope of the star rotates slightly faster than the deep radiative region (Kurtz et al., 2014), that the convective core might be rotating around 5 times faster than the other regions of the star (Hatta et al., 2019), that there is latitudinally differential rotation detected with significance more than 2σ (Hatta et al., 2019), and that the star is less oblate than expected from its rotational velocity (Gizon et al., 2016).

For more detailed information, see Section 1.3.

4.2 Non-standard modeling of KIC 11145123

Non-standard modeling of the star is discussed in this section. For computations of stellar structure and evolution, the 1-dimensional stellar evolutionary code MESA (version 9793) is utilized. The default settings of MESA (see, e.g. Paxton et al., 2011) are used unless we explicitly mention otherwise in the text. In our non-standard modeling, modifications to the chemical compositions are added to stellar models computed by MESA maintaining the hydrostatic and thermal equilibrium states. The basic concepts and the numerical scheme to carry out such envelope-modifying modeling are demonstrated in detail in Chapter 3. Eigenfrequencies of stellar equilibrium models are computed via linear oscillation code GYRE. The effects of rotation, magnetic fields, asphericity, and nonadiabaticity on the eigenoscillations of a certain model is not taken into account; these effects are considered to be significantly small for the star and there is no observational hint for the effects (e.g. Kurtz et al., 2014).

We basically follow the same procedures as adopted in Section 3.5 to perform non-standard modeling of the star, namely, candidate models are at first constructed via MESA assuming single-star evolution to reproduce the observed g-more period spacings, and then, the chemical compositions in the envelopes of the candidate models are modified with the scheme developed by us to fit the observed p-mode frequencies while fixing the deep region not to affect the g-mode period spacing already fitted in the first step. One major difference is parameter ranges surveyed for the grid-based modeling; the parameter range is chosen based on those of the previous models (e.g. Kurtz et al., 2014) in Section 3.5, but a broader parameter range is to be surveyed in this section in a more systematic way in order to find a model of the star which reproduces all of the observables as well as possible.

Finally, before going into details, we would like to clarify some physics behind the non-standard modeling. We assume that the star is (or, used to be) in a binary system and that certain amounts of mass has been accreted on the star for a while during the evolution, which was not such a violent event that only structures in the envelope have been affected. We adopt the framework described above based on the fact that the envelope of the star is rotating slightly faster than the deep radiative region is; we attribute the cause of the faster-envelope rotation to mass accretion from the outside. Another reason for the framework is the seemingly ordinary behavior of the observed g-mode period spacing; we can model the deep radiative region relatively well as the previous studies suggested (e.g. Kurtz et al., 2014), and there is no firm reason for us to modify the deep radiative region.

Other possible mechanisms to produce blue straggler stars are stellar collision or binary merger. To conduct non-standard stellar modeling based on either mechanism, we at first have to compute dynamical states via numerical computations, which are beyond our study and should be investigated in future studies.

4.2.1 Strategy

First of all, we would like to elucidate the parameters to be surveyed. They are divided into two groups corresponding to the two steps in the non-standard modeling. The set pf parameters for the first step, in which candidate models are computed, consists of mass M, initial helium abundance Y_{init}, initial metallicity Z_{init}, age (represented by the mean value of g-mode period spacings $\overline{\Delta P_{\mathrm{g}}}$), and the extent of overshooting f_{ovs}. The other set of parameters for the second step, in which envelope-modified models are computed, comprises the depth r_{c}, the width α, and the extent of the modification (the number of the modifications added to the envelope) (see Section 3.5 for the exact definitions of the variables above).

Then, the non-standard modeling of the star can be alternatively expressed in the following way: to find sets of the eight parameters with which stellar models reproducing the observables of the star are constructed. In principle, it should be possible to find some solutions to the problem if we search for the whole parameter range with infinitely small grids. But this is, of course, almost impossible to achieve. Therefore, we start with a broader parameter range with coarse grids to find candidate models which reproduce the observed global parameters of the star such as $T_{\rm eff}$ and $\log g$. This coarse-grid-based modeling enables us to exclude parts of the parameter range where there is little chance of finding the solution to the problem, and based on the results, we can redetermine another narrower parameter range with finer grids to again find candidate models by imposing tighter constraints on asteroseismic quantities such as $\Delta P_{\rm g}$, frequency separations, individual frequencies, and so on (because this parameter range is determined to reproduce the global parameters, we do not have to care about them and they are naturally satisfied with the obtained candidate models). How we impose the constraints on the asteroseismic quantities is such a technical part to describe that it is deeply explained in the following small subsection.

In any case, the same procedures as in Section 3.1 are taken after we obtain the candidate models, i.e. we gradually modify the envelope of the candidate models, compare the eigenfrequencies of the envelope-modified models with the observed ones, and finally select several models which reproduce the observables as well as possible.

Specific procedures

We firstly prepare the following grids of parameters: mass M (1.1–2.1$M_\odot$, with the step of 0.1$M_\odot$ between 1.1–1.7$M_\odot$ and with the step of 0.2$M_\odot$ between 1.7–2.1$M_\odot$, initial helium abundance $Y_{\rm init}$ (0.25–0.27, with the step of 0.01), initial metallicity $Z_{\rm init}$ (0.002–0.004, with the step of 0.001), and the extent of overshooting $f_{\rm ovs}$ (0.010, 0.020, and 0.027). Most of the previous models are relatively low-mass stars with $M \sim 1.4M_\odot$, which is the reason why the grids of the lower mass range is finer than that of the higher mass range. We assume that the star was born as an ordinary single star with the initial helium abundance of ~ 0.26, lower than that of the previous models ($Y_{\rm init} > 0.30$), and the range for initial helium abundance is thus chosen. For the extent of overshooting, $f_{\rm ovs} \sim 0.01$–0.02 is often recommended by the literatures (e.g. Paxton et al., 2011), but here we include $f_{\rm ovs} = 0.027$ because such broader overshooting region is suggested based on the analysis of the g-mode period spacing $\Delta P_{\rm g}$ pattern (see Section 2.4). Let us call the parameter range defined above “the coarse grid”.

Then, we compute evolutionary tracks for all the points in the coarse grid. The evolution is stopped when the mean g-mode period spacing of the model $\overline{\Delta P_{\rm g}}$ (one of the outputs of MESA, computed based on the integration of the Brunt-Väisälä frequency) reaches 2100 s, which is around the mean value of the observed g-mode period spacings 2070 s. We separate the models thus computed into three groups based on their atmospheric parameters ($T_{\rm eff}$ and $\log g$), namely, the 1σ group whose models reproduce the observed atmospheric parameters within 1σ, the 2σ groups which is determined in the same way as the 1σ group except that the criterion is 2σ, and the rest which consists of the models left.

Finer grids are constructed based on the input parameters of the 1σ group and the 2σ group. The details are shown in the next subsection 4.2.2 (because we do not know where should be finer grids until results of the coarse-grid-based modeling are obtained). Let us call the newly determined parameter range “the finer grid”.

We again compute evolutionary tracks for the finer grid to obtain candidate models whose envelopes are to be modified to fit the observed p-mode frequencies. Evolution is stopped first when $\overline{\Delta P_{\mathrm{g}}}$ of the model reaches 2150 s, then the timestep for evolutionary calculation is changed from the default value (around 10^7 years) to much smaller one around 10^5 years. Evolution is restarted with the smaller timestep until $\overline{\Delta P_{\mathrm{g}}}$ reaches 1950 s, and all the equilibrium models computed along the evolution between $\overline{\Delta P_{\mathrm{g}}} = 1950\,\mathrm{s}$ and $\overline{\Delta P_{\mathrm{g}}} = 2150\,\mathrm{ss}$ are saved, for which the corresponding eigenfrequencies (of both p and g modes) are computed via GYRE. Among a series of evolutionary models for a certain set of the parameters (M, Y_{init}, Z_{init}, and f_{ovs}), one model which minimizes the sum of the squared residuals (normalized by the observational uncertainties) between the modeled frequencies and the observed ones is chosen as a candidate for "candidate models". Let us call them "pre-candidate models".

The modeled p-mode frequencies are subsequently checked to determine which pre-candidate models are appropriate for "candidate models". As is described in Section 3.4, the amount of the frequency variations caused by envelope modifications via our non-standard scheme is seemingly proportional to a ratio of the envelope mode inertia to the total one (see discussions in Section 3.4). We exploit the feature to select candidate models in the following steps. First, a modeled radial-mode frequency which is closest to the observed frequency of the singlet ($\nu = 17.9635133 \pm 5 \times 10^{-7}$ d^{-1}) is chosen. Then, the difference between them $(\Delta\nu_0)_{\mathrm{mod-obs}}$ is computed (be careful not to be confused by the expression, this is not the large separation $\Delta\nu$, see, e.g., Subsection 1.2.3), which ideally becomes zero after we suitably modify the envelope of the model. Based on the assumption of the proportionality for the frequency variation caused by the envelope modification in addition to the difference $(\Delta\nu_0)_{\mathrm{mod-obs}}$, we can calculate an expected frequency variation for each mode as follows:

$$(\Delta\nu_i)_{\mathrm{expect}} = \frac{I_i^{\mathrm{env}}}{I_0^{\mathrm{env}}} (\Delta\nu_0)_{\mathrm{mod-obs}}, \tag{4.1}$$

where I_j^{env} is defined as an integration of the mode energy density, over the modified region, for the mode j (see the definition in Section 3.4), and it can be computed with the outputs of GYRE. For more information, see, e.g., Aerts et al. (2010). Finally, we compare the expected frequency variation for a particular mode with the difference between one of the observed frequencies and its closest modeled frequency $(\Delta\nu_i)_{\mathrm{mod-obs}}$, namely, we compute the following quantities for each detected peaks:

$$\Big((\Delta\nu_i)_{\mathrm{expect}} - (\Delta\nu_i)_{\mathrm{mod-obs}}\Big)^2. \tag{4.2}$$

By imposing an arbitrary criterion for the sum, several models which render the sum of the quantities (4.2) below the criterion are chosen as "candidate models". Before moving on to the envelope-modifying modeling, we have a subtle step where models are computed with the same sets of the parameters as those of the selected candidates except for the ages; the newly computed models are younger than the original candidate models by thermal timescale for the models. This is because we have to evolve envelope-modified models until they settle to the thermal equilibrium states, and it is possible that the evolution leads to deviations in fitted g-mode frequencies. Such deviations can be avoided by using the younger candidate models.

The final procedure for the envelope-modifying modeling is the same as demonstrated in Section 3.5, we do not intend to repeat it here.

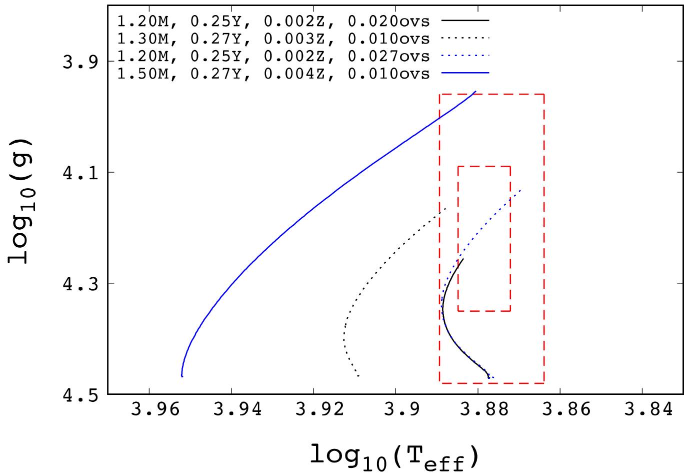

Figure 4.1: Evolutionary tracks for some of the models obtained via the coarse-grid-based modeling. Models belonging to the 1σ (2σ) group are represented by black (blue) curves. Note that two models (a model with $M = 1.20 M_\odot$, $Y_{\rm init} = 0.25$, $Z_{\rm init} = 0.002$, and $f_{\rm ovs} = 0.027$ and one with $M = 1.20 M_\odot$, $Y_{\rm init} = 0.25$, $Z_{\rm init} = 0.002$, and $f_{\rm ovs} = 0.020$) overlap each other; the parameters are the same except for $f_{\rm ovs}$.

4.2.2 Results

Coarse grids

There are two main results about the coarse-grid-based modeling. One is that low-mass models (with masses ranging from 1.10–$1.50 M_\odot$) are favored to reproduce the observed atmospheric parameters $T_{\rm eff}$ and $\log g$; all of the models in either the 1σ model or 2σ model have masses lower than $1.5 M_\odot$ not depending on the other parameters. This trend can be confirmed even when we construct the 3σ group in the same way as the other groups; the mass of the most massive model in the 3σ group is $1.70 M_\odot$. We therefore exclude 1.7–$2.1 M_\odot$ from the parameter range from now on.

Another result is that there is no model in the 1σ group which favors $f_{\rm ovs} = 0.027$. Because $f_{\rm ovs} = 0.027$ is suggested based on the analysis of the observed $\Delta P_{\rm g}$ pattern, this result implies that the models in the 1σ group are not appropriate (asteroseismically) as candidate models. Thus, we also exclude the 1σ group for further analyses (though the group is still useful for checking, for instance, the possibility that the star has evolved as a single star). Meanwhile, there are some models with $f_{\rm ovs} = 0.027$ in the 2σ group, and we concentrate on the parameter range in the following small subsections.

Figure 4.1 shows some examples of evolutionary tracks of the models obtained via the coarse-grid-based modeling. In spite of the relatively higher $\log g \sim 4.2 \pm 0.1$ (cgs units), the mean of g-mode period spacings $\overline{\Delta P_{\rm g}}$ favor the TAMS stage at which stars are less denser compared with when they are on the main sequence, possibly leading to the preference for low-mass stellar models in the coarse-grid-based modeling.

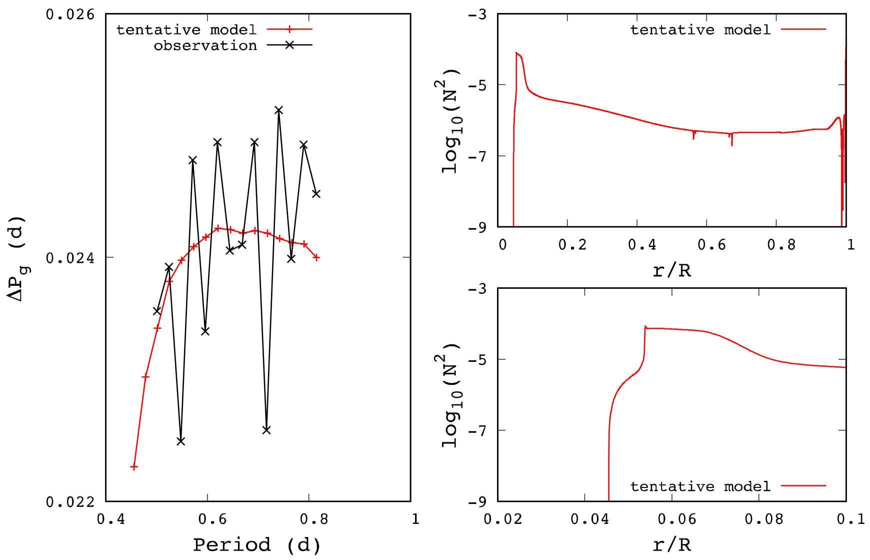

Figure 4.2: ΔP_{g} pattern for the model obtained based on the non-standard modeling (red) and that for the observation (black). The model successfully reproduces the positive slope of the observed ΔP_{g} pattern, but the other oscillatory component with a shorter period ($\Delta n \sim$ a few) cannot be confirmed with this model. Right panels show the Brunt-Väisälä frequency of the model for the whole interior of the model (top) and for an expanded look into a region just above the convective core where the chemical composition gradient develops. We see two dips in the Brunt-Väisälä frequency (top right), which are caused by the envelope modification implemented to the scheme of non-standard modeling. These features nevertheless affect the g-mode frequencies.

Finer grids

The results in the previous small subsection allow us to determine a new parameter range with finer grids. Below is the set of the finer grids: mass M (1.16–1.44$M_\odot$, with the step of 0.02$M_\odot$, initial helium abundance Y_{init} (0.25–0.27, with the step of 0.01), initial metallicity Z_{init} (0.002, fixed), and the extent of overshooting f_{ovs} (0.027, fixed). The extent of overshooting $f_{\mathrm{ovs}} = 0.027$ is fixed because of the analysis of the observed ΔP_{g} pattern of the star. The initial metallicity is fixed since all the models with $f_{\mathrm{ovs}} = 0.027$ in the 2σ group have $Z = 0.002$.

Based on the grids, we carry out the finer-grid-based modeling as described in detail in Subsection 4.2.1. We adopt 0.39 as the criterion (expressed as the sum of the quantities 4.2) above which the corresponding models are discarded, and not taken as candidate models. The criterion is determined so that about a tenth of pre-candidate models is chosen as a candidate model. With this criterion, we have selected five models as candidate models to which the envelope-modifying scheme is applied.

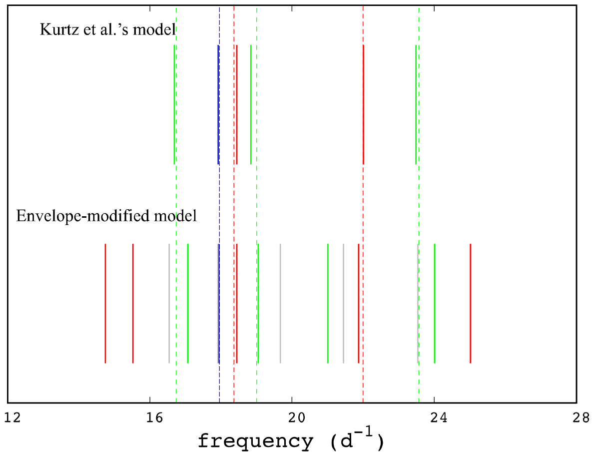

Figure 4.3: Comparison of the modeled frequencies (solid lines) with the observed ones (dashed lines) for the envelope-modified model obtained based on the non-standard modeling (bottom) and for the model of Kurtz et al. (2014). The radial, dipole, quadrupole, and octupole modes are represented by blue, red, green, and grey, respectively. Note that the colors of the observed frequencies are based on the mode identification by Kurtz et al. (2014) (see Subsection 1.3.2). In the case of the tentative model, octupole modes are sometimes better to reproduce the observed frequencies than the dipole-mode frequencies of the model, implying the possibility of a different mode identification.

Envelope-modifying modeling

The envelope-modifying modeling is applied for the five candidate models, and we end up with a tentatively best model (within the non-standard scheme) demonstrated as below. The set of the parameters of this model is $M = 1.36 M_{\odot}$, $Y_{\rm init} = 0.26$, $Z_{\rm init} = 0.002$, $f_{\rm ovs} = 0.027$, and Age $= 2.169 \times 10^9$ years old. The parameters for the modifications are $r_{\rm c} = 0.67$, $\alpha = 5 \times 10^{-3}$, and the number of modifications is 115 which corresponds to $\Delta X \sim 0.06$ (ΔX is a difference in hydrogen abundance between the candidate model and the modified model) at the surface. The logarithm of the surface gravitational acceleration and that of the effective temperature of the model are 3.9 (cgs units) and 3.87.

The $\Delta P_{\rm g}$ pattern computed for the model via GYRE is reproducing the observed positive trend which is thought to be caused by the overshooting (see Figure 4.2) (also see Section 2.4) though there is still a significant discrepancy between the observed $\Delta P_{\rm g}$ and the modeled one, especially with respect to the oscillatory component with a short period of $\Delta n \sim$ a few. However, the sum of the squared residuals (between the model and the observation) normalized by the observed uncertainties for g-mode frequencies is significantly smaller ($\sim 3 \times 10^5$) than that in the case of the previous studies (e.g. Kurtz et al., 2014) ($\sim 10^6$).

Figure 4.3 shows the comparison of the modeled p-mode frequencies with the observed ones. The radial- (blue), dipole- (red), and quadrupole- (green) mode frequencies are presented. For our tentative model, $l = 3$ modes (grey) are also illustrated. The envelope-modified model obtained in this study fits the observed radial-mode frequency better than the model of Kurtz et al. (2014). The other p-mode frequencies, nevertheless, are not fitted well in the tentative model, especially when we follow the mode identification adopted in Kurtz et al. (2014) (see the caption of Figure

4.3 for more details). The mean deviation, which is defined as the mean of the absolute value of the difference between the modeled frequencies and the modeled ones, for our model is 0.2 d^{-1} and that of Kurtz et al. (2014) is 0.1 d^{-1}. Interestingly, when we include $l = 3$ modes in the mode identification, the mean deviation for our model reduces to be 0.1 d^{-1} which is comparable to that of Kurtz et al. (2014). We discuss the point later in Section 4.4.

4.2.3 Discussions

In the preceding subsections, a totally new stellar model of KIC 11145123 has been presented via the non-standard scheme based on the assumption that the star was born as a single star with the ordinary initial helium abundance and, during the evolution, experienced some chemical composition modifications in the envelope thought be caused by, for instance, mass accretion from the outside. Though this is the first case where such non-standard modeling has been successfully carried out for the star (and based on the obtained envelope-modified model, we infer the internal rotation in the following section 4.3), several issues related to the envelope-modified model are discussed in this subsection focusing on the possibility of further improvements on the non-standard model of the star.

ΔP_{g} pattern revisited

As demonstrated in Subsection 4.2.2, the envelope-modified model successfully reproduces the positive slope of the observed ΔP_{g} pattern (Figure 4.2). Still, there seems to be a discrepancy between the modeled ΔP_{g} pattern (red in Figure 4.2) and the observed one (black in Figure 4.2) especially in terms of a short periodic component ($\Delta n \sim$ a few) seen in the observed ΔP_{g} pattern. This discrepancy has been already pointed out in Subsections 2.4.3 and 2.4.4, and it has been also suggested that to consider a perturbation to the Brunt-Väisälä frequency δN^2 could be helpful for reproducing the short periodic component based on the direct numerical computations of the eigenfrequencies for several perturbed Brunt-Väisälä frequency. In particular, adding δN^2 so that the chemical composition gradient becomes steeper is a possible solution to reproduce the shorter-period component of the observed ΔP_{g} pattern as shown in Section 3.6. Then, the question is what is the mechanism that is at work during the evolution and produces such structures?

In this small subsection, diffusion process much weaker than usually expected is assumed to be playing a key role in reproducing a Brunt-Väisälä frequency which leads to the short periodic component in the observed ΔP_{g} pattern. The validity of the assumption is partly confirmed by stellar equilibrium models computed without diffusion processes during evolution (see Subsection 2.3.2 and Figure 2.13); the ΔP_{g} patterns calculated based on the models exhibit short periodic component with high amplitudes. Actually, the amplitudes are too large to represent the observed pattern for KIC 11145123. Here we therefore consider a model with diffusion, but "much weaker" diffusion processes during evolution.

We implement such "much weaker" diffusion by changing the default criterion for the maximum diffusion velocity (diffusion_v_max = 1.d−3 adopted in MESA) to a much smaller one (diffusion_v_max = 1.d−10). In MESA, the diffusion velocity of each element in each mass shell is computed by solving Burger's equation (Burgers, 1969), which sometimes leads to unphysically large diffusion velocities in, for instance, the outermost envelope. The criterion diffusion_v_max in MESA is thus usually set to avoid such problems, and our implementation is rather crude in a sense. Nevertheless, we clearly see improvements in the behavior of a short periodic component in

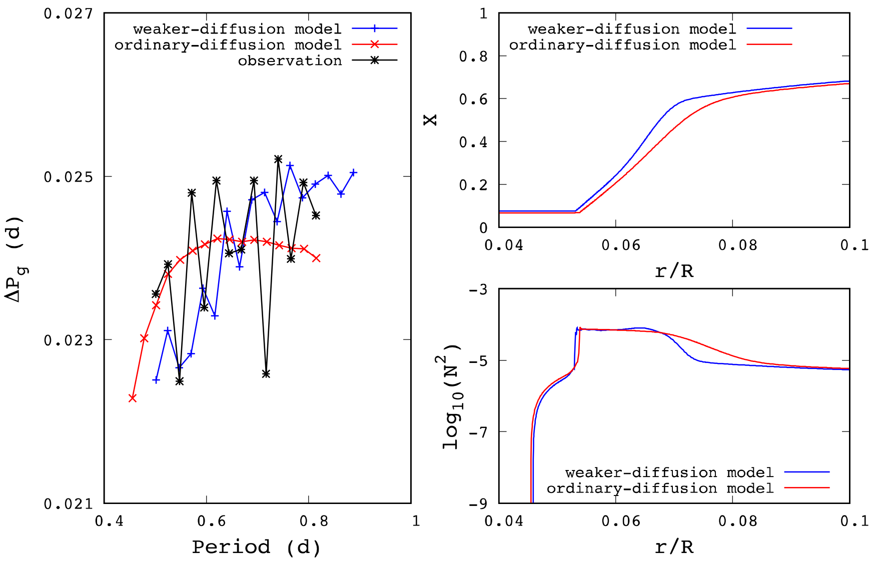

Figure 4.4: Observed g-mode period spacings $\Delta P_{\rm g}$ (black thick line) and modeled ones (the red line and the blue line) in the left panel. The red line is calculated based on the envelope-modified model, and the blue line is based on another model with weaker diffusion. The latter model successfully reproduces the short-periodic oscillatory component of the observed $\Delta P_{\rm g}$ pattern. The right panels show the corresponding hydrogen profiles (top) and Brunt-Väisälä frequencies (bottom). It is obvious that the chemical composition gradient of the weaker-diffusion model is much steeper than that of the envelope-modified model.

the $\Delta P_{\rm g}$ pattern computed with the much weaker diffusion processes during evolution (see Figure 4.4), showing a high potential of the implementation for further asterosesimic researches.

It should be, however, noted that the implementation is computationally fairly time-consuming, and that it is still hard to incorporate the scheme into, for example, the grid-based modeling of stars.

A discrepancy between the observation and the model in terms of atmospheric parameters

Although we have seen a moderate agreement between the modeled frequencies and the observed ones, there is a discrepancy between the model and the observation in terms of the atmospheric parameters, which amounts to more than 2.5σ. Actually, this discrepancy has been reported in the previous studies as well (e.g. Takada-Hidai et al., 2017), as shown in Figure 4.5. It is easily confirmed that when we focus on fitting eigenfrequencies better, the modeled atmospheric parameters, especially the surface gravitational acceleration, deviate more from the observed values (see blue lines), and vice versa (see red lines). In Figure 4.5, we plot the values of our envelope-modified model (orange diamonds), and we see the same trend that the seismic parameters are reproduced relatively well though the atmospheric parameters are not.

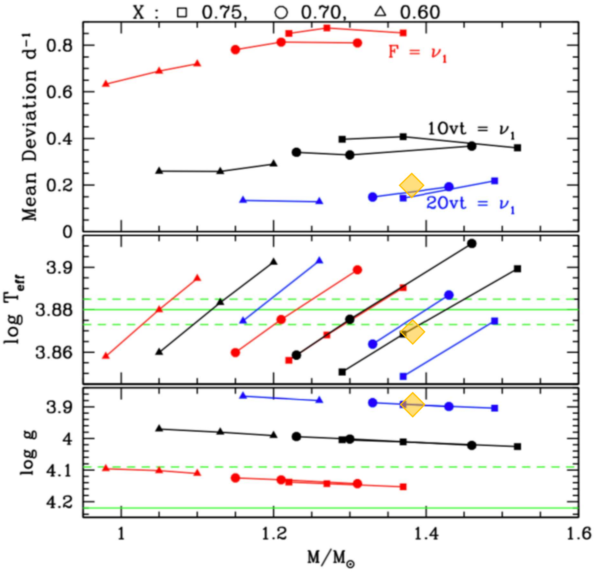

Figure 4.5: Mean deviation between the modeled frequencies and the observed ones (top), the logarithm of effective temperatures (middle), and that of the gravitational accelerations (bottom), computed for various stellar models represented by the mass (horizontal axis) and the initial helium abundance (the square, the circle, and the triangle, corresponds to the initial helium abundance of 0.75, 0.70, and 0.60, respectively). The orange diamonds are the values of our envelop-modified model. Solid green lines in the middle and the bottom panels are expressing the observed values, and the dashed lines are indicating 1σ observational uncertainties. The observed frequency of the singlet is expressed as ν_1, and F, 1Ovt, 2Ovt are representing the fundamental, the first overtone, and the second overtone, respectively. Thus, "$F = \nu_1$" (red lines) means that "the the singlet is identified as the fundamental mode in the case of the model". This figure is cited from Takada-Hidai et al. (2017), and is overplotted by us.

Such signature is also found when we check frequency separations between neighboring $l = 1$ modes (which are quantities considered to be related to the dynamical timescale of the model) assumed to be identified as the two observed triplets ($\nu = 18.366\ d^{-1}$ and $\nu = 22.001\ d^{-1}$). For instance, stellar evolutionary calculations show that, in the case of a stellar model with $M = 1.3M_\odot$, the radius around $2R_\odot$ is favored to reproduce the observed frequency separation $\Delta\nu \sim 3.6\ d^{-1}$. However, the observed value of the gravitational acceleration $\log g \sim 4.2$ (cgs) with the assumed mass ($1.3M_\odot$) indicates that the radius should be $1.4R_\odot$. There is thus a fundamental discrepancy between stellar global parameters of the star inferred seismically and those based on spectroscopy.

If we assume that the current mode identification is right, one of the possibilities to resolve the discrepancy is that the star is currently not in thermal equilibrium states and seismically estimable parameters are not physically related to spectroscopically estimable ones. To test the possibility, we investigate temporal variations of modeled atmospheric parameters from non-thermal equilibrium states (defined as just after the envelope-modification stops) to the thermal equilibrium states for a variety of the extent of the envelop modifications (Figure 4.6). We nevertheless do not find any drastic changes of the atmospheric parameters during the thermal relaxation processes, clearly ruling out our suggestion. There might be thus room for reconsidering the mode identification, but that is difficult to perform until we obtain further observations and is beyond our scope so far.

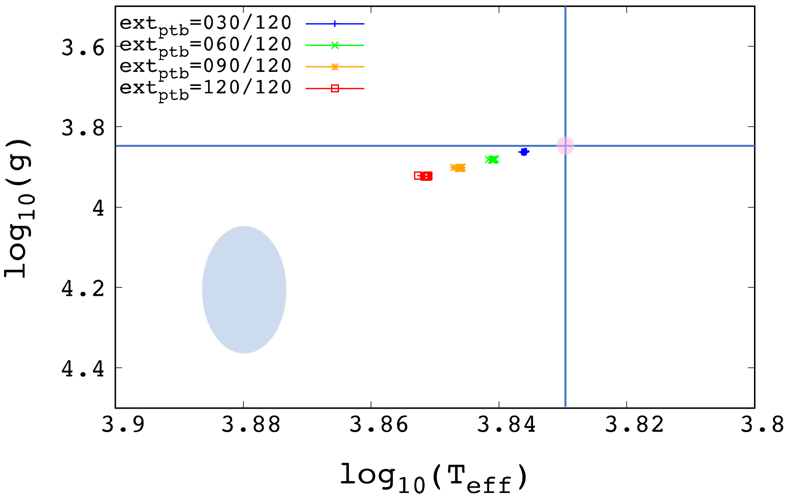

Figure 4.6: Temporal evolution of the atmospheric parameters of stellar models from when the envelop modification just stops (leftmost squares) to when the model resettles to the thermal equilibrium states (rightmost squares) for several values of the extent of the envelope modification (blue to red, smaller to larger). The pink point and the blue oval represent the values of the unperturbed model and the observed ones with rough observational uncertainties indicated. Though it is seen that the larger the extent of the modification is, the closer to observed values the modeled ones are, the temporal variations from non-thermal equilibrium states to the thermal equilibrium states are fairly small.

Is there any model reproducing the observed p-mode frequencies more precisely?

The envelope-modified model obtained via the non-standard scheme is comparable with that of Kurtz et al. (2014) in terms of the modeled p-mode frequencies (the mean deviations are both $\sim 0.2\,d^{-1}$), but there is, in principle, still room for improving the models to reproduce all the observed frequencies within the observational uncertainties. To find such an ideal model, we probably have to survey infinitely large parameter ranges if we persist to performing forward modeling. But we can alternatively search for models in an inverse manner; deviations between the modeled frequencies and the observed ones tell us to what extent we have to modify internal structures of the current (reference) model in order to reduce the deviation, which is called structure inversion in helio- and asteroseismology (see, e.g., Gough and Thompson, 1991).

In structure inversion, we have to solve a set of 1-dimensional linear integral equations expressed in the following way:

$$\left(\frac{\Delta\omega}{\omega}\right)_i = \int_0^1 \left[K_{c,\rho}^{(i)}(x)\frac{\Delta c}{c}(x) + K_{\rho,c}^{(i)}(x)\frac{\Delta\rho}{\rho}(x)\right]dx - \frac{\Delta R}{R}\int_0^1 K_{c,\rho}^{(i)}(x)dx + e_i, \tag{4.3}$$

where $\Delta q/q$ expresses the relative difference of the quantity q between a reference model and observation ($\Delta q \equiv q_{\rm star} - q_{\rm ref}$). The mode index is denoted as i, and e_i is the observational uncertainty for the mode. The fractional radius is represented by x. There are two kinds of sensitivity functions called structure kernels, one for the density $K_{\rho,c}^{(i)}(x)$, and the other for the sound speed $K_{c,\rho}^{(i)}(x)$. The structure kernels can be computed given a certain reference model together with eigenfrequencies and eigenfunctions of the model. Therefore, variables to be estimated here are $\Delta c/c$, $\Delta \rho/\rho$, and $\Delta R/R$. More details, for example, the explicit forms for the structure kernels, can be found in Appendix B.

We show an example of results obtained via structure inversion when we take the envelope-modified model as a reference model in Figure 4.7, where the so-called Regularized Least-Squares method is used (see Appendix C). The relative difference of the radius (between the reference model and KIC 11145123) is estimated to be $\Delta R/R = 0.00748 \pm 0.00009$, suggesting that the radius of the model is smaller than the real one. The sum of the residuals between the right-hand side and the left-hand side of the expression (4.3), which can be obtained after we substitute the estimated relative differences $\Delta c/c$, $\Delta \rho/\rho$, and $\Delta R/R$ for the expression, is ~ 28 which can be considered to behave well if the observations behave as Gaussian (and the number of the modes used in this analysis is 21). Therefore, if we modify the sound speed, the density, and the radius of the envelope-modified model based on the estimated relative differences, the newly constructed model can reproduce the observed frequencies quite well.

Nonetheless, there are a number of difficulties to correctly interpret the results. In the first place, we do not have any hints for the cause of the expected modification, and thus, we would end up with carrying out a series of stellar evolutionary computations after all. Another issue is related to the mode identification. Because sensitivity of structure kernels are different from mode to mode, different mode identification easily misleads us to multiple possible conclusions. Finally, for stars with outer convective envelopes, it is generally recognized that there exists a systematic deviation from the modeled frequencies and the observed ones, which is called the "surface effect" (e.g. Sonoi et al., 2017) (because the origin of the deviation is believed to be interactions between the oscillation and the near-surface superadiabatic convection). In asteroseismology, this surface effect is difficult to distinguish with the structural-origin frequency deviations, and thus, we have to be careful when we carry out asteroseismic structure inversion (see also Kosovichev and Kitiashvili, 2020).

In any case, the demonstrations in the previous paragraphs rule out the possibility that there does not exist a solution for a better model, showing that we are more or less on the right track for further modeling of the star in the forthcoming studies.

Possibility for different mode identifications

As already discussed in the previous small subsections, mode identification of the observed frequencies different from that of Kurtz et al. (2014) might help us to resolve some discrepancies we are faced with, for instance, a discrepancy between the model and the observation in terms of the atmospheric parameters. We can also find another hint suggesting the possibility of different mode identification when we see Figure 4.3; the mean deviation of frequencies decreases from 0.2 d^{-1} to 0.1 d^{-1} if we include $l = 3$ modes in the mode identification of the observed frequencies. However, we have to be cautious about changing the mode identification so passively. One of the advantages in the mode identification of Kurtz et al. (2014) is their assumption that a triplet (quintuplet) should be a $l = 1$ ($l = 2$) mode, which is a fairly reasonable assumption to take. In other words, we have to answer the following question in order to rely on a new mode identification different from that adopted in Kurtz et al. (2014): what is the reason for $l = 3$ modes observed as quintuplets? From that point of view, we have decided to be conservative in terms of the mode identification,

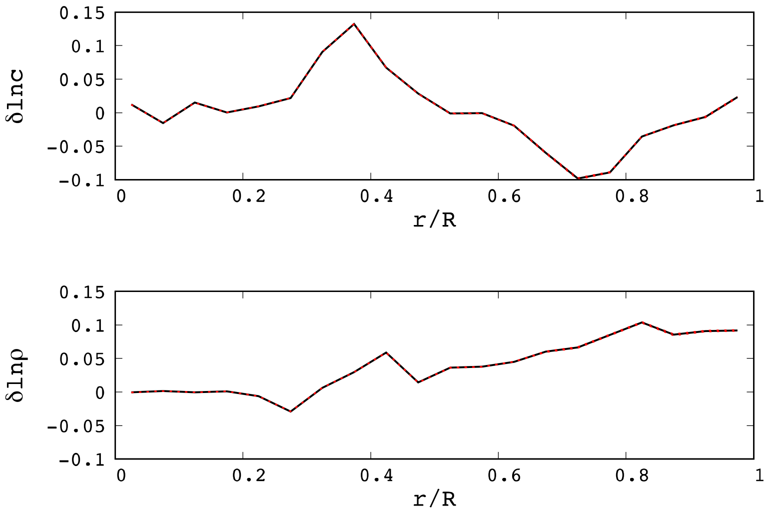

Figure 4.7: Estimated relative difference of the sound speed (top) and that of the density (bottom) between the envelope-modified model and KIC 11145123. The difference is defined as, for instance, $\Delta\rho \equiv \rho_{\rm star} - \rho_{\rm ref}$. Note that the estimated uncertainties are too small to see. The corresponding $\Delta R/R$ is 0.00748 ± 0.00009.

and we continue to follow the way of Kurtz et al. (2014) to identify the observed frequencies for the time being. It should be instructive to mention that the frequency splitting can be used for mode identification if the split frequencies are simultaneously fit combined with rotation inferences as in Benomar et al. (2009), which can be worth investigating.

4.3 Internal rotation of KIC 11145123 [1]

This section is devoted to the topic of rotation inversion, to infer the internal rotation profile of KIC 11145123. Rotation is universal, and it is generally recognized that rotation plays important roles in various types of physical processes inside stars such as dynamo mechanisms (Thompson et al., 2017) and chemical elements transport (Aerts et al., 2019). Thus, stellar rotation affects the structure and evolution of the stars (Maeder, 2009). As such, to observationally infer internal rotation profiles of stars definitely helps us to better understand the physics described above by, for instance, putting constraints on the theoretical or numerical studies as has been done in helioseismology. See Chapter 1, for more backgrounds and significance of estimation of stellar rotation.

There are several ways to infer internal rotation of stars via asteroseismology (see Sections 1.2 and 1.3). We concentrate on an perturbative approach where the internal rotation $\Omega(x, \mu)$ as a function of the radial coordinate x and the latitude variable μ (defined as $\mu = \cos\theta$ where θ is the colatitude in the spherical coordinate) is considered as a small perturbation, and thus, the frequency splitting caused by the rotation (rotational splitting $\delta\omega_{nlm}$) can be related to the internal

---

[1] Partly cited from Hatta et al. (2019)

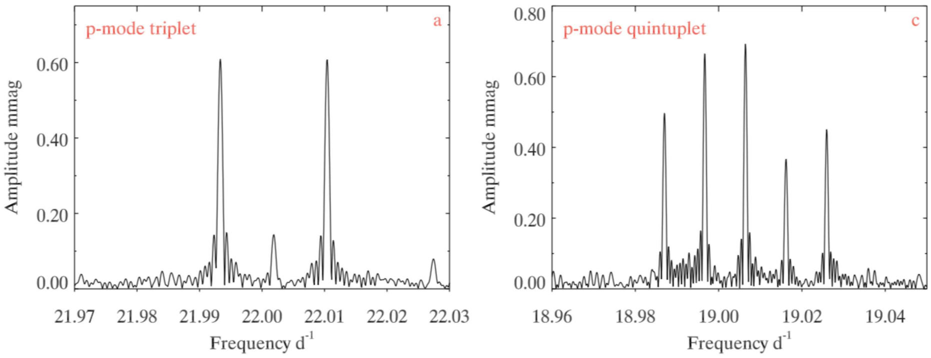

Figure 4.8: Rotational splitting of some of the p modes for KIC 11145123. The same figure as in Subsection 1.2.3.

rotation $\Omega(x,\mu)$ with some sensitivity kernels (rotational splitting kernels) computed based on the eigenfunctions of a reference model. We have the relations for all the modes for which the rotational splitting is observed, and the set of the relations can be expressed as a set of linear integral equations based on which the estimation of the internal rotation $\Omega(x,\mu)$ is performed; this procedure is called rotation inversion.

A brief introduction of the mathematical formulations necessary for conducting rotation inversion is given in the first subsection 4.3.1. Then, specific techniques for rotation inversion are presented in the next subsection 4.3.2, which include a new way of estimation based on the Bayesian statistics. We demonstrate a reference stellar model (this is actually the envelope-modified model obtained in the preceding section 4.2) and rotational splitting kernels calculated based on the reference model in Subsection 4.3.3. The results of rotation inversion are shown in the final subsection 4.3.4.

4.3.1 Mathematical formulations for rotation inversion

When we consider eigenfrequencies ω_{nlm} of a 1-dimensional (spherically symmetric) stellar model, they are degenerate with respect to the azimuthal order m, i.e. $\omega_{nlm} = \omega_{nl0}$ ($m = -l, ..., +l$). This degeneracy arises from the fact that the spherical symmetric stellar model has no preferential direction in terms of the axis of the oscillation. In other words, if there exist some mechanisms which cause deviations from the spherical symmetry, the degeneracy is broken, namely, $\omega_{nlj} \neq \omega_{nlk}$ ($j, k = -l, ..., +l$ and $j \neq k$). Such frequency splitting has been observationally confirmed for a number of stars including KIC 11145123, and the frequency splitting caused by internal rotation is especially called the rotational splitting (Figure 4.8).

Then, how can we mathematically describe the rotational splitting? Based on the assumption that the internal rotation $\Omega(x,\mu)$ is so small that we can treat it as a small perturbation, the terms higher than the first order of which are neglected, we formulate the rotational splitting in the following paragraphs.

The starting point is the equation (1.20) in Subsection 1.2.1:

$$\Delta\omega^2 = \frac{\displaystyle\int \boldsymbol{\xi}^* \cdot \Delta\mathcal{L}(\boldsymbol{\xi}) dV - \omega^2 \int |\boldsymbol{\xi}|^2 \Delta\rho dV}{\displaystyle\int |\boldsymbol{\xi}|^2 \rho dV}, \tag{4.4}$$

which is derived based on the stationarity of the eigenfunctions $\boldsymbol{\xi}$ (the variational principle). For the meanings of the parameters, see Subsection 1.2.1. Note that it is assumed that $\Delta\rho = 0$ in the following analysis in this section, because we are concentrating on the effect of internal rotation on the eigenfrequencies.

The next thing to do is to explicitly express $\Delta\mathcal{L}$; we have to formulate the perturbed linear operator to the first order in the presence of the stationary velocity field $\boldsymbol{v}_0$ which is represented by the internal rotation $\Omega(x, \mu)$ with a relation $\boldsymbol{v}_0 = \boldsymbol{\Omega} \times \boldsymbol{r}$, where the components of the rotation vector are $\boldsymbol{\Omega} = (\Omega\cos\theta, -\Omega\sin\theta, 0)$. The expression for $\Delta\mathcal{L}(\boldsymbol{\xi})$ is as below:

$$\Delta\mathcal{L}(\boldsymbol{\xi}) = 2i\omega\rho(\boldsymbol{v}_0 \cdot \nabla)\boldsymbol{\xi}. \tag{4.5}$$

For more information on the derivations, (see, e.g., Aerts et al., 2010).

Substituting the expression (4.5) for the equation (4.4), after some manipulations, leads to an expression for the rotational shift as follows:

$$\frac{\delta\omega_{nlm}}{m} = \iint K_{nlm}(r, \theta)\Omega(r, \theta)r^2 dr \sin\theta d\theta, \tag{4.6}$$

where the explicit form of the rotational splitting kernel $K_{nlm}(r, \theta)$ is

$$\begin{aligned} K_{nlm}(r,\theta) &= \frac{\rho}{I_{nl}}\Bigg[\{\xi_r^2 + l(l+1)\xi_h^2 - 2\xi_r\xi_h\}\{P_l^m(\cos\theta)\}^2 + \xi_h^2\frac{d}{\mathrm{d}\cos\theta}\left(\frac{\sin^2\theta}{2}\frac{\mathrm{d}}{\mathrm{d}\cos\theta}\{P_l^m(\cos\theta)\}^2\right) \\ &+ \xi_h^2\cos\theta\frac{\mathrm{d}}{\mathrm{d}\cos\theta}\{P_l^m(\cos\theta)\}^2\Bigg], \end{aligned} \tag{4.7}$$

where ξ_r and ξ_h are the radial and the horizontal components of the eigenfunction $\boldsymbol{\xi}$, which can be obtained by calculating the linear adiabatic oscillation of the model. The associated Legendre function is denoted by $P_l^m(\cos\theta)$. The quantity I_{nl} is defined as below:

$$I_{nl} = \int_0^R (\xi_r^2 + l(l+1)\xi_h^2)\rho r^2 dr. \tag{4.8}$$

We can separate the radial and latitudinal component of the rotational splitting kernel as follows

$$K_{nlm}(x, \mu) = K_{nl}(x)W_{lm}(\mu) + L_{nl}(x)X_{lm}(\mu), \tag{4.9}$$

where x and μ are fractional radius ($x = r/R$) and cosine of the colatitude θ, respectively. The radial components $K_{nl}(x)$ and $L_{nl}(x)$ have the following explicit forms

$$K_{nl}(x) = \frac{\rho x^2}{I_{nl}}(\xi_r^2 + l(l+1)\xi_h^2 - 2\xi_r\xi_h), \tag{4.10}$$

$$L_{nl}(x) = \frac{\rho x^2}{I_{nl}}\xi_h^2. \tag{4.11}$$

And the latitudinal components $W_{lm}(\mu)$ and $X_{lm}(\mu)$ have the following explicit forms

$$W_{lm}(\mu) = \{P_l^m(\mu)\}^2, \tag{4.12}$$

$$X_{lm}(\mu) = (1 - \mu^2)\frac{d}{d\mu}\left(P_l^m(\mu)\frac{dP_l^m}{d\mu}\right). \tag{4.13}$$

Finally, we have another expression for the rotational shift

$$\frac{\delta\omega_{nlm}}{m} = \iint \Big[K_{nl}(x)W_{lm}(\mu) + L_{nl}(x)X_{lm}(\mu)\Big]\Omega(x, \mu)dxd\mu. \tag{4.14}$$

4.3.2 Methods [2]

This subsection is dedicated to presenting some techniques for rotation inversion to estimate the internal rotation of the star based on the expression (4.14). We have a set of the equations (4.14), the number of which is identical to that of observed rotational shifts (more precisely, the number of the so-called generalized rotational splittings defined by the expression 4.38 as shown later). Rotational splitting kernels for the corresponding observed rotational shifts can be computed based on the calculation of the linear adiabatic oscillation of the model once the mode identification has been carried out. Then, what we have to do to estimate the unknown in the set of the equations (the internal rotation $\Omega(x, \mu)$) is to solve it. This is, however, almost an impossible thing to do, because the number of the equations is finite while the number of parameters describing the internal rotation $\Omega(x, \mu)$ is ultimately infinite ($\Omega(x, \mu)$ is a continuous function); this is an ill-posed problem, and we need some techniques for (not solving but) inverting the set of the equations such as the Regularized Least-Squares (RLS) method and the Optimally Localized Averaging (OLA) method, both of which are well established and have been frequently used in helioseismology (see, e.g., Thompson et al., 2017).

We would like to here present one of the standard methods, the OLA method, as well as two techniques, namely, a-few-zone modeling of the internal rotation and a newly developed Bayesian scheme. The reason for introducing the latter two methods is that we do not have a large number of rotational shifts in the case of asteroseismology compared with the case in helioseismology (see Subsection 1.2.1), and thus, it is sometimes difficult to draw definitive conclusions based on just one method (even when it is one of the standard methods) and comparisons of results obtained via different methods can help us to better understand the inversion results. In other words, there is no all-round method which enables us to solve any inverse problems completely, i.e., each inversion technique provides us with the corresponding estimate based on a particular criterion adopted for the technique as are shown in the following small subsections. Therefore, we should be cautious not to jump to seemingly satisfactory conclusions, which is especially the case in asteroseismology where the relative scarcity of observed rotational shifts easily leads to the ill-posedness of the inverse problems. (For more information on other techniques and comparisons among them, see Appendix C.)

Before moving on to the demonstrations of the three methods, we have a few remarks on what are usually common for all the inversion techniques. We usually have uncertainties arising from observation, instruments, and so on. Thus, the set of equations can be rewritten in the following form

$$d_i = \iint K_i(x, \mu)\Omega(x, \mu) dx d\mu + e_i, \tag{4.15}$$

where we have replaced $\delta\omega_{nlm}/m$ with d_i, and the mode indices (n, l, m) are replaced with a single index i identifying modes. The left-hand sides of the equation (4.14) is now represented by d_i. It is assumed that means of the uncertainties are zero

$$< e_i >= 0, \tag{4.16}$$

and that the observational uncertainty is statistically independent from each other.

---

[2] Partly cited from my master thesis.

Optimally Localized Averaging method

The first method we describe is the *Optimally Localized Averaging* (OLA) method. In OLA, we estimate a value of the internal rotation at a certain target point $\Omega(x_0, \mu_0)$ as a linear combination of the dataset $\{d_i\}$

$$\begin{aligned} & \hat{\Omega}(x_0, \mu_0) \\ = & \sum_{i=1}^{M} c_i(x_0, \mu_0) d_i \\ = & \sum_{i=1}^{M} c_i(x_0, \mu_0) \Big(\iint K_i(x, \mu) \Omega(x, \mu) dx d\mu + e_i \Big) \\ = & \iint D(x, \mu; x_0, \mu_0) \Omega(x, \mu) dx d\mu + \sum_{i=1}^{M} c_i(x_0, \mu_0) e_i, \end{aligned} \tag{4.17}$$

where the equation (4.15) is used to derive the expression above, and $D(x, \mu; x_0, \mu_0)$ is the averaging kernel which is defined as

$$D(x, \mu; x_0, \mu_0) \equiv \sum_{i=1}^{M} c_i(x_0, \mu_0) K_i(x, \mu). \tag{4.18}$$

The variance of the estimate $< |\delta\hat{\Omega}(x_0, \mu_0)|^2 >$ is evaluated as below

$$\begin{aligned} < |\delta\hat{\Omega}(x_0, \mu_0)|^2 > &= < |\sum_{i=1}^{M} c_i e_i|^2 > \\ &= < \sum_{i=1}^{M} c_i e_i \sum_{j=1}^{M} c_j e_j > \\ &= \sum_{i,j=1}^{M} c_i c_j E_{ij}, \end{aligned} \tag{4.19}$$

where the covariance matrix E_{ij} is defined as

$$E_{ij} =< e_i e_j > . \tag{4.20}$$

In an ideal case where $D(x, \mu; x_0, \mu_0) \to \delta(x - x_0, \mu - \mu_0)$, the expression (4.17) can be altered to

$$\begin{aligned} \hat{\Omega}(x_0, \mu_0) &= \int \delta(x - x_0, \mu - \mu_0) \Omega(x, \mu) dx d\mu + \sum_{i=1}^{M} c_i(x_0, \mu_0) e_i \\ &= \Omega(x_0, \mu_0) + \sum_{i=1}^{M} c_i(x_0, \mu_0) e_i, \end{aligned} \tag{4.21}$$

which indicates that $< \hat{\Omega}(x_0, \mu_0) >$ would be the true value of the function at the target point $\Omega(x_0, \mu_0)$. Therefore, the goal of the OLA method is to have the averaging kernel as well localized around the target point as possible. The condition is fulfilled, for instance, by determining the coefficients $\{c_i\}$ which minimize the following value

$$S = \iint D(x, \mu; x_0, \mu_0)\Big\{(x - x_0)^2 + x^2(\mu - \mu_0)^2\Big\} dx d\mu + \alpha \sum_{i,j=1}^{M} c_i c_j E_{ij}, \tag{4.22}$$

Minimizing S allows the averaging kernel to be large near the target point and to be small far from it (*Backus-Gilbert* method; Backus and Gilbert, 1967). In order to determine the absolute values of the inversion coefficients, a unimodular condition of the averaging kernel is considered

$$\int D(x, \mu; x_0, \mu_0) dx d\mu = 1. \tag{4.23}$$

Furthermore, to keep the estimated errors small, the variance of the estimate is also included in the equation (4.22). Thus, what we minimize is, for example,

$$S_\lambda = \int D(x, \mu; x_0, \mu_0)^2\Big\{(x - x_0)^2 + (\mu - \mu_0)^2\Big\} dx d\mu + \alpha \sum_{i,j=1}^{M} c_i c_j E_{ij} + 2\lambda(1 - \int D(x, \mu; x_0, \mu_0) dx d\mu), \tag{4.24}$$

where α is a free parameter and λ is a Lagrangian multiplier introduced to achieve the condition (4.23).

Minimizing the S_λ is completed by requiring $(\partial S_\lambda / \partial c_k) = 0$ for all k. The condition is expressed using matrices

$$\left(\begin{array}{ccc|c} & & & q_1 \\ & Q & & \vdots \\ & & & q_M \\ \hline q_1 & \cdots & q_M & 0 \end{array}\right) \left(\begin{array}{c} c_1 \\ \vdots \\ c_M \\ c_{M+1} \end{array}\right) = \left(\begin{array}{c} 0 \\ \vdots \\ 0 \\ 1 \end{array}\right) \tag{4.25}$$

where λ is replaced with c_{M+1}, and Q is a $M \times M$ matrix whose (i, j) element is

$$Q_{ij} = \int K_i(x, \mu) K_j(x, \mu)\Big\{(x - x_0)^2 + (\mu - \mu_0)^2\Big\} dx d\mu + \alpha E_{ij}. \tag{4.26}$$

The integration of each kernel q_i is used in the expression (4.25), and it is defined as

$$q_i = \int K_i(x, \mu) dx d\mu. \tag{4.27}$$

Since the matrix Q is a real and symmetric matrix, we can invert the equation (4.25) via, for example, LU-decomposition of Q. We thus obtain the inversion coefficients $\{c_i\}$. Substituting them for equations (4.17) and (4.19) provides us with the estimate at the target point.

This is not the end. After we have determined $\{c_i\}$, we have to check whether the averaging kernel is really localized around the target point or not. We also have to investigate the variance of the estimate, *error magnification*. Actually, error magnification is dependent on the choice of a trade-off parameter α, and there is a trade-off relation between the resolution of the averaging kernel and error magnification. This feature is explainable when we look at equation (4.24). If α is close to zero, the importance of the second term in equation (4.24) decreases and we have to concentrate on minimizing the first term. Whereas, if α is so large that the first term is negligible, we do not need to care about minimizing the first term. Therefore, we should find an α with which the importance of the resolution and that of error magnification is well balanced in minimizing S_λ. We describe how to find an appropriate α in detail in Subsection 4.3.4.

Finally, we would like to mention one advantage of the OLA method, that is, we can simply relate an estimated internal rotation rate at a target point $\hat{\Omega}(x_0, \mu_0)$ to the real internal rotational profile $\Omega(x, \mu)$ via the equation (4.17) with the corresponding averaging kernel $D(x, \mu; x_0, \mu_0)$, which allows us to interpret the estimate as an averaged internal rotation rate weighted by the averaging kernel. As such, not only estimates but also the averaging kernels and the inversion coefficients contain important information on the internal rotation of stars. This is partly the reason why we primarily focus on the rotation inversion via the OLA method in Subsection 4.3.4, and the subsequent discussions are mostly based on the results of the OLA method as we see in Subsection 4.3.5.

A-few-zone modeling [3]

A-few-zone modeling is a kind of the least-square methods where the sum of squared residuals between rotational shifts computed based on the parameterized internal rotation and the observed rotational shifts is minimized. We parameterize the internal rotation with just a few zones, which is the reason for the name of the method. Here, the case of three-zone modeling is presented below, though the essential procedures are the same for numbers other than three.

We assume a constant angular velocity for each of the regions, namely, the innermost region $(0 < x < x_a, 0 < \mu < 1)$: region 1, the inner region $(x_a < x < x_b, 0 < \mu < 1)$: region 2, and the outer region $(x_b < x < 1, 0 < \mu < 1)$: region 3. The positions of boundaries, denoted by x_a and x_b, are treated as free parameters. The linear integral equation (4.15) can be expressed in a much simpler form as below:

$$d_i = \sum_{j=1}^{3} K_{ij}\Omega_j + e_i, \quad i = 1, ..., M, \quad j = 1, 2, 3 \tag{4.28}$$

where K_{ij} is defined as

$$K_{ij} \equiv \iint_j K_i(x, \mu) dx d\mu, \tag{4.29}$$

and the integration is carried out over the region j.

Equation (4.28) can be rewritten in the following form

$$\boldsymbol{d} = \mathbf{K}\boldsymbol{\Omega} + \boldsymbol{e}, \tag{4.30}$$

where $\mathbf{K}$ is a 23×3 matrix (in the case of KIC 11145123, the number of the observed rotational shifts is 23). The data, the angular velocities, and the errors are denoted by $\boldsymbol{d}$, $\boldsymbol{\Omega}$, and $\boldsymbol{e}$, respectively. The linear inverse problem (4.30) was relatively easy to solve in a least-squares sense because the rank of the observation matrix $\mathbf{K}$ is found to be full.

Bayesian inversion; NEW

In this small subsection, we present novel formulations to conduct Bayesian rotation inversion. In Bayesian statistics, we have to accept an assumption that we can define 'probabilities of parameters', which are not considered to be random variables in the ordinary statistical context where

---

[3] Mostly cited from Hatta et al. (2019)

a probability can be defined only for repeatedly observable quantities. But once we accept the concept of such a subjective probability, Bayesian statistics allows us to, for example, investigate global properties of probabilities of parameters or compute probabilities of models, based on the latter of which we can conduct model comparison among possible models. In particular, such capability of the model comparison strongly motivates us to construct an inversion scheme based on Bayesian statistics, and the application can be found in Subsection 4.3.5, in which the possibility of the fast-convective-core rotation of KIC 11145123 is tested. For more thorough introductions and discussions on Bayesian statistics in astronomical contexts, readers should refer to e.g. Gregory (2005b).

First of all, let us start with one of the most fundamental equations in Bayesian statistics, the Bayes' theorem, which has the following form:

$$p(B|A) = \frac{p(A|B)p(B)}{p(A)}. \tag{4.31}$$

The equation (4.31) can be derived based on definitions of the joint probability $p(A, B)$ and the conditional probabilities $p(A|B)$ and $p(B|A)$, where A and B represent some events. For clarity (and also for the coming formulations), we rewrite the equation (4.31) as below:

$$p(\boldsymbol{\theta}|\mathbf{d}) = \frac{p(\mathbf{d}|\boldsymbol{\theta})p(\boldsymbol{\theta})}{p(\mathbf{d})}, \tag{4.32}$$

where the symbols are changed from A and B to $\mathbf{d}$ and $\boldsymbol{\theta}$, and the newly introduced symbols have more specific meanings, namely, $\mathbf{d}$ and $\boldsymbol{\theta}$ represent datasets (obtained by observation) and parameters (to be estimated). The probabilities $p(\boldsymbol{\theta}|\mathbf{d})$, $p(\mathbf{d}|\boldsymbol{\theta})$, $p(\boldsymbol{\theta})$, and $p(\mathbf{d})$ should read the posterior probability of the parameters given the dataset, the probability of the dataset given the parameters (or, the likelihood of the parameters), the prior probability of the parameters, and the probability of the dataset marginalized by all the parameters (the so-called global likelihood), respectively.

What the Bayes' theorem (4.32) indicates is actually not complex to interpret; though we have to begin with uninformative states (represented by the prior probability $p(\boldsymbol{\theta})$), once we conduct observations, we can evaluate the probability of obtaining the resultant datasets assuming a set of parameters (represented by the likelihood of the parameters $p(\mathbf{d}|\boldsymbol{\theta})$), and finally, combining the prior probability and the likelihood enables us to update our understanding of the parameters (represented by the posterior probability $p(\boldsymbol{\theta}|\mathbf{d})$).

Then, what do we have to do to apply Bayesian statistics to rotation inversion? The final goal is to compute the posterior probability of parameters describing a rotational profile given the observed rotational shifts $p(\Omega(x, \mu)|\mathbf{d})$, and as shown in the last paragraph, we need to determine functional forms of the prior probability $p(\Omega(x, \mu))$ and the likelihood $p(\mathbf{d}|\Omega(x, \mu))$ beforehand. For the prior probability, it is often recommended to adopt the uniform distribution, whose range should be reasonably broad, unless we, a priori, have strong constraints on the parameters to be estimated. Thus, we follow the recommendation in this dissertation, and the specific range for the prior probability is later shown. In the case of the likelihood, we assume that an observed rotational shift d_i is a realization from a Gaussian distribution whose mean is given by the first term on the right-hand side in the expression (4.15) with its standard deviation identical to the corresponding observational uncertainty e_i. Based on the assumption, the explicit form for the likelihood of the parameters given the rotational shift is as below:

$$p(d_i|\Omega(x,\mu)) = \frac{1}{\sqrt{2\pi}e_i}\exp\left[-\frac{1}{2}\left(\frac{d_i - \int K_i(x,\mu)\Omega(x,\mu)dxd\mu}{e_i}\right)^2\right]. \tag{4.33}$$

By further assuming that the observed rotational shift is statistically independent from each other, the explicit form for the likelihood of the parameters given the set of the observed rotational shifts is the product of the expressions (4.33) as in the following way:

$$p(\mathbf{d}|\Omega(x,\mu)) = \prod_{i=1}^{M} p(d_i|\Omega(x,\mu)), \tag{4.34}$$

where the number of the observed rotational shifts is denoted as M.

Based on the determined prior probability and the likelihood of the parameters given the set of the observed rotational shifts, we can calculate the posterior probability of the parameters following the expression (4.32), and we can subsequently obtain estimates for the parameters by, for instance, choosing a set of the parameters at which the posterior probability is maximum (called Maximum A Posterior estimation). Note that we have not determined an explicit functional form for the rotational profile $\Omega(x,\mu)$ yet, which is a necessary step for us to compute the likelihood (we have to compute the integration inside the expression 4.33). Several specific rotational profiles and the corresponding results of the Bayesian rotation inversion are presented in Subsection 4.3.5. It should also be noted that calculation of the posterior probability requires us to carry out numerical integrations via the Markov-Chain Monte Carlo (MCMC) method if the number of the parameters used to describe a rotational profile is so large that it is computationally impossible to directly evaluate the posterior probability.

In the end of this small subsection, we would like to mention a model comparison based on Bayesian statistics. The important quantity is the global likelihood $p(\mathbf{d})$, which seems to be merely a normalization constant in the expression (4.32). We can confirm the importance of the global likelihood by reconsidering the Bayes' theorem (4.32), which can be rewritten as

$$p(\boldsymbol{\theta}|\mathbf{d},M_j) = \frac{p(\mathbf{d}|\boldsymbol{\theta},M_j)p(\boldsymbol{\theta},M_j)}{p(\mathbf{d}|M_j)}, \tag{4.35}$$

where a model M_j representing a certain set of parameters is explicitly expressed, and the global likelihood can read the likelihood of the model M_j given the dataset. Then, let us consider the posterior probability of the model M_j (which could be totally a nonsense for "frequentists") as below:

$$p(M_j|\mathbf{d}) = \frac{p(\mathbf{d}|M_j)p(M_j)}{p(\mathbf{d})}, \tag{4.36}$$

and let us compare the posterior probability of the model M_j and that of another model M_k. Taking the ratio between the two posterior probabilities (called odds ratio O_{M_j,M_k}) leads to

$$O_{M_j,M_k} = \frac{p(M_j|\boldsymbol{d})}{p(M_k|\boldsymbol{d})} = \frac{p(\boldsymbol{d}|M_j)}{p(\boldsymbol{d}|M_k)}, \tag{4.37}$$

in which the ratio of the posterior probabilities of the models is represented by the ratio of the global likelihoods of the models (note that it is assumed that $p(M_j) = p(M_k)$ here). In this way, the global likelihoods $p(\mathbf{d}|M)$ are such essential quantities that we can select the most probable model given the dataset, which is practically demonstrated in Subsection 4.3.5.

4.3.3 Rotational splitting kernels for reference models

One of the most important quantities in rotation inversion is the rotational splitting kernel $K_i(x, \mu)$ which relates the internal rotation $\Omega(x, \mu)$ with the rotational shift $\delta\omega_{nlm}/m$ as seen in the expression (4.15). What the rotational splitting kernel tells us is regions where we can probe the internal rotation; for example, if the rotational splitting kernel is zero around some region, $\int K_i \Omega dx d\mu$ is also zero in the region, leading to no effects on the rotational shift $\delta\omega_i$ no matter what the internal rotation rates are there. In that sense, the rotational splitting kernel is the sensitivity kernel as well, and we can roughly grasp where we can infer the internal rotation rate by looking at splitting kernels before we carry out, for instance, the OLA method.

In this subsection, two sets of the splitting kernels computed based on two different stellar equilibrium models (the model of Kurtz et al. and the envelope-modified model obtained in Section 4.2) are shown, based on which we also propose where we can probe the internal rotation rates.

The model of Kurtz et al. (2014)

The model of Kurtz et al. (2014) is described by the following parameters: $M = 1.46M_{\odot}$, $(X, Y, Z)_{\text{init}} = (0.65, 0.34, 0.01)$, $f_{\text{ovs}} \sim 0.005$, and $\overline{\Delta P_{\text{g}}} \sim 2050\,\text{s}$.

The eigenfunctions and the frequencies for the model are computed via linear adiabatic oscillation code developed by M. Takata (see Kurtz et al., 2014), and following the explicit expressions (4.10) to (4.13), the rotational splitting kernels for 23 modes (23 is the number of the detected rotational shifts in the case of KIC 11145123) are computed. The rotational splitting kernels thus computed are roughly divided into three groups based on where they have sensitivity inside the model. Fifteen of the twenty three kernels are those for high-order g modes with $(l, m) = (1, 1)$ (upper left in Figure 4.9), two of them are for low-order p modes with $(l, m) = (1, 1)$ (middle left in Figure 4.9), three of them are for low-order mixed modes with $(l, m) = (2, 1)$ (bottom left in Figure 4.9), and the rest are for low-order mixed modes with $(l, m) = (2, 2)$ having sensitivity similar to that of low-order p modes with $l = 1$.

Because we cannot probe internal rotation rates of regions where any of the computed rotational splitting kernels do not have sensitivity, we have selected three target points for the subsequent analyses via the OLA method, namely, points in the low-latitude deep radiative region (probed by g modes), the low-latitude envelope (probed with p modes with $l = 1$), and the high-latitude envelope (probed by mixed modes with $l = 2$ and $m = 1$).

The envelope-modified model

The stellar parameters for the envelope-modified model is as follows: $M = 1.36M_{\odot}$, $(X, Y, Z)_{\text{init}} = (0.738, 0.260, 0.002)$, $f_{\text{ovs}} = 0.027$, and Age $= 2.169 \times 10^9$ years old. The eigenfunctions and the eigenfrequencies are computed via GYRE, based on which the rotational splitting kernels for the detected rotational shifts are calculated. Though the mode identification is not the same as that in the case of Kurtz et al.'s model (regarding the radial order n), basic characteristics of the splitting kernels are almost the same, and we divide the rotational splitting kernels into three groups as seen in Figure 4.9.

A slight difference can be found between $l = 2$ mixed-mode kernels of Kurtz et al.'s model and our tentative envelope-modified one, namely, the former kernel has stronger sensitivity in the outer envelope than the latter has. This difference might be caused by a difference in the envelope structures between the two models, and we see little difference between the g-mode kernels for the

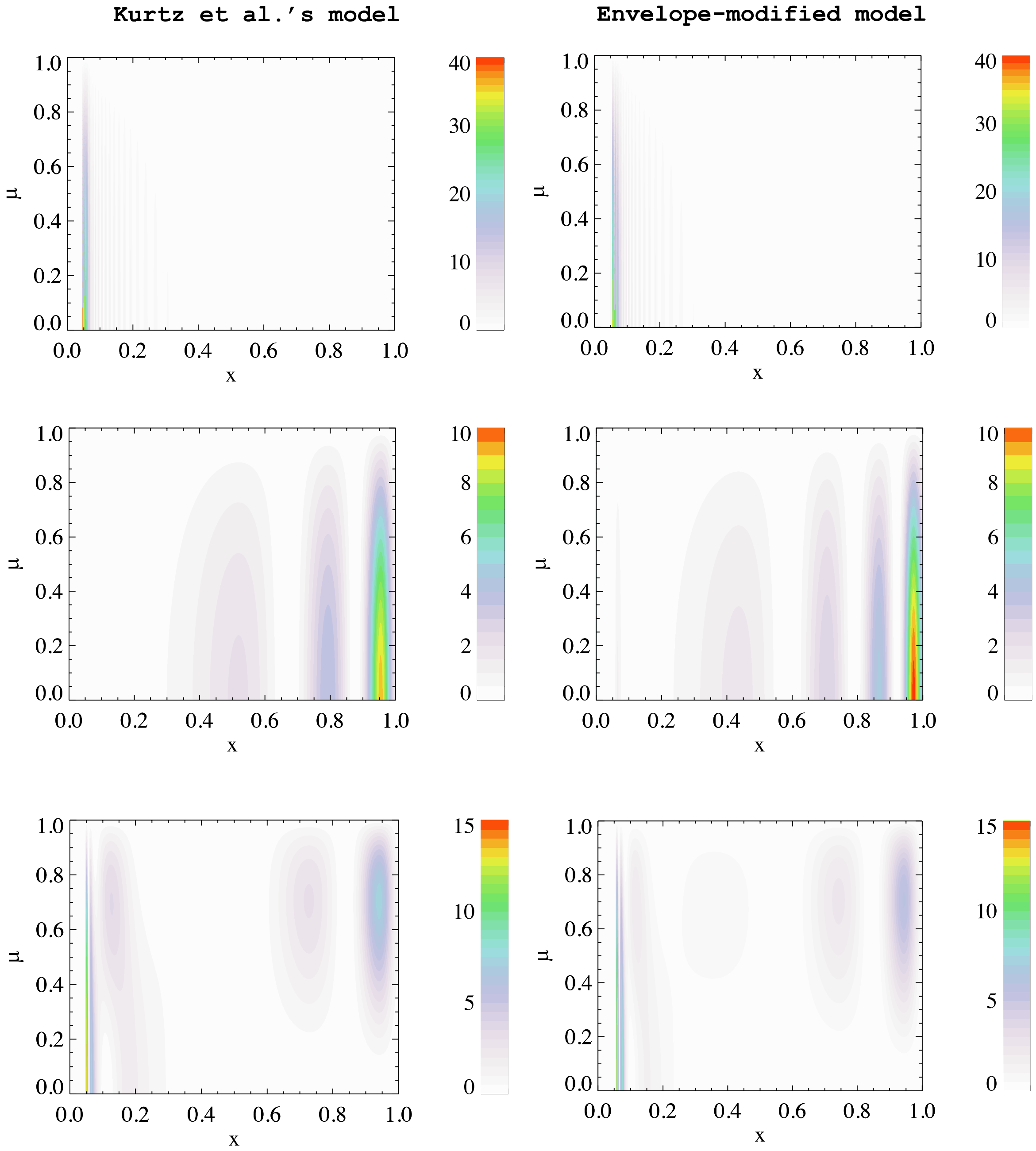

Figure 4.9: Examples of splitting kernels for the model of Kurtz et al. (2014) (left column) and splitting kernels for the envelope-modified model we have obtained in Section 4.2 (right column). We do not see a clear difference between the corresponding splitting kernels (compare left and right for each row). The kernels for a high-order g mode have sensitivity in the deep radiative region just above the convective core (top row) while the kernels for a low-order p mode have sensitivity in the envelope (middle row). The kernels for a low-order mixed mode have sensitivity both the deep radiative region and the envelope (bottom row), and in particular, they also have sensitivity in the high-latitude region. Note that the color contour level are different for each panel.

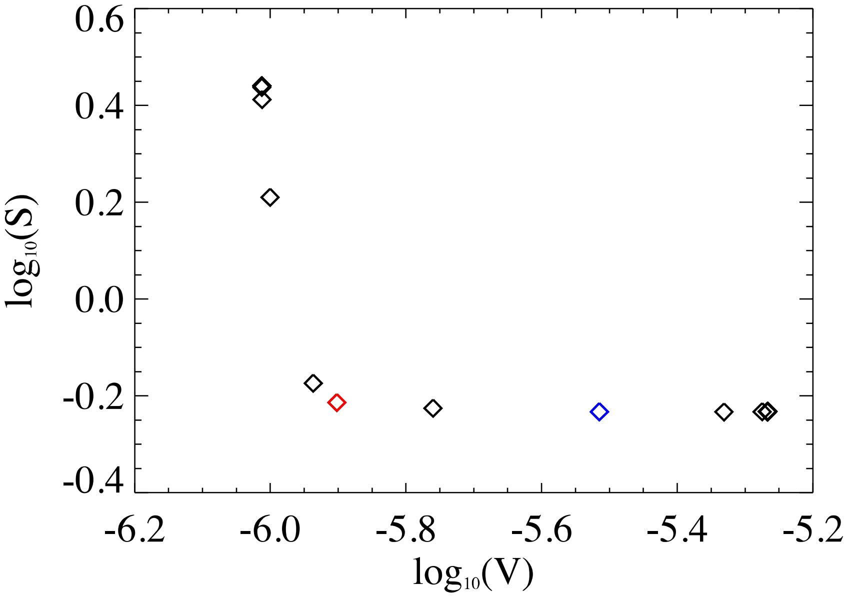

Figure 4.10: Trade-off curve in the case of rotation inversion with a target point $(x, \mu) = (0.05, 0.00)$ for the model of Kurtz et al. (2014). It is easily seen that error magnification V becomes larger as the width of the averaging kernels S becomes smaller, and vice versa. The red and blue diamonds show the values of (S, V) with which the estimates (4.39) and (4.40) are obtained, respectively.

two models, maybe resulting from the fact that we essentially do not modify the deep radiative region.

Therefore, we have three target points for carrying out rotation inversion via OLA, namely, points in the low-latitude deep radiative region, the low-latitude envelope, and the high-latitude envelope, in the same way as in the case of the model of Kurtz et al. (2014).

4.3.4 Results obtained based on OLA

With the rotational splitting kernels illustrated in the previous subsection 4.3.3 and the observed rotational shifts, we can perform rotation inversion. In this subsection, we use the OLA method, which provides us with quantities such as the averaging kernels and the inversion coefficients useful for interpreting internal rotation rates, to estimate the internal rotation rate $\hat{\Omega}(x, \mu)$ for the selected target points after we determine a value of the trade-off parameter α (see, e.g., the equation 4.26). We would like to briefly demonstrate how to determine the most probable value of α before presenting the results obtained via OLA.

We have repeated the rotation inversion 40 times for different values of α, and then, quantified the width of averaging kernels S, which corresponds to the first term in expression (4.24), and error magnification V, which corresponds to the second term divided by alpha in the same expression (4.24). We have plotted the trade-off curves (e.g. Figure 4.10), and we have chosen several values of α with which both the width of the averaging kernel S and error magnification V are sufficiently suppressed. After the selection of the candidates for a final value of α, we looked at each of the candidate's averaging kernel, and we excluded values of α with which the localization of the averaging kernel is not well achieved. Eventually, we select one or two values of α and we obtain the corresponding estimates. The same procedures have been conducted for each target point. We describe the estimates thus obtained in the following small subsections.

In the following analyses, the rotational shifts in frequencies or "generalized rotational splittings" (Goupil , 2011), are used, which are simply computed as below:

$$\delta\omega_{nlm} = \frac{\omega_{nl,m} - \omega_{nl,-m}}{2}, \tag{4.38}$$

where n, l, and m are the radial order, the spherical degree, and the azimuthal order, respectively.

The model of Kurtz et al. (2014)[4]

For the target point $(x, \mu) = (0.05, 0.00)$, we present two equally reasonable estimates (4.39) and (4.40). The first estimate is obtained for $\alpha = 10^8$, and the estimate and its standard deviation are:

$$\hat{\Omega}(0.05, 0.00) = (0.9940 \pm 0.0003)\,\Omega_{100}, \tag{4.39}$$

where $\Omega_{100} = 2\pi \times 0.01\,\mathrm{d}^{-1}$. The averaging kernel is localized well around the core region at low latitude (the upper panel in Figure 4.11), suggesting the high reliability of the estimate. The second estimate is obtained for $\alpha = 10^{10}$, and the estimate and its standard deviation are:

$$\hat{\Omega}(0.05, 0.00) = (0.9492 \pm 0.0001)\,\Omega_{100}. \tag{4.40}$$

The averaging kernel is, again, localized well around the core region at low latitude (the bottom panel in Figure 4.11).

Though we have achieved the localization of the averaging kernels reasonably well in both cases, there is a significant difference between the estimates (4.39) and (4.40). This difference can be attributed to the trade-off relation between resolution and error magnification. With the larger trade-off parameter $\alpha = 10^{10}$, suppressing error magnification is emphasized (see equation 4.24), leading to the smaller estimated standard deviation in the estimate (4.40) than that in the estimate (4.39). Meanwhile, localizing the averaging kernel is prioritized in the case of $\alpha = 10^8$, and thus, the corresponding averaging kernel behaves better than that with $\alpha = 10^{10}$; when we carefully look into the averaging kernel with $\alpha = 10^{10}$, we find that it has an oscillatory component between $x = 0.05$ and $x = 0.075$ compared with that with $\alpha = 10^8$. Therefore, we can qualitatively explain the behavior of the estimates.

For more quantitative hints, we take a look at inversion coefficients determined by rotation inversion with $\alpha = 10^8$ and those with $\alpha = 10^{10}$ (Figure 4.12). It is apparent that the averaging kernel for $\alpha = 10^{10}$ is mainly composed of the g-mode splitting kernels. On the other hand, we have also found that the averaging kernel for $\alpha = 10^8$ is composed not only of the g-mode splitting kernels but also of the mixed-mode splitting kernels. Thus, the distribution of the averaging kernels are slightly different. One possible explanation is as follows: there is a shear of the angular velocities around the core region, and thus, small differences between the two averaging kernels lead to the substantial difference in the two estimates. To test the possibility of such a fast-rotating core is one of the purposes in our three-zone modeling introduced in Subsection 4.3.5.

---

[4] Mostly cited from Hatta et al. (2019)

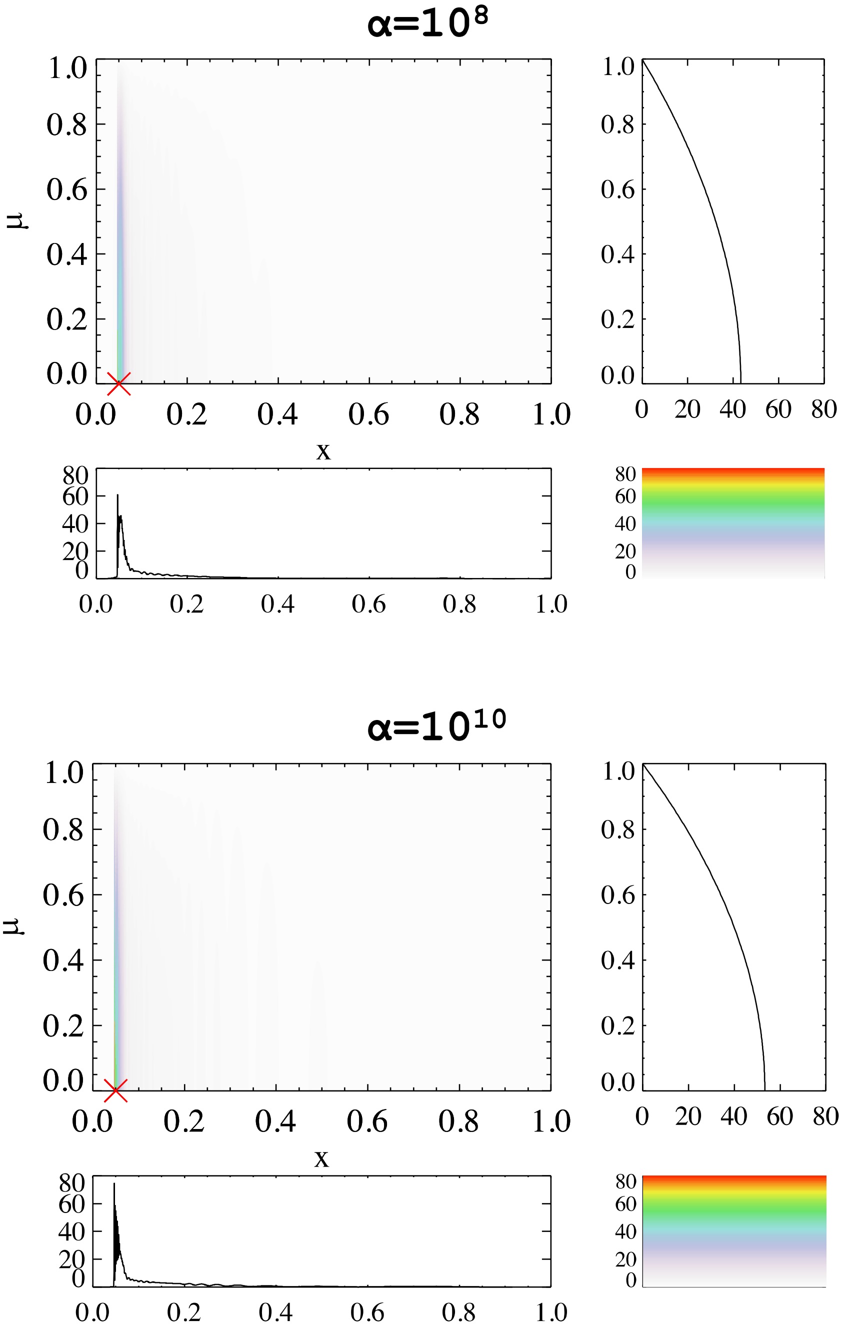

Figure 4.11: Averaging kernels for the estimate at $(x, \mu) = (0.05, 0.00)$, marked by the red cross, with $\alpha = 10^8$ (the upper-left figure in the upper panel) and with $\alpha = 10^{10}$ (the upper-left figure in the bottom panel). The model of Kurtz et al. (2014) is used. The bottom-left and the upper-right figures are slices of the averaging kernel, taken at $\mu = 0.00$ and $x = 0.05$, respectively.

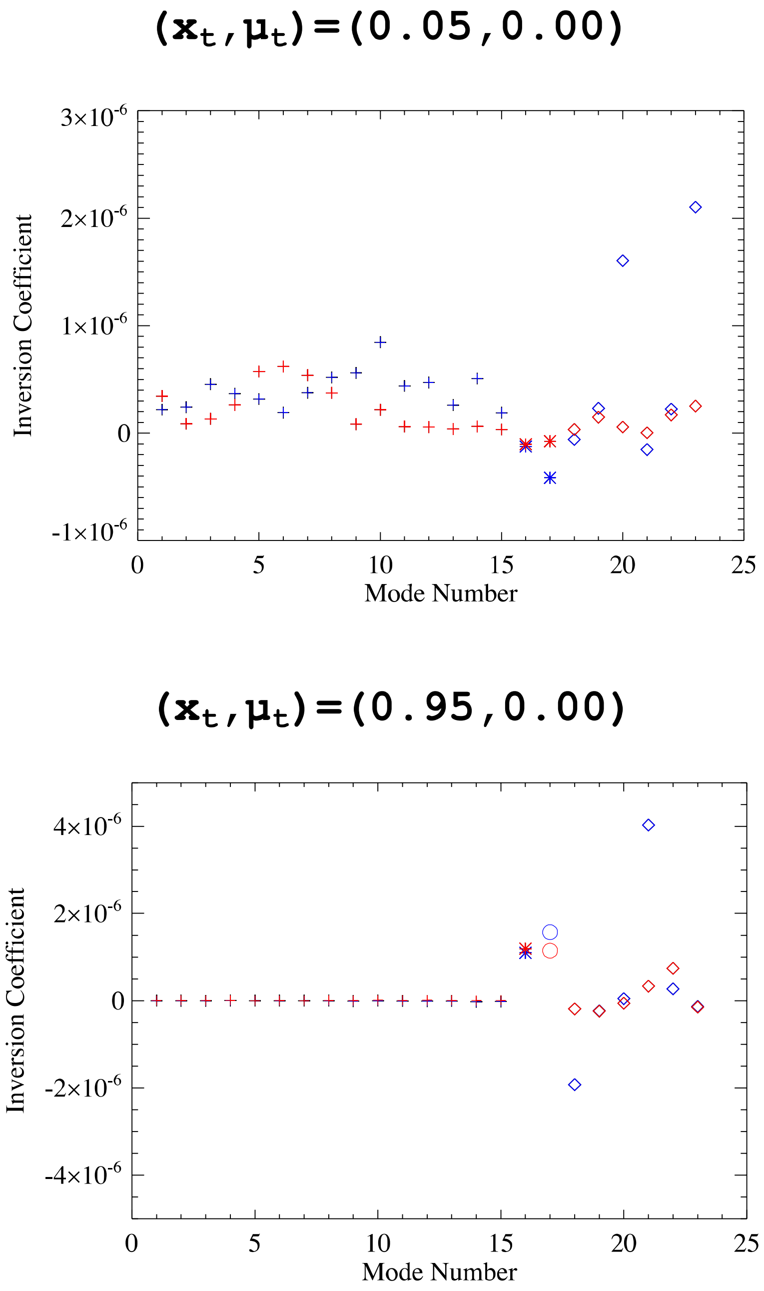

$(x_t, \mu_t) = (0.05, 0.00)$

$(x_t, \mu_t) = (0.95, 0.00)$

Figure 4.12: Inversion coefficients that result from the OLA method with $\alpha = 10^8$ (the blue marks) and $\alpha = 10^{10}$ (the red marks). The target point are $(x, \mu) = (0.05, 0.00)$ (upper) and $(x, \mu) = (0.95, 0.00)$ (bottom). The model of Kurtz et al. (2014) is used. The crosses, the asterisks, and the diamonds represent the g modes, the p modes with $l = 1$, and the mixed modes with $l = 2$, respectively. The horizontal axis, mode number, is corresponding to g modes from 1 to 15, p modes with $l = 1$ for 16 and 17, mixed modes with $(l, m) = (2, 1)$ from 18 to 20, and mixed modes with $(l, m) = (2, 2)$ from 21 to 23. Note that our inversion coefficients are for rotational splittings, not for mode frequencies.

For the target point in the low-latitude envelope, we again show two equally reasonable estimates for the target point $(x, \mu) = (0.95, 0.00)$ as follows:

$$\hat{\Omega}(0.95, 0.00) = (0.9511 \pm 0.0005)\,\Omega_{100}, \tag{4.41}$$

which has been obtained with $\alpha = 10^8$, and

$$\hat{\Omega}(0.95, 0.00) = (0.9706 \pm 0.0002)\,\Omega_{100}, \tag{4.42}$$

which has been obtained with $\alpha = 10^{10}$.

The averaging kernels for both estimates have peaks in the outer envelope (Figure 4.13), and both of them are apparently localized around the target point. Nevertheless, we see that the averaging kernel for $\alpha = 10^8$ has a higher peak than for $\alpha = 10^{10}$ because more emphasis is put on resolving the averaging kernel in the case of $\alpha = 10^8$. On the other hand, the estimate (4.41) has a larger standard deviation than the estimate (4.42) has since suppressing error magnification is less focused on in the case of $\alpha = 10^8$ than in the case of $\alpha = 10^{10}$. Thus, we clearly see the trade-off relation.

In order to see the origins of the significant difference in the two estimates, we assessed the inversion coefficients (Figure 4.12) as is done for the first estimate. In the case of $\alpha = 10^8$, the mixed-mode ($l = 2$) splitting kernels are mainly used for the averaging kernel. However, in the case of $\alpha = 10^{10}$, the p-mode ($l = 1$) splitting kernels are mostly used for the averaging kernel. The above difference should lead to the two equally reasonable estimates.

For the target point $(x, \mu) = (0.95, 0.70)$, one estimate is obtained with $\alpha = 10^8$ as follows:

$$\hat{\Omega}(0.95, 0.70) = (0.9564 \pm 0.0006)\,\Omega_{100}. \tag{4.43}$$

The weak dependence of the estimate on the trade-off parameter α is due to the small number of splitting kernels which have sensitivity in high-latitude regions; we do not have any other choice. When we increased the importance of error magnification by increasing α, we have failed in localizing the averaging kernel (the bottom panel in Figure 4.14) in contrast to the case with the smaller value of α (the upper panel in Figure 4.14). By comparing the estimate (4.43) with the estimates (4.41) or (4.42), we find the possibility that there is latitudinally differential rotation in the outer envelope. We would like to expand our discussion on the existence of the latitudinally differential rotation in Subsection 4.3.5.

The envelope-modified model

As in the last small subsection, the results of rotation inversion via the OLA method based on the envelope-modified model for the three target points, in the low-latitude deep radiative region, the low-latitude envelope, and the high-latitude envelope, are shown. The basic procedure to determine the trade-off parameter α is the same as that in the last small subsection.

The first target point is $(x, \mu) = (0.05, 0.00)$, and there is one estimate as follows:

$$\hat{\Omega}(0.05, 0.00) = (0.9765 \pm 0.0004)\,\Omega_{100}. \tag{4.44}$$

The corresponding averaging kernel is shown in Figure 4.15, and the sensitivity of the averaging kernels are not so changed depending on values of α, which is the reason why we have selected one estimate for the target point. The estimate is somewhat between those in the case of Hatta et

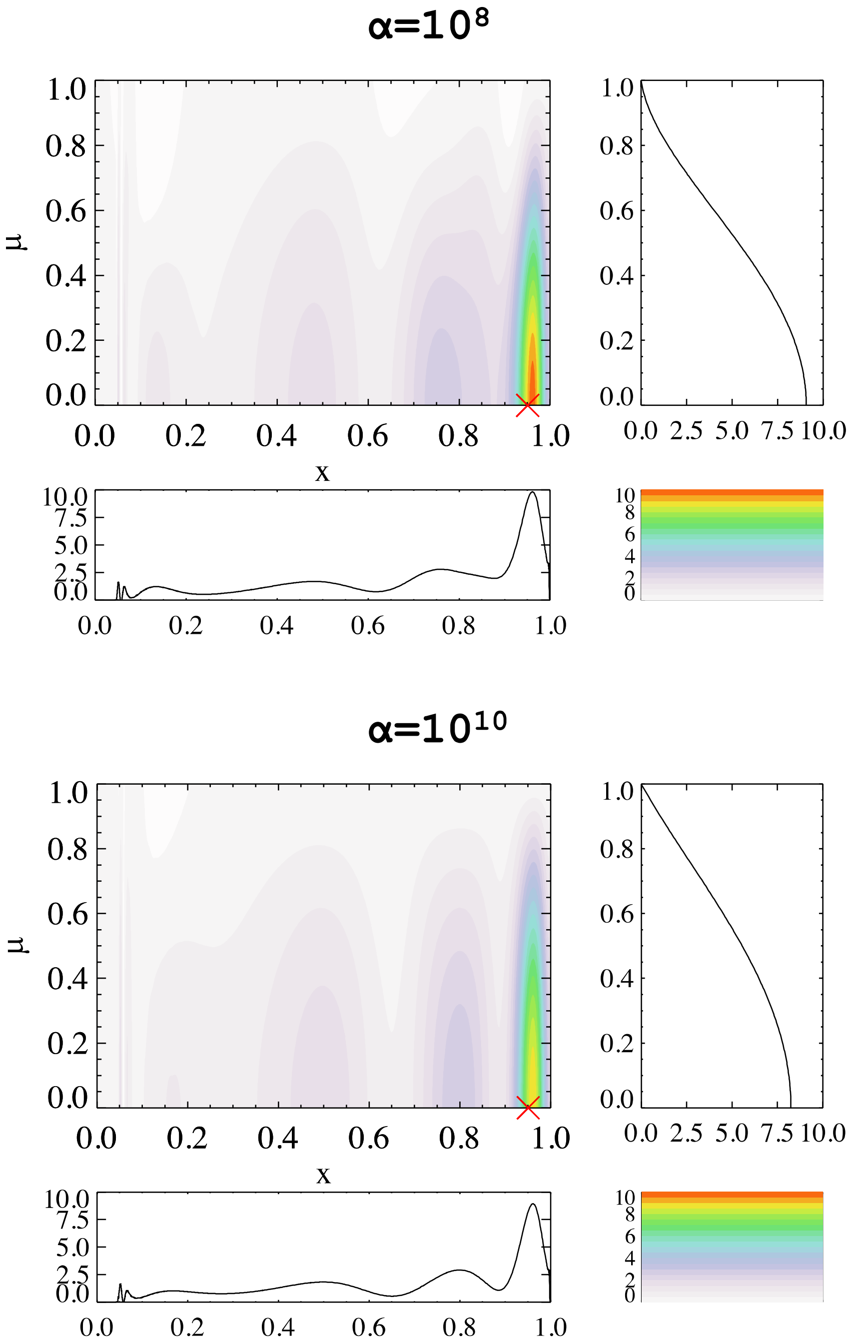

Figure 4.13: Averaging kernels for the internal rotation estimate at $(x, \mu) = (0.95, 0.00)$, marked by the red cross, with $\alpha = 10^8$ (the upper-left figure in the upper panel) and with $\alpha = 10^{10}$ (the upper-left figure in the bottom panel). The model of Kurtz et al. (2014) is used. The bottom-left figure is a slice of the averaging kernel, at $\mu = 0.00$, showing that the averaging kernel is distributed in the outer envelope. The upper-right figure is another slice of the averaging kernel, at $x = 0.95$.

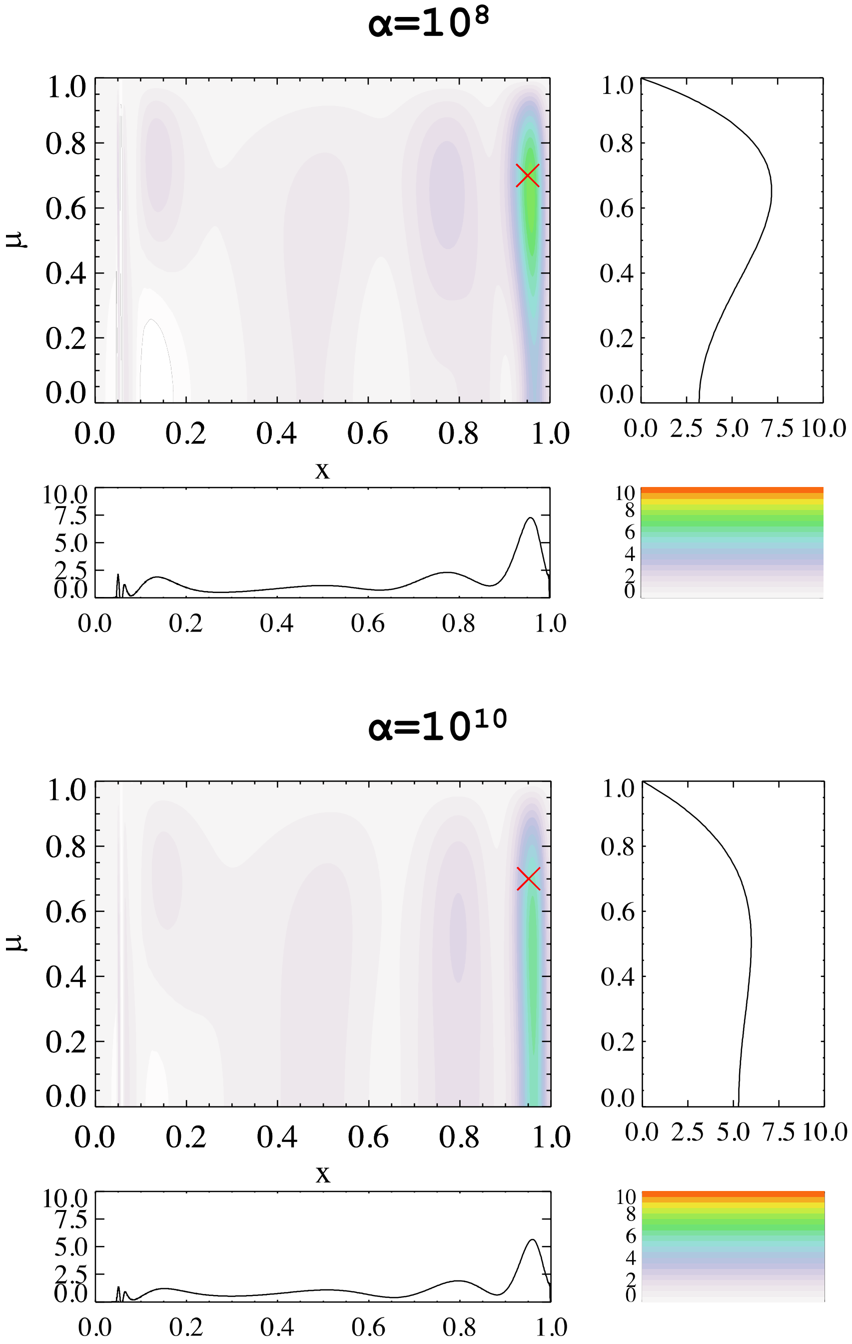

Figure 4.14: Averaging kernels for the estimate at $(x, \mu) = (0.95, 0.70)$, marked by the red cross, with $\alpha = 10^8$ (the upper-left figure in the upper panel) and with $\alpha = 10^{10}$ (the upper-left figure in the bottom panel). The model of Kurtz et al. (2014) is used. The bottom-left figure is a slice of the averaging kernel, at $\mu = 0.70$, showing that the averaging kernel is distributed in the outer envelope. The upper-right figure is another slice of the averaging kernel, at $x = 0.95$ which indicates that the maximum of the averaging kernel is located in high-latitude region.

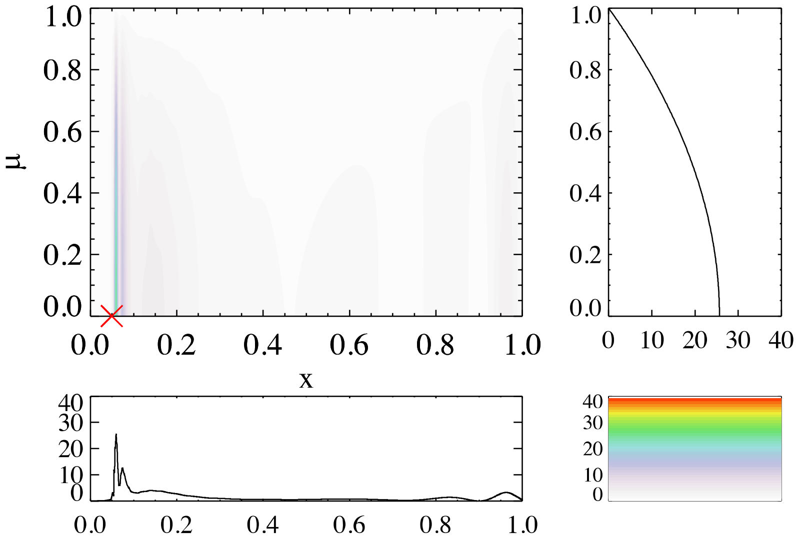

Figure 4.15: Averaging kernel for the estimate at $(x, \mu) = (0.05, 0.00)$, marked by the red cross, with $\alpha = 10^8$ (the upper-left figure). The envelope-modified model is used. The bottom-left and the upper-right figures are slices of the averaging kernel, taken at $\mu = 0.00$ and $x = 0.05$, respectively. It should be noticed that the slice of the averaging kernel at the fixed colatitude (the bottom-left figure) shows a structure different from that in the case of the model of Kurtz et al. (2014) (Figure 4.11); while this averaging kernel is mainly composed by the mixed-mode splitting kernels, the other averaging kernel is mainly composed by the g-mode splitting kernels.

al. (2019), and this is due to the sensitivity of the mixed-mode rotational splitting kernels of the envelope-modified model. As seen in Figure 4.9, the mixed-mode splitting kernels with $l = 2$ are more concentrated on the deep radiative region than those for Kurtz et al. (2014), and thus, they are more likely to be used to localize the averaging kernel; instead, the g-mode splitting kernels are not used, which is a difference between the estimate (4.40) and the one (4.44). When we carry out rotation inversion only with the g-mode splitting kernels, almost the same result as the estimate (4.40) is obtained. This is reasonable because we fixed the deep radiative region of the envelope-modified model, and the g-mode splitting kernels are accordingly not affected much, leading to similar inferences.

The second target point is $(x, \mu) = (0.95, 0.00)$, and there is again one estimate as follows:

$$\hat{\Omega}(0.95, 0.00) = (0.9809 \pm 0.0007)\,\Omega_{100}. \tag{4.45}$$

The averaging kernel is illustrated in Figure 4.16, and it is clearly seen that it is successfully localized around the target point, although the contour shows a less smooth structure compared with the averaging kernels in the case of the model of Kurtz et al. (2014) (see Figure 4.13). This is also attributed the fact that the averaging kernel here is mainly composed by the mixed-mode splitting kernels, some of which are negatively contributing to the averaging kernel, and such non-smooth structure in the averaging kernel can be seen.

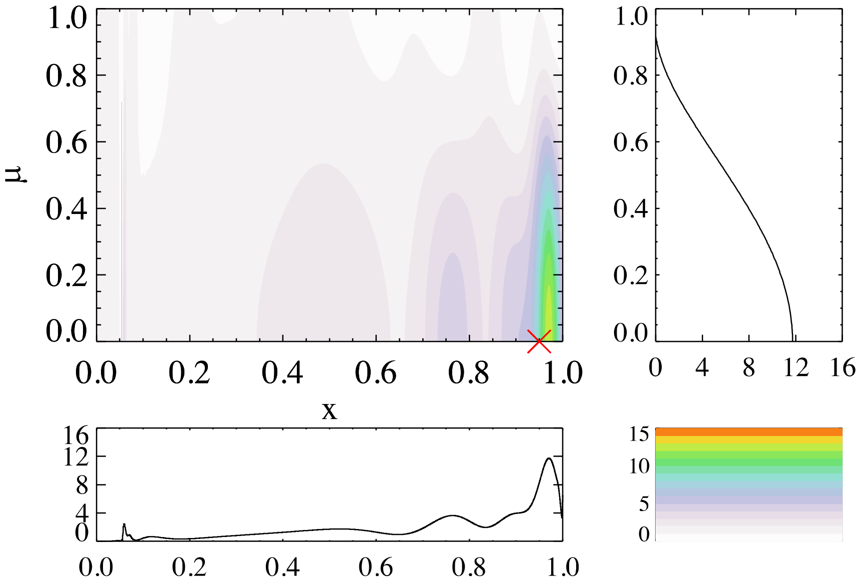

Figure 4.16: Averaging kernel for the estimate at $(x, \mu) = (0.95, 0.00)$, marked by the red cross, with $\alpha = 10^8$ (the upper-left figure in the left panel). The envelope-modified model is used. The bottom-left and the upper-right figures are slices of the averaging kernel, taken at $\mu = 0.00$ and $x = 0.05$, respectively.

The third target point is $(x, \mu) = (0.95, 0.70)$, and we have one estimate as below:

$$\hat{\Omega}(0.95, 0.70) = (0.988 \pm 0.002)\,\Omega_{100}. \tag{4.46}$$

which is obtained so that the corresponding averaging kernel is well localized around the target point. When suppressing error magnification is more prioritized, we cannot guarantee the localization of the averaging kernel, and it also has sensitivity in the low-latitude region (the bottom panel in Figure 4.17).

Though we have seemingly different estimations for the three target points depending on which model (Kurtz et al.'s model or the envelope-modified one) to be used, it should be pointed out that a general trend is common for both cases, as shown in later discussions (Subsection 4.3.5).

4.3.5 Discussions

First, we would like to compare the results of the OLA method obtained based on the model of Kurtz et al. (2014) with those obtained based on the envelope-modified model. The apparent difference between them can be explained by carefully investigating the inversion coefficients and the averaging kernels, based on which a general trend of the internal rotation of the star is inferred. Then, we would like to discuss the inferred internal rotational profile of the star from several different perspectives using inversion techniques introduced in Subsection 4.3.2, especially focusing on the existence of the fast-convective-core rotation. The latitudinally differential rotation is also discussed.

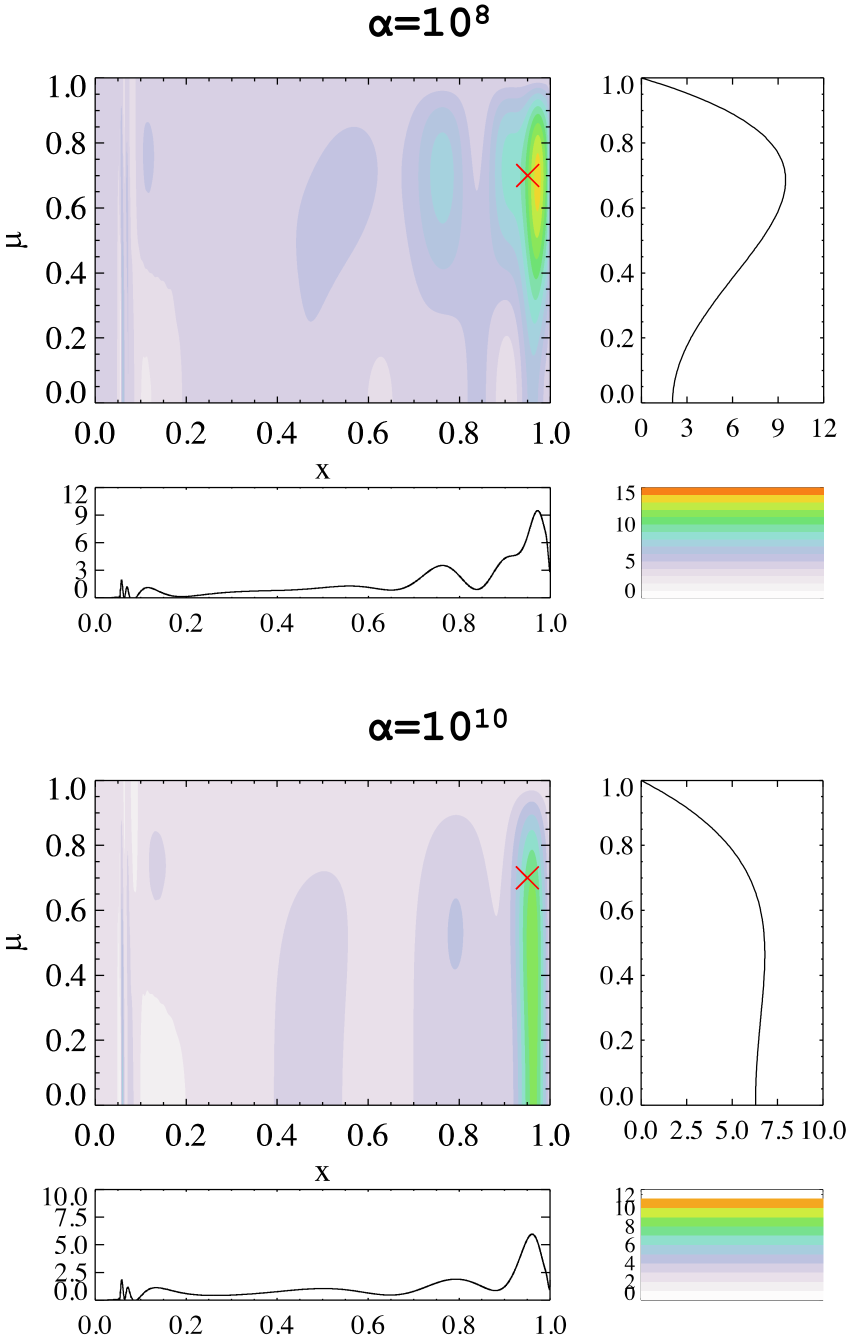

Figure 4.17: Averaging kernels for the estimate at $(x, \mu) = (0.95, 0.70)$, marked by the red cross, with $\alpha = 10^8$ (the upper-left figure in the upper panel) and with $\alpha = 10^{10}$ (the upper-left figure in the bottom panel). The envelope-modified model is used. The bottom-left and the upper-right figures are slices of the averaging kernel, taken at $\mu = 0.95$ and $x = 0.70$, respectively. The same feature as in Figure 4.14 can be observed here, namely, the averaging kernel is more localized around the target point, as the trade-off parameter α is smaller.

General trend of the internal rotation of the star obtained via the OLA method

Kurtz et al. (2014) have model-independently shown that the envelope of the star is rotating slightly faster than the deep radiative region is (see Subsection 1.3.2). But such trend is difficult to confirm with the estimates we obtained in the previous subsection; for example, in the case based on the model of Kurtz et al. (2014), the two possible estimates for the outer region (4.41) and (4.42) are between the two possible ones for the deep radiative region (4.39) and (4.40). These somewhat broader ranges of the estimates are attributed to different sets of inversion coefficients.

In the case based on the model of Kurtz et al. (2014) (blue and turquoise in Figure 4.18), it is easily seen that the g-mode rotational shifts are mainly contributing to the estimate (4.40) where the trade-off parameter α is 10^{10} (see turquoise symbols). On the other hand, when $\alpha = 10^8$ is adopted (blue symbols), not only the g-mode but also the mixed-mode ($l = 2$) rotational shifts are used for the faster estimate (4.39). Because high-order g modes cannot propagate the convective region and their mode energy density is much smaller in the envelope than that in the deep radiative region (see Figure 4.19), we consider the slower estimate (4.40), which are mainly composed by the g-mode rotational shifts, as a conservative estimate for the internal rotation rate in the deep radiative region. This conservative estimate is also reproduced in the case with the envelope-modified model if we carry out rotation inversion via OLA to infer the internal rotation rate at the target point $(x, \mu) = (0.05, 0.00)$ without p or mixed modes, indicating little model dependence of the inference. We have thus confirmed the same trend as suggested by Kurtz et al. (2014) that the envelope of the star rotates slightly faster than the deep radiative region does, since the conservative estimate (4.40) is always significantly smaller than all the estimates for the target point $(x, \mu) = (0.95, 0.00)$ no matter which model is used.

Then, what renders the estimate (4.39) to be so large? The faster estimate should result from the internal rotation of some regions where the high-order g modes cannot propagate with large amplitudes, i.e. the convective core or the outer envelope. To check the origin of the faster estimate is one of the reasons why we carry out the three-zone modeling of the internal rotation profile of the star and the Bayesian rotation inversion in the following small subsections.

We finally would like to mention the latitudinal dependence of the internal rotation of the star. Although it is difficult to draw any model-independent conclusion from the estimates for the high- and low-latitude regions in the envelope because they cover a large range of the rotational velocities, both of the two models are suggesting a trend that the high-latitude region is rotating slightly faster than the low-latitude region (compare the estimates 4.45 and 4.46 in the case of the envelope-modified model, and also see discussions that the estimate 4.41, which is slower than the only possible estimate for the high-latitude region 4.43 in the case based on the model of Kurtz et al. (2014), is more favored in terms of the localization of the averaging kernels).

Such trend has been later confirmed as well in a rather model-independent manner in one of the following small subsections.

A hint for the fast-core rotation [5]

The discussions in the preceding small subsection have allowed us to confirm one of the results of Kurtz et al. (2014) that the envelope of the star is rotating slightly faster than the deep radiative region. Then, why are the estimates, for example, (4.39), for which the mixed-mode rotational shifts are mainly used, significantly larger than the estimate obtained only by g-mode rotational

---

[5] Mostly cited from Hatta et al. (2019)

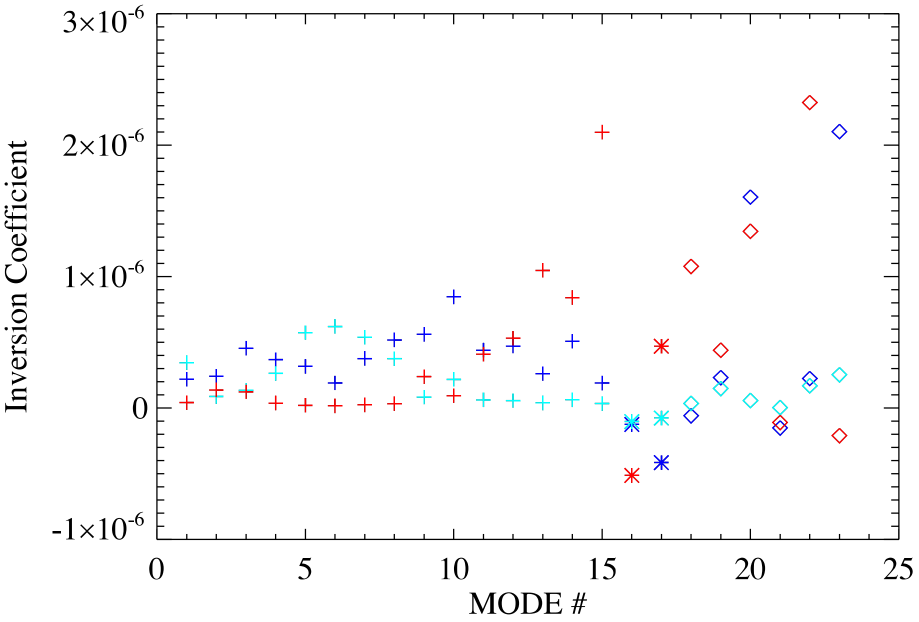

Figure 4.18: Inversion coefficients for the estimates (4.39) (blue), (4.40) (turquoise), and (4.44) (red). The definition of the horizontal axis and the meanings of the symbols are explained in the caption of Figure 4.12. In the case of the model of Kurtz et al. (2014) (blue and turquoise), the g-mode rotational shifts are more frequently used as the trade-off parameter α becomes larger. On the other hand, in the case of the envelope modified model (red), both the g-mode and the mixed-mode rotational shifts are used, leading to the estimate (4.44) which is between the two estimates (4.39) and (4.40).

shifts? One possible explanation is that there exists a velocity shear around the boundary of the convective core in which high-order g modes cannot propagate but low-order mixed modes can (see Figure 4.19). If such a velocity shear exists and the convective core is rotating much faster than the the deep radiative region above is, the estimate mainly composed by the mixed-mode rotational shifts can be affected by the fast-core rotation, leading to the relatively large estimate. To test the possibility and to obtain a hint for how fast the convective core is rotating, we have carried out the three-zone modeling of the internal rotation of the star. For detailed information about the method, see Subsection 4.3.2.

The estimates of the internal rotation which makes the residual of the inversion minimum (in the case based on the model of Kurtz et al., 2014) is as follows:

$$\Omega_1 = (5.57 \pm 0.03)\,\Omega_{100}, \tag{4.47}$$

$$\Omega_2 = (0.9348 \pm 0.0001)\,\Omega_{100}, \tag{4.48}$$

$$\Omega_3 = (1.0930 \pm 0.0006)\,\Omega_{100}, \tag{4.49}$$

which are obtained when x_a is 0.046 and x_b is 0.905. Interestingly, we have obtained a result which suggests that the innermost region rotates about 6 times faster than the other parts of the star.

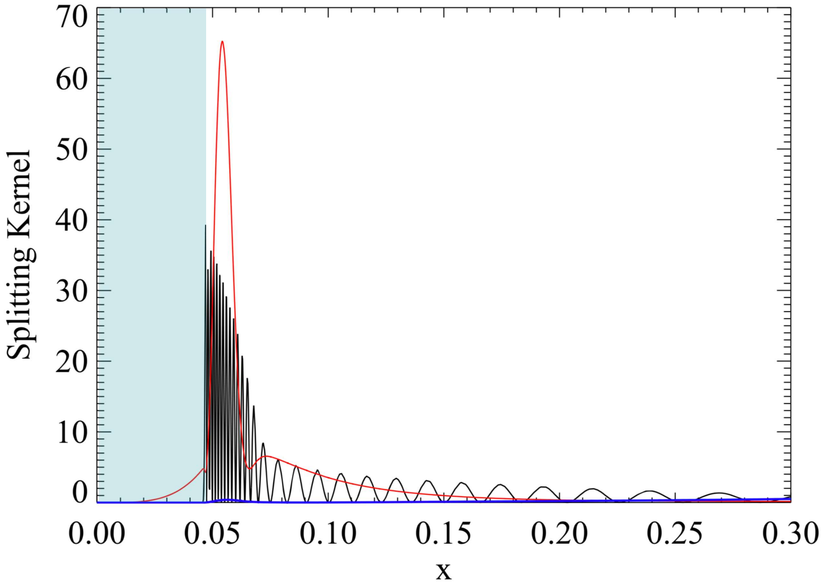

Figure 4.19: Slices of rotational splitting kernels of a high-order g mode (black), a low-order p mode (blue, almost completely overlap with the horizontal axis), and a mixed mode (red). The convective core is indicated by the area colored by turquoise. Because the buoyancy force cannot act as a restoring force, g modes cannot propagate the convective region, which is why the g-mode splitting kernel has no sensitivity inside the convective core. In contrast, the mixed-mode kernel has, though quite small, sensitivity inside the convective core.

Moreover, the inner boundary x_a is almost identical to the edge of the convective core. This result indeed indicates the existence of the shear of the angular velocities, as suggested in the last small subsection. We also see that the deep radiative region (region 2) rotates slightly slower than the outer region (region 3), which is the same trend as indicated by the result of the two-zone modeling in Kurtz et al. (2014).

The estimates of the internal rotation based on the envelope-modified model is as follows:

$$\Omega_1 = (13.48 \pm 0.09)\,\Omega_{100}, \tag{4.50}$$

$$\Omega_2 = (0.9412 \pm 0.0001)\,\Omega_{100}, \tag{4.51}$$

$$\Omega_3 = (1.1023 \pm 0.0006)\,\Omega_{100}, \tag{4.52}$$

which are obtained when x_a is 0.046 and x_b is 0.900, showing the same trend as seen in the estimates obtained by the three-zone modeling (4.47) to (4.49). Therefore, we have found a hint for the fast-convective-core rotation for both the previous model of Kurtz et al. (2014) and the envelope-modified one, indicating little qualitative model dependence of the inference.

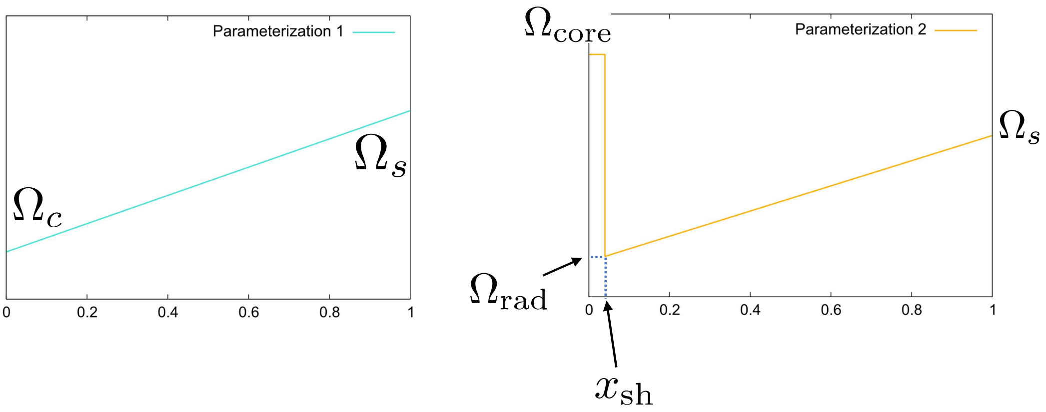

Figure 4.20: Schematic pictures for two ways of parameterizing the function $\Omega_0(x)$ in the expression (4.53). The linear profile is described with two parameters, the rotation rate at the center Ω_{c} and that at the surface Ω_{s}, linearly connected to each other (left). The other profile contains a velocity shear, and the profile is described by four parameters, namely, the rotation rate inside the core Ω_{core}, that at the outer boundary of the velocity shear Ω_{rad}, that at the surface Ω_{s}, and the position of one of the boundaries of the velocity shear x_{sh}. Note that another boundary of the velocity shear is fixed to be the convective boundary; x_{sh} could be either the inside or the outside of the convective core. Except for the inner core which is assumed to be rotating rigidly with Ω_{core}, rotation rates of the other regions are linearly expressed.

Bayesian inversion for further quantitative model selection

The three-zone modeling of the internal rotation carried out in the previous small subsection has succeeded in, qualitatively, showing that there is only a small model dependence of the inference of the fast-convective-core rotation. In this small subsection, we attempt to evaluate the plausibility of the fast-core rotation, in a more quantitative way, based on the Bayesian scheme introduced in Subsection 4.3.2, which enables us to compute the probability of a model (in this case, a certain rotational profile somehow parameterized) and also allows us to compare models to choose one best model.

The first step for the Bayesian model comparison is to define sets of models to be considered, or to determine how to parameterize the rotational profile $\Omega(x,\mu)$, based on which we compute the likelihood of parameters (see the equation 4.33). We parameterize the rotational profile as below:

$$\Omega(x,\mu) = \Omega_0(x) + \mu^2\Omega_1(x), \tag{4.53}$$

where $\Omega_0(x)$ can have a linear profile (with two parameters, namely, the rotation rate at the center Ω_{c} and that at the surface Ω_{s}) or can have a velocity shear (with four parameters, namely, the rotation rate below a velocity shear boundary x_{sh} which is assumed to be uniform Ω_{core}, the rotation rate at another edge of the shear boundary fixed to be the convective core boundary Ω_{rad}, and that at the surface Ω_{s}) (see Figure 4.20). Another function $\Omega_1(x)$, which is related to the latitudinal dependence of the internal rotation, can be zero elsewhere (with no parameters) or can have a

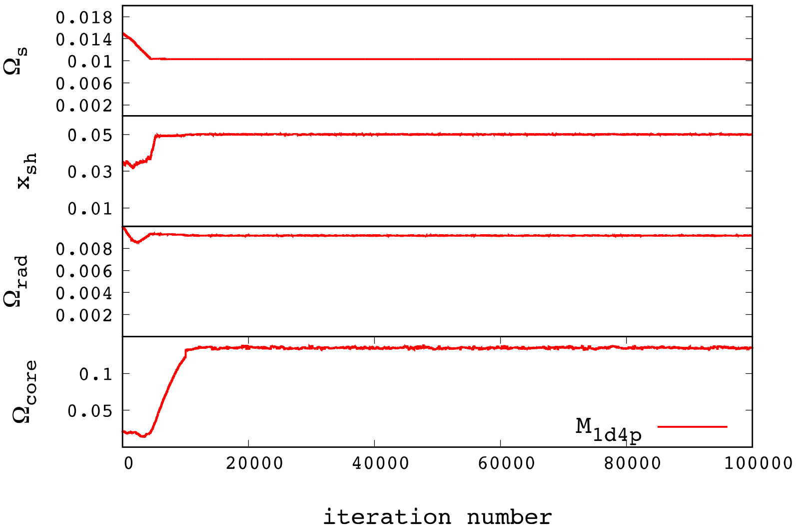

Figure 4.21: Samples obtained by the Metropolis method (Metropolis et al., 1953) which are considered to be distributed following the posterior probability. Here is the case of the parameterization $M_{1\mathrm{d}4\mathrm{p}}$, which can have a velocity shear (for the definition of the denotation, see the text). It is clearly seen that the parameters are distributed around some mean values (converged) after the iteration number reaches around 10^4. The period during which the parameters have not converged is called the burn-in period. We can also roughly estimate parameters by just looking at the converged values. For example, it is seen that a rough mean value of Ω_{core} (in the bottom panel) is about 0.13 d^{-1}.

linear profile (with two parameters, in almost the same way as a linear profile of $\Omega_0(x)$ but with additional indices as $\Omega_{1\mathrm{c}}$ and $\Omega_{1\mathrm{s}}$). With the definitions for $\Omega_0(x)$ and $\Omega_1(x)$, there are four ways of parameterization of the rotational profile in total. Let us denote the models as follows: $M_{1\mathrm{d}2\mathrm{p}}$ for linear Ω_0 and zero Ω_1, $M_{1\mathrm{d}4\mathrm{p}}$ for shear Ω_0 and zero Ω_1, $M_{2\mathrm{d}4\mathrm{p}}$ for linear Ω_0 and linear Ω_1, and $M_{2\mathrm{d}6\mathrm{p}}$ for shear Ω_0 and linear Ω_1.

Then, for each way of parameterization, the posterior probability of the parameters is computed based on the likelihood of the parameters and the prior probability. As described in Subsection 4.3.2, each prior probability for a certain parameter is assumed to be uniform as below:

$$\Omega_{\mathrm{c}},\, \Omega_{\mathrm{s}},\, \Omega_{\mathrm{core}},\, \Omega_{\mathrm{rad}}, \Omega_{1\mathrm{c}},\, \Omega_{1\mathrm{s}} \sim U[0.001, 0.3] \text{ (in units of } d^{-1}) \tag{4.54}$$

and

$$x_{\mathrm{sh}} \sim U[0.00, 0.075], \tag{4.55}$$

where $q \sim U[a, b]$ means that q is a random variable uniformly distributed in a range from a to b. The joint prior probability is computed by taking products of prior probabilities assuming that the parameters are statistically independent from each other. The likelihood is calculated with the expressions (4.33) and (4.34). The number of the mode is 23. The rotational splitting kernels of Kurtz et al.'s model are used in this analysis. We carry out the Metropolis method (Metropolis et al., 1953), which is one of the standard algorithms to carry out MCMC, to evaluate the posterior

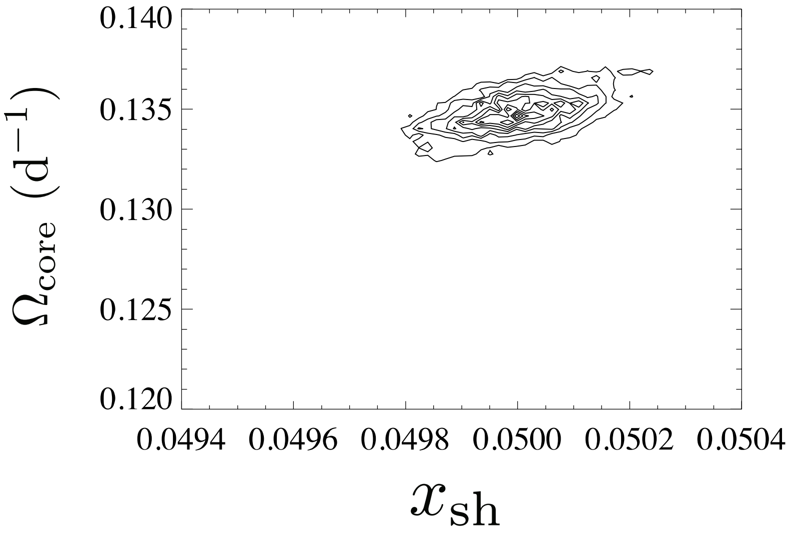

Figure 4.22: Example of the contour of the joint posterior probability of $\Omega_{\rm core}$ and $x_{\rm sh}$ marginalized by the other parameters. If we estimate $\Omega_{\rm core}$ based on the Maximum A Posteriori estimation (see the text in Section 4.3.3), $\hat{\Omega}_{\rm core}$ would be 0.135 d^{-1}. The estimated uncertainty can be also determined by, for instance, the width of the posterior probability.

probability. The convergence of samples generated via the Metropolis method has been checked by visual inspection (see Figure 4.21). A typical number of iterations is of the order of 10^5, and about a fraction of samples are discarded from the final samples as they are considered as samples in the burn-in periods (which is the period during which obtained samples are not thought to be realizations from the posterior probability distribution we would like to sample). More information on principles of MCMC, how to manage the outcomes of MCMC and so on, can be found in Gregory (2005b).

The most important part in the Bayesian model comparison is to compute the global likelihood for each way of parameterization of the rotational profile. For the computations of the global likelihoods, we follow the procedures proposed by Chib and Jeliazkov (2001) in which an exact value of the posterior probability of a particular set of the parameters is directly evaluated, and then, the global likelihood is calculated based on the relation (4.32). We have confirmed that the method correctly works for simple cases where we can analytically compute the posterior probability and the global likelihood. The logarithm of the thus obtained global likelihoods for the four models $M_{\rm 1d2p}$, $M_{\rm 2d4p}$ (no-velocity-shear profiles), $M_{\rm 1d4p}$, and $M_{\rm 2d6p}$ (with-velocity-shear profiles) are -55430, -53988, -44587, and -42977, clearly indicating that the rotational profiles with the velocity shear (the latter two) are more favored than those without the shear (the former two). We can also confirm that based on the posterior probability of $\Omega_{\rm core}$ for the models with the velocity shear, the fast-core rotation is again inferred (Figure 4.22).

Is the fast-core rotation reasonable? [6]

Aerts et al. (2017) summarized the studies on the internal rotation of main-sequence A-F type stars, and they concluded that almost all the stars investigated so far exhibited nearly rigid rotation. This is different from the result we have obtained through the present study; there can be a strong velocity shear between the convective core and the radiative region above. Our result, however, is actually not incompatible with their view because all the studies in Aerts et al. (2017) have estimated the "core" rotation based on g modes with which we cannot extract the information on the convective core. Thus, what they have inferred are internal rotation of the "deep radiative" region above the convective core. Meanwhile, our estimation of "core" rotation is based on a mixed mode which has sensitivity inside the convective core. We have succeeded in extracting information on the convective core, which enables us to reveal the fast-core rotation of KIC11145123. Furthermore, our results show that the radiative region of the star rotates nearly rigidly (e.g. see the estimates 4.48 and 4.49). This result is consistent with the current understanding of the internal rotation of A-F stars.

From the theoretical point of view, there have been a series of numerical simulations of the dynamo mechanism inside the convective core of A type stars (e.g. Browning et al., 2004; Brun et al., 2005; Featherstone et al., 2009) where internal differential rotation has been also calculated. In particular, though they focused more on the magnetism of A stars, one of their studies (Browning et al., 2004) reproduced internal rotation profile in which the convective core rotates a few times faster than the radiative region above, which is similar to what we have found in this study. The fast-core rotation in an A star might be theoretically feasible.

Latitudinally differential rotation [7]

Based on the estimates (4.45) and (4.46), we can simply conclude that the high-latitude region is rotating faster than the low-latitude region. However, this is not the case for the model of Kurtz et al. (2014); the estimates are ordered as: $\hat{\Omega}(0.95, 0.00)_{\alpha=10^8} < \hat{\Omega}(0.95, 0.70)) < \hat{\Omega}(0.95, 0.00)_{\alpha=10^{10}}$. Actually, we probably obtain innumerable estimates by changing the value of α between 10^8 and 10^{10}, and thus, it is possible that there exist estimates based on which we do not find any latitudinal dependence of the internal rotation in the outer envelope.

In order to check whether latitudinally differential rotation does exist or not, we focus on the three quintuplets which are identified as $l = 2$ and we directly compute so-called "a-coefficients" of the three multiplets. The a-coefficients are coefficients which are used in an expansion of a frequency shift as follows:

$$\omega_{nlm} - \omega_{nl0} = \sum_k a_k(n,l)\mathcal{P}_k(m;l), \tag{4.56}$$

where k is the order of the expanding polynomial $\mathcal{P}_k(m;l)$ (Ritzwoller and Lavely, 1991). In the present paper, we followed the formulation of Schou et al. (1994). It is easily shown that the odd-order terms a_{2k+1} correspond to rotational splitting by substituting the expression (4.56) into the definition (4.38). In particular, the sign of the a_3 coefficient represents the latitudinal dependence of the internal rotation; the positive (negative) value corresponds to the faster internal rotation in the low (high) latitude region. From the observed rotational shifts, we computed three a_3 coefficients for the quintuplets $(n,l) = (-1,2), (0,2), (2,2)$ with the propagated standard deviations as below:

$$a_3^{\text{obs}}(-1,2) = (-6.7 \pm 3.3) \times 10^{-6}\ \text{d}^{-1}$$

---

[6] Mostly cited from Hatta et al. (2019)

[7] Mostly cited from Hatta et al. (2019)

$$a_3^{\text{obs}}(0,2) = (0.15 \pm 1.3) \times 10^{-6}\ \text{d}^{-1}$$
$$a_3^{\text{obs}}(2,2) = (-1.8 \pm 8.6) \times 10^{-6}\ \text{d}^{-1}.$$

As we see, $a_3^{\text{obs}}(-1,2)$ is smaller than zero with more than 2σ significance, suggesting that the high-latitude region rotates faster than the low-latitude region does. Nevertheless, both $a_3^{\text{obs}}(0,2)$ and $a_3^{\text{obs}}(2,2)$ are zero within the error bars. For assessing whether there is latitudinal dependence of the internal rotation or not based on all the three a_3 coefficients, we carried out a simple statistical test. The null hypothesis we would like to reject is that $a_3(n,l) = 0$ for any multiplet, and we assume that the probability density function of each observed a_3 coefficient is distributed as Gaussian with the mean and the standard deviation equal to zero and its observational estimate, respectively. Then, we calculated probability that we measure a_3 coefficient whose absolute value is larger than that of the actually observed one, $a_3^{\text{obs}}(n,l)$, as below:

$$p(n,l) = \int_{\text{out}} \frac{1}{\sqrt{2\pi}\sigma(n,l)} \exp\left(-\frac{1}{2}\frac{(x-0)^2}{\sigma(n,l)^2}\right) dx,$$

where x is a dummy variable and $\sigma(n,l)$ is an observational estimate of the standard deviation of $a_3^{\text{obs}}(n,l)$. The integration is carried out over the region, $-\infty < x < -a_3^{\text{obs}}(n,l)$ or $a_3^{\text{obs}}(n,l) < x < \infty$. Note that $a_3^{\text{obs}}(n,l)$ represents the actual observed value here. Thus, the probability that we measure a set of a_3 coefficients $\{a_3(-1,2), a_3(0,2), a_3(2,2)\}$ which satisfies the following conditions

$$|a_3(-1,2)| \geq |a_3^{\text{obs}}(-1,2)|$$
$$|a_3(0,2)| \geq |a_3^{\text{obs}}(0,2)|$$
$$|a_3(2,2)| \geq |a_3^{\text{obs}}(2,2)|$$

are simply calculated as below:

$$p = p(-1,2) \times p(0,2) \times p(2,2),$$

and we found that the value of p is 0.033. This is more than 2σ significance but less than 3σ significance, and thus, we conclude that it is marginal to reject the null hypothesis and to claim that $a_3 \neq 0$. Nonetheless, if we admit the existence of the latitudinally differential rotation, it is implied that the high-latitude region rotates faster than the low-latitude region does since the observed a_3 coefficients seem to favor negative values. This feature is sometimes called anti-solar differential rotation (e.g. Brun et al., 2017).

4.4 Discussions overall

Detailed asterosesimic analyses of KIC 11145123 in Sections 4.2.3 and 4.3.5 have revealed a number of fascinating characteristics of the star. Firstly, based on the non-standard modeling of the star, it is shown that the star may well have experienced some chemical composition modifications during its evolution, supporting the fact that the star is spectroscopically a blue straggler (Takada-Hidai et al., 2017). Secondly, a deviation from the observed ΔP_{g} pattern between that of the obtained envelope-modified model tells us that the chemical composition gradient in the deep radiative region of the star should be much steeper than that in the current envelope-modified model, and one of the most promising candidates to render the chemical composition gradient steeper is the diffusion processes which are much weaker than those usually assumed in the ordinary stellar evolutionary calculation. Thirdly, a hint for the fast-convective-core rotation of the star has been found via several inversion techniques, while the other regions are rotating almost rigidly throughout the star as already reported by Kurtz et al. (2014).

Then, are there any relations among these results which have been independently inferred? To find answers to the question above is a major goal of this section, and the physical properties of the star inferred so far are reviewed from broader perspectives.

4.4.1 Relation between the inferred velocity shear and the internal structure

It is generally considered that a velocity shear causes instabilities around the shear boundary and finally mixes the region to some extent. Therefore, for KIC 11145123, it is expected that the inferred fast-core rotation, or the inferred rotational velocity shear between the convective core and the radiative region above, can cause instabilities which lead to mixing around the convective core boundary. Although it is almost impossible to directly observe such “extra” mixing which is at work deep inside the star, we can find a signature of the extra mixing based on the discussions about the observed ΔP_{g} pattern; it is necessary for us to somehow weaken the diffusion process inside the star to reproduce the observed ΔP_{g} pattern, and it is possible that the extra mixing caused by the rotational velocity shear around the convective boundary counteracts and effectively weakens the diffusion processes. We thus find a hint for a relation between the internal dynamics and the structure of the star.

A similar relation between internal dynamics and structure can be also found in the case of the Sun. According to results of helioseismic structure inversion, there is a discrepancy between the sound speed profile of the real Sun and that of the standard solar model at the bottom of the solar convective envelope (Christensen-Dalsgaard et al., 1996). Interestingly, the bottom of the convective envelope where the discrepancy has been found is identical to the so-called solar tachochline, a relatively strong rotational velocity shear inferred based on helioseismic rotation inversion (Thompson et al., 1996), and it is currently a commonly accepted idea in the helioseismology community that the discrepancy can be resolved if we consider extra mixing caused by the velocity shear at the solar tachochline. (See more detailed discussions in Gough et al., 1996).

Here is one caveat; in helioseismology, extra mixings at the solar tachochline are believed to mix the region uniformly (reducing effectiveness of the helium gravitational settling), but in the case of KIC 11145123, we have an opposite trend where extra mixings around the convective boundary render the chemical composition gradient to be steeper somewhere. The latter process might sound peculiar for us because mixing processes, literally, mix the chemical composition uniformly. However, whether a mixing process really leads to a locally uniform chemical composition profile or not strongly depends on the scaleheight of the mixing process and the position where the mixing is at work; if the mixing region is too thin and the mixing is occurring at the edge of the boundary (in terms of the chemical composition profile, for instance), the gradient of the chemical composition profile can be maintained though the chemical composition is uniform inside the thin mixing region, which might be the case for KIC 11145123.

4.4.2 Comparison with the case of KIC 9244992

Though it is definitely the case that the star is exhibiting a large number of intriguing physical properties in terms of the evolutionary stage, the internal structure, the internal dynamics, and the interrelations among them, difficulties arise when we consider whether the inferred properties are universal in the case of the other stars or just unique to the star; because there is only KIC 11145123, for which the convective core rotation has been inferred, we do not know that the fast-core rotation is a rare phenomena which is somehow caused by envelope-modification events the star has experienced, or that it is rather common phenomena and just a consequence of ordinary angular momentum transfer expected to be at work inside stars.

One simple way of testing the universality of the properties inferred for KIC 11145123 is to increase the number of targets and carry out statistical tests to draw general conclusions, which, unfortunately, is very difficult to realize because the number of stars for which we can perform asteroseimic analyses as done in this dissertation is fairy few (see Subsection 1.3.1); we definitely need more pulsators exhibiting, especially, resolved frequency splitting.

We nevertheless have one pulsator, KIC 9244992, which is one of the three main-sequence stars exhibiting resolved frequency splitting found by D. W. Kurtz in the Kepler targets (see Subsection 1.3.1). Asteroseismic analyses of KIC 9244992 have been already done by Saio et al. (2015) in the way mostly the same as those in Kurtz et al. (2014) (the authors are actually almost the same). The star is an F-type star (Huber et al., 2014) and the best asteroseismic model of the star has $M = 1.45M_{\odot}$, $X_{\text{init}} = 0.724$, $Z_{\text{init}} = 0.01$, and $f_{\text{ovs}} = 0.010$ (note that f_{ovs} is the extent of the overshooting, see Subsection 2.4.2). Rotation inversion indicates that the star is rotating almost rigidly with $P_{\text{rot}} \sim 65\,d$ from the core to the surface and that the core is rotating slightly faster than the envelope. As such, KIC 9244992 is roughly similar to KIC 11145123 in terms the global properties, though the former star seems to be more normal than the latter one.

We thus would like to compare properties, namely, the ΔP_{g} pattern and the convective core rotation, of KIC 11145123 and those of KIC 9244992; though the number is of course not satisfactory in a statistical sense yet, the comparison might lead us to the better understanding of interiors of stars. Firstly, we compare the observed ΔP_{g} patterns in Figure 4.23 which is cited from Saio et al. (2015). It is clearly seen that the ΔP_{g} pattern of KIC 9244992 is smoother than that of KIC 11145123, suggesting that we do not need any steep chemical composition gradient in the deep radiative region of KIC 9244992.

Secondly, we compare the convective-core rotations of the stars. Because Saio et al. (2015) did not use mixed modes in their rotation inversion (and mixed modes are essential to infer the convective core rotation as discussed in Subsection 4.3.5), we include the observed mixed-mode rotational shifts and carry out rotation inversion again. The number of the rotational shifts is 18 (12 high-order g modes with $l = 1$, 2 low-order p modes with $l = 1$, and 5 mixed modes with l higher than 3). We reproduce the equilibrium model of KIC 9244992 via MESA based on the parameters given in Saio et al. (2015), based on which the eigenfrequencies, the eigenfunctions, and the rotational splitting kernels are computed with GYRE. By using the three-zone modeling of the rotational profile, we have carried out rotation inversion, and we have found little hint of a fast-convective-core rotation in the case of KIC 9244992.

The above two comparisons might imply an interesting trend that when there (does not) exists a rotational velocity shear between the convective boundary, the ΔP_{g} pattern (does not have) has a short-periodic component with an observable amplitude. Of course, it is obvious that we cannot have a clear answer to the original question “is the inferred properties for KIC 11145123 universal?” based on the implication. Different evolutionary stages of the two stars can cause the difference in the inferred properties. Still, we also cannot rule out the possibility that the peculiarity of KIC 11145123 in terms of experiencing the envelope modifications during the evolution leads to the difference in the inferences of the two stars. In addition, the inference of the absence of the fast-convective-core rotation for KIC 9244992 suffers from the model-dependence problem, and it

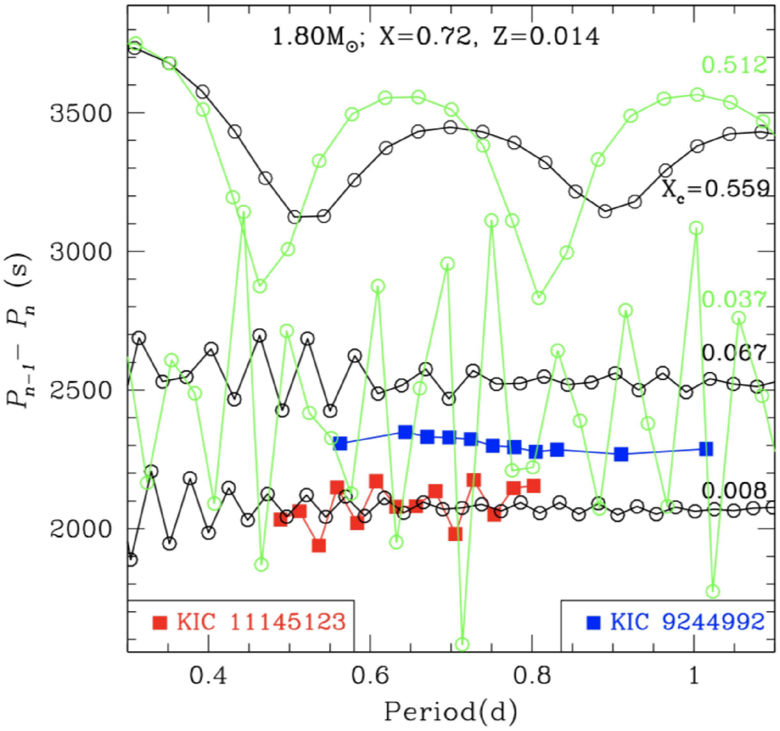

Figure 4.23: Comparison of observed modulated $\Delta P_{\rm g}$ patterns for KIC 9244992 (blue Saio et al., 2015) and for KIC 11145123 (red Kurtz et al., 2014) with theoretically calculated patterns with diffusion (black) and without diffusion (green) via a linear adiabatic oscillation code developed by M. Takata. This figure is the same as Figure 2.4, and it is cited from Saio et al. (2015).

is potentially questionable that the mixed modes assigned the spherical degrees larger than 3 in Saio et al. (2015) are correctly identified. However, this is the first case in which relations (between internal dynamics and the structure) of two different stars have been compared, which could be a good test case for further comprehensive studies on interiors of stars to be achieved in the future.

4.5 Summary of this chapter

Detailed asteroseismic analyses have been carried out for KIC 11145123.

First, The envelope-modified model of the star, whose initial helium abundance is ~ 0.26, has been constructed based on the novel scheme of the non-standard modeling developed by us. The model is also fine-tuned to reproduce the positive slope seen in the observed $\Delta P_{\rm g}$ pattern by adopting $f_{\rm ovs} = 0.027$. The discrepancy between the model and the observation for the envelope-modified model is comparable to those for previous models of the star computed assuming a single-star evolution, suggesting that the star may well have experienced non single-star evolution.

Secondly, rotation inversion has been carried out based on the envelope-modified model to infer the internal rotation of the star, especially focusing on the existence of the fast core rotation suggested by Hatta et al. (2019). Comparison of the results with previous ones by Hatta et al. (2019), in which an ordinary single-star evolutionary model obtained by Kurtz et al. (2014) is used as a reference model, shows the little qualitative model dependence of the inferences. A Bayesian scheme newly developed by us is also favoring the existence of the fast-convective-core rotation. In particular, the fast-convective-core (that the convective core is rotating around 5–10 times faster than the other regions of the star) is inferred for the both cases. Such a strong velocity shear might be triggering some kinds of extra mixing which is thought to be a cause for the short periodic component seen in the observed ΔP_{g} pattern of the star, which is totally opposite to the case of KIC 9244992 for which the fast-convective-core has not been inferred and the observed ΔP_{g} pattern does not show the short periodic component with an observable amplitude, though the analyses for KIC 9244992 are rather experimental.

Chapter 5

Conclusions

This dissertation is dedicated to detailed asteroseismic analyses of a possible blue straggler star KIC 11145123. Three main conclusions have been obtained and they are listed in the following paragraphs. In addition, some remarks on future prospects of this study are also made.

The first conclusion is that the star might have been born as a single star with an ordinary initial helium abundance of ~ 0.26 and then experienced some interactions with other stars, leading to the modification of the chemical composition in the envelope. This conclusion is obtained based on the non-standard modeling of the star where modifications of the chemical compositions are taken into account for constructing 1-dimensional stellar models. A novel scheme to compute such non-standard models has been developed in this dissertation, which is applied to the comprehensive grid-based modeling of the star, resulting in the envelope-modified model with fundamental parameters as below: $M = 1.36 M_{\odot}$, $Y_{\mathrm{init}} = 0.26$, $Z_{\mathrm{init}} = 0.002$, $f_{\mathrm{ovs}} = 0.027$, and Age $= 2.169 \times 10^9$ years old. The modification is down to the depth of $r/R \sim 0.67$ and the extent is $\Delta X \sim 0.06$ (ΔX is the difference in hydrogen abundance between the unmodified model and the modified model) at the surface. This is the first time such an envelope-modified model (which is still in both hydrostatic and thermal equilibrium states) is obtained for the star, and the discrepancy between the modeled eigenfrequencies and the observed ones is comparable to those for previous models computed based on an assumption of a single-star evolution. The conclusion that this star may well have experienced some interactions with other stars during the evolution is consistent with the formation channels of blue straggler stars, thus strengthening the argument that the star is a (probable rather than possible) blue straggler star.

Secondly, we have found that the convective core of the star is rotating around $5-10$ times faster than the other regions of the star, and we have shown the little model dependence of the inference by comparing the results of rotation inversion carried out based on the envelope-modified model and the previous model of Kurtz et al. (2014), which also leads to other inferences such as that the envelope is rotating slightly faster than the deep radiative region (confirmation of the results of Kurtz et al., 2014) and that the high-latitude region is rotating slightly faster than the low-latitude region (the inference of the latitudinally differential rotation). The indication of the fast core rotation is, especially, significant given the consensus regarding the stellar internal rotation probed by other asteroseismic analyses, that main-sequence stars are rotating almost rigidly throughout the stars and there is no strong velocity shear inside them. The apparent contradiction between the finding in this dissertation and the current understanding in the community of asteroseismology can be understood based on which type of modes we mainly use in rotation inversion. In the case of the analyses in this dissertation, mixed modes (which have, though slightly, sensitivity inside the convective core) are mainly used for probing the rotation rates in deep regions of the star, and on the other hand, high-order g modes (which have almost no sensitivity inside the convective core) are mainly used for the other asteroseismic analyses of γ Dor stars. Therefore, the second conclusion also opens a window into a series of new asteroseismic analyses of the stellar deep internal rotation focusing on mixed modes. The conclusion is of great importance as well because the fast-convective-core rotation might place a constraint on numerical simulations of angular momentum transfer inside stars which have not been established yet.

The final conclusion is that there might be an extra mixing caused by the rotational velocity shear which are thought to be at work around the convective core boundary of the star. Though exact mechanisms are not clear yet, the analysis of the observed ΔP_{g} pattern of the star evidently suggests that there should be some sharp features in the Brunt-Väisälä frequency and that "much weaker" diffusion than that adopted in ordinary 1-dimensional stellar evolutionary codes such as MESA is favorable to the observation. Interestingly enough, another δ Sct and γ Dor hybrid star KIC 9244992 exhibits a much smoother ΔP_{g} pattern and there is no hint for the fast core rotation, thus also showing the possibility that there is a relationship between the current rotational profile and the structure of the stars. To establish the relationship is one of the most highly prioritized subjects to research.

Bibliography

Abt, H. A., Morrell, N. I., 1995, ApJ Supplement Series, 99, 135

Aerts, C., Christensen-Dalsgaard, J., Kurtz, D. W., 2010, A&A Library, “Asteroseismology”

Aerts, C., Van Reeth, T., & Tkachenko, A. 2017, ApJL, 847, L7

Aerts, C., Mathis, S., Rogers, T. M., 2019, Annu. Rev. Astron. Astrophys., 57, 35

Appourchaux, T., Gizon, L., Rabello-Soares, M. -C., 1998, A&A Supplement, 132, 107

Appourchaux, T., et al., 2010, Astron Astrophys Rev, 18: 197-277

Backus, G. E. & Gilbert, J. F. 1967, Geophysical Journal, 13, p.247

Baglin, A., et al., 2006, ESA SP-1306, ISBN 92-902-465-9., p.33

Bastian, N., Lardo, C., 2018, Annu. Rev. Astron. Astrophys., 56, 83

Bedding, T. R., et al., 2011, Nature Letters, VOL 471, p. 608-611

Benomar, O., Appourchaux, T., Baudin, F., 2009, A&A, 506, 15

Benomar, O., Bazot, M., Nielsen, M. B., et al. 2018, Science, 361, 1231

Boffin, M. J., et al., 2015, Astrophysics and Space Science Library, 413

Bouabid, M.-P., Dupret, M.-A., Salmon, S., et al. 2013, MNRAS, 429, 2500

Bradley, P. A., Guzik, J. A., Miles, L. F., et al. 2015, ApJ, 149, 68

Brogaard, K., et al., 2018, MNRAS, **481**, 5062-5072

Browning, M. K., Brun, A. S., & Toomre, J. 2004, ApJ, 601, 512

Brun, A. S., Browning, M. K., & Toomre, J. 2005, ApJ, 629, 461

Brun, A. S., Strugarek, A., Varela, J., et al. 2017, ApJ, 836, 192

Buldgen, G., Salmon, S., Noel, A., 2019, Frontiers in Astronomy and Space Sciences, 6, id.42

Burgers, J. M., 1969, Flow Equations for Composite Gases (New York: Academic)

Chaplin, W. J. and Miglio, A., 2013, Annu. Rev. Astron. Astrophys., 51: 353-392

Chen, Y. H., 2016, MNRAS, **458**, 1190-1198

Chen, X., et al., 2020, ApJ, 895, 136

Chib, S., Jeliazkov, I., 2001, Journal of the American Statistical Association, 96, 453, Theory and Methods

Christensen-Dalsgaard, J., 1984, Space Research Prospects in Stellar Activity and Variability, Proceedings of the Workshop, p. 11

Christensen-Dalsgaard, J., Monteiro, M. J. P. F. G., Thompson, M., J., 1995, MNRAS, **276**, 283

Christensen-Dalsgaard, J., et al., 1996, Science, Volume 272, Issue 5266, pp. 1284-1286

Cunha, M. S., et al., 2015, ApJ, 805, 127

Cunha, M. S., et al., 2019, MNRAS, **490**, 909-926

Deheuvels, S., García, R. A., Chaplin, W. J., et al. 2012, ApJ, 756, 19

Deubner, F.-L., 1974, Solar Physics, 39, 31

Dupret, M.-A., et al., 2005, A&A, 435, 927

Dyson, J., Schutz, B. F., 1979, Proc.R.Soc. London A **368**, 389

Featherstone, N. A., Browning, M. K., Brun, A. S., & Toomre, J. 2009, ApJ, 705, 1000

Fuller, J., Piro, A. L., Jermyn, A. S., 2019, MNRAS, 485, 3661

Gabriel, M., Noels, A., 1977, A&A, 54, 631

Gabriel, M., Noels, A., Montalban, J., Miglio, A., 2014, A&A, 569, A63

Gizon, L., et al., 2016, Science Advances, **2**: e1601777

Gough, D. O., et al., 1996, Science, Volume 272, Issue 5266, pp. 1296-1300

Goupil, M. 2011, Lecture Notes in Physics, 832, 223

Gregory, P. C., 2005b, Bayesian Logical Data Analysis for the Physical Sciences: A Comparative Approach with *Mathematica* Support (Cambridge University Press)

Hatta, Y., Sekii, T., Takata, M., Kurtz, D. W., 2019, ApJ, 871, 135

Herwig, F. 2000, A&A, 360, 952

Huber, D., et al., 2014, ApJS, 211, 2

Kawaler , S. D., Sekii, T., & Gough, D. 1999, ApJ, 516, 349

Kippenhahn, R., Weigert, A., and Weiss, A. 2012, A&A Library

Kley, W., Lin, D. N. C., 1996, ApJ, 461, 933

Koch, D. G., et al., 2010, ApJ Letter, 713: L79-L86

Kosovichev, A. G., Kitiashvili, I. N., 2020, IAUS, 354, 107

Kunitomo, M., Guillot, T., Takeuchi, T., Ida, S., 2017, A&A, 599, A49

Kurtz, D. W., Saio, H., Takata, M., et al. 2014, MNRAS, 444, 102

Leighton, R., et al., 1962, ApJ, vol. 135, p.474

Leonard, P. J. T., 1989, AJ, 98, 217

Li, G., et al., 2020, MNRAS, **491**, 3586

Lund, M. N., Miesch, M. S., & Christensen-Dalsgaard, J. 2014, ApJ, 790, 121

Maeder, A. 2009, Physics, Formation and Evolution of Rotating Stars (Berlin: Springer)

Metropolis, N., Rosenbluth, A., Rosenbluth, M., 1953, J. Chem. Phys., 21, 188

Michaud, G., Alecian, G., Richer, J., 2015, A&A Library, “Atomic Diffusion in Stars”

Miglio, A., et al., 2008, MNRAS, **386**, 1487-1502

Miglio, A., et al., 2013, MNRAS, **429**, 423-428

Montgomery, M. H., Metcalfe, T. S., Winget, D. E., 2003, MNRAS, **344**, 657

Morel, P. and Thevenin, F., 2002, A&A 390, 611-620

Murphy, S. J., et al., 2016, ApJ Letters, 827: L17 (4pp)

Nomoto, K. 1982, ApJ, 253, 798

Paxton, B., Bildsten, L., Dotter, A., et al. 2011, ApJ Supplement Series, 192, 3

Paxton, B., Cantiello, M., Arras, P., et al. 2013, ApJ Supplement Series, 208, 4

Paxton, B., Marchant, P., Schwab, J., et al. 2015, ApJ Supplement Series, 220, 15

Paxton, B., Schwab, J., Bauer, E. B., et al. 2018, ApJ Supplement Series, 234, 34

Paxton, B., Smolec, R., Schwab, J., et al. 2019, ApJ Supplement Series, 243, 10

Pedersen, M. G., Aerts, C., Papics, P. I., Rogers, T. M., 2018, A&A, 614, A128

Pijpers, F. P. 2006, Imperial College Press, “methods in helio- and asteroseismology”

Ricker, G. R., et al., 2014, SPIE, 9143, 20

Ritzwoller, M. H. & Lavely, E. M. 1991, ApJ, 369, 557

Saio, H., Kurtz, D. W., Takata, M., et al. 2015, MNRAS 447, 3264

Sanchez Arias, J. P., et al., 2017, A&A, 597, A29

Schou, J., Christensen-Dalsgaard, J., & Thompson, M. J. 1994, ApJ, 433, 389

Schou, J., et al., 2012, Solar Physics, Volume 275, Issue 1-2, pp 229-259

Sonoi, T., et al., 2017, A&A, 600, A31

Takada-Hidai, M., et al., 2017, MNRAS, **470**, 4908-4924

Takata, M. and Gough, D. O., 2001, "Helio- and Asteroseismology at the Dawn of the Millennium" (ESA SP-464)

Takata, M., Gough, D. O., 2003, ESASP, 517, 397

Tassoul, M., 1980, ApJ Supplement Series, **43**: 469-490

Tayar, J., & Pinsonneault, M. H. 2013, ApJL, 775, L1

Gough, D. O., Thompson, M. J., 1991, University of Arizona Press, "Solar interior and atmosphere", p. 519-561

Thompson, M. J., Toomre, J., Anderson, E. R., et al. 1996, Sci, 272, 1300

Thompson, M. J., Brun, A. S., Culhane, J. L., Gizon, L., Roth, M., Sekii, T., 2017, Space Sciences Series of ISSI, "Helioseismology and Dynamics of the Solar Interior"

Townsend, R. H. D. and Teitler, A., 2013, MNRAS **435**, 3406-3418

Unno, W., Osaki, Y., Ando, H., Saio, H., & Shibahashi, H. 1989, Univ. Tokyo Press, "Nonradial Oscillations of Stars"

Walker, G., et al., 2003, PASP, **115**: 1023-1035

Weiss, A., Hillebrandt, W., Thomas, H.-C., Ritter, H., 2004, Advances in Astronomy and Astrophysics, "Cox & Giuli's principles of stellar structure" Extended Second Edition

Winget, D. E., Robinson, E. L., Nather, E., 1982, ApJ, 262, 11

Appendix A

Another resettling scheme without assuming adiabatic processes

In Chapter 3, we develop a novel numerical scheme which enables us to obtain a hydrostatic equilibrium model based on the assumption that a perturbed state oscillates around a new equilibrium point adiabatically. We can expand the formulation by assuming non-adiabatic oscillation as well, and the newly developed scheme might be helpful for further carrying out the non-standard modeling of KIC 11145123 including other possible mass accretors.

The starting point of the formulation is to express the pressure perturbation δP with the density perturbation $\delta\rho$ and the temperature perturbation δT via formal equation of state as below:

$$\frac{\delta P}{P_{\rm md}} = \chi_\rho \frac{\delta\rho}{\rho_0} + \chi_T \frac{\delta T}{T_0}, \tag{A.1}$$

where partial derivatives of thermodynamic quantities are defined as

$$\chi_\rho \equiv \left(\frac{\partial \ln P_{\rm md}}{\partial \ln \rho}\right)_T \tag{A.2}$$

and

$$\chi_T \equiv \left(\frac{\partial \ln P_{\rm md}}{\partial \ln T}\right)_\rho . \tag{A.3}$$

Inserting the expression (A.1) into the equation (3.13) leads to the following form

$$-\frac{d}{dm}\left(\frac{\chi_\rho P_{\rm md}}{\rho_0}\delta\rho + \frac{\chi_T P_{\rm md}}{T_0}\delta T\right) = -\frac{Gm}{4\pi r_0^4}\frac{4\xi_r}{r_0} - \delta h, \tag{A.4}$$

which can be further converted using the relation (3.22)

$$\begin{aligned}
& 4\pi r_0^2\rho_0^2\left(\frac{\chi_\rho P_{\rm md}}{\rho_0}\right)\frac{d^2\xi_r}{dm^2} \\
+ \quad & \left[4\pi r_0^2\rho_0^2\frac{d}{dm}\left(\frac{\chi_\rho P_{\rm md}}{\rho_0}\right) + \left(\frac{\chi_\rho P_{\rm md}}{\rho_0}\right)\left(\frac{2\rho_0}{r_0} + 4\pi r_0^2\rho_0^2\frac{d\rho}{dm} + \rho_0\frac{d}{dm}(4\pi r_0^2\rho_0^2)\right)\right]\frac{d\xi_r}{dm} \\
+ \quad & \left[\frac{d}{dm}\left(\frac{\chi_\rho P_{\rm md}}{\rho_0}\right)\frac{2\rho_0}{r_0} + \left(\frac{\chi_\rho P_{\rm md}}{\rho_0}\right)\frac{d}{dm}\left(\frac{2\rho_0}{r_0}\right) + \frac{Gm}{4\pi r_0^4}\frac{4}{r_0}\right]\xi_r \\
- \quad & \left(\frac{\chi_T P_{\rm md}}{T_0}\right)\frac{d(\delta T)}{dm} - \frac{d}{dm}\left(\frac{\chi_T P_{\rm md}}{T_0}\right)\delta T + \delta h = 0.
\end{aligned} \tag{A.5}$$

Since we do not assume the adiabatic oscillation to resettle perturbed models, the temperature perturbation cannot be expressed only with the density perturbation (as the expression 3.16), and thus, there are two (unknown) variables, namely, ξ_r and δT, to be determined by solving a set of differential equations; we need one more equation. To have one more differential equation, we focus on the equation for the temperature gradient (3.3). For simplicity, we assume that the temperature gradient is equal to the radiative one (it is quite challenging to consider perturbed temperature gradients in convective region because we have to couple, for example, the mixing length theory to describe relations among the perturbed quantities), and the equation for an unperturbed state is as below:

$$\frac{dT_0}{dm} = -\frac{3\kappa_0 l_0}{64\pi^2 a c_{\mathrm{ph}} r_0^4 T_0^3}, \tag{A.6}$$

where a and c_{ph} are the radiative constant and the speed of light in vacuum.

Let the opacity of the perturbed model be denoted as κ_{md}, and it can be computed by interpolating, for instance, the OPAL opacity table in a way similar to that when we compute P_{md}, namely,

$$\kappa_0 = \kappa(\rho_0, T_0, \mu_0) \rightarrow \kappa_{\mathrm{md}} = \kappa(\rho_0, T_0, \mu_1). \tag{A.7}$$

We can derive a linear perturbed differential equation for the equation (A.6) following the way we derive the one (A.5) (see details in Subsection 3.2.2), and the linear differential equation has the following form:

$$\frac{\kappa_{\mathrm{md}}\rho_0}{4\pi r_0^2}\frac{l_0}{c_{\mathrm{ph}}}\epsilon_\rho\frac{d\xi_r}{dm} + \frac{\kappa_{\mathrm{md}}}{16\pi^2 r_0^5}\frac{l_0}{c_{\mathrm{ph}}}(2\epsilon_\rho + 4)\xi_r - \frac{4aT_0^3}{3}\frac{d(\delta T)}{dm} - \left[4aT_0^2\frac{dT_0}{dm} + \frac{\kappa_{\mathrm{md}}}{16\pi^2 r_0^4}\frac{l_0}{c_{\mathrm{ph}}}\frac{\epsilon_T}{T_0}\right]\delta T + \delta Q = 0, \tag{A.8}$$

in which the local luminosity l_0 is assumed to be fixed, and we also have partial derivatives with respect to the perturbed opacity κ_{md} as follows:

$$\epsilon_\rho \equiv \left(\frac{\partial \ln \kappa_{\mathrm{md}}}{\partial \ln \rho}\right)_T \tag{A.9}$$

and

$$\epsilon_T \equiv \left(\frac{\partial \ln \kappa_{\mathrm{md}}}{\partial \ln T}\right)_\rho, \tag{A.10}$$

which satisfies the relation in the following way,

$$\frac{\delta\kappa}{\kappa_{\mathrm{md}}} = \epsilon_\rho\frac{\delta\rho}{\rho_0} + \epsilon_T\frac{\delta T}{T_0}. \tag{A.11}$$

The deviation from the radiative equilibrium δQ is defined as

$$\delta Q \equiv \frac{4aT_0^3}{3}\frac{dT_0}{dm} + \frac{\kappa_{\mathrm{md}}}{16\pi^2 r_0^4}\frac{l_0}{c_{\mathrm{ph}}}. \tag{A.12}$$

The set of the two linear differential equations (A.5) and (A.8) can be solved for an appropriate set of the boundary conditions. In addition to the two existing ones (which can be found in Section 3.3), the third boundary condition is, for instance, $\delta s = 0$ in a moderately deep interior where the oscillation is considered to be adiabatic.

Appendix B

A brief introduction to structure inversion [8]

As briefly demonstrated in Subsection 4.2.3, in asteroseismology and helioseismology, what we would like to estimate are differences in structure variables, for example, density and sound speed, between a real star and the model of the star. If we assume that the differences are so small that we can treat them as perturbations, then, the differences in eigenfrequencies can be related to those of the structures using equation (1.20). Actually, the relation can be rewritten in the following form

$$\left(\frac{\Delta\omega}{\omega}\right)_i = \int_0^R \left[K_{c,\rho}^{(i)}(r)\frac{\Delta c}{c}(r) + K_{\rho,c}^{(i)}(r)\frac{\Delta\rho}{\rho}(r)\right] dr. \tag{B.1}$$

The differences of eigenfrequencies, density, and sound speed between a real star and the model are denoted as $\Delta\omega$, Δc, and $\Delta\rho$, respectively. They are defined as below

$$\Delta\omega \equiv \omega_{\text{star}} - \omega_{\text{ref}} \tag{B.2}$$

$$\Delta c \equiv c_{\text{star}} - c_{\text{ref}} \tag{B.3}$$

$$\Delta\rho \equiv \rho_{\text{star}} - \rho_{\text{ref}}. \tag{B.4}$$

These differences are related to each other via two functions called *sound speed kernel* ($K_{c,\rho}^{(i)}(r)$) and *density kernel* ($K_{\rho,c}^{(i)}(r)$), both of which can be calculated based on the reference model. Here, an index i is used to represent a certain eigenmode.

We are able to observe the eigenfrequencies of a star, thus, we can calculate the value (B.2). Though there still remains two unknown functions, namely, $\Delta c/c$ and $\Delta\rho/\rho$, the set of equations (B.1) enables us to estimate the unknowns via *inversion techniques* that we explain in Subsection 4.3.2 and Appendix C. After we estimate these two relative differences, a new model can be obtained by adding the estimated differences to the original reference model in the following manner

$$c_{\text{star}} = c_{\text{ref}} + \widehat{\Delta c}, \tag{B.5}$$

$$\rho_{\text{star}} = \rho_{\text{ref}} + \widehat{\Delta\rho}. \tag{B.6}$$

---

[8] This appendix is mostly based on Subsection 2.3.1 in my master thesis, and most parts are citations from the original article.

The mark $\hat{}$ has been used to emphasize that they are just estimates. The above procedure is called *structure inversion.* We can model a star more precisely based on the differences of the eigenfrequencies.

Explicit forms of the structure kernels are complex and the derivation of them requires some efforts, but the procedure is basically the same as we derive the rotational splitting kernels in Subsection 4.3.1; what we have to do is to obtain an explicit form for $\Delta\mathcal{L}$ in the presence of the density and sound speed perturbations, and substitute $\Delta\mathcal{L}$ for the expression (1.20). After some manipulations (see e.g. Gough and Thompson, 1991), explicit forms of the structure kernels can be obtained as below:

$$\omega^2 I_{nl} K_{c,\rho}^{(i)}(r) = \rho c^2 \chi^2 r^2, \tag{B.7}$$

for the sound speed kernel $K_{c,\rho}^{(i)}(r)$, and

$$\begin{aligned} &\omega^2 I_{nl} K_{\rho,c}^{(i)}(r) \\ = \quad - \quad & \frac{1}{2}\omega^2(\xi_r^2 + l(l+1)\xi_h^2)\rho r^2 + \frac{1}{2}\rho c^2 \chi^2 r^2 \\ - \quad & GM_r \rho \xi_r \chi - 4\pi G \rho r^2 \int_r^R \left(\chi + \frac{1}{2}\frac{d\ln\rho}{ds}\xi_r\right)\rho(s)\xi_r(s)ds + 2\pi G \rho^2 r^2 \xi_r^2 + GM_r \rho \frac{d\xi_r}{dr}\xi_r \\ - \quad & \frac{8\pi G}{2l+1}\rho\Big((l+1)r^{-l}(\xi_r - l\xi_h)\int_0^r (\rho\chi + \xi_r\frac{d\rho}{ds})s^{l+2}ds - lr^{l+1}(\xi_r + (l+1)\xi_h)\int_r^R (\rho\chi + \xi_r\frac{d\rho}{ds})s^{-(l-1)}ds\Big) \end{aligned} \tag{B.8}$$

for the density kernel $K_{\rho,c}^{(i)}(r)$, where the mode inertia is expressed by I_{nl} (for the definition, see Section 3.4) and the quantity χ is defined as follows:

$$\chi(r) \equiv \frac{1}{r^2}\frac{d}{dr}(r^2\xi_r) - \frac{l(l+1)}{r}\xi_h \tag{B.9}$$

which corresponds to the radial component of the divergence of the eigenfunction $(\nabla \cdot \boldsymbol{\xi})$.

In the expressions (B.7) and (B.8), all the variables are dimensional. Let us consider the structure kernels for dimensional variables as below:

$$x \equiv r/R \tag{B.10}$$

$$\tilde{c} \equiv \sqrt{\frac{R}{GM_\star}}c \tag{B.11}$$

$$\tilde{\rho} \equiv \frac{R^3}{M_\star}\rho \tag{B.12}$$

$$\tilde{\omega}_{nlm} \equiv \sqrt{\frac{R^3}{GM_\star}}\omega_{nlm}. \tag{B.13}$$

Based on the fact that the structure kernels for dimensional variables are invariant even though they are converted for dimensionless variables, the following two identities can be derived (Takata and Gough, 2003)

$$\frac{1}{2}\int K_{c,\rho}^{(i)}(x)dx + \int K_{\rho,c}^{(i)}(x)dx = \frac{1}{2}, \tag{B.14}$$

$$\int K_{c,\rho}^{(i)}(x)\frac{d\ln(c/r)}{d\ln r}dx + \int K_{\rho,c}^{(i)}(x)\frac{d\ln\rho}{d\ln r}dx = 0, \tag{B.15}$$

with which we have an altered expression for the one (B.1)

$$\left(\frac{\Delta\omega}{\omega}\right)_i = \int_0^1 \left[K_{c,\rho}^{(i)}(x)\frac{\Delta c}{c}(x) + K_{\rho,c}^{(i)}(x)\frac{\Delta\rho}{\rho}(x)\right]dx - \frac{\Delta R}{R}\int_0^1 K_{c,\rho}^{(i)}(x)dx. \tag{B.16}$$

Equation (B.16) is different from equation (B.1) in terms of the existence of an effect of $\Delta R/R$ on $\Delta\omega/\omega$. In helioseismology, it is usually assumed that $\Delta R/R$ is zero because the radius of the solar model is fitted to the observed radius (Christensen-Dalsgaard et al., 1996). Thus, equation (B.1) is frequently used to infer the solar interior. However, in asteroseismology, there is an uncertainty in the radius of the model except for the case in which the radius has been determined interferometrically. So we have to take the effects of $\Delta R/R$ on $\Delta\omega/\omega$ into account as the expression (B.16). Actually, there are a few studies (Takata and Gough, 2001) which attempt to estimate the solar $\Delta R/R$ using equation (B.16) in order to measure the solar radius more precisely; in this case, what we obtain as "the solar radius" is the radius of the Sun sensed by the p modes, which can be slightly different from the one defined as the radius, for instance, at the solar photosphere.

Appendix C

Methods for linear inverse problems [9]

A part of Chapter 4 is devoted to introducing a few methods for linear inverse problems, but we do not explain one standard method which is frequently used in helio- and asteroseismology, namely, the Regularized Least-Squares (RLS) method. In this appendix, a basic framework of the RLS method is briefly presented, and then, we compare the two standard methods, the OLA method demonstrated in Section 4.3 and the RLS method. Since inverse problems in helio- and asteroseismology are often ill-posed, obtaining estimates via several different methods is helpful for us to interpret behaviors of estimates.

The starting point

What we would like to solve in helio- and asteroseismology are 1-dimensional integral equation

$$\left(\frac{\Delta\omega}{\omega}\right)_{nl} = \int_0^1 \left[K_{c,\rho}^{(nl)}(x)\frac{\Delta c}{c}(x) + K_{\rho,c}^{(nl)}(x)\frac{\Delta\rho}{\rho}(x)\right]dx - \frac{\Delta R}{R}\int_0^1 K_{c,\rho}^{(nl)}(x)dx \tag{C.1}$$

or 2-dimensional integral equation as follows:

$$\frac{\delta\omega_{nlm}}{m} = \iint K_{nlm}(x,\mu)\Omega(x,\mu)dxd\mu. \tag{C.2}$$

We usually have errors arising from observation, instruments, and so on. Thus, the sets of equations can be rewritten in the following forms

$$d_i = \int_0^1 \left[K_{c,\rho}^{(i)}(x)\frac{\Delta c}{c}(x) + K_{\rho,c}^{(i)}(x)\frac{\Delta\rho}{\rho}(x)\right]dx - \frac{\Delta R}{R}\int_0^1 K_{c,\rho}^{(i)}(x)dx + e_i \tag{C.3}$$

and

$$d_i = \iint K_i(x,\mu)\Omega(x,\mu)dxd\mu + e_i, \tag{C.4}$$

where the mode indices (n, l, m) are replaced with a single index i identifying modes. The left-hand sides of equations (C.1) and (C.2) are now represented by d_i. It is assumed that means of the errors are zero

$$< e_i >= 0. \tag{C.5}$$

---

[9] This appendix is mostly based on Chapter 3 in my master thesis, and some parts are citations from the original article.

Equations (C.1) and (C.2) have different characteristics in terms of the number of unknowns and the dimensions. However, the fundamental procedures to solve them are almost the same as solving the following 1-dimensional integral equation with one unknown function, namely,

$$d_i = \int K_i(r) f(r) dr + e_i\,, \;\; (i = 1, ..., M), \tag{C.6}$$

where the number of the identified modes is denoted by M, and $f(r)$ is an unknown function which we would like to estimate. Therefore, from now on, we focus on how to solve equation (C.6).

Regularized Least-Squares (RLS)

The RLS method is a variation of Least-Squares fitting methods, and ill-posedness of an original set of linear equations can be lifted by imposing certain regularizations as we see below. Let us start with discretizing equation (C.6)

$$d_i = \sum_{j=1}^{N} K_i(r_j) f(r_j) \Delta r_j + e_i\,, \;\; (i = 1, ..., M), \tag{C.7}$$

where N is the number of mesh points, and Δr_j is defined as below:

$$\begin{cases} \Delta r_1 = r_2 - r_1 \\ \Delta r_k = (r_{k+1} - r_{k-1})/2 \\ \Delta r_N = r_N - r_{N-1}. \end{cases} \tag{C.8}$$

Then, the set of the integral equation (C.6) can be expressed using matrices

$$\boldsymbol{d} = \boldsymbol{K}\boldsymbol{f} + \boldsymbol{e}, \tag{C.9}$$

where $\boldsymbol{K}$ is a $M \times N$ matrix. The data, the function, and the errors are denoted by an M-dimensional vector $\boldsymbol{d}$, an N-dimensional vector $\boldsymbol{f}$, and an M-dimensional vector $\boldsymbol{e}$, respectively. The (i, j) element of $\boldsymbol{K}$ is defined as

$$K_{ij} = K_i(r_j)\Delta r_j. \tag{C.10}$$

Equation (C.9) can be solved if there exists $\boldsymbol{K}^{-1}$, but, this is scarcely the case owing to the irregularity of $\boldsymbol{K}$. Not to mention that $\boldsymbol{K}$ is usually not square. Instead of finding the exact solution $\boldsymbol{f}$ which satisfies equation (C.9), we attempt to find least-squares solutions $\hat{\boldsymbol{f}}$ which minimize the *residual*

$$S_{\mathrm{LS}} = |\boldsymbol{d} - \boldsymbol{K}\hat{\boldsymbol{f}}|^2. \tag{C.11}$$

The least-squares solutions are given by requiring $\nabla_{\hat{\boldsymbol{f}}} S_{\mathrm{LS}} = 0$ which leads to the following conversions

$$\nabla_{\hat{\boldsymbol{f}}} \Big(|\boldsymbol{d} - \boldsymbol{K}\hat{\boldsymbol{f}}|^2 \Big) = 0 \tag{C.12}$$

$$\rightleftharpoons \nabla_{\hat{\boldsymbol{f}}} \Big((\boldsymbol{d}, \boldsymbol{d}) - 2(\hat{\boldsymbol{f}}, \boldsymbol{K}^T\boldsymbol{d}) + (\hat{\boldsymbol{f}}, \boldsymbol{K}^T\boldsymbol{K}\hat{\boldsymbol{f}}) \Big) = 0, \tag{C.13}$$

where $(\boldsymbol{a}, \boldsymbol{b}) = \boldsymbol{a}^T\boldsymbol{b}$ for arbitrary vectors $\boldsymbol{a}$ and $\boldsymbol{b}$ is used. The above equation can be continued as

$$\rightleftharpoons 2\boldsymbol{K}^T\boldsymbol{K}\hat{\boldsymbol{f}} - 2\boldsymbol{K}^T\boldsymbol{d} = 0, \tag{C.14}$$

using $\nabla_{\hat{\boldsymbol{f}}}(\boldsymbol{a},\hat{\boldsymbol{f}}) = \boldsymbol{a}$ and $\nabla_{\hat{\boldsymbol{f}}}(\boldsymbol{M}\hat{\boldsymbol{f}},\boldsymbol{M}\hat{\boldsymbol{f}}) = (\boldsymbol{M}+\boldsymbol{M}^T)\hat{\boldsymbol{f}}$, for an arbitrary matrix $\boldsymbol{M}$. We thus obtain the least-squares solution

$$\hat{\boldsymbol{f}} = (\boldsymbol{K}^T\boldsymbol{K})^{-1}\boldsymbol{K}^T\boldsymbol{d}, \tag{C.15}$$

if $(\boldsymbol{K}^T\boldsymbol{K})^{-1}$ exists. This solution is a more practical one because $\boldsymbol{K}^T\boldsymbol{K}$ is square. Nevertheless, the rank of the matrix $\boldsymbol{K}^T\boldsymbol{K}$ is the same as that of the matrix $\boldsymbol{K}$. Therefore, it is necessary to modify $\boldsymbol{K}^T\boldsymbol{K}$ so that it has an inverse. This procedure is called *regularization*.

Regularization is frequently conducted based on an assumption that the unknown function f should be flat or smooth. In other words, the integral of the first or the second derivative of f should be small

$$\int \left|\frac{df}{dr}\right|^2 dr, \quad \text{for flatness} \tag{C.16}$$

or

$$\int \left|\frac{d^2f}{dr^2}\right|^2 dr, \quad \text{for smoothness.} \tag{C.17}$$

These expressions can also be discretized to the following vector form

$$|\boldsymbol{L}\boldsymbol{f}|^2, \tag{C.18}$$

where $\boldsymbol{L}$ is a differential operator.

Let us consider minimizing the sum of the residual S_{LS} and the flatness (or smoothness) of $\boldsymbol{f}$, namely,

$$S_{\text{RLS}} = |\boldsymbol{d}-\boldsymbol{K}\hat{\boldsymbol{f}}|^2 + \alpha|\boldsymbol{L}\hat{\boldsymbol{f}}|^2. \tag{C.19}$$

A trade-off parameter α is used. Then, a condition similar to equation (C.12) should be valid:

$$\nabla_{\hat{\boldsymbol{f}}}\Big(|\boldsymbol{d}-\boldsymbol{K}\hat{\boldsymbol{f}}|^2 + \alpha|\boldsymbol{L}\hat{\boldsymbol{f}}|^2\Big) = 0 \tag{C.20}$$

which can be solved in the same way as solving equation (C.12), and we have

$$\hat{\boldsymbol{f}} = (\boldsymbol{K}^T\boldsymbol{K}+\alpha\boldsymbol{L}^T\boldsymbol{L})^{-1}\boldsymbol{K}^T\boldsymbol{d}. \tag{C.21}$$

In the above equation, $\boldsymbol{K}^T\boldsymbol{K}$ is regularized by adding the regularizing term $\alpha\boldsymbol{L}^T\boldsymbol{L}$. The $\hat{\boldsymbol{f}}$ in equation (C.21) is the regularized least-squares solution. In the RLS method, all the components of $\boldsymbol{f}$ are estimated at once.

This is nevertheless not the end. We have to see whether the residual $|\boldsymbol{d}-\boldsymbol{K}\hat{\boldsymbol{f}}|^2$ is small or not. We also need to confirm if the flatness or the smoothness of $\hat{\boldsymbol{f}}$ is reasonable or not. They are related to each other and the behavior is determined by the choice of the free parameter α. After compromising to select an acceptable α, we obtain the corresponding inversion matrix $\boldsymbol{R} = (\boldsymbol{K}^T\boldsymbol{K}+\alpha\boldsymbol{L}^T\boldsymbol{L})^{-1}\boldsymbol{K}^T$. Subsequently, the sum of the variances of the estimates at all the mesh points can be derived using the following equation

$$\begin{aligned} <|\delta\hat{\boldsymbol{f}}|^2> &= <|\boldsymbol{R}\boldsymbol{e}|^2> \\ &= <(\boldsymbol{R}\boldsymbol{e})^T\boldsymbol{R}\boldsymbol{e}> \\ &= <\mathrm{tr}\Big(\boldsymbol{R}\boldsymbol{e}(\boldsymbol{R}\boldsymbol{e})^T\Big)> \\ &= \mathrm{tr}\Big(\boldsymbol{R}<\boldsymbol{e}\boldsymbol{e}^T>\boldsymbol{R}\Big) \\ &= \mathrm{tr}\Big(\boldsymbol{R}\boldsymbol{E}\boldsymbol{R}\Big), \end{aligned} \tag{C.22}$$

where we use a relation $(\boldsymbol{c}, \boldsymbol{c}) = \boldsymbol{c}^T\boldsymbol{c} = \mathrm{tr}(\boldsymbol{c}\boldsymbol{c}^T)$, for an arbitrary vector $\boldsymbol{c}$. The mark ^{T} denotes transpose of a matrix. The fourth line in (C.22) is justified because the matrix $\boldsymbol{R}$ is not statistical.

Though the RLS method does not put a priority on optimizing the averaging kernels, it is still meaningful to take a look at the averaging kernels since RLS is also one of the linear inversion techniques. We obtain an averaging kernel at a certain mesh point, say, the i-th point of the meshes as the i th row of $\boldsymbol{RK}$.

Comparison of OLA and RLS

The OLA method (details can be found in Section 4.3) and the RLS method are both *linear inversion techniques*, which means that we estimate an unknown as a linear combination of a dataset

$$\hat{\boldsymbol{f}} = \boldsymbol{Rd}. \tag{C.23}$$

The goal of the OLA method is to have an averaging kernel as localized around the target point as possible. Remember that equation (C.6) can be discretized and expressed as a matrix equation

$$\boldsymbol{d} = \boldsymbol{Kf} + \boldsymbol{e}, \tag{C.24}$$

equation (C.23) can be rewritten in the following manners

$$\begin{aligned} \hat{\boldsymbol{f}} &= \boldsymbol{R}(\boldsymbol{Kf} + \boldsymbol{e}) \\ &= \boldsymbol{RKf} + \boldsymbol{Re}. \end{aligned} \tag{C.25}$$

Then, the OLA's goal can be interpreted as

$$\boldsymbol{RK} \to \boldsymbol{I}_N \tag{C.26}$$

where $\boldsymbol{I}_N$ is an N-dimensional identity matrix. Here is a reason why we can estimate only one unknown value in the OLA method. The i-th row of $\hat{\boldsymbol{f}}$, namely, $\hat{f}_i$ is calculated as the inner product of the i-th row of $\boldsymbol{RK}$ and $\boldsymbol{f}$, if we neglect the errors. To calculate the i-th row of $\boldsymbol{RK}$, we need the i-th row of $\boldsymbol{R}$ and all the components of $\boldsymbol{K}$. In other words, we do not have to determine all the components of $\boldsymbol{R}$ to estimate $\hat{f}_i$.

On the other hand, we aim to minimize a residual $|\boldsymbol{d} - \boldsymbol{K}\hat{\boldsymbol{f}}|^2$ in the RLS method. Inserting equation (C.24) results in

$$\begin{aligned} |\boldsymbol{d} - \boldsymbol{K}\hat{\boldsymbol{f}}|^2 &= |\boldsymbol{d} - \boldsymbol{KRd}|^2 \\ &= |(\boldsymbol{I}_M - \boldsymbol{KR})\boldsymbol{d}|^2. \end{aligned} \tag{C.27}$$

where $\boldsymbol{I}_M$ is an M-dimensional identity matrix. Thus, the goal of the RLS method is achieved by

$$\boldsymbol{KR} \to \boldsymbol{I}_M. \tag{C.28}$$

Here is a big difference from the OLA method. In order to estimate $\hat{f}_i$, we need the i-th row of $\boldsymbol{K}$ and all the components of $\boldsymbol{R}$. It is required for us to determine all the components of $\boldsymbol{R}$ for just one estimate $\hat{f}_i$. However, once we determine $\boldsymbol{R}$ completely, we also obtain other estimates than $\hat{f}_i$. This is the reason why we obtain the estimates at once in the RLS method.

Note that, in the ideal case where the ill-posedness of inverse problems is negligible (of course this is never the case), solutions obtained by the RLS method and those obtained by the OLA method should be almost identical to one another.

We describe a common property between OLA and RLS as a final topic in this subsection. It is the treatment of error magnifications. We would like to reconsider the condition (C.26) in the OLA method with respect to the norm of the difference between the true vector $\boldsymbol{f}$ and the estimated vector $\hat{\boldsymbol{f}}$

$$\begin{aligned} |\boldsymbol{f} - \hat{\boldsymbol{f}}|^2 &= |\boldsymbol{f} - \boldsymbol{R}\boldsymbol{d}|^2 \\ &= |\boldsymbol{f} - \boldsymbol{R}(\boldsymbol{K}\boldsymbol{f} + \boldsymbol{e})|^2 \\ &= |(\boldsymbol{I}_N - \boldsymbol{R}\boldsymbol{K})\boldsymbol{f} + \boldsymbol{R}\boldsymbol{e}|^2. \end{aligned} \tag{C.29}$$

Though the condition (C.26) can cause the first term in the last line of equation (C.29) to be close to zero, the second term remains. It is not always the case that the condition (C.26) can lead to a small $|(\boldsymbol{I}_N - \boldsymbol{R}\boldsymbol{K})\boldsymbol{f} + \boldsymbol{R}\boldsymbol{e}|^2$. In fact, it is very difficult for us to evaluate $|(\boldsymbol{I}_N - \boldsymbol{R}\boldsymbol{K})\boldsymbol{f} + \boldsymbol{R}\boldsymbol{e}|^2$ directly because there are an unknown vector $\boldsymbol{f}$ and an unknown matrix $\boldsymbol{R}$. Moreover, we do not know the exact elements of the error vector $\boldsymbol{e}$. Therefore, in the OLA method, we consider $|(\boldsymbol{I}_N - \boldsymbol{R}\boldsymbol{K})\boldsymbol{f}|^2$ and $|\boldsymbol{R}\boldsymbol{e}|^2$ separately using the free parameter α.

Then, let us look at the residual (C.27). We notice that there is no term corresponding to the error magnification. However, it is known that the sum of the estimated variances (C.22) in the RLS method decreases with the increasing α. So, error magnification is controlled by a free parameter α as in the OLA method.